



A University of Sussex PhD thesis

Available online via Sussex Research Online:

<http://sro.sussex.ac.uk/>

This thesis is protected by copyright which belongs to the author.

This thesis cannot be reproduced or quoted extensively from without first obtaining permission in writing from the Author

The content must not be changed in any way or sold commercially in any format or medium without the formal permission of the Author

When referring to this work, full bibliographic details including the author, title, awarding institution and date of the thesis must be given

Please visit Sussex Research Online for more information and further details

Photocatalytic Oxidation of Organic Compounds with Nanocatalysts



Munirah Sulaiman Alhar

Supervisor: Dr Qiao Chen

A Thesis Submitted for the Degree of Doctor of Philosophy

School of Life Sciences

University of Sussex

December 2020

Declaration

I hereby declare that this thesis has not been and will not be, submitted in whole or in part to another University for the award of any other degree.

SignedMunirah Alhar

Acknowledgements

First, my gratitude goes to the Royal Embassy of Saudi Arabia Cultural Bureau in the UK, for granting me a scholarship for this program. I thank the management of the Hail university, Saudi Arabia for making this dream a reality.

I would like to express my sincere gratitude and obligation to my main supervisor, Dr Qiao Chen, for the patient guidance, encouragement and advice he has provided throughout my time as his student. I was incredibly grateful to have a supervisor who cared so much about my work. I also would like to thank my second supervisor, Professor John Spencer for his advice, help and support.

I would also like to extend my appreciation to my nano group past members for their interest and some fruitful discussions about the project: Dr Daniel Commanduer, Dr Emmanuel Kamba, Dr Giacomo Canciani, Dr Thomas Draper, Dr Brnyia Alwhshe, Dr Amin Qasim, Dr Fang Yuanxing. Many thanks to all of them for their efforts and advice. I also want to thank the former MChem students: Jack Davies and Geoffrey Nash for their support during their MChem program.

I would also like to thank the summer students whom it was a pleasure to work alongside. I would finally especially like to thank all those at the University of Sussex who made my time so rewarding especially for kind help from the teaching lab. I like to dedicate my most special thanks to my family for the support they provided me through my entire life.

Summary

This study focuses on the development of high efficiency nanostructures and their applications in the photocatalytic oxidations of organic molecules in a single phase and two phases.

Through in-situ precipitation techniques, cubic Ag_3PO_4 nanocrystals and particle Ag_3PO_4 were successfully synthesised. The precipitation method was used for the preparation of Ag_3PO_4 nanocrystals by reacting with Na_2HPO_4 and using ammonia as the mediate agent to control their morphologies. Furthermore, $\text{Ag}_3\text{PO}_4/\text{TiO}_2$ nanocomposite containing a different proportion of TiO_2 -P25 and Ag_3PO_4 nanocomposites were synthesised. The optimal nanocomposites mixture ratio was determined by investigating their photocatalytic activities by photocatalytic degradation methylene blue. In addition, the relationship between the catalysts morphologies, stability and their photocatalytic activity were studied.

The indirect oxidation of benzyl alcohol (BA) to benzyl aldehyde (BAD) was investigated using Electrochemical (ECO) and Photocatalytic electrochemical oxidation methods (PECO) in two-phase reactions. For the ECO, the oxidation of BA to BAD under different conditions was achieved using a batch reactor set up and using stainless steel as electrodes. While for PECO, TiO_2 nanotubes were synthesised via electrochemical anodization process in fluoride-containing organic electrolytes. Furthermore, the TiO_2 nanotubes were used as photoanode for photocatalytic selective oxidation of benzyl alcohol to benzaldehyde. PECO showed higher BA conversion as well as BAD selectivity comparing to ECO.

Application of biphasic systems can significantly improve the selectivity production. Photocatalytic oxidation of BA to BAD using a TiO_2 photocatalyst and Cl^-

ion as a radical mediator in a biphasic reaction method. An aqueous suspension of commercial TiO_2 -P25 catalyst was used for the oxidation in a batch photo-reactor set up in the photocatalytic oxidation of BA to BAD. The effect of various reaction parameters and conditions on the TiO_2 photo-reactivity were tested. The two phases (organic and aqueous) ratio plays an important role as well as the pH. The effect of catalyst loading, and different types of acid were also studied. The mechanism of the photocatalytic oxidation of BA to BAD was proposed. Finally, the effect phenyl-ring substitution groups on the photocatalytic activity were investigated.

Borrowing hydrogen (BH) or hydrogen autotransfer (HA) methodologies were traditionally used for the production of amines from alcohols. This study investigated photocatalysis's feasibility as an alternative greener process for the N-alkylation of amines using TiO_2 -P25 as the photocatalyst. In the BH or HA process, hydrogen is extracted temporarily by alcohol to form corresponding the intermediate aldehyde or ketone by photocatalyst, making alcohol as an alkylating agent. By condensation with an amine in situ, such an intermediate is converted into an imine. Subsequent addition of converts the imine intermediate to the amine product with a newly formed C-N bond. Initial findings were positive, with low imine intermediate yields indicating that the photocatalytic reaction worked, but the benzyaniline effect was not observed. Optimization experiments were performed, where pH 2 was determined to be the optimal condition for BA oxidation. In addition, aniline was gradually added to the reaction mixture over time by a liquid pump. This controls the increasing feeding of aniline to react with the produced benzaldehyde to avoid aniline's excessive oxidation at the early stage. Finally, the final benzyaniline product was made by reacting with the H_2 gas added into the reaction mixture. Therefore, the photocatalysis is established for the first time as a viable technique for amine N-alkylation.

Nanostructured semiconductor photocatalysts including pure TiO_2 and metal-doped TiO_2 were synthesised through controlled hydrolysis methods and characterized by XRD pattern, BET surface area, photoluminescence emission spectroscopy and UV-Vis diffuse reflectance spectroscopy. Photocatalytic performances of the synthesised NPs were evaluated by photooxidation of benzyl alcohol to benzaldehyde under UV-light irradiation. Evaluation of TiO_2 metal-dopants (mole%) showed that the 0.7% V-doped TiO_2 possessed the lowest bandgap at 2.88 eV and the highest photocatalytic activity of alcohol photooxidation at the rate constant of $62 \times 10^{-3} \text{ min}^{-1}$. This was followed by 0.4 % Fe-doped TiO_2 with a bandgap of 2.94 eV and an alcohol photooxidation rate constant of $60 \times 10^{-3} \text{ min}^{-1}$. The 0.8%Ag-doped TiO_2 did not reduce the bandgap significantly and had a bandgap of 3.00 eV with a modest alcohol photooxidation rate constant of $52 \times 10^{-3} \text{ min}^{-1}$.

Photo-epoxidation of styrene was achieved using the designed reactor with TiO_2 -P25 photocatalyst containing NaCl as a chlorine radical source. Catalyst loading effects on the styrene conversion, reaction products and product selectivities were investigated by GC-MS, and it was found that neutral pH favours the selectivity of the epoxide enantiomers. The photocatalytic epoxidation of styrene was also analysed using various concentration of the NaCl. The photocatalytic epoxidation of styrene mechanism was also proposed.

Table of Contents

Declaration.....	i
Acknowledgements.....	ii
Summary.....	iii
Table of Contents.....	vi
List of Figures.....	xi
List of Abbreviations.....	xviii
CHAPTER 1 Fundamentals of Photocatalytic Synthesis.....	1
1.1 Introduction	1
1.2 Green Chemistry	2
1.2.1 Principles and Benefits of Green Chemistry	3
1.2.2 Catalysis in Organic Synthesis	7
1.2.3 Green Oxidation for Fine Chemical Synthesis	9
1.3 Photocatalytic Oxidation	18
1.4 Semiconductors as Photocatalysts	19
1.4.1 Direct and Indirect Semiconductors	23
1.4.2 Titanium Dioxide Photocatalysis	24
1.4.3 Semiconductor–TiO ₂ Heterojunctions	27
1.5 Optimization of TiO ₂ Photocatalyst	28
1.6 Aims and Objectives.....	31
1.7 Thesis overview	31
CHAPTER 2 Research Instrumentation.....	34
2.1 Introduction	34
2.2 Scanning Electron Microscopy	35
2.3 Energy Dispersive X-Ray Spectroscopy	39
2.4 X-Ray Diffraction	42
2.5 Optical Properties Characterization	46
2.5.1 UV-Vis Absorption Spectroscopy.....	46
2.5.2 UV-Vis Diffuse Reflectance Spectroscopy	48
2.6 Gas Chromatography	51
2.6.1 Flame Ionisation Detection	54
2.6.2 Mass Spectrometry	56
2.7 Photoluminescence (PL) Spectroscopy	59
2.8 Dynamic Light Scattering (DLS)	62

2.9 Specific Surface Area from BET (Brunauer, Emmett and Teller) measurement.....	63
2.10 Proton Nuclear Magnetic Resonance (NMR).....	64
CHAPTER 3 Synthesis of $\text{Ag}_3\text{PO}_4/\text{TiO}_2$ Nanocomposites for Enhanced Photocatalytic Degradation of Aqueous Organic Pollutants.....	
Pollutants.....	68
3.1 Introduction	68
3.1.1 Removal of Organic Pollutants from Water and Wastewater	70
3.1.2 The Structure and Physical Properties of Ag_3PO_4 Photocatalyst.....	73
3.1.3 Optimization of TiO_2 -Based Photocatalytic System.....	75
3.2 Experimental	78
3.2.1 Materials and Reagents.....	78
3.2.2 Preparation of Ag_3PO_4 Nanoparticles	79
3.2.3 Preparation of $\text{Ag}_3\text{PO}_4/\text{TiO}_2$ Nanocomposites.....	80
3.2.4 Preparation of Crystallised Cubic Ag_3PO_4 Nanoparticles	80
3.2.5 Morphological, Crystallinity and Optical Characterization of Ag_3PO_4 Based Nanoparticles and Nanocomposites.....	82
3.2.6 Evaluation of Photoactivity of TiO_2 (P25 and Rutile), Ag_3PO_4 and Their Composites Through The Degradation of MB.....	82
3.3 Results and Discussion	84
3.3.1 Characterization of Pure Ag_3PO_4 and $\text{Ag}_3\text{PO}_4/\text{TiO}_2$ Nanoparticles.....	84
3.3.2 Morphology and Dynamic Scattering Light of Cubic Ag_3PO_4	86
3.3.3 Structure and Composition of Two Types $\text{Ag}_3\text{PO}_4/\text{TiO}_2$ Nanocomposite.....	90
3.3.4 XRD Study of The $\text{Ag}_3\text{PO}_4/\text{TiO}_2$ Nanocomposite	92
3.3.5 UV-Vis Spectra of Ag_3PO_4 Microcrystala(Particle and Cubic) and $\text{Ag}_3\text{PO}_4/\text{TiO}_2$	95
3.3.6 Effect of $\text{Ag}_3\text{PO}_4/\text{TiO}_2$ Nanocomposite Mix Proportions on Photocatalytic Activity.....	100
3.3.7 Photocatalytic Activity of Cubic Ag_3PO_4 on MB Degradation.....	105
3.4 Conclusions.....	107
CHAPTER 4 Electrochemical and Photo- Electrochemical Oxidation of Alcohols to Aldehydes.....	
4.1 Introduction	108

4.2 Experimental	112
4.2.1 Chemical Reagents	112
4.2.2 Chloride-Mediated ECO of BA to BAD.....	113
4.2.3 TiO ₂ Nanotube Preparation for PECO of BA to BAD.....	114
4.2.4 Photoelectrochemical Oxidation Using TiO ₂ NT Films	116
4.3 Results and Discussion	117
4.3.1 Effect of ECO Voltage on Conversion and Selectivity	117
4.3.2 Effect of the Mediator Type and Concentration on ECO	120
4.3.3 Characteristics of The Synthesized TiO ₂ NT for PECO.....	123
4.3.4 Effect of TiO ₂ Annealing Time on PECO.....	127
4.3.5 Effect of Agitation on PECO on BA conversion and BAD selectivity	128
4.3.6 Comparison Between ECO and PECO Under Various Voltages (1.0-3.0V).....	129
4.4 Conclusion	131
CHAPTER 5 Highly Selective Photocatalytic Oxidation of Alcohol to Aldehydes with a Radical mediator in Biphasic	
Reactions.....	133
5.1 Introduction: Synthesis of Carbonyl Compounds	133
5.2 Experimental Section	136
5.2.1 Chemicals Reagents	136
5.2.2 Photocatalytic Oxidation of Alcohols to Aldehydes	136
5.3 Results and Discussion	138
5.3.1 Kinetic Analysis on the Photocatalytic Oxidation of Benzyl Alcohol and its Derivatives.....	139
5.3.2 Catalyst Loading and Catalyst Type	139
5.3.3 Effect of Chloroform to Acid Ratio on the photocatalytic oxidation of BA to BAD	142
5.3.4 Effect of Acid-Type	144
5.3.5 Proposed Reaction Mechanism.....	148
5.3.6 Change in Concentration of Reactants and Products	151
5.3.7 Effect of Phenyl-Ring Substitution on BA.....	152
5.4 Conclusion	155
CHAPTER 6 Photocatalytic N-alkylation of Amine with Alcohol.....	156
6.1 Introduction	156

6.2 Experimental	162
6.2.1 Materials	162
6.2.2 Photocatalytic Reactor Design.....	164
6.2.3 Bi-phasic Photocatalytic Reaction System.....	164
6.2.4 Effect of pH	165
6.2.5 Effect of Aniline Concentration	165
6.2.6 Effect of Hydrogen Injection Rate	166
6.2.7 Effect of Injecting Large Volumes of Aniline Solution	166
6.3 Results and Discussion	167
6.3.1 GC-FID Analysis.....	167
6.3.2 Analysis of the Initial Reaction.....	169
6.3.3 pH Optimization.....	169
6.3.4 Effect of Aniline Concentration/Amount	170
6.3.5 Reduction of Imine with Hydrogen	178
6.4 Conclusion	179
CHAPTER 7 Synthesis and Photocatalytic Properties of Metal-dopedTiO₂.....	181
7.1 Introduction	182
7.1.1 Titanium Dioxide as A photocatalyst.....	182
7.1.2 Optimization of TiO ₂ Photocatalysts	184
7.2 Experiment.....	187
7.2.1 Materials and Reagents.....	187
7.2.2 Synthesis of Metal Doped TiO ₂ Nanoparticles	187
7.2.3 Characterization of metal dopedTiO ₂ photocatalysts	189
7.2.4 Photocatalytic Oxidation of Benzyl Alcohol Using Metal-doped TiO ₂	189
7.3 Results and Discussion	190
7.3.1 Ag-doped TiO ₂ NPs Characterization and Evaluation of its Photocatalytic Activity....	190
7.3.2 Fe-doped TiO ₂ NPs Characterization and Evaluation of its Photocatalytic Activity....	198
7.3.3 V-doped TiO ₂ NPs Characterization.....	206
7.3.4 Comparison Between P25 and Ag-, Fe- and V- doped TiO ₂ NPs.....	211
7.4 Conclusions.....	213
CHAPTER 8 Photocatalytic Asymmetric Epoxidation of Styrene.....	214

8.1 Introduction	214
8.1.1 Photocatalytic Epoxidation	214
8.1.2 Asymmetric Photocatalytic Epoxidation	217
8.2 Experimental	220
8.2.1 Materials and Equipment.....	220
8.2.2 Photocatalytic Reactor Design.....	220
8.3 Results and Discussion	222
8.3.1 GC-MS Analysis.....	222
8.3.2 The Effect of Catalysts (TiO ₂) Loading.....	225
8.3.3 The Effect of Reactor pH Conditions	228
8.3.4 The Effect of Radical Concentration	232
8.3.5 Reaction Mechanism.....	233
8.4 Conclusion	236
CHAPTER 9 Conclusions and Further Work.....	237
9.1 Conclusions.....	237
9.2 Further work.....	240
Bibliography.....	242

List of Figures

Figure 1.1 A schematic diagram of Jabłoński diagram showing the various relaxation pathways of the relaxation of photoexcited electrons.	15
Figure 1.2 A schematic diagram of the band transition during electronic excitation in semiconductors.....	21
Figure 1.3 Band positions of several semiconductors with some selected redox potentials measured at pH 7. Adapted from Michael G. ¹⁷¹	22
Figure 1.4 A schematic diagram displays the bandgap for various semiconductors as a function of the momentum of electrons. (A) Direct semiconductors, a direct electron transfer is necessary due to the momentum match. (B) Indirect semiconductors, an indirect electron transfer is needed due to a shift in momentum.	24
Figure 1.5 Bandgap structures and carrier charge migration of three categories of semiconductor–TiO ₂ heterojunctions. ¹⁸⁶	28
Figure 1.6 A schematic diagrams of crystal structures of the three main phases of TiO ₂	29
Figure 2.1 The cross-sectional view of a scanning electron microscope.	37
Figure 2.2 The electron excitation, (A) the primary (PE) and secondary electrons (SE), (B) back scattered electrons (BSE) generation, (C) x-ray emission processes and (D) Auger electron generation caused by the reabsorption of x-rays.	41
Figure 2.3 The interaction of x-rays with the atomic planes of a crystal governed by Bragg's law.	42
Figure 2.4 An illustration of components of a typical double beam UV-vis spectrophotometer.....	46
Figure 2.5 A diagram illustrating the principles of an integrating sphere in measuring the diffuse reflectance of a given sample.	50
Figure 2.6 A schematic description of principles components of a gas chromatograph set-up.	51
Figure 2.7 A schematic diagram of the key components of an FID detector.	55
Figure 2.8 A schematic diagram of an ion trap detector used in GC-MS.....	57
Figure 2.9 Jablonski diagram displaying photoluminescence.....	60
Figure 2.10 PL spectrophotometer instrumental setup. It was adopted. ²²⁵	61
Figure 2.11 Illustration of NMR.....	65
Figure 2.12 Two proton energy levels, from quantum mechanics, in a magnetic field of magnitude B_0	66
Figure 3.1 The molecular structure of methylene blue dye.	71
Figure 3.2 The representation of pathway of MB degradation with corresponding molecular fragments and their mass.	72

Figure 3.3 Unit-cell structure of cubic Ag_3PO_4 , showing (A) ball and stick and (B) polyhedron configurations. Red, purple, and blue spheres represent O, P, and Ag atoms, respectively. Adapted from Xinguo, Ma. ²⁶³	74
Figure 3.4 A schematic diagram of the band structure and the photo-induced charge separation process in $\text{Ag}_3\text{PO}_4/\text{TiO}_2$ composite.....	77
Scheme 3.1 The scheme of the formation process of the Ag_3PO_4 (cubes and particles) using different precursors.	79
Figure 3.5 Experimental setup for the photocatalytic degradation of MB.....	83
Figure 3.6 (A) SEM images of the Ag_3PO_4 microparticles with a scale bar of 5 μm and (B) DLS measurement of particle size distribution.....	85
Figure 3.7 Representative SEM images and DLS measurements of cubic Ag_3PO_4 microcrystals synthesised with different concentration of NH_3^+ : (A, B) 0.10 M, (C, D) 0.15 M, (E, F) 0.20 M and (G, H) 0.30 M.	87
Figure 3.8 XRD spectral patterns of Ag_3PO_4 samples synthesised without (A) and with (B) the addition of NH_3	89
Figure 3.9 An SEM image of the $\text{Ag}_3\text{PO}_4/\text{TiO}_2$ -P25 (60:40) nanocomposite.	91
Figure 3.10 An SEM image of the $\text{Ag}_3\text{PO}_4/\text{TiO}_2$ -rutile (60:40) nanocomposite.	92
Figure 3.11 XRD pattern of $\text{Ag}_3\text{PO}_4/\text{TiO}_2$ -P25 nanocomposites of different weight ratios. Triangle and dot denote TiO_2 -P25 and Ag_3PO_4 , respectively.....	93
Figure 3.12 XRD pattern of $\text{Ag}_3\text{PO}_4/\text{TiO}_2$ -rutile nanocomposites of different weight ratios. Dot, triangle, asterisk, and cross denote Ag_3PO_4 , TiO_2 , AgNO_3 , and NaH_2PO_4 , respectively.	95
Figure 3.13 UV-Vis diffuse reflectance spectra of pure Ag_3PO_4 and $\text{Ag}_3\text{PO}_4/\text{TiO}_2$ nanocomposites. ...	96
Figure 3.14 Tauc plot of $\text{Ag}_3\text{PO}_4/\text{TiO}_2$ -P25 (60:40 wt%) nanocomposite.....	97
Figure 3.15 (A) UV-Vis absorption spectra of cubic Ag_3PO_4 of (0.15 M $[\text{NH}_3^+]$) microcrystals and particle Ag_3PO_4 and (B) corresponding Tauc plots of Ag_3PO_4 microcrystals.....	98
Figure 3.16 (A) PL emission spectrum of $\text{Ag}_3\text{PO}_4/\text{TiO}_2$ P25 (60:40 wt%) nanocomposite under UV-vis irradiation. (B) PL excitation spectra of pure Ag_3PO_4 , $\text{Ag}_3\text{PO}_4/\text{TiO}_2$ P25(60:40 wt%) physical mixture and $\text{Ag}_3\text{PO}_4/\text{TiO}_2$ P25 (60:40 wt%) nanocomposite.	99
Figure 3.17 Variation of MB absorption against irradiation time using Ag_3PO_4 , P25, $\text{Ag}_3\text{PO}_4/\text{P25}$ nanocomposites, in darkness and without catalyst, under visible light.....	101
Figure 3.18 The optimised reaction rate constants (k) from different catalysts.	102
Figure 3.19 Variation of MB absorption against irradiation time using $\text{Ag}_3\text{PO}_4/\text{rutile}$ composites...	104

Figure 3.20 Photocatalytic activity of Ag_3PO_4 microcrystals formed at different concentrations of NH_3 , C1 (0.10 M), C2 (0.15 M), C3 (0.20 M), C4 (0.30 M) and IP are the irregular Ag_3PO_4 particles without addition of NH_3 . Inset: photos of MB decomposed by Ag_3PO_4 microcrystals of C2.	105
Scheme 4.1 Selective oxidation of benzyl alcohol to benzaldehyde by two-phase electrolysis.	110
Figure 4.1 The batch reactor assembly for the radical-mediated electrochemical oxidation of BA. .	113
Figure 4.2 The anodization set with two-electrode and applied voltage remotely controlled by a computer.....	115
Figure 4.3 The suggested mechanism of the hydroxide islands formation.	115
Figure 4.4 The batch reactor assembly for the chloride-mediated photocatalytic electrochemical oxidation (PECO) of BA.....	116
Figure 4.5 The effect of various voltage on the current densities.	118
Figure 4.6 (A) The effect of voltage on BA conversion and (B) the effect of voltage on BAD selectivity (reaction time, 2h).	119
Figure 4.7 Effect of the reaction time on the conversion of BA, the selectivity of BAD and Benzoic acid at 3.0V.	120
Scheme 4.2 The possible mechanism for the mediator biphasic oxidation of BA. ³¹⁹	121
Scheme 4.3 Extension of the reaction pattern for electrochemical incineration of organics suggested by Comninellis to the case of active chlorine-mediated electrochemical incineration. ³²⁸	122
Figure 4.8 The effect of different types of mediators on (A) oxidation of BA and (B) formation of BAD.	123
Figure 4.9 SEM images of the Ti plate surface after (A) polishing, (B) 30s acid treatment, (C) 90s acid treatment and (D) after acid treatment for 90 s followed by ultrasonic cleaning in water before anodization.	124
Figure 4.10 SEM images of (A) the top view and (B) the bottom view of TiO_2 nanotubular arrays...	125
Figure 4.11 XRD pattern of TiO_2 NT films annealed at 450° C for different durations from 30 to 180 mins at time intervals of 30 mins.....	126
Figure 4.12 Effect of TiO_2 NT annealing time on the BA conversion and BAD yield at constant 3.0 V for 1 h of the reaction time.	127
Figure 4.13 The effect of agitation rate on the BA conversion rate (%) and BAD selectivity (%).	128
Figure 4.14 Comparison of BA conversion rate (%) using ECO and PECO (reaction time,1h).	130
Figure 4.15 Comparison of (A) BAD selectivity (%) and (B) BAD yield produced using ECO and PECO (reaction time,1 h).	131
Figure 5.1 A diagram of the reactor setup for the photocatalytic oxidation of benzyl alcohol to aldehyde.....	137

Figure 5.2 (A) Kinetics plot of benzyl alcohol photooxidation following pseudo-first-order. (B) The effect of catalyst loading on the reactivity of the TiO ₂ photocatalyst. The system reactivity increased with increasing catalyst loading. An optimal loading was established at 4g/L.....	141
Figure 5.3 (A) Optimisation curves of volume % effects of chloroform and all HCl concentration and (B) Optimisation curves of volume % effects of chloroform at the optimised HCl concentration(0.25M).....	142
Figure 5.4 The effect of pH on the reactivity of the TiO ₂ photocatalyst.....	144
Figure 5.5 The effect of acid-type on the reactivity of TiO ₂ with the presence of NaCl. HNO ₃ , HCl, H ₂ SO ₄ and with no acid.	145
Figure 5.6 The single aqueous phase reaction mechanism proposed by Higashimoto <i>et al.</i> ³⁶²	149
Figure 5.7 The mechanism of biphasic photocatalytic oxidation of BA in the presence of O ₂ using TiO ₂ under UV light.	150
Figure 5.8 The change in concentration of the reactants (BA) and the products (Benzoic acid and BAD) through a 20 hour reaction period.	151
Figure 5.9 The change in percentage conversion of BA, yield and selectivity of BAD through a 20-hour photocatalysis period.....	152
Figure 5.10 A Hammett plot for the oxidation of BA to BAD. Y-axis is the Log (k _x /k _H) while X-axis is the σ is the substituent constant.	154
Scheme 6.1 C-N bond formation by different methods. A) Traditional method including alkyl halides and B) Greener pathway by borrowing hydrogen.	157
Scheme 6.2 Alcohol N- alkylation using an iron catalyst. Cp*H=1,2,3,4,5-pentamethylcyclopenta-1,3-diene. 1,2,4-TMB = 1,2,4-trimethylbenzene.....	158
Scheme 6.3 The mechanism of hydrogen autotransfer; X= CH, N; [M] = transition-metal catalyst. .	160
Scheme 6.4 Chemical structure of two transition-metal complexes catalyst for N-alkylation of amines.....	161
Scheme 6.5 Photocatalytic N-alkylation of aniline with benzyl alcohol under various conditions. ...	162
Figure 6.1 A photocatalytic reactor design. The metal halide lamp is enclosed in a water-cooled inner jacket.....	164
Figure 6.2 A typical GC-FID spectrum of the sample from the organic layer during the reaction.	167
Figure 6.3 (A) Rate and (B) yield of BDA formation at different pH values.	170
Figure 6.4 (A) Rate and (B) yield of BDA formation against aniline quantity.	171
Figure 6.5 The yield of BDA (vs BA) against the injected aniline throughout the reaction period.....	172
Figure 6.6 GC-FID data of the organic layer under acidic conditions.	173
Figure 6.7 BDA yield when an aniline solution was injected autonomously.	174

Figure 6.8 BDA yield change over time at different aniline flow rates.	175
Figure 6.9 BDA yield compared to the different aniline delivery rates.	176
Figure 6.10 BDA Yield compared to the rate of aniline delivery when using a large stock aniline solution.	177
Figure 6.11 The yield of benzylaniline against time.....	178
Figure 7.1 Mechanism of TiO ₂ photocatalysis: hv ₁ : pure TiO ₂ ; hv ₂ : metal-doped TiO ₂	183
Figure 7.2 Procedure for synthesizing of metal doped TiO ₂ photocatalysts.	188
Figure 7.3 XRD patterns of (A) Pure TiO ₂ , and Ag-doped TiO ₂ nanoparticles calcined at 400°C, (B) 0.8mol% Ag-doped TiO ₂ nanoparticles calcined at 400, 500 and 600°C.	191
Figure 7.4 Photoluminescent (PL) emission spectra of pure TiO ₂ , and Ag-doped TiO ₂ (0.2, 0.5, 0.8 mol. %) NPs under UV-vis irradiation.....	195
Figure 7.5 (A) Band gaps obtained from Tauc plots calculated from diffuse reflectance spectra of pure and Ag-doped TiO ₂ NPS.(B) Effect of increasing Ag content on the bandgap energy.	196
Figure 7.6 Photocatalytic activity of Ag-doped TiO ₂ at different Ag concentrations (A) and various calcination temperatures of 0.8%Ag-dopedTiO ₂ (B).	197
Figure 7.7 The XRD patterns of (A) TiO ₂ , and Fe-doped TiO ₂ nanoparticles calcined at 400°C, (B) 0.4mol% Fe-doped TiO ₂ nanoparticles calcined at 400, 500 and 600°C.....	199
Figure 7.8 Photoluminescence spectra of pure and Fe-doped TiO ₂ nanoparticles at different dopant concentrations calcined at 500°C.	202
Figure 7.9 (A) Band gaps obtained from Tauc plots calculated from diffuse reflectance spectra of pure and Fe-doped TiO ₂ NPS. (B) Effect of increasing Fe content on the bandgap energy.	203
Figure 7.10 Photocatalytic activity of (A) Fe-doped TiO ₂ at different Fe concentrations and (B) various calcination temperatures of 0.4%Fe-dopedTiO ₂	204
Figure 7.11 The XRD patterns of (A) TiO ₂ and V-doped TiO ₂ nanoparticles, and (B) 0.7mole%V-doped TiO ₂ nanoparticles at different calcination temperatures.....	206
Figure 7.12 Photoluminescence spectra of pure and V-doped TiO ₂ nanoparticles at different dopant concentrations.	209
Figure 7.13 Photocatalytic activity of (A) V-doped TiO ₂ at different V concentrations and (B) different calcination temperatures.....	210
Figure 7.14 Kinetics plot of benzyl alcohol photooxidation by P25, synthesised TiO ₂ , 0.8Ag-dopedTiO ₂ , 0.4Fe-dopedTiO ₂ and 0.7V-dopedTiO ₂	211
Figure 8.1 Epoxide chemical structure.....	215

Figure 8.2 General reaction scheme for the photocatalytic epoxidation of styrene using a TiO ₂ catalyst and O ₂ gas under mild conditions with continuous illumination from a light source. Benzaldehyde is not seen but contains side products of the reaction.	217
Figure 8.3 (A) Chemical structure of the catalyst produced by the Sharpless method. (B) Mechanism of Sharpless asymmetric epoxidation depicting the origin of the stereo-selectivity. (C) Chemical structure of the Jacobsen's catalyst. (D) Mechanism of the Jacobsen's asymmetric epoxidation. ⁵¹⁴⁻⁵¹⁶	219
Figure 8.4 Custom-built photocatalytic reactor.	221
Figure 8.5 GC-MS chromatography of the final reaction mixture after 30 min from the photocatalytic reaction.	223
Figure 8.6 The effect of TiO ₂ photocatalyst loading on the styrene conversion. Styrene conversion increased with increasing TiO ₂ loading, with an optimal conversion rate (40 %) corresponding to an optimal photocatalyst load of 0.20 g. Further TiO ₂ loading beyond 0.20 g did not increase the conversion rate.	226
Figure 8.7 The effect of TiO ₂ photocatalyst load on enantiomeric excess(ee). A photocatalyst load of 0.2 g was determined to be optimal for an optimal ee of 50 %.	227
Figure 8.8 The GC-MS chromatography of the photoepoxidation reaction in acidic, neutral and basic mediums.	228
Figure 8.9 The effect of pH (pH 4-12) on the styrene epoxidation conversion rate. Styrene conversion increased with increasing pH with an optimal conversion rate (40 %) corresponding to the neutral pH 7. Alkaline pH (pH > 7-14) resulted in a decline in the styrene conversion rate to 30 %.	229
Figure 8.10 The effect of pH (pH 4-12) on the purity of styrene oxide. Enantiomeric excess (ee%) of styrene oxide was lowest (0%) at pH 4 to 6. This indicated there was a racemic mixture of styrene oxide enantiomers, which reflects low purity.	230
Figure 8.11 The effect of pH condition on benzaldehyde yield. The BAD yield was high (7-11%) at lower acidic pH range (4-6), which declined from pH 7-12 (4.8 - 2.8 %). Thus, lower pH conditions favoured BAD while higher pH conditions did not favour BAD.	231
Figure 8.12 The effect of radical source concentration on styrene conversion. Styrene conversion decreased with increasing NaCl concentration from 54% (at 0.0 NaCl) to 40% (at 1 M NaCl).	232
Figure 8.13 The effect of chlorine radical concentration on (A) The purity of styrene oxide and (B) Benzaldehyde yield.	233
Figure 8.14 Representation of photocatalytic mechanism for the epoxidation of styrene using TiO ₂ and molecular oxygen anion proposed by Ohno <i>et al.</i> ⁵²¹	234

Figure 8.15 Representation of photocatalytic epoxidation mechanism of styrene in a biphasic system.

..... 235

Scheme 8.1 A) The chloride species formed in the aqueous phase.^{319,328} B) The epoxidation reaction

mechanism includes the Mn species.⁵²⁴ 235

List of Abbreviations

$^{\circ}\text{C}$	Degrees Celsius
K	Degrees Kelvin
M	Moles per litre
wt %	Percentage weight
α	Absorption coefficient of a material
γ	Initial adsorption velocity
E	Photonic efficiency
λ	Wavelength
-r	Rate of a chemical reaction
σ	Hammett constants
ν	Frequency
ξ	Photonic efficiency of reactions
Φ	Quantum yield
A	Absorbance
AO	Atomic orbitals
E _g	Band gap energy
C%	Percent conversion
Å	Angstrom
CVD	Chemical vapour deposition
CB	Conduction band
<i>J</i>	Current
<i>D</i>	Crystalline domain size
DI	Deionised
θ	Diffraction angle
DC	Direct Current
e^{-}	Electron
<i>m</i>	Electron mass
EDX	Energy dispersive x-ray
S ₀	Ground energy state
FID	Flame ionisation detector

GC	Gas chromatography
h	Plank constant
h^+	Hole
$^1\text{HNMR}$	Proton nuclear magnetic resonance
HOMO	Highest occupied molecular orbital
ICDD	International centre for diffraction data
IQE	Internal quantumefficiency
L-H	Langmuir Hinshelwood
LUMO	Lowest unoccupied molecular orbital
TTIP	Titanium tetraisopropoxide
UV	Ultraviolet
UVA	Ultraviolet light ($315 \leq \lambda \leq 400$ nm)
VBM	Valence band maximum
Vis	Visible
VOCs	Volatile organic compounds
XRD	X-ray diffraction
FWHM	Full width half maximum
MS	Mass spectroscopy
MW	Average molecular weight
eV	Electron volt
E	Energy
EDX	Energy dispersive x-ray spectroscopy
p	Momentum
SEM	Scanning electron microscopy
NRs	Nanorods
NTs	Nanotubes
PL	Photoluminescence
PV	Photovoltaic
V_{RHE}	Potential vs Reversible Hydrogen Electrode

η	Power
BA	Benzyl alcohol
BAD	Benzaldehyde
ECO	Electrochemicaloxidation
BDA	Benzylideneaniline

CHAPTER 1 Fundamentals of Photocatalytic Synthesis

1.1 Introduction

Organic synthesis is an important process for the production of unique organic molecules, crucial to chemical and pharmaceutical industries.¹ It entails the synthesis of organic compounds using tailored chemical synthesis routes, making it possible to produce complex, tailor-made, biologically active products and heterocyclic pharmaceutical compounds amongst other new organic materials.^{1,2} It empowers organic chemists and chemical technologists to explore countless molecules for industrial and pharmaceutical applications. However, many organic synthesis routes generate hazardous by-products or chemical wastes that are energy-dissipating and environmentally unfriendly.³ For instance, the efficiency analysis of organic synthesis routes used in the chemical and pharmaceutical industries indicated that the amount of chemical waste generated was about 5–100 times for every kilogram of useful products.³ This generation of chemical waste poses great challenges in chemical resource conservation, leading to environmental and health concerns.³

Chemical wastes, some of which are toxic, are a threat to the environment due to its tendency to resist the most known natural/biological degradation processes. For instance, large quantities of organic pollutants in water have remained a significant environmental challenge, threatening aquatic ecological systems and human health. Common organic pollutants, including pesticides, aromatic hydrocarbons, phenols, plasticizers, biphenyls, detergents, oils, greases and antibiotics, have disrupted natural ecosystems worldwide.³⁻⁷ They are produced as a result of industrial and agricultural activities. Persistent organic pollutants (POPs), typically containing

benzene rings, are of great concern because they are toxic and can persist in the environment over long periods and bioaccumulate in biological systems to toxic levels.⁸ These pollutants include polychlorinated biphenyls, polychlorinated dibenzo-*p*-dioxins and dibenzofurans, besides some organochlorine pesticides, such as hexachlorobenzene, dichlorodiphenyltrichloroethane, dibenzo-*p*-dioxins (dioxins) and dibenzo-*p*-furans (furans). These POPs enter a human body through water and food chain, where they exhibit a high tendency to bioaccumulate, biomagnifying in most natural ecosystems.⁹ Benzene-containing POPs are biologically active and have been linked to different types of cancer.^{4,8} These can be addressed through strategies used for the organic synthesis of various tailor-made compounds. This is the concept of green chemistry, also known as environmentally benign chemistry or sustainable chemistry in organic synthesis. It addresses chemical resource utilization and chemical waste challenges by applying 'smart' chemical principles throughout the synthesis processes: feedstocks, reactions, solvents and separations.³ Besides, green chemistry provides possible strategies for the decomposition of some organic wastes in the environment, especially in the air, water and wastewater.

1.2 Green Chemistry

The concept of green chemistry is increasingly embraced to safeguard the environment, solve the global energy crisis and control organic chemical pollutants.^{3,10,11} In the broadest sense, green chemistry is a sustainable chemical technology that uses a set of principles to reduce or eliminate the use or generation of hazardous solvents and reagents. It also strives to create renewable resources for chemical feedstocks and thus minimize the output of potentially hazardous chemical bioproducts and energy consumption.^{12,13} It applies across the life cycle of a chemical product, including its design, synthesis, manufacturing, application to industrial or

pharmaceutical processes, and ultimate disposal.¹⁴ It also includes the prevention of accidents and pollution. The acceptance of the green chemistry concept has been stimulated by globally increasing implementation of strict environmental laws that limit the use or emission of certain organic compounds known to be unfriendly to the environment.¹⁵⁻¹⁷

1.2.1 Principles and Benefits of Green Chemistry

According to the United States Environmental Protection Agency (2017), 12 principles of green chemistry have been developed by Paul Anastas and John Warner.¹⁸ The first principle is the prevention or reduction of chemical waste. This principle depends on the design of chemical syntheses, focusing on preventing toxic wastes that require treatment or clean-up. The concept of E-factor (*E*) was introduced to quantify the production of waste, as shown in Equation 1.1. It was defined as the mass ratio of the waste to the desired product. The waste includes everything but the desired product. *E* takes the chemical yield into account and includes reagents, solvent losses, all process aids and even fuel (although this is often difficult to quantify).

$$E = \frac{\text{Mass of waste}}{\text{Mass of desired products}} \times 100 \quad (\text{Eqn 1.1})$$

The second principle is to maximize the use of atoms by minimizing the loss of atoms during synthesis from starting materials (chemical feedstocks) to the final product.^{3,19,20} This is especially important in organic syntheses that use multiple reagents in stoichiometric quantities calculated as atom economy (*AE*), as shown in Equation 1.2. Although the concept of *E* might be difficult to quantify, *AE* is much easier to quantify and compare. In contrast, *AE* is applied to individual steps but the *E* factor is applied to a multistep process, thus facilitating a holistic assessment of a complete process.²¹ The highest *AE* seeks to maximize the incorporation of chemical feedstocks into the final product of any given reaction. The essence of this principle is to increase

chemical efficiency to reduce the quantity of chemical feedstock, hence eliminating side products and chemical wastes.^{3,14,17}

$$AE = \frac{\text{The molecular weight of the desired product}}{\text{The molecular weight of all products}} \times 100 \quad (\text{Eqn 1.2})$$

The third principle is to design less hazardous organic synthetic routes. The goal of this principle is to use and generate chemical substances with little or no toxicity to humans or the environment.^{3,14,22} Chemical reactions often involve toxic chemicals as reagents or by-products. However, a toxic catalyst had better catalytic activity compared with its alternatives. This principle states that, whenever possible, toxic chemicals should be avoided or at least contained.

The fourth principle is the design of safer chemical products, which are efficacious in their respective intended use, yet have little-to-no toxicity to natural ecosystems or the environment.²³ This is in tandem with the fifth principle, which recommends, where possible, the avoidance of solvents, mass separation agents and other chiral auxiliary chemicals. Safer options and reaction conditions should be carefully selected to reduce chemical hazards where the use of the aforementioned chemicals is unavoidable. Both the fourth and fifth principles aim to first assure safe handling of chemical feedstocks and chemical products during manufacturing. Further, they aim to protect the environment from potentially unfriendly toxic chemicals.^{3,14}

The sixth principle is all about designing energy-efficient synthesis routes. It encourages the design of routes involving chemical reactions that can be activated and sustained at room temperature and normal atmospheric pressure, whenever possible. The goal of this principle is to enhance energy efficiency during chemical synthesis, thus not only saving costs but also protecting the environment from the excessive use or dissipation of energy.^{3,14} Most chemical reactions are activated by thermal energy, that is heating reactants, in turn increasing the kinetic energy of

molecules by increasing their travelling speed. A portion of this kinetic energy is converted into potential energy during the collision, which allows the formation of transition states, leading to the formation of desired products. Although a majority of commercial chemical processes use this approach, thermally activated reactions are normally less energy efficient. Reaction vessels and transfer tubes need to maintain the temperature, as chemical products also carry the thermal energy. Reactors can be thermally insulated, and the thermal energy in chemical products can be extracted. However, the extraction of thermal energy can never be 100% efficient, and sometimes it is challenging to reuse this energy. In some chemical processes, energy is the dominant cost. Thus, new energy-efficient chemical reaction activation processes need to be developed to reduce energy wastage and production cost.

In this thesis, I developed a green approach based on photocatalytic oxidation processes. Molecules are activated to excited states using photons with photocatalysts. The process is operated at room temperature and atmospheric pressure with minimal energy cost. Ideally, photons can be trapped in a reaction vessel until every photon is used, thus minimizing energy wastage. The technical challenge in a photocatalytic oxidation process is to control the reaction kinetics and pathways. Oxidation readily occurs, and organic molecules can be simply converted into CO₂ and water. Hence, we developed a unique biphasic system to protect organic products.

The seventh principle is the use of renewable chemical feedstocks rather than depletable chemical resources, such as petrochemicals, natural gas, coal and mining products. Renewable feedstocks, typically from agricultural or recycled products, are considered green. Thus, the goal of this principle is to use sustainable environmentally friendly sources of chemical feedstock to reduce the depletion of natural resources.^{3,14}

The eighth principle is to avoid the use of unnecessary derivatization, which entails the use of blocking groups, protection/deprotection of groups and temporary modification of physical/chemical processes during organic synthesis.²⁴ One of the most effective ways of doing this is to use enzymes or site-specific catalysts. Enzymes are so specific that they can often react with one reactive site of a molecule and leave the rest of the molecule. Hence, the protection of groups is often not required. Chemical derivatives, which often require additional reagents, increase the generation of chemical waste. Alternatively, this is achieved by avoiding temporary modifications in chemical feedstocks to force the selectivity of products.^{3,14,24} This is consistent with the ninth principle encouraging the use of catalysts, rather than stoichiometric reagents, which are often used in excess and only once. The purposes of using catalysts in chemical syntheses are to enhance product selectivity and reduce chemical wastes, besides avoiding unnecessary derivatization.^{3,14} Using a specific catalyst in a chemical reaction allows the change in reaction pathways through the formation of new complexes in the transition state. Therefore, it can activate specific chemical bonds within reactants to facilitate a lower energy barrier. The challenge here is to design and synthesize such a specific catalyst before understanding the kinetics and reaction mechanisms.

The tenth principle is the design of chemical products that are biodegradable to nontoxic components by natural environmental processes at the end of their function. The goal of this principle is to ensure that materials that cannot be recycled or reused degrade into innocuous molecules rather than toxic substances. This helps avoid disrupting natural ecosystems by the accumulation of these materials in the environment. The eleventh principle is to monitor and control pollution in real-time to minimize or eliminate its effect. The technology used for this purpose includes portable

and affordable chemical sensors. These generate signals to detect the increasing levels of waste before irreversible environmental damage is caused. Finally, the twelfth principle is to minimize the potential for accidents related to chemical reactions. This is achieved by either choosing chemical feedstock (solids, liquids or gases) with clearly known physical and chemical properties or changing the reaction process to lower the reaction temperature and pressure. It aims to minimize the potential for catastrophic chemical accidents, including explosions, fires and releases to the environment.¹⁴ My project of developing photocatalytic organic reactions could, in principle, minimize hazards of chemical reactions by performing them at room temperature and atmospheric pressure. The benefits of green chemistry in organic synthesis are as follows: enhance production, reduce the impact of chemicals on the environment, increase safety standards for chemical industry workers and consumer products, and reduce global warming by decreased greenhouse gas emission and reliance on fossil fuels.¹⁷ The research work in this project offers the opportunity to explore green approaches while maintaining a reasonable reaction rate and *AE*.

1.2.2 Catalysis in Organic Synthesis

The use of catalysts in organic syntheses (as well as the decomposition of undesired chemical by-products) is one of the most widely studied principles of green chemistry.^{15,25,26} This is partly because multiple catalytic strategies exist for any chemical synthesis route or chemical decomposition. Attempts to choose an optimal catalytic strategy from many options have never been straightforward and often require a trial-and-error approach.

Organic synthesis involves two types of catalysis: homogenous and heterogeneous. The choice depends on the number of phases in which the catalytic reaction is conducted.

Homogeneous catalysis is a single-phase reaction commonly involving miscible reactants and catalysts. It provides benign synthesis routes with numerous advantages. It offers the best contact between reactants and catalysts and hence can effectively lower the activation energy. Therefore, it reduces the input thermal energy, and the reaction has higher selectivity and yield, with fewer unwanted by-products. However, homogeneous catalysts have a common major limitation: separation is required to recover the catalyst,²⁷⁻²⁹ which involves the use of extra energy and organic solvents. Homogeneous catalysts are in the form of large molecular compounds, which may not be thermally stable during the separation from the chemical products.^{29,30} Hence, sometimes it may not be possible to recover the expensive catalysts. Meanwhile, homogeneous catalysis is normally carried out in a batch reactor rather than in a continuous-flow reactor because the catalyst, reactants and products are in the same phase. Hence, the reaction process is interrupted at the end of the reaction, leading to a change in reaction conditions and generating more chemical waste. This makes homogeneous catalysis expensive in terms of the use of energy and solvents, with more chemical waste and the potential loss of the catalyst.

Heterogeneous catalysis is either bi- or multiphasic, where catalysts are immiscible with reactants, that is, catalysis is normally in the solid phase while reactants and/or products are in the gas or liquid phase. Heterogeneous catalysts, such as Au/Al₂O₃,³¹⁻³³ Au/C,³⁴⁻³⁶ Au/TiO₂,³⁷⁻³⁹ Au/CuO,⁴⁰⁻⁴² Au/Pd–TiO₂,⁴³⁻⁴⁵ and Au/SiO₂,⁴⁶⁻⁴⁸ are superior to homogeneous catalysts because they are associated with higher catalytic efficiencies and less environmental pollution.⁴⁹ In fact, about 90% of all industrial organic synthesis processes are based on heterogeneous catalysis.⁴⁹ The disadvantage of this multiphase arrangement is that the contact between catalysts and reactants is limited by the surface area of the solid.⁵⁰⁻⁵² Hence, efforts were made

to develop nanostructured catalysts that can improve the contact area and increase the reactivity. Meanwhile, the specific size of the mesoporous structure helps improve the reaction selectivity.⁵³⁻⁵⁵ The advantage of heterogeneous catalysis is not only that the selectivity and reactivity can be controlled independently but also that the catalyst can be readily separated from reactants and products. Solid catalysts are relatively easy to immobilize within continuous-flow reactors, which are popularly used in the chemical industry. A chemical reaction continues until the catalyst becomes inactive. Most heterogeneous catalytic reactions are carried out at high temperature and pressure. In addition, the chemical feed rate is controlled because the temperature and pressure are relatively easy to adjust. The *AE* is usually high in optimized heterogeneous catalysis; the energy cost is also normally very high. In fact, globally, the Haber–Bosch process, which produces ammonia, consumes 3%–5% of all-natural gas produced. This is equivalent to ca. 1%–2% of the energy generated worldwide.^{56,57} Therefore, a major part of the cost in such industrial processes is due to energy consumption. Furthermore, catalysis at high temperature speeds up catalyst deactivation, reducing selectivity and product yield.⁵⁸ This led to an urgent need to develop alternative chemical processes that can efficiently operate at low temperature and normal pressure, specified in the third and sixth principles of green chemistry.^{3,14,22}

1.2.3 Green Oxidation for Fine Chemical Synthesis

Green chemistry promotes the use of green oxidation catalysts that can mediate oxidation at mild conditions with high selectivity and conversion yield. Aggressive oxidizing reagents are mostly used in a conventional oxidation process, such as hydrogen peroxide (H_2O_2),⁵⁹⁻⁶² ozone (O_3),⁶³⁻⁶⁶ fluorine (F_2),⁶⁷⁻⁶⁹ chlorine (Cl_2),⁷⁰⁻⁷² nitric acid (HNO_3) and nitrate compounds,⁷³⁻⁷⁵ sulfuric acid (H_2SO_4),⁷⁶⁻⁷⁸ peroxydisulfuric acid ($\text{H}_2\text{S}_2\text{O}_8$),⁷⁹ peroxymonosulfuric acid (H_2SO_5),^{80,81} potassium

permanganate (KMnO_4),⁸²⁻⁸⁴ chromium trioxide (CrO_3),⁸⁵⁻⁸⁷ and dichromate ($\text{Cr}_2\text{O}_7^{2-}$).⁸⁸⁻⁹⁰

All these reagents have serious drawbacks, such as difficulty in operation, extreme conditions (high temperature), long reaction times and high costs. For instance, hydrogen peroxide is a powerful reagent that reacts with a large range of substances. It is therefore diluted during transport as a safety measure. However, high concentrations are required for purification. Hydrogen peroxide can irritate the eyes, skin, and lungs and change and damage the DNA.^{91,92} Furthermore, it causes cell death.⁹³ Ozone is also advantageous for oxidation reactions. However, it produces undesired by-products with a high risk of causing cancer, as well as chlorine.⁹⁴ During the process, high salt loading is used, which requires several washing stages to reduce the salt content.⁹⁵ These reagents are environmentally aggressive, strong oxidants, and toxic.⁹⁶ Chromium (Cr) compounds also pose health and environmental risks. Cr (VI) can cause heart diseases, allergic reactions, nose irritation and bleeding weakened immune system, lung cancer and even death. High concentrations of Cr in water due to metal disposal can damage the gills of fish.^{97,98}

On the contrary, oxygen (O_2) is a renewable oxidant regularly used in the chemical industry.⁹⁹⁻¹⁰¹ Although O_2 is freely available in the atmosphere, it has two major limitations. The O_2 molecule is very stable. A pair of chemical bonds are present between O atoms: a σ bond and a π bond. Hence, the bond order is 2. The O-O bond length is 1.208 Å with a bond energy of 498 kJ/mol.¹⁰²⁻¹⁰⁵ In comparison, the O_3 and H_2O_2 have bond orders of 1.5 and 1, with O-O bond lengths of 1.277 and 1.490 Å, respectively. Similarly, the bond energy of the O-O bond in O_3 and H_2O_2 is 364 kJ/mol and 142 kJ/mol, respectively, which are very low compared with those in O_2 .¹⁰⁶⁻¹⁰⁸ Table 1.1 summarises the comparison between O_2 , O_3 and H_2O_2 .¹⁰⁹ The table shows

that O_3 and H_2O_2 are much more reactive than O_2 . Oxidation with O_2 requires the breaking of the O-O double bond to form reactive atomic oxygen radicals. Therefore, expensive noble metals or metal oxides, including ruthenium (Ru), rhodium (Rh), palladium (Pd), silver (Ag), iridium (Ir) and platinum (Pt), are used in heterogeneous oxidation processes to activate the O_2 molecule.¹¹⁰⁻¹¹⁴ These processes also require high reaction temperature and pressure to dissociate or weaken adsorbed O_2 molecules. They can be much greener if they are carried out at lower temperature and pressure, avoiding the use of costly noble metals. Another problem encountered when using dissociated O_2 as an oxidizing agent is that the activated oxygen species is normally very reactive. Most organic molecules are readily completely mineralized into CO_2 and H_2O .¹¹⁵⁻¹¹⁷ Thus, oxidation selectivity towards desired products is difficult to maintain. Many heterogeneous processes try to improve the selectivity by either reducing the catalyst reactivity or controlling the reaction duration (optimizing the chemical flow rate).¹¹⁸⁻¹²⁰ Developing more selective oxidation strategies with less environmental impact is in high demand.¹⁷

Table 1.1 Direct comparison of bond order, bond length and bond energy between O_2 , O_3 and H_2O_2 .

Molecule	Structure	Bond order	Bond length (Å)	Bond energy (kJ/mol)
O_2	O=O	2	1.208	498
O_3	O=O-O	1.5	1.277	364
H_2O_2	H-O-O-H	1	1.490	142

The design of oxidation catalysis processes following the principles of green chemistry has the potential to enhance selective oxidation and produce green chemical products at lower energy costs and with less environmental impact. However, such processes in green organic synthesis are yet to be fully explored

because oxidation catalysis in organic synthesis is influenced by many factors. The choice of a catalyst, the nature of a solvent and the physical state of reactants and their dispersion can affect the contact and mixing of reactants, which in turn affect the reaction kinetics. Reaction conditions, especially the pH, temperature, pressure and concentrations of reactants, can directly impact the reaction selectivity and conversion.

For instance, selective partial oxidation of both aliphatic and aromatic alcohols to their respective aldehydes has been traditionally achieved using several homogeneous catalysts involving heavy metals (such as Pd, Ir, Ru and Mo) or organic oxidizing reagents (such as pyridinium chlorochromate)¹²¹⁻¹²⁴ to block further oxidation to carboxylic acids.¹²⁵⁻¹²⁷ Given that homogeneous catalyst is typically in the same phase as the target reactants, their optimal conditions require a batch reactor with high pressure and/or organic solvents. These reactor conditions increase not only the cost but also environmental pollution due to the use of large amounts of organic solvents and toxic heavy metals. These metals are generally difficult and expensive to treat, and hence the process can significantly disrupt environmental and ecological stability.⁴⁹ Alternatively, organic oxidizing reagents can also be used for the partial oxidation of alcohols. However, they increase environmental pollution due to their hazardous and toxic nature.¹²⁸ For instance, pyridinium chlorochromate, an important reagent in organic synthesis, is used primarily for the selective oxidation of alcohols to carbonyl compounds. This tedious reaction workup, carcinogenicity and aquatic toxicity make pyridinium chlorochromate hazardous to the natural environment.¹²⁹

Apart from conventional heterogeneous catalysis, which uses thermal energy to activate catalytic reactions, the interest in photocatalysis for oxidation has increased. Photocatalysis can be both heterogeneous or homogeneous with a potential to catalyse partial or complete oxidation of organic compounds as desired.¹³⁰

In such processes, visible and ultraviolet (UV) photons, rather than heat, are used to excite molecules or catalysts. For homogeneous photoreactions, either molecular catalysts or reactants can be excited to their electronic excited states, promoting electrons from the highest occupied molecular orbital (HOMO) to the lowest unoccupied molecular orbital (LUMO) and thus facilitating further reactions. It has all the advantages and disadvantages of a conventional homogeneous reaction. It typically uses a large quantity of solvents with equal difficulty to purify products and recover functional catalysts. Generally, a π bond, rather than a σ bond, is more likely to be photoexcited because π electrons require lower energy for excitation. The direct excitation of σ electrons typically needs high-energy UV light ($\lambda < 250$ nm), which can result in uncontrolled dissociation of reactants before oxidation, thus impacting the selectivity and yield of the photo-oxidation process.

In homogenous photocatalysis systems, reactants and photocatalysts are in the same phase. These reactions are usually limited to liquid phases. Furthermore, organic homogeneous photocatalysts have been used widely in photosynthetic reactions.¹³¹ Transition metal complexes are the most commonly used homogeneous photocatalysts.¹³² The use of inorganic complexes as homogeneous photocatalysts has several advantages. They are clearly displayed by the cation of tris(bipyridine)ruthenium (II) chloride ($[\text{Ru}(\text{bpy})_3]\text{Cl}_2$), $[\text{Ru}(\text{bpy})_3]^{2+}$. Only mild photon energies are needed ($\lambda \approx 450$ nm) to generate high-energy electrons through metal-to-ligand charge transfer.¹³² High quantum efficiency (QE), long excited-state lifetime, and low energy requirement make $[\text{Ru}(\text{bpy})_3]^{2+}$ one of the most important homogeneous photocatalysts for the exploitation of solar energy. The separation and recovery of catalysts in a homogenous system are difficult due to the contact between the catalyst and reagents. This complication highly inhibits the industrial application of

homogeneous photocatalysts. The synthesis of organometallic complexes usually requires complicated procedures involving the use of expensive reagents.¹³³ Hydrogen is produced by three efficient homogeneous catalytic systems, for example, in aqueous solutions using π -conjugated platinum(II) arylacetylide sensitizers in concert with a cobaloxime catalyst.^{133,134}

Heterogeneous photocatalysis, on the contrary, uses solid-state catalysts while reactants are dissolved in a liquid or gas phase. Unlike transition metal catalysts, which have continuous electronic states, semiconducting transition metal oxides (STMOs) have an energy region with an empty density of states (a conduction bandgap). Photons are absorbed by STMO catalysts to excite the electrons from the valence band maximum (VBM) to the conduction band minimum (CBM). The energy difference between the VBM and CBM defines the bandgap energy. STMOs are typically used as photocatalysts due to their suitable bandgap energies and band edge positions.¹³⁵ The valence band (VB) represents the highest occupied states dominated by the O^{2-} orbital. Meanwhile, the conduction band (CB) represents the lowest unoccupied states dominated by the empty orbital of the metal ion. When a photon has energy larger than the bandgap, it can be absorbed by an STMO catalyst. In this process, a hole is created following the excitation of an electron in the VB.¹³⁶

The existence of the bandgap implies that no states exist to facilitate the recombination of an electron (e) and hole (h) directly within a system.¹³⁷ Therefore, photoexcited electrons in the CB, as well as holes in the VB, are relatively stable with a limited lifetime. With the existence of an electron-hole pair (e–h pair), a nanocrystal can be regarded as a nano battery with the photo energy stored as electric energy. Such a battery is capable of driving electrochemical reactions on its surface with chemical components in the electrolyte, with a relatively low energy barrier. However,

if this energy is accumulated in the catalyst for longer than the e–h pair lifetime, the electrons move to the VB and recombine with the corresponding hole. During this process, the excess energy is released either as heat or as photons. If the excess energy is released in the form of light, it is conventionally defined as photoluminescence. The intensity of this luminance signal can be used to indicate the charge recombination rate.¹³⁸ Such exciton recombination is undesirable in a photocatalytic process because it reduces the QE of the initially absorbed photons. However, such recombination can be effectively minimized if the e–h pair lifetime is extended or the charge separation is improved.¹³⁹ Commonly, during the introduction of dopants into composite materials, an internal electrical field is formed at the interface due to the difference in the electron affinity of the STMO and dopant. This field can drive photoexcited electrons and holes to move in opposite directions, which results in a better separated e–h pair, in turn improving the QE of the photocatalytic process. Thus, the doping of vanadium¹⁴⁰, copper and nitrogen¹⁴¹ in the titania structure shows a remarkable absorption shift towards the visible region compared with pure TiO₂ powder (P25 Degussa). Both Teruhisa and Ohno groups noted that S-doped TiO₂ photocatalysts caused significant absorption in the visible region and increased photodegradation of methylene blue.^{142,143}

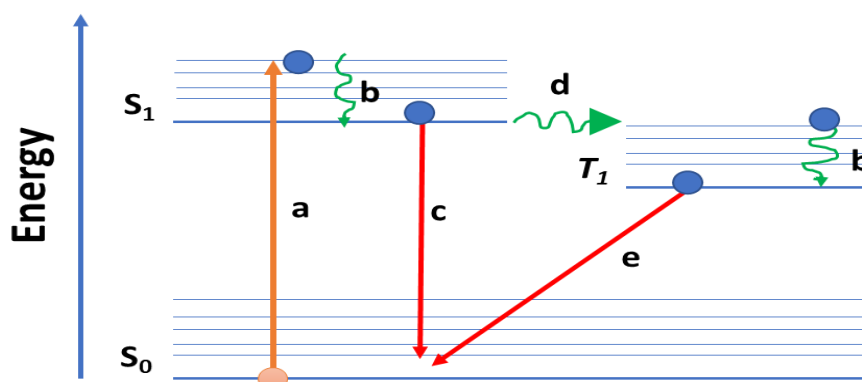


Figure 1.1 A schematic diagram of Jablonski diagram showing the various relaxation pathways of the relaxation of photoexcited electrons.

When a molecule absorbs a photon, electrons move to the excited state from the HOMO, as indicated by *a*, Figure 1.1. Kasha's rule states that a nonradiative internal transition occurs in the excited electrons at a higher vibrational state, thus moving them to the vibrational ground state in the LUMO, as indicated by *b* in Figure 1.1.¹⁴⁴ If the photoexcited electron directly transitions to the LUMO, then it is prohibited from transferring directly to the orbital's lowest vibrational energy state in line with the Franck–Condon Principle. The electron is instead subjected to a nonradiative process to reach the lowest vibrational energy state of the LUMO before subsequent electronic transitions as indicated by *c* Figure 1.1. The excited electrons are then moved to a state of relaxation, which occurs in two main pathways. The process relaxes the excited electrons from the LUMO to the HOMO in a radiative transition process from S_1 to S_0 , as shown in Figure 1.1. Consequently, excess energy is emitted through fluorescence in the form of photons, as indicated by *c* in Figure 1.1. However, a change in the spin state of the excited electron from a single to a triplet (T_1) can also occur through intersystem crossing (ISC). The concept brings about the second pathway, as indicated by *d* in Figure 1.1.

A loss in energy for the electron in T_1 brings it back to S_0 . During this process, photons are continually emitted through phosphorescence, as indicated by *e* in Figure 1.1. The intersystem crossing means more excited electrons undergoing fluorescence compared with those undergoing phosphorescence.¹⁴⁵

The determination of QE is important to estimate the efficiency of a photochemical reaction. QE is defined based on the quantity of incident light and photogenerated electrons within a specified time. It is expressed mathematically as

$$QE = \frac{\text{Photogenerated electrons}}{\text{Incident photons}} \quad (\text{Eqn 1.3})$$

Equation 1.3 is very significant. However, it only applies to photovoltaic cells and similar systems that generate electric current by direct light irradiation. The photovoltaic cells only respond to wavelengths of specific energies. Thus, the determination of internal quantum energy is of importance. The concept only accounts for the number of photons absorbed by a given material and is therefore considered to be preferential. The population formed in the excited state plays a crucial role in photochemical reactions. The subsequent sections will provide insight into the role played by photoexcited electrons in photocatalytic and photosynthetic reactions.

A series of different reactions are initiated after a light is introduced, inducing photochemical reactions. This study mainly focused on the chemical interactions that occur between reacting species because of the resulting transformation of toxic compounds into industrially useful chemicals that are less toxic and industrially useful.

When several chemical species come together, intense interactions occur between them. The rate at which these reagents interact limits the efficiency of a photochemical reaction. In essence, the quantum yield (Φ) also plays a role in determining the efficiency of a photochemical system. The quantum yield is defined as the ratio of the number of molecules going through a reaction to the number of photons absorbed during the reaction, as expressed in Equation 1.4.

$$\Phi = \frac{\text{Molecules undergoing reactions}}{\text{Absorbed photons}} \quad (\text{Eqn 1.4})$$

Preference is often given to the photonic efficiency of reactions (ξ) because the experimental determination of the exact amount of species going through reactions is not always easy. On the contrary, the photonic efficiency is defined as the ratio of the number of product molecules to the number of photons absorbed as expressed in Equation 1.5. The equation is also used to quantify the extent of the effect of photonic excitation in chemical reactions.

$$\xi = \frac{\text{Reaction products}}{\text{Absorbed photons}} \quad (\text{Eqn 1.5})$$

Photocatalysis and photosynthesis are the two main categories to which several forms of photochemical reactions belong.¹⁴⁵

An effective photocatalysis process can facilitate either reductive reactions (using excited electrons) or oxidative reactions (using generated holes) to produce reduced or oxidized products, respectively. For instance, a large number of studies investigated the reduction of CO₂ on TiO₂ and other metal oxides.¹⁴⁶ Abundant solar energy can convert CO₂ into fuels such as methane. Previous studies focused on the development of nanostructured photocatalysts.^{147,148} Also, photocatalytic oxidation has been widely used to degrade organic compounds using TiO₂ as a photocatalyst due to its superior characteristics such as low cost, chemical stability and nontoxicity. Usually, CO₂ and H₂O are the final products.¹⁴⁹⁻¹⁵¹ Photocatalytic redox reactions occur on the surface of a photocatalyst. During the catalytic process, excited electrons/holes and gas or liquid reactants meet on the surface of STMOs simultaneously. Hence, photocatalysts exist generally in the form of nanoparticles (NPs) or nanoscale thin films to maximize the surface area with the best light illumination. Such forms are clearly distinct from the conventional thermally activated catalysts, where only the surface area and pore dimensions are essential to control.

1.3 Photocatalytic Oxidation

Photocatalysis finds a useful application in the oxidation of alcohols to aldehydes and the decomposition of deleterious, benzene-containing, organic pollutants to simpler, benign molecules. It is an important strategy in green chemistry for the organic synthesis and the neutralization of chemical pollutants (in water and wastewater). Photocatalytic oxidation efficiency is based on the efficiency of electron-hole ($e^- + h^+$)

pairs to generate highly oxidative hydroxyl radicals (OH^\bullet), superoxide radicals ($\text{O}_2^{\bullet-}$) and sulfate anion radicals ($\text{SO}_4^{\bullet-}$), which oxidize alcohols to aldehydes. For instance, advanced photo-oxidation processes (APOP) have become feasible for the degradation of benzene-containing organic species.¹⁵² APOP relies on highly reactive radical species, such as HO^\bullet , $\text{O}_2^{\bullet-}$ and $\text{SO}_4^{\bullet-}$, generated from photochemical processes.¹⁵³ These radicals exhibit very strong oxidizing potentials, making them good candidates for the oxidative decomposition of a wide range of benzene-containing organic pollutants.¹⁵⁴ However, the photochemical decomposition of organic pollutants is not a spontaneous and efficient process, and therefore a photocatalyst must be present.

Heterogeneous photocatalytic oxidation of hazardous organic compounds in aerated aqueous systems enhances the selective oxidation of target organic compounds in wastewater treatment.^{155,156} Transition metal oxides are good photocatalyst candidates for the photocatalytic decomposition of deleterious organic compounds using UV light from sun rays due to their semiconductor properties. When a semiconductor is irradiated with a UV light source of sufficient energy, they generate high-energy-state ($e-h$) pairs. During this process, the electron is excited from the VB to the CB of the semiconducting oxide, becoming (e_{CB}^-) and thus resulting in the formation of a positive hole (h_{VB}^+) in the VB as shown in Equation 1.6.



1.4 Semiconductors as Photocatalysts

Photocatalysts refer to semiconductor solids crystalline in nature, which initiate reactions in the presence of light but are not used up in the overall reaction.¹⁵⁷ For a photocatalytic reaction to being considered efficient, it must have a photo-active catalyst. Ideally, solar light must be able to activate the reaction effectively.

Furthermore, the catalyst must also be chemically and biologically inert, photostable, inexpensive and nontoxic.

Most of the photocatalysts reported do not meet the aforementioned criteria. For instance, GaAs, PbS and CdS are toxic and easily corroded, rendering them insufficiently stable for catalysis in aqueous media. ZnO is also unstable because it readily dissolves in an acidic or a basic aqueous solution and the reaction yields Zn(OH)_2 on the surface of the particle, which makes the catalyst inactive after some time.¹⁵⁸ Fe_2O_3 , SnO_2 and WO_3 all have a CB edge at an energy level below the reversible hydrogen potential,^{159,160} which results in a bottleneck for the entire process because the photocatalyst releases photoexcited electrons that do not have enough reduction power for water. In semiconductor particles, electrons can be excited from the VB (the highest energy band occupied by electrons) to the CB (the lowest unoccupied energy band).^{161,162} Generally, anion species such as O_2^- in oxides dominate the VB states, whereas empty states of metal cations dominate the CB states. Figure 1.2 illustrates the electronic excitation and transition that occur within the bands of a semiconductor. A particle must first be supplied with energy for electrons to be excited. The energy supplied must be equal to or greater than the energy gap between VBM and CBM.¹⁶³⁻¹⁶⁵ When photons or heat excite electrons, they leave a positively charged hole (h^+) as they transit from the VB to the CB, as denoted by *a* in Figure 1.2. This results in the generation of an electron-hole pair, and the pair requires energy to dissociate into free electrons in the CB and holes in the VB. If the electron-hole pair is not dissociated, it is considered as an exciton, which is a single particle.

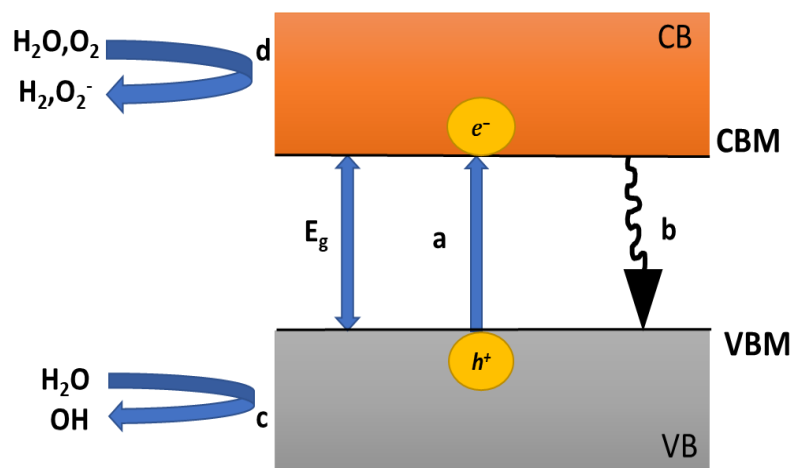


Figure 1.2 A schematic diagram of the band transition during electronic excitation in semiconductors.

The excitation depends on the intensity of light coupled with appropriate wavelength and material thickness. A photocatalyst can only remain active if targeted molecules quickly trap the e^- - h^+ pair generated from photonic excitation. The trapping is crucial in helping to separate charge and reducing the incidence of recombination denoted by b in Figure 1.2. This also helps reduce charge recombination/fluorescence by reducing charge mobility. Ultimately, photoexcited electrons and holes travel to the surface of the photocatalyst particle. If sufficient redox potential is left with these electrons and holes, they carry out surface redox reactions, which create radicals in instances where H_2O and O_2 are used as the reaction media. The highly reactive OH^\bullet comes from the oxidation of adsorbed water or OH^- . Similarly, the reduction of molecular oxygen to superoxide ($O_2^{\bullet-}$) can also be induced by reducing the power of electrons. Highly reactive species can drive organic reactions, such as photo-epoxidation of alkenes and degradation of microorganisms and organic pollutants.^{166,167}

High charge mobility is an essential property of semiconductors, which enables the application of semiconductors to the fields of photovoltaics, photodegradation and photoelectrolysis.¹⁶⁸⁻¹⁷⁰ Before an electron and a hole recombine, oxidation must

occur. Thus, photoexcited electrons travel towards the cathode, while holes travel to the surface to facilitate oxidation. This process reduces the redox potential of the electron and hole, also using a lot of energy. Thus, the transport of electrons and holes restricts the overall kinetics in instances where the mobility is not high enough.

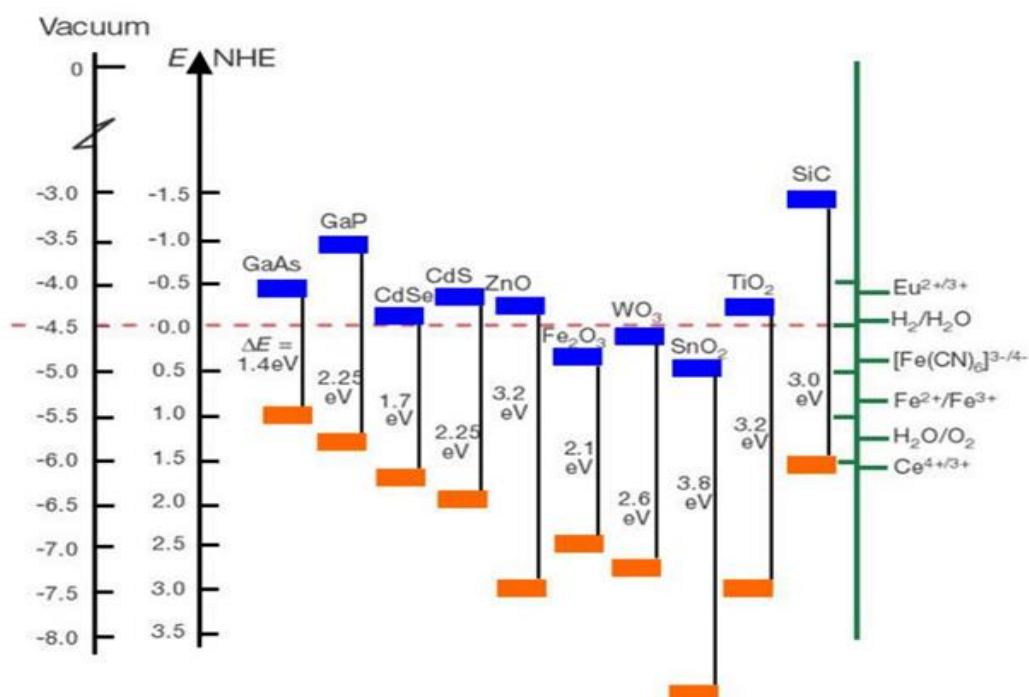


Figure 1.3 Band positions of several semiconductors with some selected redox potentials measured at pH 7. Adapted from Michael G.¹⁷¹

Generally, bandgaps of semiconductors are important in influencing photocatalytic activities of semiconductors. Bandgaps are determined by the nature of the crystal in terms of the electronic configuration and arrangement of atoms (ions). Different semiconductors exhibit different bandgaps as shown in Figure 1.3. The blue colour represents the lower edge of the CB, while the orange colour represents the upper edge of the VB as shown with the corresponding bandgap expressed in electron volt (eV). Using the vacuum level or the normal hydrogen electrode (NHE) as the reference, various band energies of semiconductors are indicated. The standard potentials of several redox couples are also presented on the right, relative to the standard hydrogen electrode potential (Figure 1.3).¹⁷¹

1.4.1 Direct and Indirect Semiconductors

In semiconductors, the bottom of the conduction and the top of the valence band have different values of electron momentum in the k space. The k space is created in one of three directions in the p space; it is frequently three-dimensional but principally can have any definite number of dimensions. However, the r space is a set of position vectors; it has the dimensions of length and defines a point in space. The p space is a set of momentum vectors in a physical system with the units of [mass] [length] [time]⁻¹. The k space is a set of wave vectors; it has the dimensions of reciprocal length.

Semiconductors are classified as direct and indirect semiconductors according to a forbidden change in the momentum associated with the electronic transition from the VB to the CB, as shown in Figure 1.4. The VBM has the same electronic momentum as the CBM in the direct bandgap of semiconductors. Its electronic transition is described as a direct transition because the momentum is conserved during the excitation. Electrons can rapidly recombine with holes because electrons tend to lower the energy of holes for a semiconductor with a direct bandgap. In this electron transition, photons with energy $h\nu$ are released in the recombination process, without any change in the electron momentum (red arrow). For an indirect semiconductor as shown in Figure 1.4B, the CBM and the VBM have different values of electronic momentum. Subsequently, a change in momentum is needed for the electronic transition from the VB to the CB. In addition, without the shift in momentum, the excited electron will not relax from the lowest energy state in the CB to the maximum energy state in the VB. The momentum needed during the excitation and relaxation process is usually given in the form of phonons (which are the vibration of atoms in the crystal lattice) for such an indirect bandgap system. The electrons recombine with the VB holes after relaxation and emit photons with energy ($h\nu$) (dark red arrow). Typically, these transitions are prohibited and

comparatively slow. In certain cases, the recombination in the semiconductor of the indirect bandgap is non-irradiative in nature and typically results in heat due to energy coupling with phonons, (green arrow).

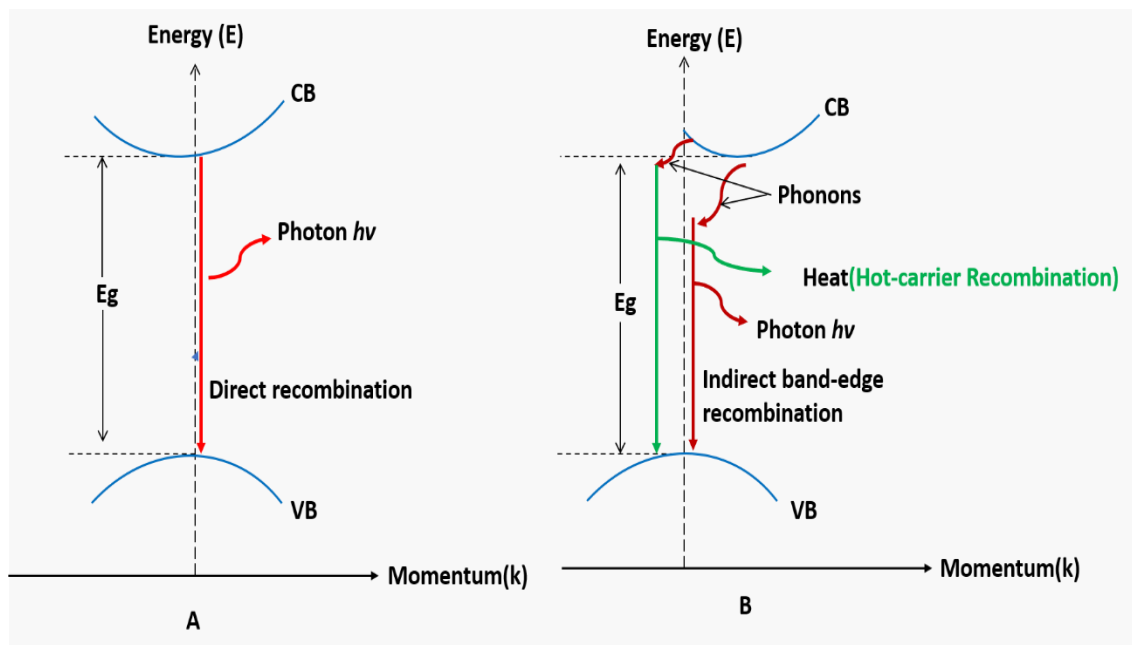


Figure 1.4 A schematic diagram displays the bandgap for various semiconductors as a function of the momentum of electrons. (A) Direct semiconductors, a direct electron transfer is necessary due to the momentum match. (B) Indirect semiconductors, an indirect electron transfer is needed due to a shift in momentum.

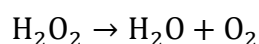
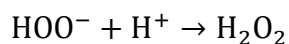
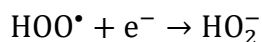
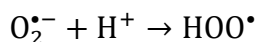
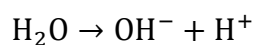
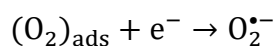
The properties and efficiency of semiconductor metal oxide are partly influenced by the type, size, and morphology of the crystal. With dimensions ranging from a few nanometers to several hundred nanometers, nanostructured metal oxides give a broad surface-to-volume ratio that is substantially greater than that of the bulk material. Therefore, by synthesizing metal oxides into nanostructures, the efficiency of these materials could effectively be increased.¹⁷²⁻¹⁷⁴

1.4.2 Titanium Dioxide Photocatalysis

TiO₂ is the most commonly used photocatalyst at present. Several novel heterogeneous photocatalytic reactions have been reported using TiO₂ as a photocatalyst for many applications, including solar cells, photocatalytic hydrogenation

and environmental treatments.¹⁷⁵ This is because of its stability under light irradiation; it is both chemically and biologically inert, less expensive and readily available in industrial quantities.¹⁷⁶ Regarding chemical stability, TiO_2 is mostly stable under extreme photoreactor conditions, particularly under strongly acidic or alkaline aqueous conditions. TiO_2 was demonstrated by Honda and Fujishima in 1972 to be highly efficient in the photocatalytic degradation of aquatic and atmospheric organic compounds. In a photocatalytic system, photoactivated TiO_2 initiated a chain photoreaction by splitting water molecules to generate highly reactive hydroxyl and peroxide radicals. These reactive radicals are useful for the degradation of organic compounds. Thus, the TiO_2 -based photocatalytic system is already being applied for the photodegradation of organic substances for environmental sanitation.¹⁷⁷

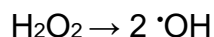
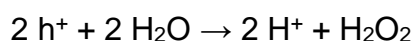
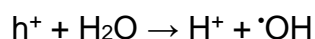
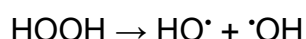
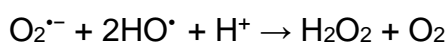
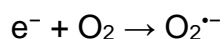
In an aqueous TiO_2 -based photocatalytic system, photogenerated electrons (e_{CB}^-) attack dissolved O_2 molecules in water to generate superoxide radicals ($\text{O}_2^{\cdot-}$), which subsequently attack protons generated from the dissociation of water to produce an intermediate radical (HOO^\cdot).¹⁷⁸ The intermediate radical (HOO^\cdot) is also attacked by photogenerated electrons (e_{CB}^-) to produce a hydroperoxyl ion ($\text{HO}_2^{\cdot-}$), which subsequently undergoes protonation to hydrogen peroxide (H_2O_2). H_2O_2 undergoes decomposition to generate O_2 molecules, restarting the chain reaction (Reaction Scheme 1.1). However, efficiencies of these photocatalytic systems are not always optimal because a fraction of photogenerated electrons (e_{CB}^-) and holes (h_{VB}^+) always undergo recombination, effectively reducing the photocatalytic efficiency.

Reaction Scheme 1.1: generate oxygen molecules

The reaction is sustained between positive holes and the available moisture to generate hydroxyl radicals ($\bullet OH$). The generated $\bullet OH$ radicals are both highly oxidative and nonselective with a redox potential (E_0) of approximately +3.06 V.^{155,179,180} For example, heterogeneous photocatalytic oxidation of a wide variety of organic compounds has been widely studied using polycrystalline titanium (IV) dioxide (TiO_2). This photocatalyst is activated by a UV light source and oxygen (or air). In the field of photocatalysis, solar UV radiation is considered a potentially sustainable photocatalyst activator as opposed to artificial irradiation.¹⁸¹ Given that TiO_2 has a relatively low bandgap energy of approximately 3.2 eV compared with photons of solar UV light (3–30 eV), exposure to sunlight can spontaneously photo generate the e–h pair on the surface of the TiO_2 photocatalyst as shown in Equation 1.7.^{155,182}



The photogenerated e–h pair ($e^- + h^+$) initiates oxidative (Reaction Scheme 1.2) and reductive (Reaction Scheme 1.3) reactions to generate the highly oxidative $\bullet OH$.¹⁸³ TiO_2 as a photocatalyst has been widely studied.^{130,147,184,185} Heterogeneous photocatalytic oxidation of hazardous organic compounds in aerated aqueous systems enhances the selective oxidation of the target organic compounds in wastewater.^{155,156}

Reaction Scheme 1.2: Oxidative reactions due to positive hole (h_{vb}^+)**Reaction Scheme 1.3:** Reductive reactions due to excited electron (e^-)**1.4.3 Semiconductor–TiO₂ Heterojunctions**

Excitons can be generated due to the excitement that occurs when a semiconductor forms a heterojunction with TiO₂. However, the respective positions of CB and VB of the semiconductor relative to the NHE influence the transition process. Generally, semiconductor–TiO₂ heterojunctions have three main categories, as shown in Figure 1.5.¹⁸⁶ The C-I is the first category where both semiconductors are either n-type or p-type. In this case, the CB of TiO₂ is higher than that of semiconductor X, while the VB of TiO₂ is lower than that of X. This means that electrons from the CB and the VB hole of TiO₂ migrate to those of X, an example of X is Fe₂O₃. The second category is C-II, where electrons and holes move in different directions. Electrons migrate from the CB of TiO₂ to that of Y, while holes migrate from the VB of Y to that of TiO₂; examples of Y include SnO. In this case, the excitons are readily separated, hence extending photo charge lifetime within the composite catalyst, making it preferable.

The third and final category is C-III, where charge carriers migrate in an identical direction like C-II. However, the CB and VB positions of the two semiconductors, TiO₂ and Z, have a huge gap between them. As a result, the effective separation and migration of charge carriers require a high amount of energy.¹⁸⁶

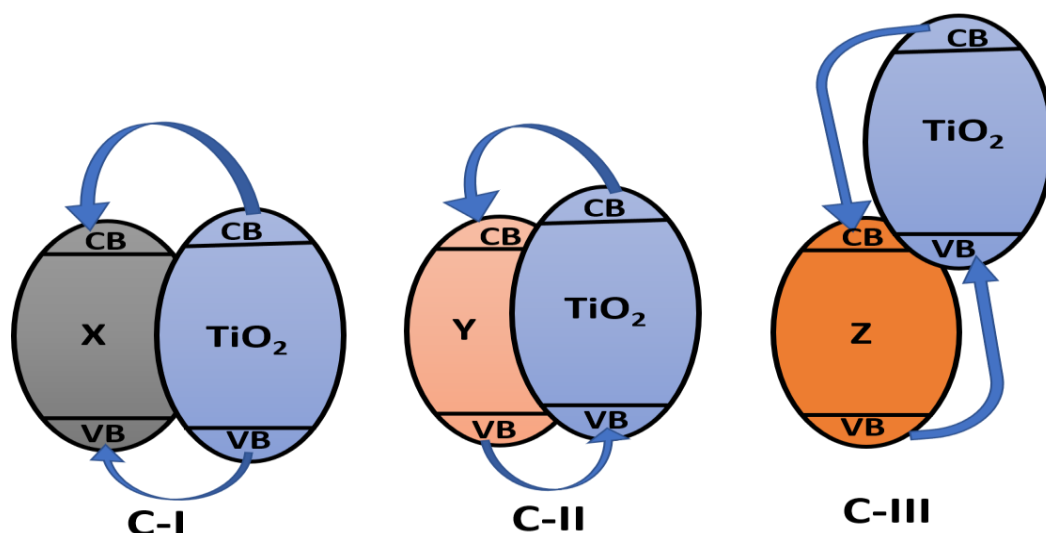


Figure 1.5 Bandgap structures and carrier charge migration of three categories of semiconductor–TiO₂ heterojunctions.¹⁸⁶

Numerous reports have been published on heterojunctions between two wide bandgap semiconductors, ZnO–TiO₂. Pan *et al.*¹⁸⁶ reported the fabrication of TiO₂ nanobelt–ZnO nanorod heterojunction with improved charge separation attributed to the reduction of quasi-Fermi energy level. ZnO has a bandgap of 3.37 eV.¹⁸⁷ Also, the CB and VB have a slightly more negative potential compared with that of TiO₂ (3.2 eV).¹⁸⁸ In heterojunctions, the alignment of the Fermi level determines the relative positions of CBM and VBM. When heterojunctions of these semiconductors are irradiated, holes are generated in the VB and electrons are excited to the CB. Ultimately, the potential difference between semiconductors makes electrons migrate to the CB of TiO₂, which is accompanied by the migration of holes from the VB of TiO₂ to that of ZnO.^{189,190}

1.5 Optimization of TiO₂ Photocatalyst

Among the major TiO₂ polymorphs (rutile, anatase and brookite) (Figure 1.6), the two main polymorphs are rutile and anatase. The anatase phase shows the most effective photocatalytic activity¹⁹¹⁻¹⁹³ due to its higher density of localized states and absorbed

$\cdot\text{OH}$ and slower recombination of photogenerated charge carriers compared with the rutile phase.¹⁹⁴⁻¹⁹⁶ Rutile has a smaller bandgap (3.03 eV) compared with anatase (3.20 eV).¹⁹⁷ Another main drawback of TiO_2 as a photocatalyst is the large bandgap, which allows the absorption of wavelengths of light falling within the UV range only, making up only 5%–7% of the solar spectrum.¹⁹⁸ This limits the efficiency of photocatalytic systems and has been the subject of much interest in green chemistry.¹⁸⁵

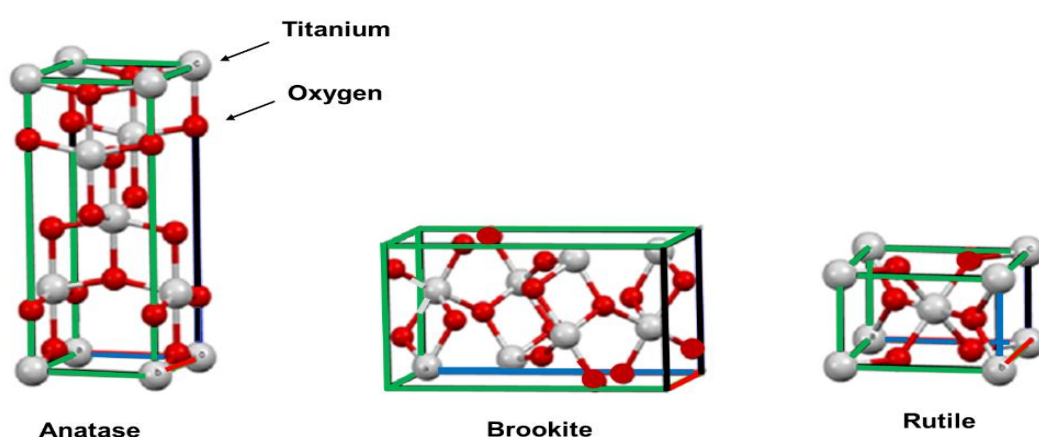


Figure 1.6 A schematic diagrams of crystal structures of the three main phases of TiO_2 .

Optimization of the anatase TiO_2 photocatalyst for advanced oxidation is multifactorial. It requires optimization of the morphology (size and shape) of major catalytic TiO_2 polymorphs (rutile and anatase), minimization of e–h recombination and optimization of photoreactor conditions.¹⁹⁹ To start with, the catalytic activity of any given solid catalyst is influenced by its size and shape. The smaller the particle sizes of a solid catalyst, the higher its catalytic activity. This is because the smaller the particle size, the higher the catalytic surface area. The surface area of TiO_2 is significantly low compared with those of other transition metal catalysts.²⁰⁰ It can be enhanced further by reducing its size to the nanoscale. TiO_2 NPs are commercially available worldwide for use in a wide range of applications. TiO_2 NPs have a small

surface area to volume ratios and exhibit different physical and chemical properties compared with fine particle analogues, which may alter their catalytic activity.²⁰¹

Regarding shape, TiO₂ NPs also have the advantage of a better nanocrystalline or microcrystalline structure rather than an amorphous structure. The morphology of a nanomaterial (geometric shape and dimension) has a significant impact on its physical and chemical properties. For instance, hollow-shaped TiO₂ morphologies exhibit a greater photocatalytic decomposition of dimethyl sulfoxide compared with TiO₂ spheres.²⁰² Calcination temperatures influence the size, surface area and nanocrystalline structure of TiO₂ NPs. Therefore, it is possible to optimize TiO₂ photocatalysts by determining the ideal calcination temperature. Further, e–h recombination in the TiO₂ photocatalyst underpins its suboptimal photocatalytic performance. Which can be restricted or inhibited by combining TiO₂ with other light-activated semiconductors, especially transition metals.²⁰³ Lowering the TiO₂ bandgap has the advantage of allowing the absorption of a broader spectrum of light for photocatalysis. This can be achieved by the doping of TiO₂, with a dopant of choice attached to Ti or O sites of the TiO₂ photocatalyst.²⁰⁴⁻²⁰⁸

Finally, as photocatalytic reactor conditions may be extreme in terms of acidity and alkalinity, it is desirable that TiO₂ exists predominantly as anatase. A recent study by Tsega and Dejene demonstrated that subjecting TiO₂ to pH 4.4–6.8 did not alter its structural, morphological and optical properties, with the anatase phase being predominant. However, under a more extreme acidity condition (pH 3.2), rutile, brookite and anatase phases of TiO₂ coexisted, with rutile being the predominant phase. Therefore, a photocatalytic reactor pH range of 4.4–6.8 is optimal for TiO₂, which can be easily controlled.²⁰⁹ Electrochemical oxidation with and without

photocatalysis is an important green oxidation strategy, especially in the biphasic system. This has been used for the oxidation of alcohols to aldehydes.²¹⁰

1.6 Aims and Objectives

The goals of the thesis were as follows: (1) to develop green chemistry oxidation catalysts by the optimization of physical and chemical properties of a TiO₂ photocatalyst; (2) to optimize single- and two-phase heterogeneous photocatalytic oxidation for both organic synthesis and oxidation using TiO₂ as the main photocatalyst; (3) to compare homogenous and heterogeneous photocatalytic oxidation and apply it to a variety of organic compounds. All procedures were performed at low temperature and atmospheric pressure. Highly efficient and selective processes were used, including the optimization of physical and chemical properties of the TiO₂ photocatalyst and the optimization of reaction conditions, such as pH and ratio of reactants.

1.7 Thesis overview

This thesis provides a comprehensive study of water purification properties of TiO₂-based nanomaterials. It comprises nine chapters. Chapter 1 provides an introduction to the thesis and outlines the goals of the study. This includes green chemistry, green oxidation catalysts for fine chemical synthesis, heterogeneous and homogenous photocatalytic oxidation and electronic structure of photocatalytic semiconductors.

Chapter 2 presents the main instruments used for the characterization of synthesized photocatalysts and those used for product analyses. Powder x-ray diffraction (XRD), Scanning electron microscope (SEM), UV-Vis diffuse reflectance spectroscopy, Photoluminescence spectroscopy (PL) and Brunauer–Emmett–Teller (BET) were used for catalyst analyses. Gas chromatography-mass spectrometry (GC-MS), Gas chromatograph with flame ionized detection (GC-FID), and nuclear magnetic

resonance (NMR) were used for product analyses. The basic principles of each of these instruments are also discussed.

Chapter 3 discusses the photodegradation of organic pollutants using methylene blue as an organic standard. First, the degradation was attempted with commercial TiO_2 -P25. The synthesised catalyst was further improved by doping with Ag_3PO_4 . The degradation was achieved in a single phase using photocatalysts as the only catalyst. The characterization of synthesised $\text{TiO}_2/\text{Ag}_3\text{PO}_4$ composites is also discussed.

Chapter 4 presents a very interesting comparison between different biphasic oxidation systems to achieve the desired products. A new extensive environmentally friendly technique is discussed in detail. Benzyl alcohol was oxidized to benzaldehyde (intermediate compound), preventing further oxidation to benzoic acid. The oxidation was studied in two systems: electrochemical oxidation and photocatalytic electrochemical oxidation. Experimental details on the synthesis and characterization of TiO_2 nanotubes are also provided.

Chapter 5 investigates photooxidation properties of TiO_2 under biphasic reaction conditions. The pH level, the ratio of reactants and catalyst loading were optimized. A kinetic study was attempted on the photocatalytic oxidation of benzyl alcohol to obtain the desired compound (benzaldehyde). Inorganic species were tested in this system and showed increases in reaction rate constants. The effect of phenyl-ring substitution on photocatalytic oxidation was investigated. In addition, the possible reaction mechanism of biphasic photocatalytic oxidation of benzyl alcohol is outlined.

Chapter 6 focuses on the developmental design of the photocatalytic N-alkylation of aniline. Benzyaniline was synthesized using the two-phase photocatalytic

oxidation of benzyl alcohol. TiO_2 -P25 was the photocatalyst used to test the functionality of the designed system. The mixture of H_2 and O_2 was crucial in the photocatalytic n-alkylation of aniline for benzylaniline synthesis. Effects of pH, reactant concentration and hydrogen flow rate were investigated.

Chapter 7 provides the experimental details for the synthesis of photocatalyst nanostructures used in the photocatalytic oxidation of alcohol. First, the oxidation was attempted using as-synthesised TiO_2 . The synthesised catalysts were further improved by doping with a variety of transition metals. Ag-, V- and Fe-doped TiO_2 NPs were synthesised by controlled hydrolysis methods method. The characterization of the synthesised photocatalysts and their photocatalytic activity evaluation is also presented.

Chapter 8 describes a kinetic study performed on the photoepoxidation of styrene. The photocatalytic epoxidation of styrene with TiO_2 -P25 photocatalyst, containing NaCl as a chlorine radical source, was examined. Also, pH level, catalyst loading, and radical loading were investigated. An asymmetric column was used to detect the products. The conversion, yield and selectivity were determined. In the acidic medium, benzaldehyde (unwanted product) was detected, while in the alkaline medium, a sharp decrease in benzaldehyde (BAD) was noticed. General conclusions of the findings of this study and future perspectives are presented in Chapter 9.

CHAPTER 2 Research Instrumentation

This chapter provides an overview of the scientific instrumentation used in this work for characterising nanostructured photocatalysts as well as analysing chemical species from the photocatalytic reactions.

2.1 Introduction

The objectives of the present study were achieved using several analytical techniques, for both the investigation of the structures and the photocatalytic properties of the TiO_2 based photocatalysts. The structure and electronic properties of the synthesized photocatalysts were investigated and visualized using scanning electron microscopy (SEM), powder x-ray diffractometer (XRD) and a UV-Visible diffuse reflectance spectrometer (DRS), while for surface area analysis was performed using Brunauer–Emmett–Teller (BET) analysis. Here, SEM was useful for the characterization of the morphology, while XRD was used for studying the crystal structure of the TiO_2 based photocatalysts. On the other hand, DRS was employed for the determination of the bandgap and electronic structure of the synthesized photocatalysts.

The above techniques were supplemented with gas chromatography-mass spectroscopy (GC-MS), gas chromatography-flame ionization detection (GC-FID). Both GC-MS and GC-FID were used for quantitative measurement of the concentrations of reactants and products. GC-MS measures the molecular weight of the ionised chemical fragments after being separated by the column. For chemical species that are not commercially available, GC-MS was used to identify the chemical species and its concentration. GC-FID relies on the retention time to distinguish all chemicals. Finally, to determine the molecular structure of products of photooxidation benzyl alcohol, Nuclear Magnetic Resonance (NMR) was used. In this project, we used standard chemicals to confirm the retention time before quantifying the chemical

concentrations. In this chapter, the theoretical backgrounds of the instrumentation methods are provided, along with analytical principles and mechanisms and related techniques.

2.2 Scanning Electron Microscopy

In modern nanotechnology, electron microscopy is arguably the most powerful tool as it allows the visualization of nanostructure morphology of interest with relatively high resolution of down to several nanometres (nm).²¹¹ In the present study, SEM imaging was extensively employed to visualize the nanostructures of the synthesized TiO₂-based photocatalysts, used for the oxidation of different organic compounds as described in Chapters 3 and 4.

SEM is analogous to optical microscopy (OM). Although, the key difference between the two techniques is that OM uses photons (visible light with a wavelength from 400 to 700 nm), while SEM uses a high energy electron beam with short wavelength to interact with the sample atoms and to produce signals. These signals carry information about the sample surface topography. A high-energy electron is emitted during this work by thermionic emission from a tungsten filament, accelerated in the 10-30 kV range at standard energy. Before touching the sample, this high energy electron beam is finely focused through many electrostatic and electromagnetic lenses.

SEM was originally developed in 1935 and subsequently fine-tuned to its final usability in 1961.²¹¹⁻²¹³ The modern SEM was designed to overcome the inherent poor resolution limit in traditional optical microscopy. In wave-based detection systems, the highest resolution achievable is constrained by the wavelength of the light source. This implies that the low resolution of optical microscopes is due to their wavelength, which is in the narrow visible light range. The limitation of a narrow wavelength is overcome

in the SEM instruments by employing electrons rather than light. The momentum and the wavelength of a free electron are determined by its kinetic energy. Electrons can be easily accelerated by an electric field as they are attracted to the positive electrode (cathode). By increasing the voltage applied between the cathode and anode, the kinetic energy of an electron can be increased. The wavelength of the electron is governed by de Broglie law, which states that the wavelength of a particle is inversely proportional to its momentum, Eqn 2.4.

$$E = h\nu \quad (\text{Eqn 2.1})$$

$$c = \lambda\nu \quad (\text{Eqn 2.2})$$

$$E = \frac{hc}{\lambda} = pc \quad (\text{Eqn 2.3})$$

Where E and p are the energy and momentum of the photon ν and λ are the frequency and wavelength of the photon, h is the Planck constant and c is the speed of light. Thus, the wavelength of material particles, λ is:

$$\lambda = \frac{h}{p} \quad (\text{Eqn 2.4})$$

It is possible to change the wavelength of the electrons by changing the electron momentum that is used for imaging.

Since the electrons are negatively charged, they repel each other, known as the space charge effect. This effect will degrade the lateral focus of the electron beam and the image resolution. By increasing the kinetic energy, not only is the diffraction limit reduced, but also the space charge effects. Hence the beam profile is smaller, and the beam is better focused, resulting in high-resolution imaging. Alternatively, space charge can also be effectively reduced by decreasing the density of the electron beam current, although the brightness and contrast of the image will suffer as well.

As the electrons utilised by SEM are high energy charged particles, they are ready to ionise molecules, which distorts the beam focus with reduced electron density. Hence, to operate effectively, SEM requires high vacuum conditions in the range $10^{-6} - 10^{-10}$ Torr. This vacuum condition protects the electron gun filament, stabilises the electron beam intensity and maintains its focus profile by limiting the interaction with gaseous molecules and particles, occurring under ambient pressure. The vacuum condition also protects the hot filament from oxidation and prolongs its service life. The structure and principle of a typical SEM instrumentation are illustrated in Figure 2.1. The first part of the SEM is the electron gun.

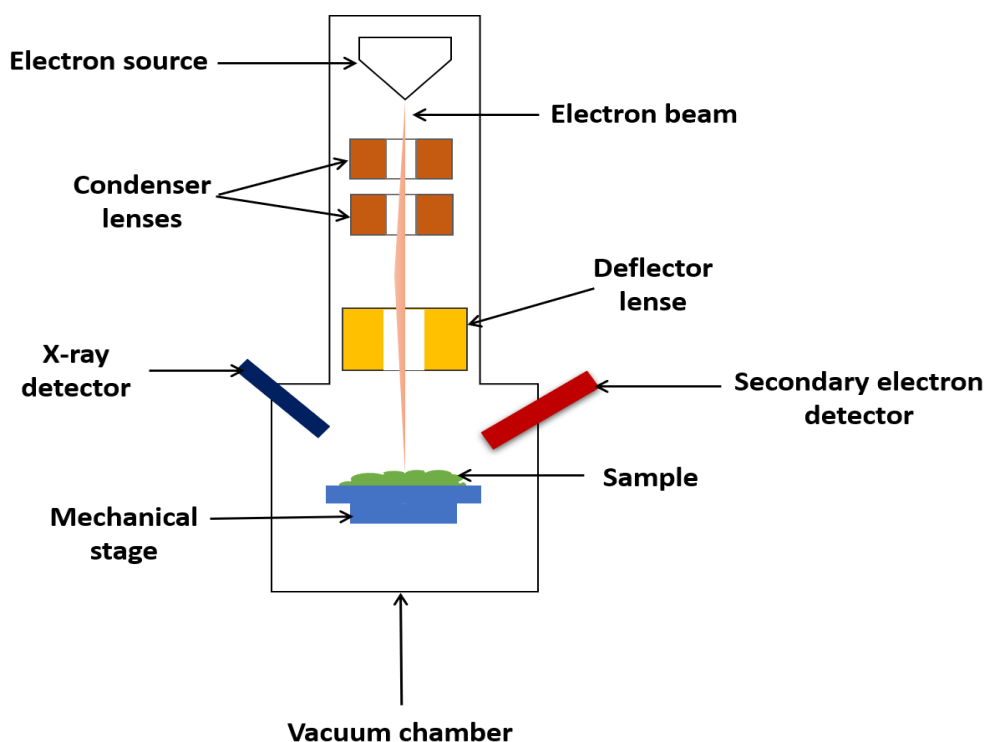


Figure 2.1 The cross-sectional view of a scanning electron microscope.

When running the SEM instrument, the electrons are ejected from a hot tungsten filament and accelerated to the desired velocity by a direct current (DC) electric field from (20 kV) within the electron gun. There are different electron sources used in SEM instruments, with tungsten filaments being the most common due to relatively low cost and reasonable stability. Tungsten filaments emit free electrons

through thermionic emission, which were accelerated by an electric field.²¹¹ The next parts of the SEM are the condenser lenses, the accelerated electrons are focused into a narrow beam using an array of a condenser and probe lenses to bombard the surface of the sample under study. Next, the beam position is rapidly scanned across the sample surface by using a series of scanning coils with an input signal. The location of the sample imaged can be adjusted using a mechanical stage. A series of deflector coils allow small shifts in the beam location while placing a mechanical stage underneath the sample allows for larger shifts in the studied area. When the electrons bombard on the surface of a sample, they undergo elastic and inelastic scattering, which can be monitored using appropriate detectors. They generate images of the sample surface with image contrast determined by either the topography or electron scattering probability.

Electrons that undergo elastic scattering (back scattered electrons), occur following the interaction between the electrons of the incident beam and the atomic nuclei of the sample. The back scattered electrons keep their original kinetic energy and are deflected directly from the atoms in the sample, using the sample like a reflecting mirror. If the sample surface is perpendicular to the incident beam, as, in most SEMs, the reflected electrons form a cone profile along the incident beam. Thus, the detectors of the backscattered electron are normally placed almost vertically above the sample. Since the backscattered electrons are high-energy, they can penetrate deeper into the sample with a larger lateral profile, due to the elastic scattering mean free path. Thus, the back scattered electron images are generally achieved under lower resolutions. However, as the electron scattering cross-section is proportional to the nuclear mass, heavier elements reflect more electrons and give high brightness in

the back scattering image. So, although low resolution, back scattered electrons can be used to distinguish light elements (dark) from heavy elements (bright).

To achieve high-resolution images, SEM also detects inelastic-scattered electrons, termed as secondary electrons. Secondary electrons are emitted when the incident beam of electrons eject core electrons from the surface atoms of the material under study. This leaves a vacancy at the core level which allows electrons at the upper level to relax into the vacancy. During this process, excess energy can be released as x-ray which will ionise a secondary electron from the upper level. Such electrons have a low kinetic energy of 200 - 500 eV, which can only penetrate from out of the sample at a depth of 5 nm, determined by the inelastic mean free path. So, an electron profile as small as 3 nm can be formed which guarantees the best resolution in SEM image. Since the secondary electrons possess relatively low kinetic energy, they can be deflected by employing a weak electric field (~500 V). This allows them to be separated from the back scattered electrons. Normally, the secondary electron detectors are mounted horizontally, just above the sample.

Interestingly, although SEM instruments are designed to investigate the morphological properties of nanostructures by the detection of secondary electrons, they can also be used in the identification of elemental composition. This can be achieved by analysing the energy of the x-ray emission during the relaxation of a higher state electron into the core vacancy using an energy dispersive x-ray (EDX) detector.

2.3 Energy Dispersive X-Ray Spectroscopy

The elemental composition of a sample can be detected using an SEM equipped with an energy dispersive x-ray (EDX) detector using x-ray fluorescence. When an electron is ejected from the core-shell of the atoms of a sample, it results in the formation of

vacancies within the atoms. The formed vacancy allows the relaxation of another electron in the outer shell towards the core-shell of the atoms and it releases x-ray. The x-ray energy is determined by the energy difference between two atomic orbitals which is fundamentally determined by the nuclear charge of the atom, i.e. the atomic number. Thus, it is element-specific and therefore, allows the discrimination of the different atomic species within the sample. Furthermore, the intensity of the detected x-rays is directly proportional to the number of atoms within the irradiated sample. Thus, SEM equipped with EDX allows a qualitative and quantitative elemental analysis of sample surfaces. As the focused primary electron beam scans across the sample, the 2D distribution of the targeted atoms can also be established. This technique is named elemental mapping.

The most typical signals detected are high-resolution topographic images using secondary electrons. Figure 2.2 shows the processes for the generation of secondary electrons, x-ray emission and Auger electron generation from the sample. After exciting a core level electron of the sample, an upper-level electron will relax in order to fill in the core level. As a result, some energy will be released equal to the energy difference between the corresponding upper level and core level orbitals. This energy will be used for either the release of an Auger electron from a higher level or as x-ray fluorescence emission which can be recorded by energy dispersive x-ray spectroscopy (EDX). In contrast, the secondary electrons have lower kinetic energy (10-300 eV) than the primary electron.

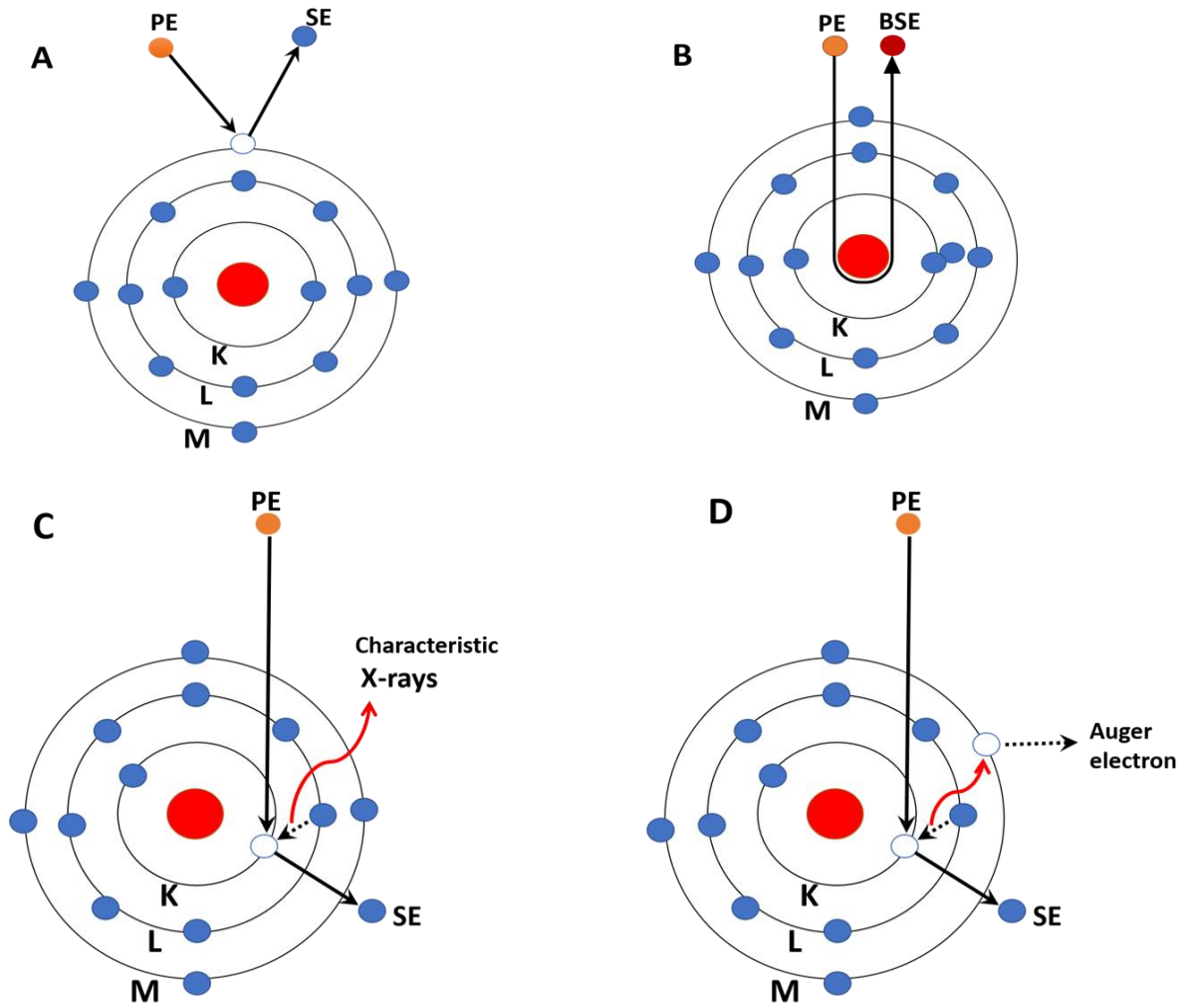


Figure 2.2 The electron excitation, (A) the primary (PE) and secondary electrons (SE), (B) back scattered electrons (BSE) generation, (C) x-ray emission processes and (D) Auger electron generation caused by the reabsorption of x-rays.

In this study, SEM was employed primarily for qualitative analysis, to determine the morphology and elemental composition of the synthesised TiO_2 -based nanostructures (See Chapters 3 and 4). The equipment used was the Jeol-JSM 820 and the Leica Stereoscan 420 Scanning Electron Microscopes, the latter was equipped with a cryogenically cooled EDX detector.

2.4 X-Ray Diffraction

The morphology and elemental compositional information determined from SEM equipped with an EDX detector do not provide any useful information regarding the arrangement of atoms in the crystal structure. This can be probed using an x-ray diffractometer (XRD) to study the diffraction properties of the x-rays from materials. Materials with crystalline structures, such as crystalline TiO_2 and WO_3 have their atoms arranged in a highly ordered, periodic fashion. When x-rays interact with these periodic structures, they are diffracted according to Bragg's law, shown in Figure 2.3. The diffracted x-rays subsequently undergo constructive or destructive interference depending on the phase relationship of the diffracted beams. This interference can be detectable and provide information about the crystal structures.²¹² The interaction of x-rays with the atomic planes of a crystal structure is shown in Figure 2.3.

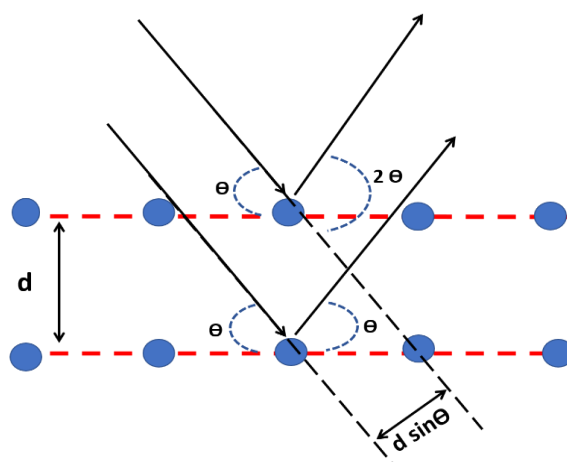


Figure 2.3 The interaction of x-rays with the atomic planes of a crystal governed by Bragg's law.

According to Bragg's law, when x-rays reach the surface of crystalline materials, they are diffracted by the atomic planes of a crystal. The diffraction angle, (θ) at which constructive interference patterns of x-rays are observed is determined by the wavelength (λ) and the inter-planar spacing (distance, d) in a crystalline sample, as shown in Equation 2.5.^{214,215} From Figure 2.3, with a reflection angle arrangement,

the diffracted x-rays are measured at an angle (θ) in relation to the sample stage containing the crystalline sample. In such an arrangement, relative to the incident beam, the diffracted x-ray is measured at an angle of 2θ , as shown in Figure 2.3. Thus, in a typical powder XRD, the relative angles of the sample stage and the x-ray detector in relation to the x-ray gun, are placed at θ and 2θ , respectively.

$$n\lambda = 2d \sin(\theta) \quad (\text{Eqn 2.5})$$

Since different crystalline phases exhibit different XRD patterns, it is possible to characterise the crystal structure of an unknown sample by comparing to its signature pattern in a database. Single-crystal XRD and powder XRD are the main types of XRD techniques used to study the crystal structure of a sample. Single-crystal XRD is suitable for the characterization of large crystalline samples. The sample forms diffraction patterns in 3D space. Thus, the diffraction data is collected from all possible orientations, which allows the construction of 3D patterns of the constructive interference spots. This data can be used to predict the crystal structures. The disadvantages of the single-crystal XRD technique are that it is time-intensive and requires relatively large single crystals. These limit its application to nanotechnology where crystals are normally small.

On the other hand, powder XRD is a more rapid technique compared to the single-crystal XRD. In powder XRD, the diffraction of the incident x-ray beam is studied along a single axis of rotation on a crystalline sample. This explains why the powder XRD technique is not time-intensive, unlike the single-crystal XRD technique. However, limiting x-ray diffraction studies to a single axis of the sample implies that the powder XRD technique generates less informative spectra. Thus, using the Powder XRD technique, it is impossible to pinpoint the exact unit cell of any given chemical species of interest without refinement. However, the powder XRD spectrum allows the

possibility to identify crystallographic planes using Miller indices, corresponding to the constructive interference observed in the spectrum.

Since different crystalline materials exhibit unique powder XRD patterns due to inherently different lattice spacing, unknown crystalline samples can be identified by referring to a database of powder XRD signatures. Powder XRD is especially useful in nanotechnology as it allows the modelling and generation of novel nanocrystalline materials from materials with known crystal structures. This is because powder XRD provides sufficient depth of analysis within a relatively short analysis time. Furthermore, the powder XRD pattern provides means for the quantitative determination of the relative composition of each chemical species as well as other properties such as crystallinity and crystallite size in a given crystalline sample.

The principle of quantitative analysis of samples using powder XRD is based on the relative intensities of the diffraction peaks of different crystals from a mixed sample. For a specific crystal powder, the relative intensities of diffraction from different crystal planes are constant. The diffraction ratio between different phases in a powder sample is proportional to the molar ratio of the phases. Thus, by comparing the intensities of the diffraction peaks it is possible to determine the relative compositions of each chemical species in a mixed crystalline powder sample. However, the situation becomes complicated if the crystals are not randomly oriented, such as vertically aligned nanorods or nanotubes. In such cases, the sample texture is determined by the crystal alignments, which dominates the diffraction intensities. Hence, for such samples, quantitative measurement of the crystal composition must consider the texture effects.

The crystallinity of a nanomaterial can be quantitatively analysed using the shift of the diffraction peak position or the broadness of diffraction peaks. Due to

imperfections in the crystalline structure, lattice separation distance can be distorted locally. Such distortion becomes more obvious if the sample is heavily doped, as the crystalline sample deviates from the ideal crystal. Such distortions result in constructive x-ray interference at slightly different θ values from an ideal crystal and, therefore, the diffraction peaks are broadened in the XRD spectra. Alternatively, for pristine crystals, the width of the diffraction peak is directly associated with the size of the crystal domain. Smaller crystal domain size results in less coherent interferences, hence the diffraction becomes broader while its intensity decreases. In essence, a less crystalline, nanostructured material will yield broad XRD peaks while a highly crystalline material will exhibit very narrow peaks.

The broadness of a powder XRD peak provides information for the determination of the crystallite size of each crystal plane detected. This is guided by Scherrer's relationship, described in Equation 2.6.²¹⁶

$$D_{avg} = \frac{k\lambda}{\beta \cos \theta} \quad (\text{Eqn 2.6})$$

Where D_{avg} is the mean crystallite domain size of a given plane; the constant k is the shape factor of the studied crystal lattice in the range 0.62-2.08 based on the shape of the crystal lattice; λ is the wavelength of the incident x-rays; θ is the angle of the diffraction peak, and β is the full width half maximum (in radians, FWHM) of the studied peak adjusted for instrument broadening.

In the present study, powder XRD was used to analyse the crystalline nanostructures produced (See Chapter 3) and the effect of metal doping on the TiO₂-based photocatalysts (See Chapter 7). All powder XRD studies were performed using a Siemens D500 powder diffractometer equipped with a Cu anode plate with a peak x-ray wavelength of 1.54 Å. All diffraction data were captured in $\theta/2\theta$ mode.

2.5 Optical Properties Characterization

2.5.1 UV-Vis Absorption Spectroscopy

A UV-Vis spectrophotometer is a powerful analytical tool for studying the optical properties of metal oxide semiconductor materials. The optical bandgap energy of the materials can be calculated from the absorption and transmission spectra.

In a typical UV-Vis spectrometer, a beam of monochromatic light is divided by a beam splitter into two beams of equal intensity, which are directed to pass through the sample and the reference cell, shown in Figure 2.4. The transmitted light intensities are measured simultaneously as I (sample) and I_0 (reference), respectively. Normally, the light intensity through the sample (solution or thin film) is less than that through the reference (blank) due to light absorption.

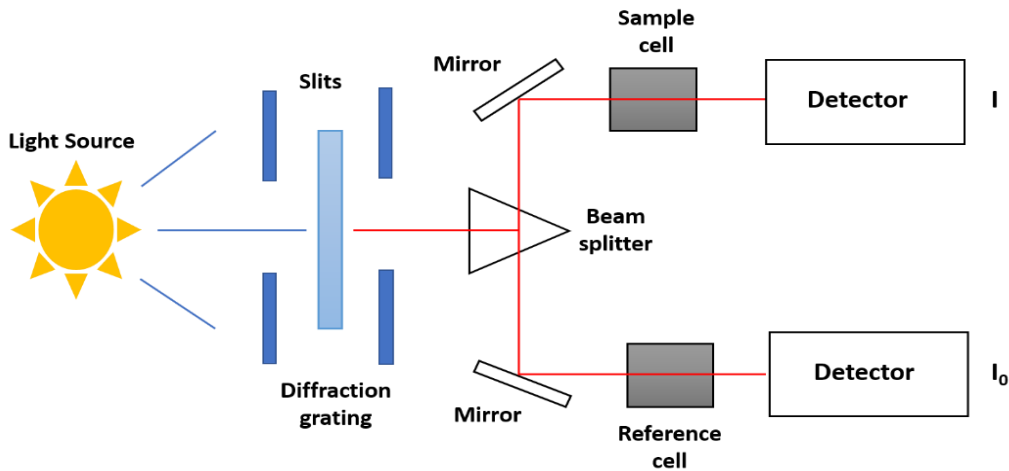


Figure 2.4 An illustration of components of a typical double beam UV-vis spectrophotometer.

Transmission (T), is expressed as the percentage ratio of I and I_0 , Equation 2.7. The absorbance, A , of the sample as a function of wavelength is defined by Equation 2.8:

$$T = \frac{I}{I_0} \quad (\text{Eqn 2.7})$$

$$A = -\log_{10} \frac{I}{I_0} = -\log_{10} T \quad (\text{Eqn 2.8})$$

According to the Beer-Lambert law,²¹⁷ the absorbance is proportional to the sample molar concentration, shown in equation 2.9. Where α is the extinction coefficient, b is the length of the beam in the absorbing medium and c is the concentration of the absorbing species.

$$A = \alpha bc \quad (\text{Eqn 2.9})$$

However, given that each metal oxide semiconductor exhibits different bandgap energies, they should also exhibit different absorption edges. This means that only the photons with their energy higher than the bandgap energy can be absorbed. Thus, the optical bandgap energy can be related to the absorption coefficient and photon energy according to the Tauc expression as shown in Equation 2.10.^{217,218}

$$(\alpha h\nu)^{1/n} = A(h\nu - E_g) \quad (\text{Eqn 2.10})$$

Where α is the absorption coefficient; A is a constant determined by electron-hole mobility of a material; h is Planck's constant; ν is the frequency of the incident photon, $h\nu$ is the photo-energy given by Equation 2.11; E_g is the bandgap energy; n is $\frac{1}{2}$ or 2 for either direct or indirect electronic transitions, respectively.

$$h\nu = \frac{hc}{\lambda} = \frac{1240}{\lambda(\text{nm})} \text{eV} \quad (\text{Eqn 2.11})$$

For thin film samples, the absorption coefficient is given by Equation 2.12:

$$\alpha = \left(\frac{1}{t}\right) \ln \left(\frac{1}{T}\right) \quad (\text{Eqn 2.12})$$

Where t is the film thickness measured from a cross-sectional SEM image; and T is the optical transmittance. To get the bandgap energy, a Tauc plot of $(\alpha h\nu)^{1/n}$ vs $h\nu$ will be generated. The linear region of the plot will be extrapolated to the value of $(\alpha h\nu)^{1/n}=0$. Under such condition, $E_g = h\nu$.

However, UV-Vis absorption spectrometry has limitations. Given that the absorption spectrum (hence absorption coefficient) of a sample relies on the light transmitted through the sample, only liquids, gases and thin-film solid materials can be tested. Band gaps of opaque materials such as powders, thick films and bulk materials, can be determined using a reflectance UV-Vis spectroscopy. This alternative technique was originally developed by Kumar *et al.* who successfully applied it for the determination of band gaps of thick films.²¹⁹

2.5.2 UV-Vis Diffuse Reflectance Spectroscopy

Important photo-electric properties of photoactivated catalysts were discussed extensively in Chapter 1. Here, it is demonstrated that several photo-electric properties of photocatalysts such as charge mobility, conductivity and bandgap can be measured using different analytical techniques. The determination of the bandgap size of a material is especially important during photochemical reactions. In the present study, the bandgap energies of the synthesised semiconductor photocatalysts were determined using UV-Vis diffuse reflectance spectroscopy and the bandgap energy was correlated with their photocatalytic activities.

The bandgap energy of semiconducting material is usually determined by studying its UV-Vis absorption spectrum. In essence, by monitoring the range of wavelengths at which a given material absorbs the light source, the minimum quantity of energy required to achieve photonic excitation can be quantified using the UV-Vis absorption

Reflectance spectroscopy is an alternative technique for measuring samples where transmitted light intensities that are too low to measure, especially in metal sheets or semiconductor films that are too thick. This technique employs an integrating sphere (Ocean Optics ISP-REF) with an inbuilt tungsten-halogen light source covering

wavelengths in the range 300-1000 nm, a 7 mm beam port diameter and an incidence angle of 10° .^{219,220} The absorption coefficient can be calculated according to Equation 2.13.

$$2\alpha t = \ln \frac{(R_{max}-R_{min})}{(R-R_{min})} \quad (\text{Eqn 2.13})$$

Where t is the film thickness, R_{max} and R_{min} are the maximum and minimum reflectance; and R is the reflectance as a function of photon energy. From Equation 2.13, the absorption coefficient can be calculated with known film thickness. Bandgap energy values then can be determined using the Tauc plot Equation 2.10.

When a beam of light is incident on the sample surface, it undergoes specular and diffuse reflection. Specular reflection occurs when a beam of light is directly reflected on a uniformly smooth (polished) surface in a single angle equal and opposite to incidence. In the case of unsmooth or non-uniform surfaces, diffuse reflection occurs in all directions, loosely proportional to the total smooth or uniform surface area present. However, part of the incident light not reflected penetrates the subsurface of the material through refraction and partial absorption. The internal reflection results in light scattering. The scattered light with an attenuated intensity may be emitted back into the air in multiple directions. In UV-Vis reflectance spectroscopy, the wavelength of the light absorbed by the sample analyte is determined by analysing the diffuse reflectance spectrum. A diffusely reflected beam of light has an attenuated intensity relative to the light absorption properties of the material. Thus, it is possible to determine the UV-VIS absorption of a studied sample from its diffuse reflectance spectrum.

A Tauc plot for the determination of a sample bandgap from its diffuse reflectance can be generated by combining Equations 2.10 and 2.13. Due to the scattering nature, the diffuse reflectance of a sample is usually too weak to be detected

from a single point. Therefore, an integrating sphere is usually needed to aid in the convergence of the diffuse reflections from multiple directions into a single sufficiently strong signal for spectroscopic detection. The basic principles of integrating spheres for measuring the diffuse reflectance of a given sample is illustrated in Figure 2.5. When a light source is shone onto the sample analyte through an aperture in the integrating sphere, the omnidirectional diffuse reflections of the sample are intercepted by the walls of the integrating sphere, which is coated with a white diffuse reflecting material. The intercepted beams are further scattered within the sphere without energy loss due to absorption, thus effectively concentrating the diffusely reflected light. Through using a detector, a diffuse reflectance spectrum of a sample in relation to the incidence light wavelength can be generated. A baffle plate is positioned between the detector and light source, usually needed to avoid the blinding of the detector by the light source.

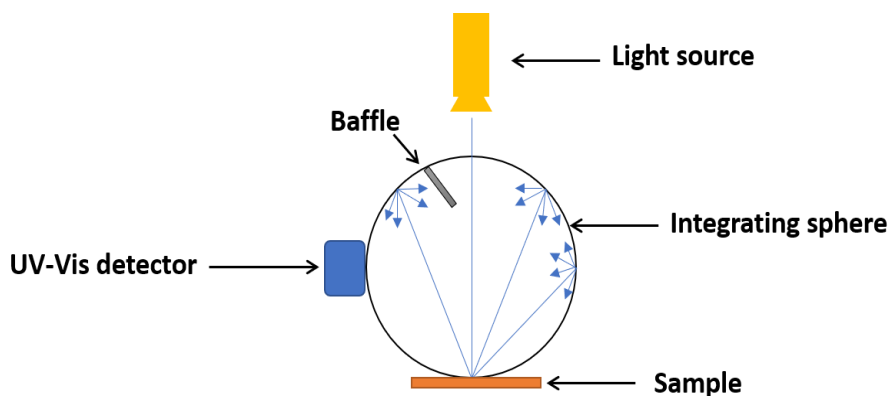


Figure 2.5 A diagram illustrating the principles of an integrating sphere in measuring the diffuse reflectance of a given sample.

Diffuse reflectance spectroscopy allows the study of bandgap energies of heterogeneous photocatalysts. This provides gainful insights into the processes involved in heterogeneous photocatalysis. In the present study, diffuse reflectance spectroscopy was employed to determine the bandgap of the nanostructures

synthesised in Chapter 3 as well as transition metal-doped TiO₂ photocatalysts shown in Chapter 7.

2.6 Gas Chromatography

Analytical methods for studying the kinetics of photocatalytic reactions or photodecomposition are as important as the material characterisation techniques discussed above. Monitoring the chemical species and their concentrations from photocatalytic reactions as a function of reaction time gives a quantitative assessment of reactivity and selectivity of photocatalytic processes. However, monitoring the concentration of a specific product species in a mixture containing a variety of chemical species is complicated. Gas Chromatography (GC) is an analytical technique frequently used for qualitative and quantitative analysis of complex chemicals mixtures. GC, originally developed by James and Martin (1952), has remained one of the most powerful analytical techniques for modern organic chemistry.²²¹ A GC separates chemical compounds from a complex mixture based on their unique polarities which influence their interactions with the stationary phase of a chromatography column.

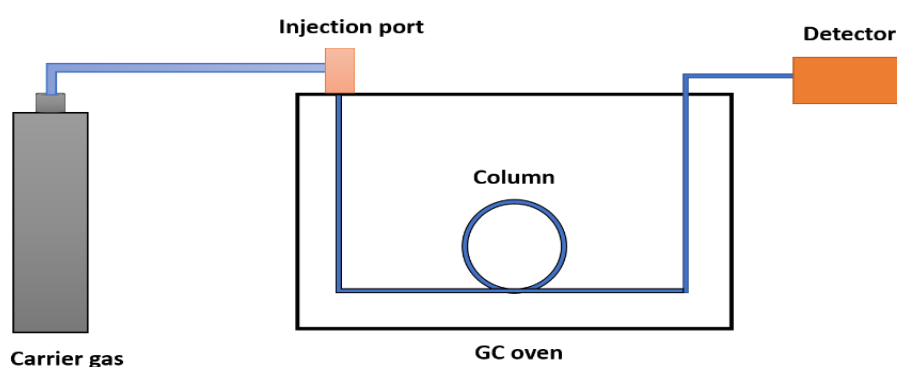


Figure 2.6 A schematic description of principles components of a gas chromatograph set-up.

Essential components of a GC system are illustrated in Figure 2.6. In the GC set-up, the mobile phase (a carrier gas, usually helium or hydrogen), flows through the

GC separation column at a controlled pressure. A small quantity of liquid analyte ($\sim 0.01 - 100 \mu\text{L}$) or a gaseous analyte ($\sim 100 \mu\text{L}$) is injected into the system through an injection port maintained at high temperature for vaporising the liquid sample. The vaporised sample is mixed and carried by the carrier gas to move within the GC column. For analytes with relatively low trace concentrations, a splitless injection is used without any dilution. However, in cases of high concentrations of chemicals in the analyte, the sample vapour is introduced into the GC column using split injection. The split injection allows the controlled portion of the vaporised sample to enter the GC system with excess analytes purged out by the carrier gas through a separated port.

In the capillary GC column, the vaporised samples interact with the stationary phase. A capillary GC column is a very narrow, long silica tube. On the interior surface of the capillary GC column, it is coated with chemicals, which are stable at high temperature. Chemicals in the mobile phase adsorb and desorb by the stationary phase at different rates, which determine the diffusion rate and the retention time of each chemical species travelling through the GC column. This results in the separation of the chemical species in the sample analyte. The time taken for eluates of each separated chemical species to arrive at the end of the GC column is the retention time. The degree of chemical separation in retention time through the GC column are influenced by several factors including the flow rate of the carrier gas, the nature of the stationary phase and the temperature of the column. The elution speeds of different chemical species are influenced by the time each chemical spends adsorbed onto the stationary phase. Therefore, raising the temperature shortens the retention times by decreasing the adsorption rates of chemicals while lowering the temperature prolongs the retention times. However, a temperature increase can result in a

disproportionate decrease in the elution times of some chemical species relative to others, resulting in poor chemical separations. To minimize this effect, the temperature in a GC system is precisely controlled using a highly efficient oven as shown in Figure 2.6.

Retention time (RT) is the amount of time that a compound spends in the column after it has been injected and is usually quoted in units of seconds or minutes. When a sample contains several compounds, each compound in this sample will spend a different amount of time in the column depending on its chemical composition. Several factors affect RT, the first factor is boiling point (bp), components with low bp will spend more time in the gas phase than others with high bp therefore their RT will be shorter. The second factor is column temperature, with high column temperature the compounds will desorb faster therefore their RT will be shorter, this can give poor separation as the compounds need to interact with the stationary phase. Carrier gas flow-rate is the third factor, a high flow-rate will give a low RT and poor separation. The last factor is column length, with a long column the compounds have longer RT and better separation. However, a diffusive effect can occur which causes the peak width to broaden when a component has a very long transit time in the column.²²²

Polar and nonpolar chemical species preferentially adsorb onto polar and nonpolar stationary phases of the GC column, respectively. GC systems are equipped with either polar or non-polar columns based on the nature of the analytes. If the analytes are an enantiomeric mixture where species with different chirality need to be separated, a chiral column should be used. The stationary phase of a chiral column is coated with chiral species. In such a situation, the chiral separation is normally relatively weak. In order to improve the chiral resolution, the column temperature and carrier gas flow rate need to be significantly reduced, resulting in better interaction with

the stationary phase and longer retention time. Similar conditions should also be used, if the analyte contains multiple chemicals with very similar strength of interaction with the stationary phase, although they are not chiral species.²²³

Upon elution from the GC column, different chemical species are delivered into special detectors with different sensitivities and tailored detection limits. In the present study, two types of GC detectors were used for measuring chemical species, including Flame Ionisation Detection (FID) and Mass Spectrometry (MS). The details of both detectors are described in the following sections.

2.6.1 Flame Ionisation Detection

An FID is the simplest and arguably the most robust detector for a GC system, which involves an ionisation flame. A cross-section of an FID is illustrated in Figure 2.7. As the chemical eluates exit the GC column in the gas phase, they are usually premixed with a fuel gas (commonly H_2). The fuel/eluate mixture is channelled through the FID system where it is mixed with an oxidant gas source (usually air). As the resulting eluate/fuel/oxidant mixture is channelled through the nozzle head of the FID, a flame is formed which ionises the eluate. The resulting eluate ions are collected by a series of negatively charged plates connected to an ammeter. The collected ions generate an electric current (detected by the ammeter) as they collide with the collector plates. The detected electric current is proportional to the concentration of the elute and can be amplified and recorded. The spent combustion products of the eluates are purged out of the FID system through an exhaust port. Although the FID system is cost effective and efficient, it has some limitations. Firstly, FID can only discriminate between different chemical species by the difference in the retention time. Therefore, standards for each chemical species in the analysed mixture must be used.

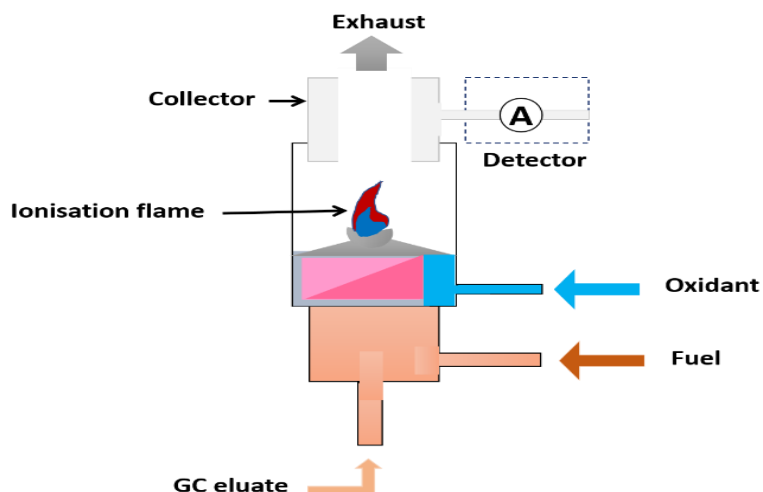


Figure 2.7 A schematic diagram of the key components of an FID detector.

However, even with available standards, the retention time is also affected by the GC operation conditions. Hence, it is critical to maintain exact GC conditions, such as column temperature and gas flow rate, otherwise, the retention time should be calibrated every time. Nevertheless, FID remains an important analytical tool in aiding sample analyte analysis on a GC system.

The interpretation of FID data is based on the following assumptions. The intensity of the electric current detected by FID is proportional to the number of ions reaching the detector at a given time. Therefore, the FID signal is proportional to the concentration of the eluates in the sample analytes. As such, FID signals should be calibrated with standard concentrations for different eluates for the quantitative determination of their concentration in the sample mixture. FID is the basic detection method used in well-defined chemical systems with known chemical components because it cannot directly identify the chemical species, it can only measure concentrations. The peak retention time can simply be determined from expected chemical standards. Moreover, FID has limited dynamic detection range defined by the resolution output signal voltage from 1 to 1000 mV.

In this thesis, GC-FID was employed to measure the concentrations of benzyl alcohol (BA), benzaldehyde (BAD), benzoic acid (BC) (Chapter 4, 5 and 7), benzyl alcohol, benzaldehyde, benzylideneaniline and benzy laniline (Chapter 6). During the experiments, the concentrations of products were quantified by calibrating and monitoring the area under the peaks in the GC-FID spectra, corresponding to each chemical (Perkin Elmer auto-system). The GC-FID system was equipped with a 50 m wax capillary column. The gas flow rate was kept at 1.5 ml min^{-1} . The oven and injection temperatures were maintained at 250°C to detect BAD and BC, the results of the photooxidation of benzyl alcohol. For Chapter 6 a temperature of 180°C was used for BAD and benzy laniline. H_2 gas was used as the carrier gas and fuel, supplied from a hydrogen generator.

2.6.2 Mass Spectrometry

The mass spectrometer is widely used in both qualitative and quantitative analyses of organic compounds. This is because MS presents a large amount of information about a molecule in comparison to other GC detectors such as the flame ionization detector, (FID). However, MS is more expensive, it is a useful instrument for the identification of chemical species. The mass of the molecule together with its ionisation fragments can be measured. It has a much larger detection range from several hundred counts (determined by the noise level) to millions of counts. Hence, it enables measurement from very low to a very high concentration.

There are several available designs for MS detectors within GC-MS systems but all of them contain three main components: Including the ion source, the mass selector, and the detector. The basic structure of a typical ion trap MS is shown in Figure 2.8. Its operation includes ionizing the eluents from the GC and separating their ions with respect to their mass-to-charge ratio. Electron ionization (EI) is one of the

ionization techniques used in MS. It is the most common technique as the ion source in most GC-MS setups due to its high efficiency and reliability. Via a transfer line, GC column eluates are introduced into the MS and bombarded with high energy electrons inside the ionization chamber to become ionised. The ionisation chamber in the GC-MS system is normally maintained at high temperature (up to 300°C) in order to avoid the condensation and deposition of GC eluates within the system. The ionization filament in an ionization chamber is heated and emits high energy electrons through thermionic emission. The molecules are fragmented into smaller species due to the high energy of the electron beam. Depending on the instrument; ions are either formed within or injected into the ion trap assembly from an external source. The trapped ions determine the applied RF potential to produce ion ejection through excitation, resulting in a mass selective ejection.

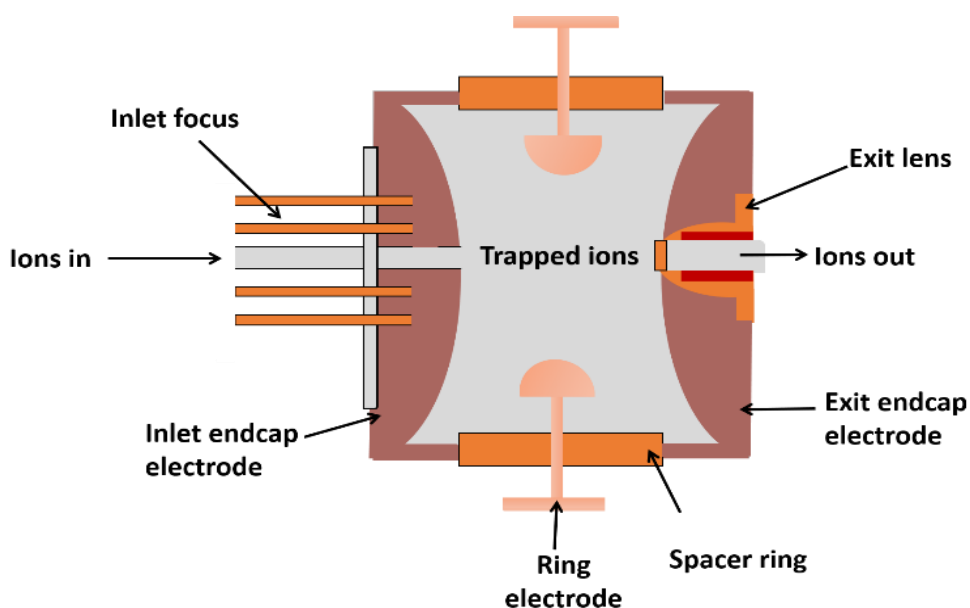


Figure 2.8 A schematic diagram of an ion trap detector used in GC-MS.

The role of a mass selector is to separate the ions based on their mass-to-charge ratios using electric or magnetic fields. The motion of ions in electric or magnetic fields in a vacuum are governed by Newton's second law of motion (Equation

2.15) and the Lorentz force law (Equation 2.14). Combining the two laws gives Equation (2.16).

$$F = q(E) + (v \times B) \quad (\text{Eqn 2.14})$$

$$F = ma \quad (\text{Eqn 2.15})$$

$$a \left(\frac{m}{q} \right) = E + (v \times B) \quad (\text{Eqn 2.16})$$

Where F is the force applied to a given ion; q is the charge of the ion; E is the strength of the electric field affecting the ion; a is the acceleration of the ion, and $v \times B$ is the vector cross product of the ion velocity and magnetic field.

From Equation 2.16, it is clear that the path taken by an ion in a magnetic field is directly proportional to its mass-to-charge ratio. This is consistent with quadrupole mass selector commonly used in GC-MS systems for selective filtration of ions. A quadrupole mass selector (Figure 2.8) consists of four cylindrical rods placed parallel to each other. An electric field is induced between the parallel rods using a direct current (DC) voltage. The ions generated from the ion source enter the electric field where they are accelerated based on their mass-to-charge ratio. It is possible to control the path of the ions by varying the magnetic field strengths, to induce their trajectory towards an MS detector or to collide with the rods. In essence, a quadrupole detector can be used in two ways 1) a single ion detection modality, where the specific mass-to-charge ratio is only allowed to reach the MS detector. And 2) a scanning modality where a range of mass-to-charge ratios are scanned to discriminate between the different ions created from the fragmentation of the studied species.

Quadrupole-filtered ions collide with a detector, which quantifies their concentrations, relative to their mass-to-charge ratios at a given time. A mass spectrum is simply a plot of the mass-to-charge ratio versus signal intensity. Since each chemical species undergoes unique fragmentation, each species, therefore,

generates a unique mass spectrum that can be used to identify unknown species using spectral signatures in an MS database. The quantitative determination of the concentration of the unknown species within a mixture is given by the intensity of the peaks versus elution time. However, MS often requires low vacuum because of the low mean free path of ionic species in air. MS under low vacuum allows the detection of the generated ions. Both vacuum pumps (turbomolecular pumps) and the filament for the generation of ions makes GC-MS equipment more costly and more fragile than GC-FID equipment.

In this thesis, both GC-FID and GC-MS were extensively used to study organic reaction products. In the GC-MS system, Helium was used as the carrier gas with a gas flow rate up to 1.4 ml/min. In a typical experiment, a small volume of analyte liquid (0.6 μ l) was injected into the GC column using an automated split injection, at an injector temperature of 250°C.

2.7 Photoluminescence (PL) Spectroscopy

Since the absorption of excitation photons, photoluminescence is light produced by the relaxation of photoexcited atoms or molecules. A direct product of electron-hole recombination, which is the most significant energy decay pathway, is the optical emission from an excited semiconductor.²²⁴ In the process, illustrated in Figure 2.9 (similar to Figure 1.1), the photoexcited electrons lose their excitation energy and easily relax to the lowest level of the conduction band in two different steps. Firstly, electron relaxation within the lowest conduction band happens during the excited state lifetime by losing minor quantities of energy as heat (lattice vibration). Secondly, the excited electrons in the upper level relax to the minimum of the conduction band. Such relaxed electrons in the conduction band will further relax to the valance band, combining with the holes. Energy is released in the form of photons of longer

wavelengths than the excitation photons during this latter phase. This process is defined as photoluminescence.

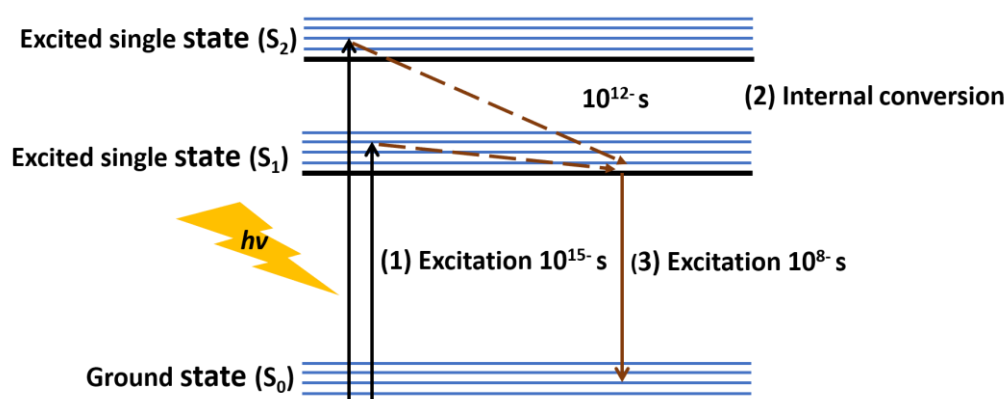


Figure 2.9 Jablonski diagram displaying photoluminescence.

The PL emission intensity allows the evaluation of the recombination rate of the photo-generated charge carriers. The key drawback of this approach is that, because of the relaxation to the bottom of the conduction band through non-radiative transitions, it does not provide details about the whole electronic structure of the material studied. Another problem comes from the environment and sample impact on the PL signal, which may limit the absolute analysis the quantum yield of charge recombination. For instance, the PL intensity could be affected by the thin film thickness and nanocrystals textures. Hence, it is important to accurately control the experimental conditions.

Figure 2.10 shows the setup of a typical PL spectrophotometer. In the fluorometer, a bright xenon arc lamp is used as a source of excitation light. The xenon arc lamp has a continuous spectrum from 250 to 800 nm, which has sufficient energy to excite various materials. Monochromators are used to select the wavelength of the excitation source and the emission measurement. A beam splitter is provided to reflect a part of the excitation light to the reference detector, used to monitor the wavelength and intensity of the excitation light. Polarizers are used in both excitation and emission

light paths for studying fluorescence anisotropy. During PL measurements, excitation light is focused on the centre of the solid sample or liquid cell. If the energy of the excitation photons is greater than the bandgap energy of the semiconductor / electronic transition energy in a molecule, the excitation photons will be absorbed, resulting in electronic excitations of electrons and holes. The fluorescence light will be emitted if the excited electrons recombine with the holes and can be detected aided by a photomultiplier tube.

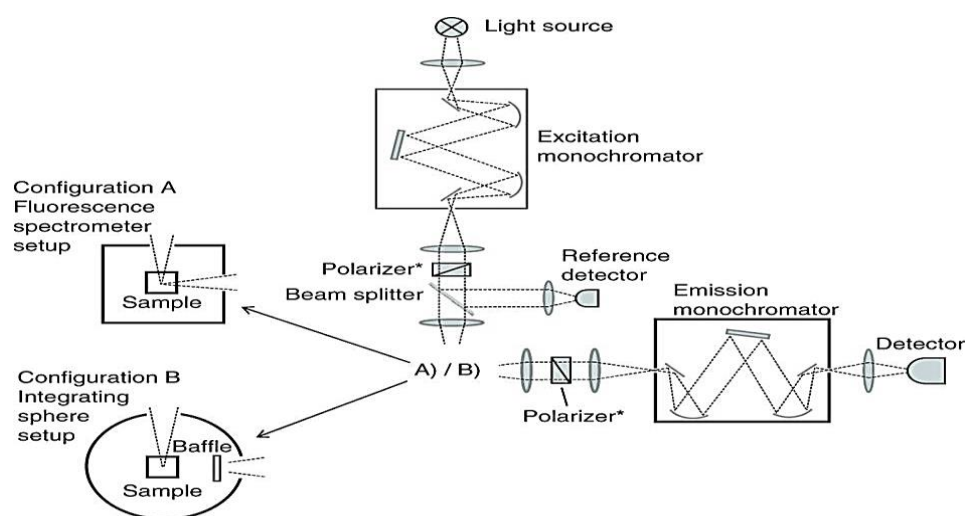


Figure 2.10 PL spectrophotometer instrumental setup. It was adopted.²²⁵

Furthermore, samples are typically suspended in solution and measured, and solid substrates can be characterized by placing them at an angle of 45° in the level. The chance of any reflective light entering the detector is present. A high energy excitation at 320 nm was therefore selected, with a slightly lower detection range (350-600 nm). The fluorescent intensity indicates the general rate of electron-hole recombination which is an undesired property in the semiconductor.

In this project, PL analyses were performed to study the effect of metal-doping on the electronic properties of TiO_2 photocatalysts. The study was to evaluate the recombination rate of photo-generated charge carriers when used as photocatalysts during the photo-oxidation process. PL emission spectra were recorded at room

temperature using an LS45 fluorescence spectrometer. Samples were excited with a xenon arc lamp in the UV region.

2.8 Dynamic Light Scattering (DLS)

Dynamic light scattering (DLS) is the technique that can be used to determine the size distribution of molecules, nanoparticles, proteins or spherical colloidal polymers and particles usually in the submicron field, but is often referred to as photon correlation spectroscopy (PCS) by measuring the random variations in the light intensity scattered from a suspension or solution.²²⁶

Light can be scattered by a molecule or a particle with a diameter much smaller than the wavelength of the light if the molecule has polarizability different from its surroundings which are called Rayleigh scattering. Small particles in suspension, however, undergo random thermal movement known as Brownian motion. This random motion is demonstrated by the Stokes-Einstein equation.

$$D = \frac{KT}{6\pi\mu a} \quad (\text{Eqn 2.17})$$

while K is the Boltzmann constant, T is the temperature, μ is the viscosity of the solution and a is the hydrodynamic radius of the particle. A significant characteristic of (Eqn 2.17) is that it is independent of the diffusion species charge. Therefore, this equation can be applied to neutral molecules and particles in the solution.

A monochromatic light source, usually a laser, is sent through the molecule or particle solution in a typical DLS experiment, and the scattered light intensity is detected as a function of scattering angle and time. Usually, the detector is a photo multiplier that is located at 90° to the light source and absorbs the scattered light from the sample. In order to target the light source to the middle of the sample holder, collimating lenses are often used. The lenses also avoid saturation of the

photomultiplier tube.²²⁷ Particles can be dispersed in a variety of liquids. Only the liquid refractive index and viscosity need to be known for interpreting the measurement results.

2.9 Specific Surface Area from BET (Brunauer, Emmett and Teller) measurement

BET is the initials of the three people who created the mathematics needed for the measurement to work. Brunauer, Emmett, and Teller demonstrated an approach utilises a measurement of the gas physisorption to obtain a "surface area" value for a sample. The gas molecules will move through particles and through all pores, cracks, and surface roughness, such that the sample's full microscopic surface area is measured. BET analysis requires an 'Adsorption isotherm' measurement and that because the BET model uses the relative pressure of the adsorptive, at the adsorption temperature, the gas must be condensable-in other words, the "gas" is simply a vapour. The amount of gas (usually nitrogen) adsorbed to the surface of the particles is measured at the boiling point of nitrogen (-196°C). at this temperature, nitrogen gas is below the critical temperature therefore it condenses on the particles' surface. It is assumed that the gas condenses in a monolayer on the surface of particles thus since the size of gas atoms are known, the volume of adsorbed (condensed) gas is correlated with the overall surface area of the particles, including the surface pores. The surface area of a sample under the study can be calculated by the BET equation (Eqn 2.18).²²⁸

$$\frac{p}{n_a (p_0 - p)} s_{total} = \frac{1}{n_m C} + \frac{(C - 1)}{n_m C} \cdot \frac{p}{p_0} \quad (Eqn 2.18)$$

Where, the equilibrium (p) and the saturation (p_0) pressure of adsorbates at the temperature of adsorption, the n_m is the monolayer capacity (Eqn 2.19) and C is the BET constant (Eqn 2.20).

$$n_m = \frac{1}{\text{gradient} - \text{intercept}} \quad (\text{Eqn 2.19})$$

$$C = 1 + \frac{\text{gradient}}{\text{intercept}} \quad (\text{Eqn 2.20})$$

The BET equation is usually plotted as an adsorption isotherm at a relative pressure (P / P_0) between 0.05-0.35, to determine these values, and it suggests giving a straight line. Therefore, the n_m value can be found from the gradient and measure the surface area using the molecular cross-sectional area (Eqn 2.21).

$$S_{total} = \frac{n_m N s}{V} \quad (\text{Eqn 2.21})$$

Where N is Avogadro's number, s the adsorption cross-section of the adsorbing species, and V the molar volume of the adsorbate gas. The BET constant (C) is also determined from the intercept and gradient and is correlated with the first adsorbed layer adsorption energy. Consequently, the C value is an indicator of the extent of the interactions between adsorbent/adsorbate. For instance, C is usually between 100-200, and if it is lower by 20 that means there is a significant adsorbent/adsorbate and the BET method is invalid, while if it is greater than 200, indicates the sample may contain large porosity.

2.10 Proton Nuclear Magnetic Resonance (NMR)

Another important analytical method for identifying organic compounds is NMR. It is useful for determining the chemical content, purity and molecular structure of a given sample, and quality control and analysis. It works under the concept of electromagnetic wave absorption, like IR or UV. As shown in Figure 2.11, in the radio

frequency (rf) region, a sample can absorb electromagnetic radiation under suitable conditions in a magnetic field. The electromagnetic radiation absorbed is particular to the sample.

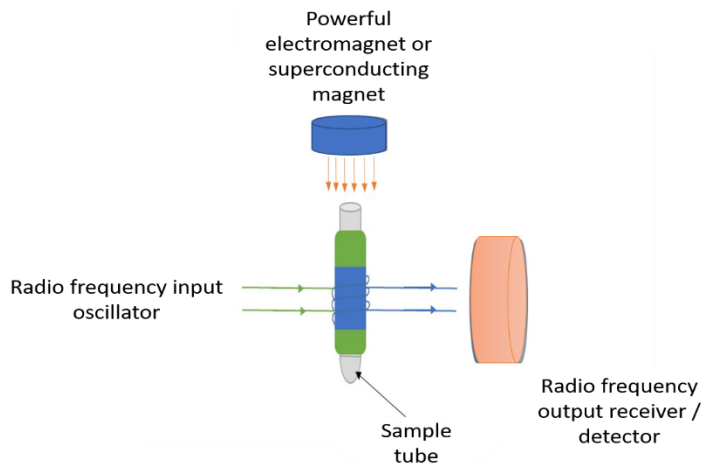


Figure 2.11 Illustration of NMR.

However, within the molecule of a sample, absorption is a characteristic of specific nuclei. It is known that all nuclei are charge carriers, causing them to spin on the nuclear axis, resulting in a magnetic dipole moment being produced along the axis. In terms of quantum numbers, the angular momentum of the rotating charge is sometimes defined as I , with values expressed in increments of $1/2$ (i.e. $0, 1/2, 1, 3/2$). When I is zero, it implies that there is no spin. There is an intrinsic magnitude of the produced dipole, expressed in terms of the nuclear magnetic moment, μ . It is possible to use the atomic mass and atomic number to calculate the spin number, I .

However, if the nucleus I value is equal to or greater than one, the nucleus will have a non-spherical charge distribution. This leads to the production of a moment of electric quadrupole that affects the relaxation time. Broadening of signal peaks and coupling with neighbouring nuclei, therefore, are affected. The orientation of a nucleus is determined by its spin number in a magnetic field and is represented as $2I + 1$. A proton has a spin number of $1/2$, which is described in Figure 2.12, reveals two types

of energy called α and β . There is a higher proton population (N) at the lower energy level, following the Boltzmann distribution.

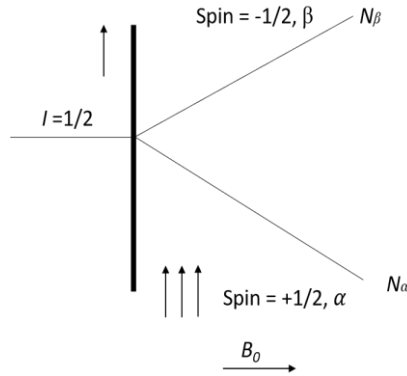


Figure 2.12 Two proton energy levels, from quantum mechanics, in a magnetic field of magnitude B_0 .

The energy change between the spin states of α and β is defined by:

$$\Delta E = \frac{h\gamma}{2\pi} B_0 \quad (\text{Eqn 2.22})$$

Where h indicates the Planck constant, which means that ΔE is directly proportional to the applied magnetic field, B_0 , as all the other parameters are constants, as shown in Figure 2.12. The proportionality constant between the magnetic moment, μ , and the spin number, I , is γ , called the magnetogyric ratio and is expressed as:

$$\gamma = \frac{2\pi\mu}{hI} \quad (\text{Eqn 2.23})$$

When two energy levels for the proton are determined, energy in the form of rf radiation (ν_1) can be applied to initiate the transition between the two energy states in a stationary strong magnetic field, B_0 . As shown in Equation (2.24), rf radiation and the magnetic field of strength are related:

$$\nu_1 = \frac{\gamma}{2\pi} B_0 \quad (\text{Eqn 2.24})$$

Since

$$\Delta E = h\nu \quad (\text{Eqn 2.25})$$

ν_1 is expressed in units of megahertz (MHz). In order to put the proton into a resonance state, a frequency of 100 MHz at a magnetic field strength of 2.35 tesla(T) is therefore required. The resonance state is when energy is absorbed by a proton and transits from the lower energy level, or α spin state, to the higher energy level, or β spin state. A signal corresponding to this transition is determined at this stage, and a spectrum for the nucleus is obtained.

CHAPTER 3 Synthesis of $\text{Ag}_3\text{PO}_4/\text{TiO}_2$ Nanocomposites for Enhanced Photocatalytic Degradation of Aqueous Organic Pollutants

The present study aimed to synthesize the cubic, particle Ag_3PO_4 through simple reaction and $\text{Ag}_3\text{PO}_4/\text{TiO}_2$ nanocomposite containing a different proportion of TiO_2 and Ag_3PO_4 by in situ precipitation techniques and determine the most optimal nanocomposite mixtures. Moreover, the relationship among morphologies, photocatalytic activity and stability in the degradation of typical organic pollutants were discussed in this study.

3.1 Introduction

Persistent organic pollutants (POPs), typically containing benzene rings, are of great concern due to their toxicity nature, ability to bioaccumulate to toxic levels in biological systems, and the ability to persist in the environment.²²⁹⁻²³¹ Photocatalytic degradation of such organic pollutants is a promising strategy for environmental restoration since it can be a green chemistry process if it only uses sunlight as the energy source.²³²⁻²³⁴ Attempts to develop a photocatalyst that is both efficient in visible light and stable have been made, though they are yet to be successful.^{235,236}

In this work, I focus on the developing silver phosphates (Ag_3PO_4) and its hybrid with TiO_2 as the model catalysts for visible light photocatalytic degradation of POPs.²³⁷⁻²³⁹ The precipitation method was used for the preparation of Ag_3PO_4 nanocrystals by reacting with Na_2HPO_4 and using ammonia as the mediate agent to control their morphologies.^{203,240} The crystal structure, surface morphology and chemical properties of the photocatalyst were characterized by SEM, XRD, DLS and UV-Vis. The as-prepared Ag_3PO_4 has a cubic-type structure, and the morphologies are controlled by adjusting the concentration of 30% ammonia solution.²⁴¹ The

photocatalytic activities of Ag_3PO_4 with different morphologies were measured by the degradation of methylene blue (MB) under visible light irradiation. The results showed that the cubic Ag_3PO_4 microcrystals synthesised with 0.15 M 30% ammonia solution possessed the better photocatalytic activity using either ultraviolet or visible light irradiation than that of the commercial Degussa P25, and Ag_3PO_4 synthesised under different conditions.

$\text{Ag}_3\text{PO}_4/\text{TiO}_2$ composites synthesized by in-situ precipitation (co-precipitation) technique and evaluated its photodegradation activity on aqueous solutions containing aromatic compounds.^{242,243} The composites allowed enhanced the activity and stability of Ag_3PO_4 . The high dispersion of TiO_2 particles over the surface of Ag_3PO_4 created heterojunction interfaces, as revealed by scanning electron microscopy (SEM). The UV-Vis diffuse reflectance spectroscopy data revealed that the TiO_2 component did not hinder the composite's ability to absorb visible light. The advantages of using TiO_2 were further investigated through the photoluminescence studies, which showed a decrease in exciton recombination rates in the composite materials with respect to the pure Ag_3PO_4 . The composite materials were shown to have an increased photodegradation activity when compared to pure particle Ag_3PO_4 .

Additionally, the inclusion of TiO_2 in the composites has resulted in a higher reaction rate, with optimal photoactivity observed with 60:40 (wt%) mix proportion of the $\text{Ag}_3\text{PO}_4/\text{TiO}_2$ composites. Further studies on the crystallinity of the TiO_2 were used to determine the impact of the relative concentrations of the anatase and rutile crystal structures on the photodecomposition properties of the composite catalysts. From the observed activity of TiO_2 composite structures, it is possible to see the future development of enhanced photocatalysts to decompose pollutants in water.

3.1.1 Removal of Organic Pollutants from Water and Wastewater

Environmental aromatic organic pollutants include polychlorinated biphenyls (PCBs), polychlorinated dibenzo-p-dioxins and dibenzofurans (PCDD/Fs), organochlorine pesticides (OCPs), hexachlorobenzene (HCB), dichloro-diphenyl-trichloroethane (DDT), dioxins and furans in water and wastewater.²⁴⁴⁻²⁴⁶ Many commercial decontamination methods are available, including coagulation, precipitation, ozonation, ion exchange, reverse osmosis, advanced oxidation processes and adsorption techniques.^{4,247,248} However, the application of these techniques is limited by the high consumption of energy and chemicals which require high capital and operational costs.²⁴⁹⁻²⁵¹ This has warranted a continued effort to develop green yet cost-efficient techniques. The efficient photocatalytic oxidation process is potentially feasible for the decomposition of organic pollutants under ambient conditions.¹⁵² The method relies on the photochemically generated reactive radical species, such as HO^\bullet , $\text{O}_2^{\bullet-}$, and $\text{SO}_4^{\bullet-}$, which oxidatively decompose the organic pollutants to simple environmentally benign molecules, such as CO_2 and water.^{153,154} However, a photocatalyst must be present to transform the photoenergy into the reactive radical species.

Here, I used the MB dye as a laboratory standard model to determine the photocatalytic activity of $\text{Ag}_3\text{PO}_4/\text{TiO}_2$ composite. Methylene blue, also known as methylthioninium chloride, is a water-soluble dye. The molecular structure of MB is shown in Figure 3.1. It contains an extended conjugated system, which is normally used as a model for studying aromatic organic pollutants. The concentration of MB dye in water can be quantitatively monitored by measuring the UV-Vis absorption at MB peak wavelength (λ_{max}) of 664 nm. Oxidative radicals generated by $\text{Ag}_3\text{PO}_4/\text{TiO}_2$ composite can react with MB to decompose it to simple aromatic compounds. The

possible reaction pathway is suggested in Figure 3.2, although it is well known that detecting the MB degradation intermediates is difficult and need more complicated instruments.^{252,253}

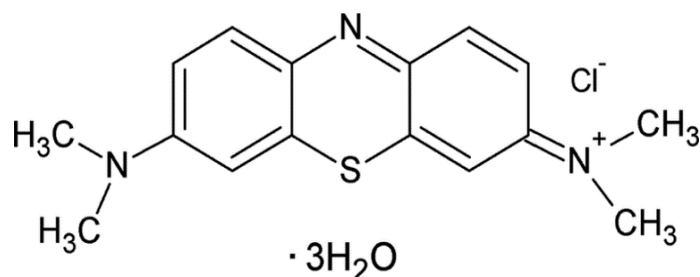


Figure 3.1 The molecular structure of methylene blue dye.

It is well known that two oxidative agents are the initiators of the degradation process: Photo-formed holes h^+ (mainly involved in the reaction of decarboxylation and/or OH^\cdot radicals, classified as highly active and degrading but non-selective agents can be produced.²⁵⁴ The formed OH^\cdot radicals attack the C-S+=C functional group in MB. Therefore, the initial stage of MB disintegration can be due to the cleavage of the C-S+=C functional group bonds in MB. In fact, sulfoxide (identified at $m/e=303$) was the first product extracted from MB degradation. A third OH^\cdot attack produces sulfonic acids found in metabolites at $m/e = 230, 218$ and 158 . Other fragments detected are amine molecules, including *N,N*-Dimethyl-1,4-phenylenediamine. The amines are further oxidised by OH^\cdot radicals to produce phenol compounds, detected at $m/e = 136, 167$ and 94 (Figure 3.2).^{252,253,255}

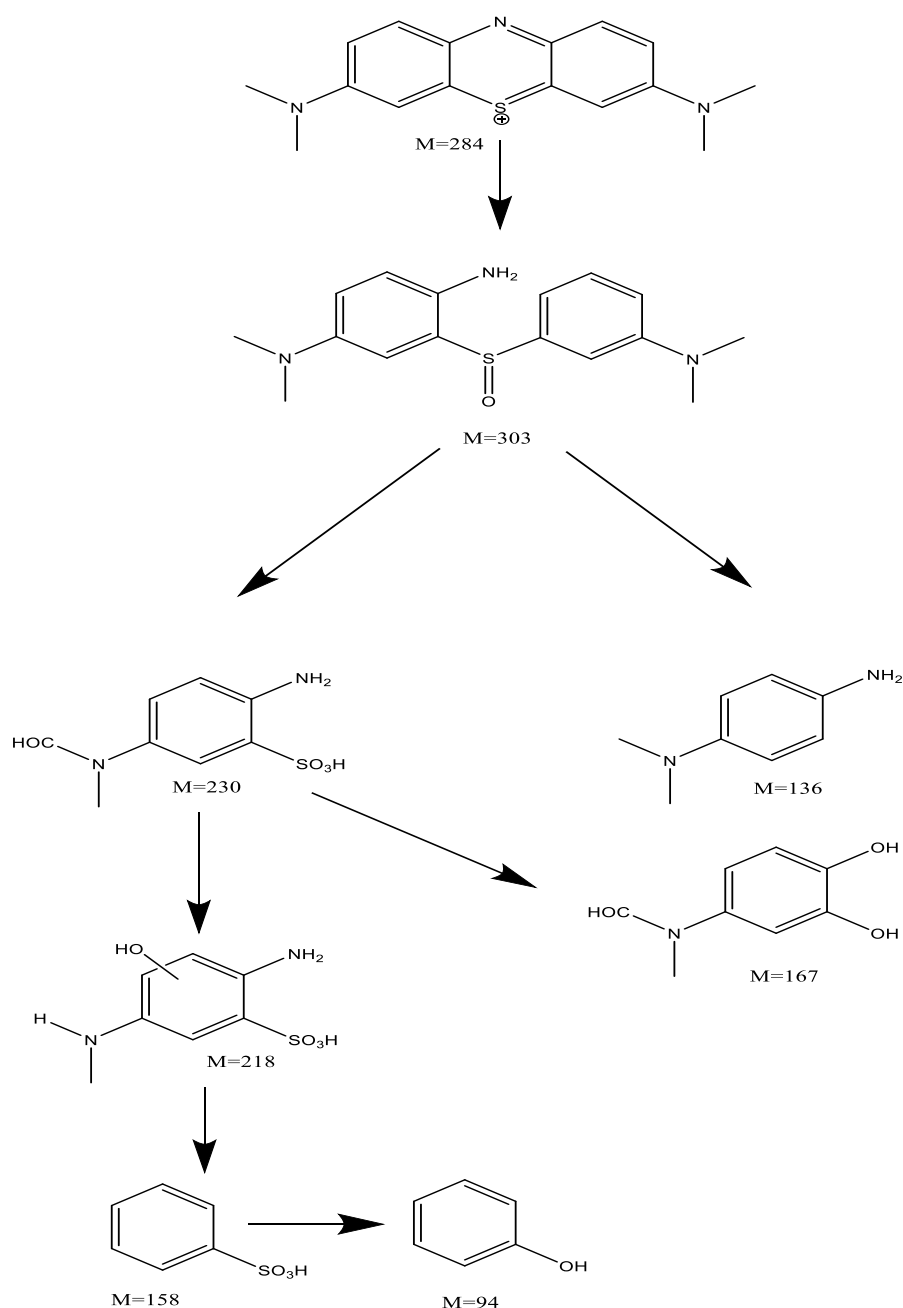


Figure 3.2 The representation of pathway of MB degradation with corresponding molecular fragments and their mass.

Transition metal oxides are good photocatalyst candidates for photocatalytic decomposition of organic compounds using sunlight. TiO_2 is used as a standard photocatalyst in this study due to its high reactivity under UV irradiation, excellent chemical, physical and biological stability, low-cost and abundant in industrial quantities.¹⁷⁶ It creates excited electrons and holes which can react with water molecules to generate highly reactive HO^\bullet and $\text{O}_2^{\bullet-}$ radicals. These radicals can initiate

a chain of radical mediated reactions that degrade organic compounds.^{177,178,183} However, TiO_2 , as a photocatalyst, has its limitation. The most critical drawback of TiO_2 is that it has a relatively large bandgap energy of 3.2 eV, so it only absorbs the UV portion of the sunlight with wavelength short than 385 nm. The majority of the solar energy sits in the visible range peaked at a longer wavelength. Hence, only about 5% of the solar energy can be used by TiO_2 . In order to overcome this problem, many efforts have been made to reduce the bandgap energy of TiO_2 . Many studies have been undertaken to improve and modify TiO_2 by coupling other semiconductor materials, doping metal and non-metal elements and surface modification with inorganic acids.²⁵⁶⁻²⁵⁸ Doping elements, such as S, N, C and B may expand the absorption ability of TiO_2 to visible light. These elements could decrease the TiO_2 bandgap by contributing their p-orbitals in the valence band and substitute the oxygen atoms from the lattice of TiO_2 .²⁵⁹ Furthermore, coupling TiO_2 with narrow bandgap semiconductors could also enhance the photocatalytic activity due to the extension of the absorption to the visible region and possibly enhancing the charge separation by introducing the matched heterogeneous junction.²⁶⁰ In this work, I developed the composite photocatalysts by decorating TiO_2 nanoparticles on the outside of narrow bandgap Ag_3PO_4 microcrystals.

3.1.2 The Structure and Physical Properties of Ag_3PO_4

Photocatalyst

Semiconductor photocatalysis as a green and environmentally friendly technology has been widely used for the removal and degradation of pollutants in the air purification and water disinfection processes. The narrow bandgap semiconductors are essential for the degradation of an organic compound since they can absorb a wide range of sunlight.²⁶¹ Silver orthophosphate (Ag_3PO_4) is an n-type semiconductor with an

indirect bandgap of 2.36 eV and direct bandgap of 2.43 eV. It has attracted considerable attention since its photoactivity was discovered by *Yi et al.* in 2010, due to be able to harness visible light to oxidize water and decompose organic compounds.²⁶² It has been identified as one of the most promising photocatalytic materials for photooxidative capabilities of O_2 evolution from water splitting as well as organic dye decomposition under visible light irradiation due to its appropriate band edges.

Ag_3PO_4 has a body-centred cubic crystal structure with $P43n$ space group and a lattice constant of 6.004 Å. The structure consists of two isolated, regular PO_4 tetrahedra (P-O distance of ~ 1.539 Å). The six Ag^+ ions are distributed among twelve sites of twofold symmetry as shown in Figure 3.3. Ag_3PO_4 possesses a very deep valence band, located approximately +2.9 V vs. NHE (Normal Hydrogen Electrode, pH=0), and therefore is more than powerful enough for the water oxidation reactions.

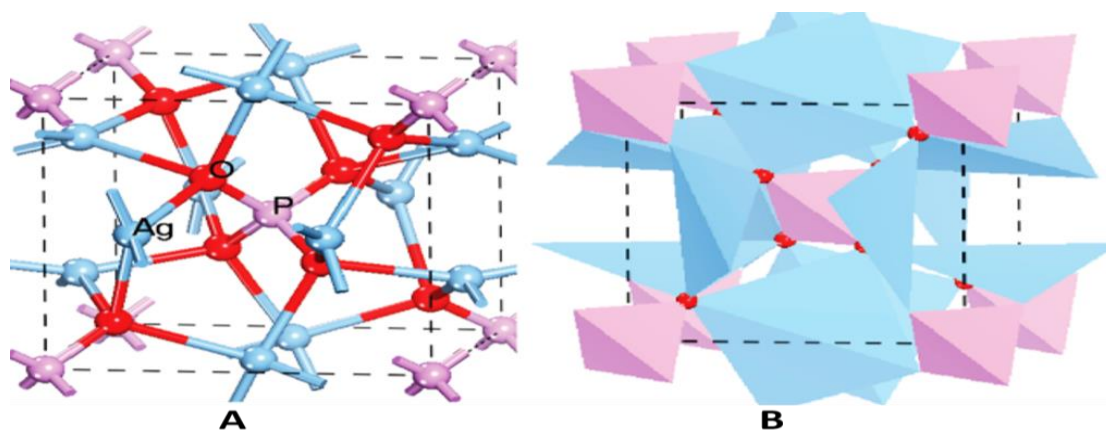
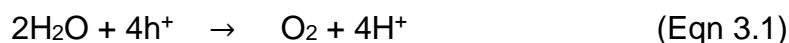


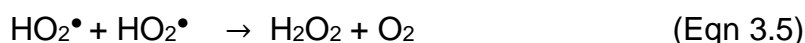
Figure 3.3 Unit-cell structure of cubic Ag_3PO_4 , showing (A) ball and stick and (B) polyhedron configurations. Red, purple, and blue spheres represent O, P, and Ag atoms, respectively. Adapted from Xinguo, Ma.²⁶³

However, the conduction band is located at +0.45 V vs. NHE (pH=0), meaning that H^+ cannot be reduced to H_2 under standard conditions. Thus, the compound alone cannot be used for bias-free water splitting. To overcome this, the semiconductor could be used in a photoelectrochemical (PEC) cell under slight electrical bias or use

an electron scavenger to assist the water oxidation. In the latter case, the most efficient electron scavenger is free Ag^+ . By preventing recombination using an electron scavenger, the highly oxidizing valence band hole either oxidizes water or organic contaminants via the following reactions.²⁶⁴ A typical water photooxidation using a photocatalyst can be described as:



The OH^\bullet radicals can also be generated by the oxidation of water:



The valence band of Ag_3PO_4 is formed from both Ag d band and O p band, while for a typical oxide, the valence band is dominated only by the O p band. The contribution of transition metal electronic states in the valence band can increase the hole mobility, and the holes are thereby likely to migrate to the surface of Ag_3PO_4 to for the high efficient oxidation reactions.^{166,265} For instance, Ag_3PO_4 has shown to yield very high quantum efficiency of nearly 90% for the evolution of O_2 from water under visible light irradiation. The combination of its narrow bandgap of 2.45 eV (direct) and the appropriate position of valence-band (VB) edge, as well as its band character, makes Ag_3PO_4 a good candidate for photocatalytic oxidation reaction, which is sensitive to the visible-light.²

3.1.3 Optimization of TiO_2 -Based Photocatalytic System

Among various semiconductors, TiO_2 has been widely used in various applications due to its high oxidizing power, good chemical stability, non-toxicity and low cost.²⁶² Unfortunately, due to its wide bandgap, TiO_2 only shows the photocatalytic ability

under ultraviolet (UV) light irradiation. This limits the solar light absorption since the power of UV light occupies less than 5% in that of all the solar light.²⁶⁶ Thus, the development of novel visible light responsive TiO_2 photocatalysts is urgently needed.

Optimization by synergistic effects of TiO_2 and other visible light sensitive semiconductors is possible. Silver phosphate (Ag_3PO_4) is one of the promising semiconductors due to its ability to absorb visible light up to 530 nm. Furthermore, electron-hole recombination, which is known to reduce catalytic efficiency, is very low in Ag_3PO_4 nanoparticles compared to many other narrow-band gap semiconductors. Thus, Ag_3PO_4 is a potential excellent photocatalyst as compared to many other semiconductors.^{267,268} However, Ag_3PO_4 cannot function as a standalone photocatalyst due to poor photostability and can be easily reduced to silver.²⁶⁹ Therefore, the photostability of Ag_3PO_4 has to be improved which can be achieved by combining with other semiconductors that are efficient and chemically stable. In this project, the composite of TiO_2 and Ag_3PO_4 was designed, synthesized and tested for its photocatalytic activities. As TiO_2 and Ag_3PO_4 have a different bandgap, effectively, a broader range of wavelength of sunlight can be absorbed, which improves solar energy efficiency.

By coupling Ag_3PO_4 nanoparticles with TiO_2 can have an influence on the surface charge distribution of TiO_2 , which can promote the separation of photo-generated electrons, and therefore, effectively restraining electron-hole recombination.²⁰³ Due to the difference in the band edge positions between the TiO_2 and Ag_3PO_4 , it is expected that the photoexcited electrons and holes are better separated at the interface between TiO_2 and Ag_3PO_4 . This could also help to improve the stability of Ag_3PO_4 by limiting the reduction of Ag^+ with photogenerated electrons.

The $\text{Ag}_3\text{PO}_4/\text{TiO}_2$ composite can form a well-matched heterojunction structure. The relative band edge positions of Ag_3PO_4 and TiO_2 with respect to the V_{NHE} are shown in Figure 3.4.²⁷⁰ The conduction band minimum of the Ag_3PO_4 and TiO_2 are at +0.45 and -0.5 eV, respectively, while the corresponding conduction band maxima are at +2.9 and +2.7 eV. Thus the bandgap energies of Ag_3PO_4 and TiO_2 are 2.45 and 3.2 eV, respectively.²⁷¹ As shown in Figure 3.4., the slightly more positive of the valence band of Ag_3PO_4 means that the photoexcited electrons remain in the CB of Ag_3PO_4 while the photogenerated holes in the VB of the Ag_3PO_4 are transferred to the VB of TiO_2 . Hence, the charge separation at the interface between Ag_3PO_4 and TiO_2 are improved. significantly.²⁴² In this work, I used fluorescence spectroscopy study to confirm the improved charge separation between Ag_3PO_4 and TiO_2 .

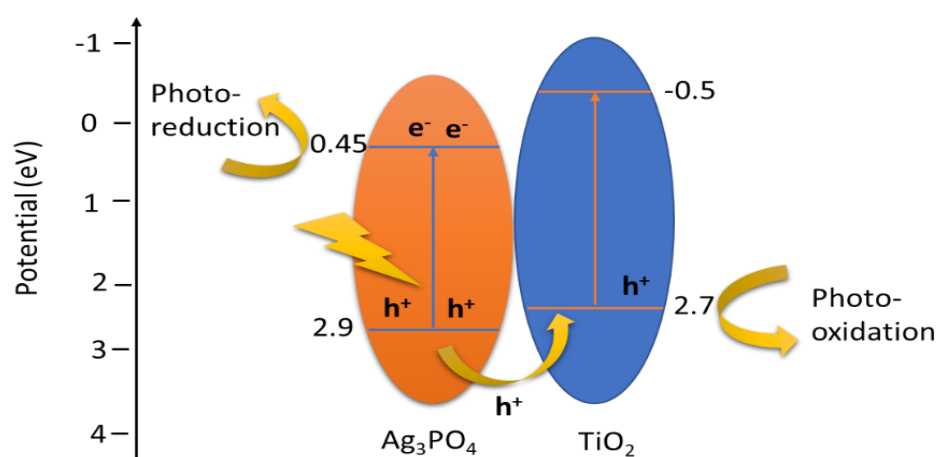


Figure 3.4 A schematic diagram of the band structure and the photo-induced charge separation process in $\text{Ag}_3\text{PO}_4/\text{TiO}_2$ composite.

The size of Ag_3PO_4 crystals is normally larger than $1\ \mu\text{m}$, while the size of TiO_2 in P25 is about 21 nm which is much smaller.⁴² Hence, by modifying the surface of Ag_3PO_4 crystals with TiO_2 nanoparticles, it is possible to increase the surface density of photocatalytic centre with anticipated enhancement in the photocatalytic decomposition of organic pollutants.

In the $\text{Ag}_3\text{PO}_4/\text{TiO}_2$ composite, if TiO_2 modified the surface of Ag_3PO_4 , the photocatalytic activity was found to be improved.²⁴³ Other studies have developed high efficient photoelectrodes with, $\text{Ag}_3\text{PO}_4/\text{TiO}_2$ and $\text{Ag}/\text{Ag}_3\text{PO}_4/\text{TiO}_2$ heterostructures.²⁷² The composite material can be created with either TiO_2 or Ag_3PO_4 as the core material. With TiO_2 as the core, the composite is described as $\text{TiO}_2/\text{Ag}_3\text{PO}_4$. On the other hand, when Ag_3PO_4 is the core material, the composite is defined as $\text{Ag}_3\text{PO}_4/\text{TiO}_2$. For a typical core-shell composite material, the core material is the major component. Most studies have explored the $\text{Ag}_3\text{PO}_4/\text{TiO}_2$ composites since TiO_2 forms smaller crystal particles than Ag_3PO_4 . Compared with $\text{TiO}_2/\text{Ag}_3\text{PO}_4$, it is expected that $\text{Ag}_3\text{PO}_4/\text{TiO}_2$ is more sensitive to the visible light since the narrow bandgap Ag_3PO_4 core is the major component. This is because normally, the thickness of the shell is very thin. Furthermore, since Ag_3PO_4 is readily to form the large crystal, it is difficult to control the morphology of Ag_3PO_4 on the surface of TiO_2 .²⁰³ These challenges have prevented the application of the $\text{TiO}_2/\text{Ag}_3\text{PO}_4$ composite in photocatalytic systems. From the band structures illustrated in Figure 3.4, the hole will transfer from Ag_3PO_4 to the TiO_2 . The attachment of TiO_2 nanoparticles on the surface helps to facilitate the utilizing of holes to create oxidative radicals in the solution.

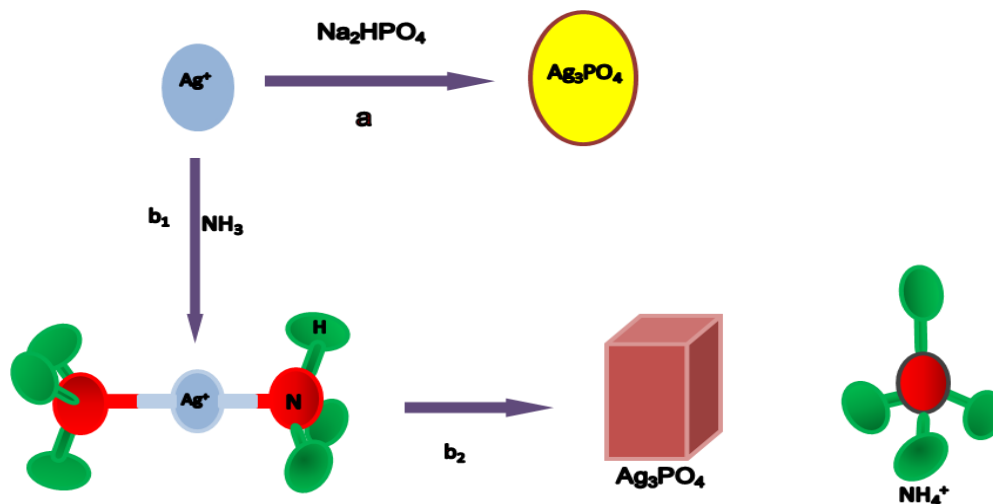
3.2 Experimental

3.2.1 Materials and Reagents

The chemicals used in this experiment, included AgNO_3 (of > 99 % purity), Na_2HPO_4 , and TiO_2 (Aeroxide[®] P25; formerly Degussa P25), which consists of a mixture of two phases (~75% anatase and ~25% rutile), NH_3 solution and MB dye were purchased from Sigma Aldrich, UK. The chemicals were used as received without further purification unless otherwise stated. Deionized water was prepared in the laboratory

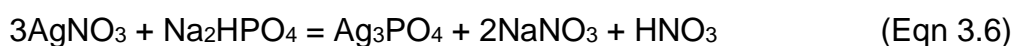
using the Suez/Purite Select deionization unit. Philips CDM-T Halogen 150W Metal Halide Lamp was obtained commercially obtained from Philips Centre (Guildford, UK).

3.2.2 Preparation of Ag_3PO_4 Nanoparticles



Scheme 3.1 The scheme of the formation process of the Ag_3PO_4 (cubes and particles) using different precursors.

Pure Ag_3PO_4 was synthesized using the precipitation method also described in scheme 3.1.^{269,273} The precipitation reaction is described in equation 3.6.



Briefly, under ambient conditions, 1.8 g of AgNO_3 was dispersed in 15 mL deionized water using a magnetic stirrer followed by a dropwise addition of 30 mL 0.15 M Na_2HPO_4 . The resultant solution becomes pale yellow milky coloured. The mixture was stirred for 30 minutes. Afterwards, the product was centrifuged and collected. The resulting light-yellow powder was then washed with deionized water to remove soluble reaction products of NaNO_3 and HNO_3 as well as the excess Na_2HPO_4 . The sample was dried at 65°C in an oven overnight. Here, the reaction between the AgNO_3 and Na_2HPO_4 is too fast to control the morphology and only spherical porous particles were obtained.

3.2.3 Preparation of $\text{Ag}_3\text{PO}_4/\text{TiO}_2$ Nanocomposites

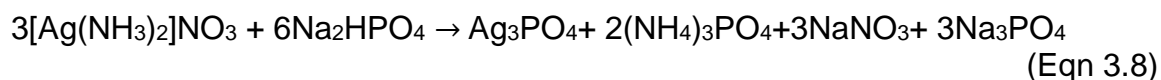
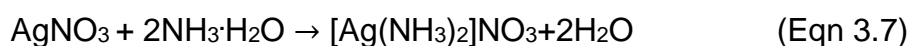
P25 is as known as a commercial form of TiO_2 , which show highly efficient as a photocatalyst due to absence of mass transfer limitation, a mixture of the anatase and rutile polymorphs of 80% and 20% respectively. P25 nanopowder (Degussa, Germany) has the averaged particle size of 15 nm. It was used in the preparation of $\text{Ag}_3\text{PO}_4/\text{TiO}_2$ nanocomposites. In this case, Ag_3PO_4 was synthesised with the present of P25. 80 g of TiO_2 was suspended in 40 mL deionized water using a magnetic stirrer. The suspension was further dispersed by sonicating for 5 min. After sonication, 24 g of AgNO_3 was added to the suspension and then magnetically stirred for 10 minutes. 30 mL of 0.15 M Na_2HPO_4 was added dropwise to the suspension with continuously stirring for 4 hours. The suspension was filtered using a filter paper. The collected precipitates were washed several times with deionized water, before drying at 65°C overnight. The resultant $\text{Ag}_3\text{PO}_4/\text{TiO}_2$ nanocomposite contained 20 wt% Ag_3PO_4 and 80 wt% P25. Similar procedures were followed for the preparation of $\text{Ag}_3\text{PO}_4/\text{TiO}_2$ nanocomposites with different wt% between Ag_3PO_4 and P25 of 40:60, 50:50, 60:40 and 80:20. A similar procedure was also followed for the preparation of $\text{Ag}_3\text{PO}_4/\text{rutile}$ powders for photocatalytic comparison experiment.

3.2.4 Preparation of Crystallised Cubic Ag_3PO_4 Nanoparticles

Ag_3PO_4 cubic nanocrystals were synthesized using a similar precipitation process (scheme 3.1) but with added NH_3 to stabilise Ag^+ by forming $[\text{Ag}(\text{NH}_3)_2]^+$.²⁴¹ AgNO_3 was dissolved in water to form an aqueous solution at room temperature, and ammonia aqueous solution was added drop by drop to the above solution until the solution became transparent. In order to control the morphology and size of the cubic silver phosphate, I prepared different concentrations of the silver ammonia ($[\text{Ag}(\text{NH}_3)_2]^+$) complex of 0.10, 0.20, 0.30 M 30% ammonia solution. Then, 4 mL

Na₂HPO₄ aqueous solution (0.15 M) was added dropwise to form olivine Ag₃PO₄ crystals with cubic structure. The stabilisation of Ag⁺ with NH₃ slows down the reaction with PO₄³⁺ and the precipitation of Ag₃PO₄. This gives more time for the formation of high quality crystalline cubic Ag₃PO₄. The resulting product was washed with deionised water several times and dried at 60 °C for five hours.

The synthesis process can be represented by reactions described in equations 3.7 and 3.8:



It should be noted that the intermediate [Ag(NH₃)₂]⁺ complex plays a critical role in the producing of the Ag₃PO₄ sub-microcubes. In contrast, without NH₃, irregular spherical structures of Ag₃PO₄ particles were formed when the AgNO₃ reacts directly with Na₂HPO₄ under the same conditions. The description of different Ag₃PO₄ morphologies made from the precursors AgNO₃ and [Ag(NH₃)₂]⁺ is illustrated in Scheme 3.1.²⁶⁹

Without NH₃, the free Ag⁺ ions react with PO₄³⁺ spontaneously with rapid nucleation, resulting in the similar growth rates of the different plans of Ag₃PO₄ particles. This forms the spherical morphology. In comparison, when [Ag(NH₃)₂]⁺ is formed as the precursor, the formation of Ag₃PO₄ will involve the dissociation of [Ag(NH₃)₂]⁺, which will restrict the release of free Ag⁺ ions. Such restriction slows down the Ag₃PO₄ growth rate, allowing the selective growth of specific crystal planes determined by the surface energy, rather than reaction kinetics.

3.2.5 Morphological, Crystallinity and Optical Characterization of Ag_3PO_4 Based Nanoparticles and Nanocomposites

The morphologies and nanostructures of Ag_3PO_4 cubic crystals, nanoparticles and the corresponding TiO_2 nanocomposites were characterized by a scanning electron microscope (SEM) (JSM 820M, Jeol). The crystallinity and orientation of the nanostructures were analyzed by a powder x-ray diffractometer (XRD) (Siemens D500) using $\text{Cu K}\alpha$ radiation ($\lambda = 1.5418 \text{ \AA}$) at the acceleration of 40 kV with a constant emission current of 30 mA.

The UV-Vis absorption spectra of diluted, suspended solution were recorded using a UV-Vis spectrophotometer (Thermospectronic UV 300). The band gaps of solid or thin film materials were determined by reflectance absorption measurements using an Ocean Optics ISP-REF integrating sphere equipped with a built in tungsten-halogen illumination source (300 nm to 1000 nm) and the charge recombinations were characterised using PL spectra recorded with a fluorescence spectrometer (Perkin Elmer LS45).

3.2.6 Evaluation of Photoactivity of TiO_2 (P25 and Rutile), Ag_3PO_4 and Their Composites Through The Degradation of MB

The photocatalytic activities of the synthesised Ag_3PO_4 cubic, particles and Ag_3PO_4 based nanocomposites were evaluated by studying the degradation of methylene blue (MB) under UV-vis irradiation. A 0.05 g portion of the photocatalyst was evenly dispersed in a 100 mL of MB solution (10 mg/L) by magnetic stirring.

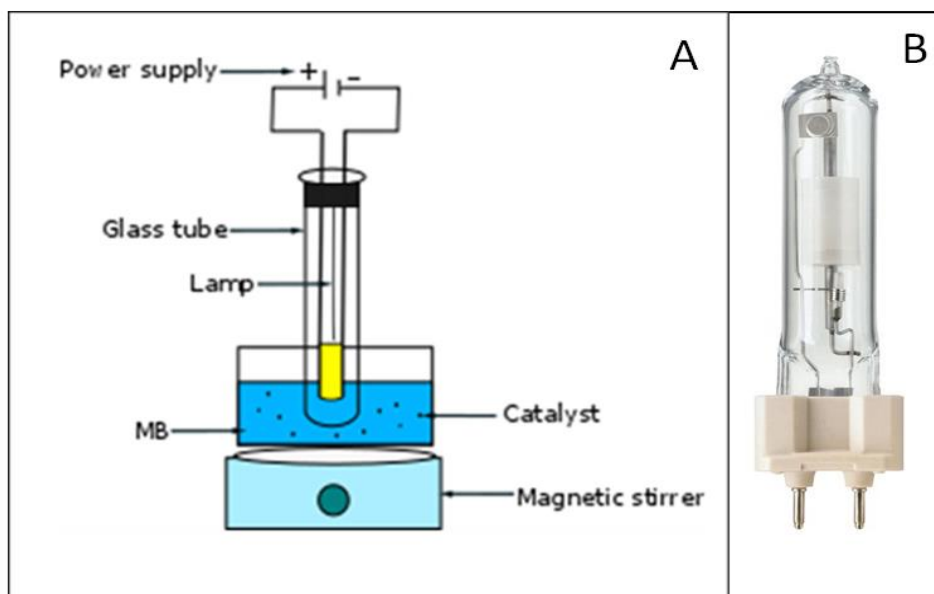


Figure 3.5 Experimental setup for the photocatalytic degradation of MB.

The suspension was then irradiated using a 150 W ceramic metal halide lamp (MASTERColour CDM-T 942 G12, 4200K cool white colour Philips). The setup is illustrated in Figure 3.5A and the lamp is shown in Figure 3.5B. The lamp offers high efficacy with bright white light. It has very good colour rendering with stable colour during the lifetime. The MB solution was sampled from the reaction solution at a fixed interval of 1 min. The sample solution contains the catalyst solid and was centrifuged at 1000 rpm for 20 s. The residual concentrations of MB in the supernatant were measured using the UV-Vis spectroscopy. After the measurement, both the supernatant and the photocatalysts were returned into the reactor. The degree of photodecomposition of the MB dye was calculated based on the change in the absorption intensity at its maximum wavelength (λ_{\max}) of 664 nm, described in Equation 3.9.

$$\text{degradation \%} = \frac{(A^0 - A_t)}{A^0} \times 100 \quad (\text{Eqn 3.9})$$

Where A° is the initial absorbance of MB, proportional to the initial concentration of MB; and A_t is the absorbance at time t , proportional to the residual concentration of MB.

3.3 Results and Discussion

3.3.1 Characterization of Pure Ag_3PO_4 and $\text{Ag}_3\text{PO}_4/\text{TiO}_2$ Nanoparticles

The morphologies of nano photocatalysts and their nanocomposites can influence their photocatalytic activity.²⁷⁴ Different exposed crystal planes of the catalysts have different atomic densities and atom spacing. Some structures are more reactive than the others due to a good match of the atomic structures, and more importantly, the appropriate electronic structures. The density of surface defects can also play a crucial role in the catalytic kinetics. Different crystal planes presented on the surface of nanocatalysts can also affect the selectivity of the catalysis, due to the influence of surface electronic structures and surface chemical bonding properties. Hence, it is important to control the crystal morphology of nanocatalysts to optimise the catalytic performance. It has been reported that changing the morphology of the Co_3O_4 nanoparticles from spherical nanoparticles to nanorods enhance the activity of these nanoparticles.²⁷⁵ Wenfeng Lin and co-workers reported that the cubic, octahedral or rhombic dodecahedral palladium nanocrystals gave different oxidation kinetics for ethanol and ethylene glycol.²⁷⁶ The combined electrochemical measurements and density functional theory calculations revealed that nanofacet-dependent affinity and reactivity of OH_{ads} and CO_{ads} were closely linked to the C2 alcohol oxidation activities, with the highest reactivity found on the Pd nanocubes bounded by facets.²⁵⁹

Another important morphological property of the nanomaterials is their large surface area. For typical chemical reactions on solid surfaces, the reaction rate constants are positively proportional to the adsorption of reactants on the solid surface. Hence, in comparison with bulk materials, the larger surface area of nanocatalysts promotes faster reactions. For example, TiO_2 sol with a particle size of 22.5 nm was synthesised for the degradation of methylene blue (MB) solution under UV irradiation.²⁷⁷ It was found that after 160 min photocatalytic degradation, 92.3% of the MB was degraded. The small particle size caused the increase in the specific surface area, which lead to the acceleration of the photocatalytic reaction.

Here, we study how the synthetic conditions can affect the surface morphologies of Ag_3PO_4 and TiO_2 nanoparticles and their nanocomposites. SEM images of typical Ag_3PO_4 nanoparticles are displayed in Figure 3.6A.

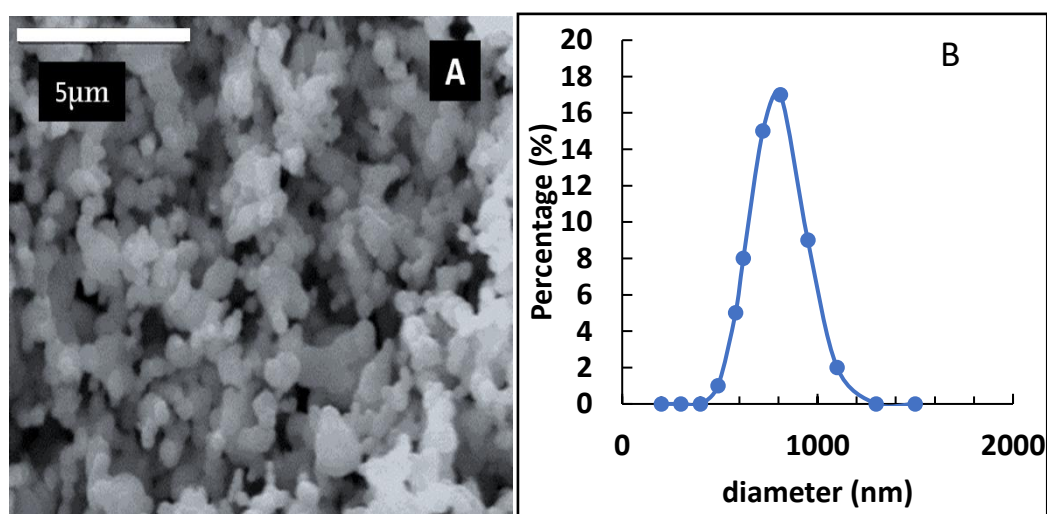


Figure 3.6 (A) SEM images of the Ag_3PO_4 microparticles with a scale bar of 5 μm and (B) DLS measurement of particle size distribution.

It shows the surface morphology and size of the synthesized Ag_3PO_4 nanoparticles. The nanoparticles appeared to be spherical with a smooth surface. The particle size distribution was measured with DLS, shown in Figure 3.6B. The averaged particle size is 800 nm (peak of the size distribution) with a distribution width of 350

nm, determined from the full width at half maximum (FWHM). The relative broad size distribution is the result of Oswald ripening or the aggregation of fine particles. Since Ag_3PO_4 has very low solubility in water, the Oswald ripening will be limited. Hence, the particle size distribution is probably determined by the aggregation.

3.3.2 Morphology and Dynamic Scattering Light of Cubic Ag_3PO_4

If the reactivity of Ag^+ is controlled by forming a complex with NH_3 , as shown in Eqn 3.7 and 3.8 mentioned in the experimental section, good quality of cubic shaped Ag_3PO_4 can be formed.²⁶⁹ The presence of NH_3 ligand stabilises the Ag^+ and increases the solubility of Ag_3PO_4 . As such, the precipitation and crystal growth for the formation of Ag_3PO_4 becomes slower. Hence good quality crystals can be formed. Figures 3.7A-H show the SEM images and the particle size distributions of the cubic Ag_3PO_4 microcrystals synthesized with different concentrations of $[\text{Ag}(\text{NH}_3)_2]^+$ at room temperature.

It can be seen that with the addition of NH_3 , the regular cubic crystal morphology was formed and the particle size of Ag_3PO_4 crystal was increased as the concentration of 30% ammonia solution was increased from 0.10 M to 0.30 M. Quantitative measurements were carried out via dynamic light scattering (DLS), shown in Figures 3.7B, D, F, and H. The averaged cubic crystal sizes were 462, 480.4, 550.7, and 700.2 nm, while the FWHM of the distributions were 220.5, 242.9, 142.5, and 301.3 nm for the NH_3^+ concentrations of 0.10 M, 0.15 M, 0.20 M, and 0.30 M, respectively. The result is summarised in Table 3.1.

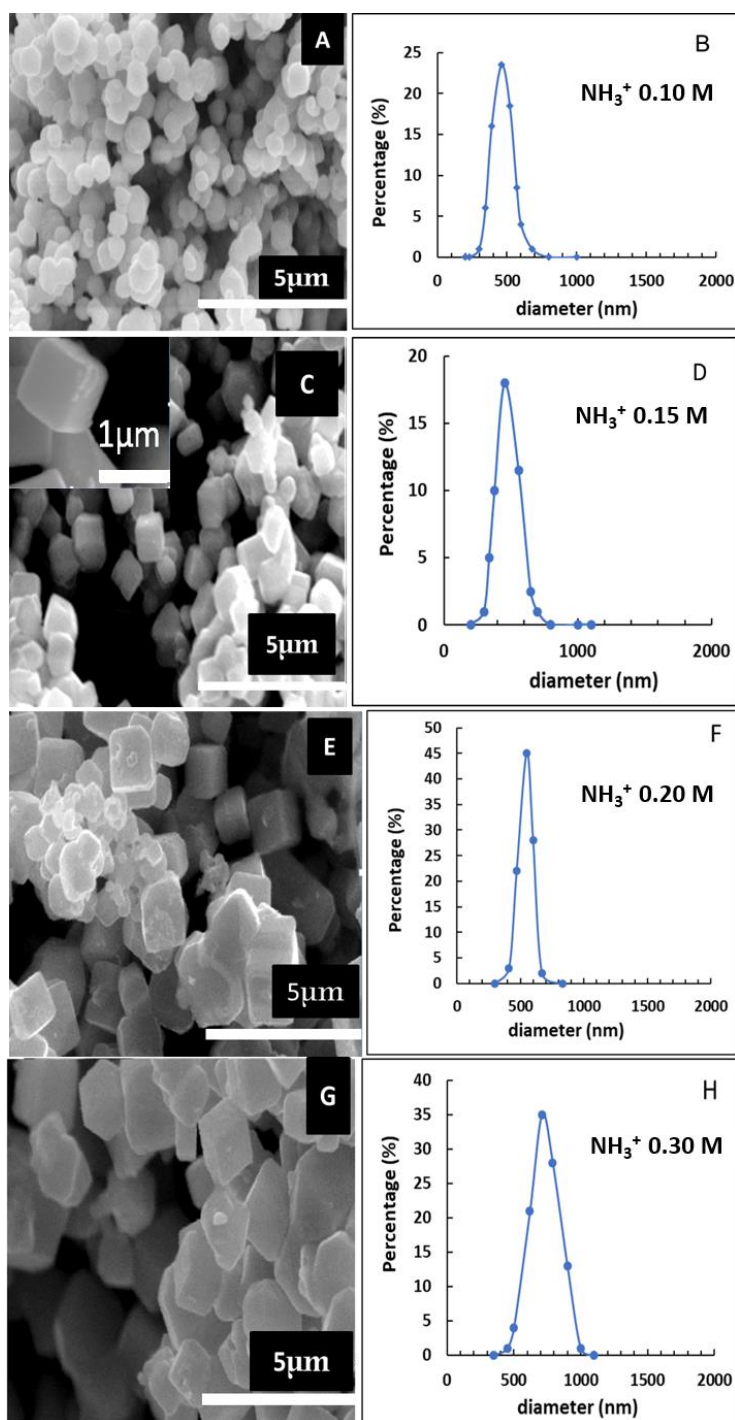


Figure 3.7 Representative SEM images and DLS measurements of cubic Ag_3PO_4 microcrystals synthesised with different concentration of NH_3^+ : (A, B) 0.10 M, (C, D) 0.15 M, (E, F) 0.20 M and (G, H) 0.30 M.

Clearly, the DLS data has a significant error due to the fast precipitation for the large particles during the DLS procedure. The NH_3 in the growth solution plays an important role on the morphology of the cubic Ag_3PO_4 and the particles size. As shown, when the concentration of NH_3 increases, the size of the Ag_3PO_4 cubic crystals

was monotonically increased. At 0.10 M, most of the Ag_3PO_4 crystals have soft edges and the cubic shape is not well defined. By increasing the concentration of NH_3 to 0.15 M, the morphological quality of the cubic Ag_3PO_4 is much more improved with much less aggregation. This suggests that the dominant (100) plane of the cubic crystal of Ag_3PO_4 is well defined with much less density of surface defects.

Here, NH_3 regulates the concentration of free Ag^+ available to react with PO_4^{3-} by forming a stable and soluble complex of $[\text{Ag}(\text{NH}_3)_2]^+$. A typical crystal growth process involves nucleation, growth and Oswald ripening. If the nucleation rate is much faster than the growth rate, small and irregular particles will be formed, and precipitation becomes the dominant process. With reduced Ag^+ concentration, the nucleation rate is reduced while maintaining the growth rate. Under such condition, large and perfect crystals are formed. If both nucleation and growth are slower than Oswald ripening, the size distribution will become broader, and the average crystal size will increase. The crystal size distribution is also affected by the concentrations of the $\text{Ag}(\text{NH}_3)_2^+$. The narrowest distribution was achieved at the concentration of 0.20 M. By increasing it further to 0.30 M, the size distribution was increased to 301.3 nm, which is the results of crystal aggregation.

Table 3.1 A summary of the average size and the width of distribution vs NH_3^+ concentrations.

$[\text{NH}_3]$ (M)	Average diameter (nm)	FWHM (nm)
0.00	800.0	350.0
0.10	462.0	220.5
0.15	480.4	242.9
0.20	550.7	142.5
0.30	700.2	301.3

The crystal structure and phase composition of polycrystalline materials were also analyzed using the non-destructive x-ray Diffraction (XRD) technique, which is based on the interference of the reflected x-ray from the atoms. XRD structural analysis

revealed that the synthesized Ag_3PO_4 nanoparticles were of high purity. The XRD peaks of both cubic and particular samples can be assigned to the Ag_3PO_4 when in comparison with the reference XRD spectrum (JCPDS Card No. 06–0505), in Figure 3.8.

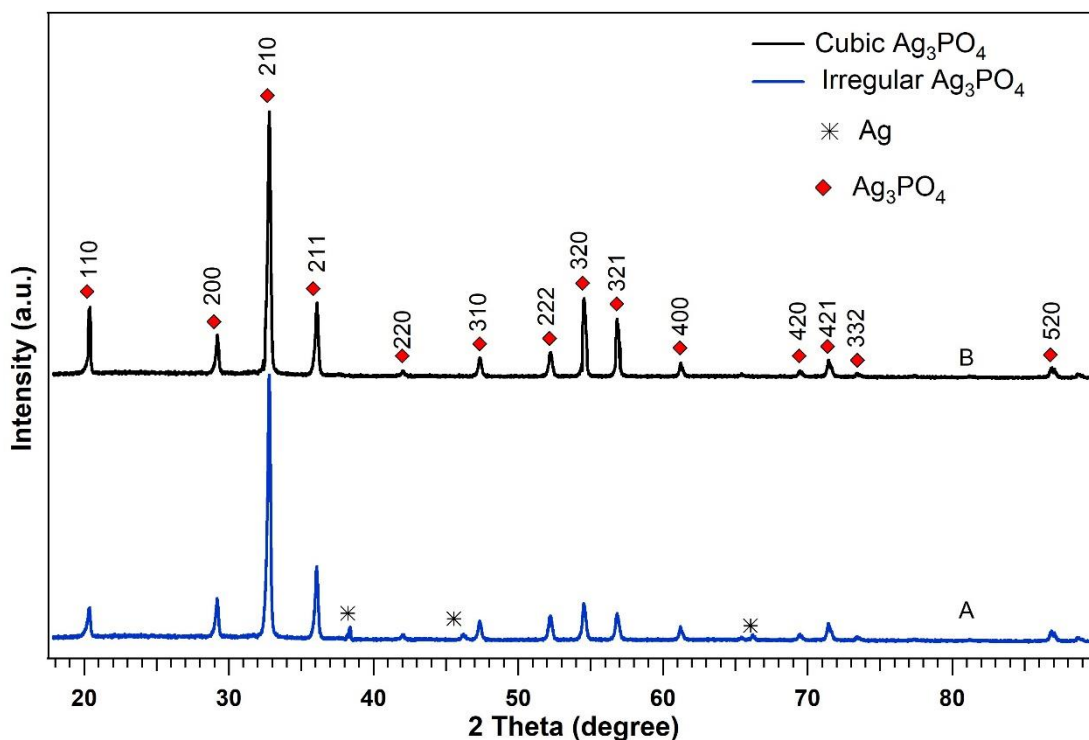


Figure 3.8 XRD spectral patterns of Ag_3PO_4 samples synthesised without (A) and with (B) the addition of NH_3 .

Samples synthesised with or without the addition of NH_3 exhibit a cubic crystalline structure which is consistent with previous reports.²⁷⁸ Using a complex precipitation strategy, Bi *et al.* synthesized single-crystalline Ag_3PO_4 cubes with sharp corners, edges, and smooth surfaces.²⁶⁹ The sharp diffraction peaks indicate that Ag_3PO_4 microcrystals are high quality with good crystallization. Weak diffraction peaks from metallic Ag was been observed in the XRD pattern of irregular Ag_3PO_4 , which was synthesised without the addition of NH_3 . AgNO_3 is known to decompose into element Ag under light illumination. With the stabilisation of Ag^+ with NH_3 , such decomposition can be effectively avoided before the formation of Ag_3PO_4 . Meanwhile,

the intensity of the (110), (320) and (321) peaks from the cubic Ag_3PO_4 are remarkably higher than those from the irregular Ag_3PO_4 crystals. This suggests that the overall crystal quality of the cubic crystals is much better than the irregular Ag_3PO_4 crystals.

3.3.3 Structure and Composition of Two Types $\text{Ag}_3\text{PO}_4/\text{TiO}_2$ Nanocomposite

3.3.3.1 $\text{Ag}_3\text{PO}_4/\text{P25TiO}_2$ Synthesis

There are many reports about the $\text{Ag}_3\text{PO}_4/\text{TiO}_2$ composite, which used Ag_3PO_4 as the sensitizer for TiO_2 -P25 to extend the active light wavelength to the visible region. In addition, Ag_3PO_4 can also enhance the charge separation in P25 due to the potential field at the interface between the Ag_3PO_4 and TiO_2 . The SEM images in Figure 3.9 show the morphology and sizes of the $\text{Ag}_3\text{PO}_4/\text{TiO}_2$ (60:40 weight ratio) nanocomposites. The sample was synthesised by employing a simple, green and versatile synthetic route based on the growth of Ag_3PO_4 on TiO_2 -P25 nanoparticles suspended in water. A portion of Na_2HPO_4 was gradually added to a solution of AgNO_3 with suspended TiO_2 -P25. The $\text{Ag}_3\text{PO}_4/\text{TiO}_2$ nanocomposite exhibits large Ag_3PO_4 crystals coated with amorphous TiO_2 particles. As expected, the TiO_2 particles were uniformly distributed on the surface of the Ag_3PO_4 . The heterojunctions formed between the two catalysts could imply that the $\text{Ag}_3\text{PO}_4/\text{TiO}_2$ nanocomposite has a better charge separation for photocatalysis as compared to each pure material of Ag_3PO_4 and TiO_2 . In this $\text{Ag}_3\text{PO}_4/\text{TiO}_2$ nanocomposite, the two photocatalytic components adhere tightly to each other to form an interface. Its photocatalytic performance can be optimized synergetically. The smooth surface on the Ag_3PO_4 cubes has a low surface area and low density of surface defects. A uniform distribution

of the particular TiO_2 increased the catalytic surface area of the $\text{Ag}_3\text{PO}_4/\text{TiO}_2$ nanocomposite.

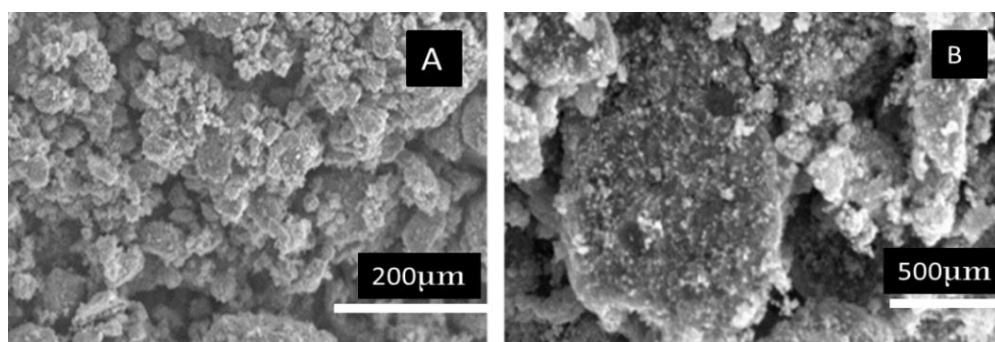


Figure 3.9 An SEM image of the $\text{Ag}_3\text{PO}_4/\text{TiO}_2\text{-P25}$ (60:40) nanocomposite.

The success of the formation of the $\text{Ag}_3\text{PO}_4/\text{TiO}_2$ nanocomposite is based on the ability of the $\text{TiO}_2\text{-P25}$ to adsorb positively charged metal ions. In the present study, the Ag^+ ions (from AgNO_3 solution) were absorbed on the TiO_2 nanoparticles prior to precipitation. The addition of PO_4^{3-} ions resulted in the reaction between the Ag^+ and PO_4^{3-} ions to form Ag_3PO_4 on the surface of TiO_2 , yielding $\text{Ag}_3\text{PO}_4/\text{TiO}_2$ nanocomposite with TiO_2 on the surface of Ag_3PO_4 cubic crystals.²⁴³

3.3.3.2 $\text{Ag}_3\text{PO}_4/\text{TiO}_2\text{-rutile}$ Synthesis

Rutile phase of TiO_2 is an important semiconductor and it has many applications, for instance, plastics, paints, and sun-screen products to protect skin from damages by UV-rays.²⁷⁹ However, many reports confirmed that the pure rutile phase TiO_2 has a relatively poor photocatalytic performance with respect to the anatase TiO_2 .²⁸⁰ This can be due to that, anatase has indirect gap while rutile has a direct gap and that could affect the electron-hole recombination.²⁸¹ Also, rutile has a shorter photoexcited electron lifespan and thus a higher recombination rate compared to anatase, while anatase charge carriers are subjected to competition between hole trapping and recombination processes allowing charge carriers to have a longer lifespan.²⁸² To observe the synergistic effect between the two phases, the method used for the P25 synthesis must ensure good communication between the two phases. The catalyst

preparation method would also have a direct effect on the interfacial boundary morphology, which will in turn influence the electronic energy levels of electron-hole pairs.²⁸³ Also, to obtain the necessary TiO₂ phase composition, the calcination temperature of the catalysts must be closely regulated, with the phase transformation of anatase to rutile starting at around 550°C.²⁸⁴ Many authors have observed that the presence of surface phase junctions in mixed-phase TiO₂ promotes the transfer of electrons between the two phases upon photoexcitation and thus enhances the separation of charges, decreases recombination and consequently increases photocatalytic activity.²⁸⁴⁻²⁸⁶

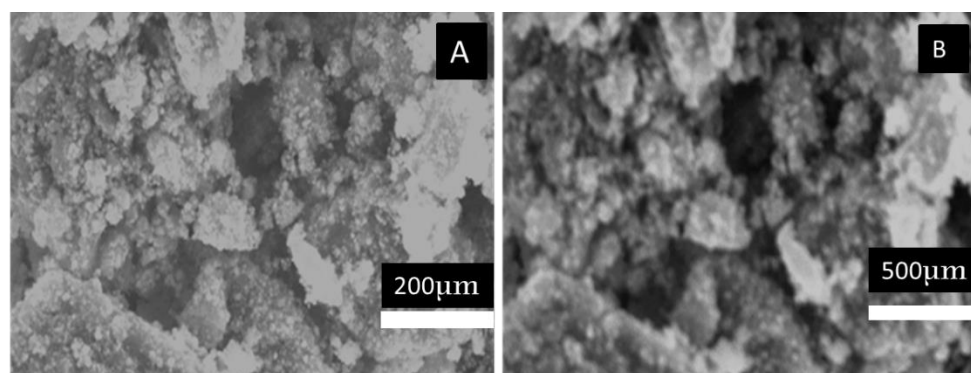


Figure 3.10 An SEM image of the Ag₃PO₄/ TiO₂-rutile (60:40) nanocomposite.

Before the photocatalytic degradation of organic molecules, the morphology of the nanocomposite was examined with SEM. Figure 3.10 shows representative SEM images of the Ag₃PO₄/ TiO₂-rutile (60:40) nanocomposite. The commercial rutile, used in the preparation of nanocomposite, has an average particle size around 100 nm. It can be seen from Figure 3.10, that the synthesized nanocomposite has the Ag₃PO₄ and rutile NPs well mixed, although it is difficult to distinguish between the Ag₃PO₄ and TiO₂-rutile. At a relatively high rutile content, some rutile NPs formed aggregates, as can be seen from the SEM images.

3.3.4 XRD Study of The Ag₃PO₄/TiO₂ Nanocomposite

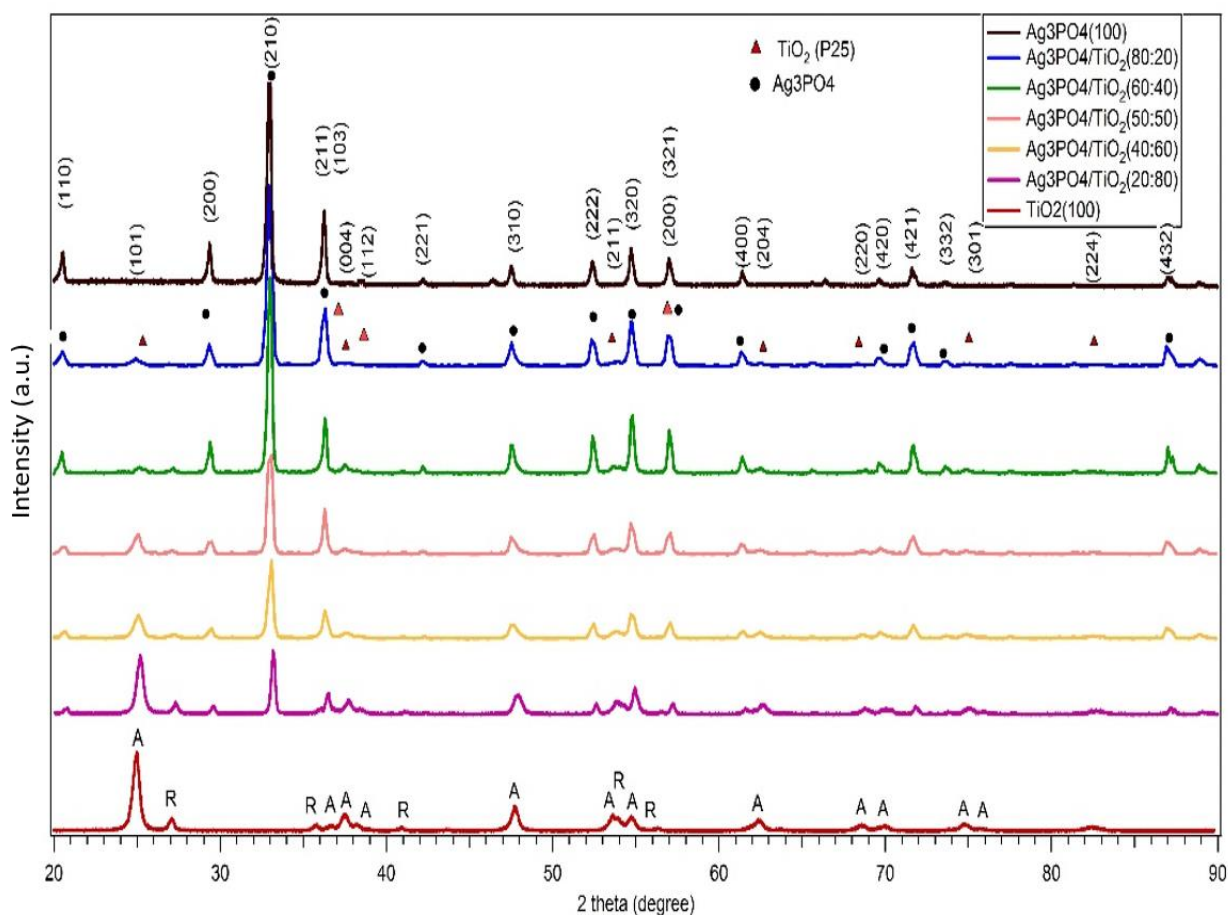


Figure 3.11 XRD pattern of $\text{Ag}_3\text{PO}_4/\text{TiO}_2$ -P25 nanocomposites of different weight ratios. Triangle and dot denote TiO_2 -P25 and Ag_3PO_4 , respectively.

It can be observed that the TiO_2 -P25 diffraction pattern exhibits sharp peaks at 2θ of 25.24° , 37.75° , 48.12° , 53.75° , 55.02° , 62.51° , 68.80° , 70.51° , 75.00° and 83.12° indexed to (101), (004), (200), (105), (320), (204), (220), (420), (332) and (224) crystal planes of the anatase phase (JCPDS Card No.21-1272), respectively. These peaks are marked with letter “A”. There are additional small diffraction peaks at $2\theta = 27.56^\circ$, 41.36° , 54.37° and 56.69° corresponding to (110), (111), (211) and (220), which are assigned to the rutile phase of TiO_2 (JCPDS Card No.21-1276), labelled with letter “R”. This confirms that P25 is a mixture of rutile and anatase. The quantitative analysis reveals that the sample is dominated with 83% anatase.

Pure Ag_3PO_4 exhibited diffraction peaks at $2\theta = 20.5^\circ, 29.5^\circ, 33^\circ, 36.5^\circ, 38.50^\circ, 42.51^\circ, 48.02^\circ, 53.06^\circ, 55.33^\circ, 57.5^\circ, 62.12^\circ, 70.21^\circ, 72.00^\circ, 74.03^\circ$, and 87.51° , indexed to (110), (200), (210), (211), (220), (310), (222), (320), (321), (400), (420), (420), (421), (332), (520), respectively (JCPDS Card No. 06–0505). The peak from the (210) plane has the highest diffraction intensity.

Table 3.2 Component ratio of the $\text{Ag}_3\text{PO}_4/\text{P25}$ nanocomposites catalysts from XRD measurements

$\text{Ag}_3\text{PO}_4/\text{P25}$ wt%	$\text{Ag}_3\text{PO}_4(\%)$	Anatase (%)	Rutile (%)
0/100	0	83	17
20/80	19	67	14
40/60	39	51	11
50/50	49	42	9
60/40	61	32	7
80/20	80	16	4
100/0	100	0	0

By increasing the proportion of the Ag_3PO_4 , its diffraction peaks gradually intensified at the expense of the TiO_2 peaks, thus reflecting their proportions in the $\text{Ag}_3\text{PO}_4/\text{TiO}_2$ nanocomposites as shown in Table 3.2. The component compositions were measured using the manufacturer's software HighScore Plus 4.0 (Siemens). The XRD patterns show that the diffraction peak intensity of TiO_2 decreased with the decrease of TiO_2 concentration in the composites. The measured component concentrations were in good agreement with the preparation ratio, which suggests there was no significant loss of chemicals during the sample preparation.

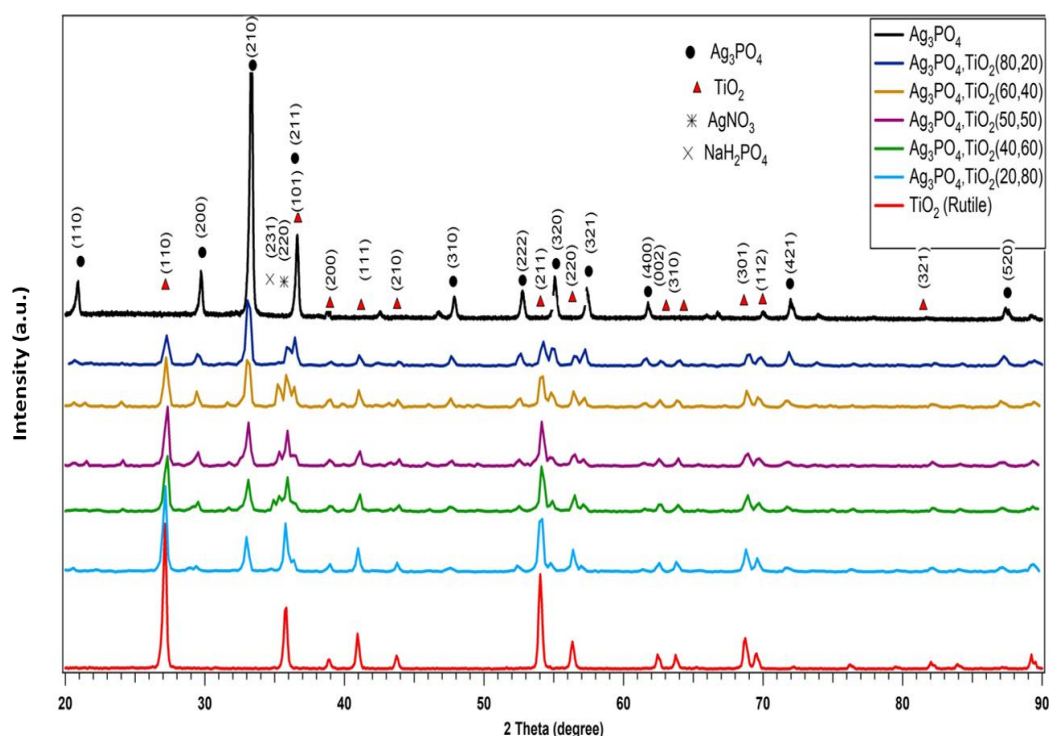


Figure 3.12 XRD pattern of $\text{Ag}_3\text{PO}_4/\text{TiO}_2$ -rutile nanocomposites of different weight ratios. Dot, triangle, asterisk, and cross denote Ag_3PO_4 , TiO_2 , AgNO_3 , and NaH_2PO_4 , respectively.

XRD patterns of pure TiO_2 -rutile and $\text{Ag}_3\text{PO}_4/\text{TiO}_2$ -rutile nanocomposites were shown in Figure 3.12 with strong diffraction peaks at 27.56° , 41.36° and 54.37° indicating TiO_2 in the rutile phase in the composites which clearly show that the Ag_3PO_4 nanoparticles have been successfully loaded onto the surface of TiO_2 support, as we observed in the SEM images in Figure 3.10. However, the diffraction peaks of TiO_2 become weak as the concentration of Ag_3PO_4 was increased.

3.3.5 UV-Vis Spectra of Ag_3PO_4 Microcrystalals (Particle and Cubic) and $\text{Ag}_3\text{PO}_4/\text{TiO}_2$

The band gaps of the photocatalysts were measured by UV-Vis absorption or UV-Vis diffuse reflection (DRS) for suspension solutions or the thin film sample. For liquid suspension samples, certain light can transmit through, which carries the absorption signal, assuming the scattering is wavelength independent. On the other hand, for the

solid samples, such as thin-film, very little light can transmit through, unless the film is ultra-thin. In such a case, the absorbance has to be measured through reflection mode with DRS. The former is used to characterise samples in thin-film form or in liquid form, where there is not much dispersion. And the latest, used for powders or thin films of high surface roughness. Also, I used both UV-vis and DRS spectroscopies for Ag_3PO_4 to ensure that both are constant, and the sample absorption wasn't intruded with the solvent.

The reflectance of $\text{Ag}_3\text{PO}_4/\text{TiO}_2$ as a function of the weight percentage was measured in a range of wavelengths from 200 to 900 nm. The results are shown in Figure 3.13. Pure Ag_3PO_4 particles exhibited the maximum reflectance value of about 6.6×10^3 (a.u) at the wavelength of 550 nm, which was generally higher than nanocomposite mixes, except for the $\text{Ag}_3\text{PO}_4/\text{P25 TiO}_2$ composites with 80:20 wt% and 20:80 wt%. The $\text{Ag}_3\text{PO}_4/\text{TiO}_2$ with 60:40 wt% and 50:50 wt% exhibited the lowest reflectance of 3.9×10^3 a.u. It can be expected that these two samples should have the highest light absorbance.

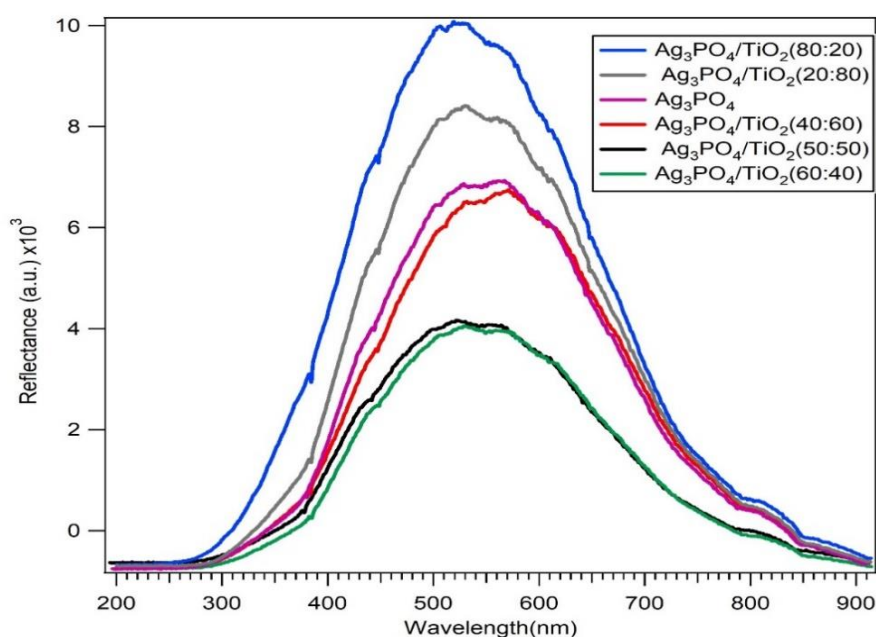


Figure 3.13 UV-Vis diffuse reflectance spectra of pure Ag_3PO_4 and $\text{Ag}_3\text{PO}_4/\text{TiO}_2$ nanocomposites.

The attenuation constant, α , can be calculated using the reflectance, R , as a function of wavelength, described in Equation 3.10.²¹⁹ Using the calculated attenuation constant, the bandgap energy of the material can be determined using the Tauc plot, described in Equation 3.11.

$$\alpha = \frac{\ln\left[\left(\frac{R_{\max}-R_{\min}}{R-R_{\min}}\right)\right]}{2} \quad (\text{Eqn 3.10})$$

$$\alpha h\nu = A(h\nu - E_g)^n \quad (\text{Eqn 3.11})$$

Where R is the reflectance of the samples at a specific wavelength. R_{\max} and R_{\min} are the highest and the lowest reflectance. R_{\min} is also used as the baseline reflectance. E_g is the bandgap energy, ν is the frequency of the light and h is the Planck constant. A is a constant and n is $\frac{1}{2}$ for a direct bandgap material. To get the band gap value, E_g , for a direct bandgap material, Equation will be changed to:

$$(\alpha h\nu)^2 = A(h\nu - E_g) \quad (\text{Eqn 3.12})$$

The value of the bandgap is obtained by plotting $(\alpha h\nu)^2$ vs $h\nu$ and to extrapolate the straight-line part to the x-axis. The value represents the condition of $(\alpha h\nu)^2 = 0$, hence $E_g = h\nu$.

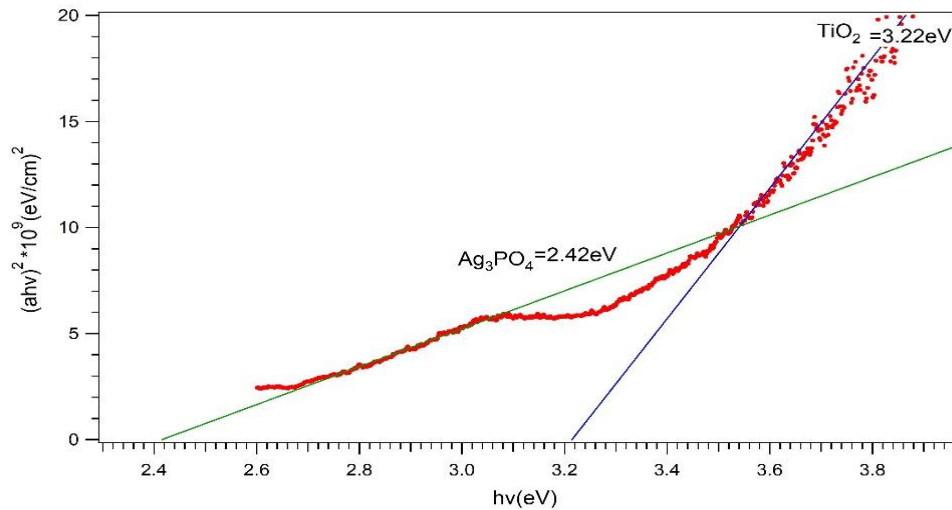


Figure 3.14 Tauc plot of $\text{Ag}_3\text{PO}_4/\text{TiO}_2\text{-P25}$ (60:40 wt%) nanocomposite.

The Tauc plot of $\text{Ag}_3\text{PO}_4/\text{TiO}_2$ nanocomposite (60:40) % is shown in Figure 3.14. The plot shows two parts of straight lines. One gives smaller bandgap energy of 2.42 eV while the other gives larger bandgap energy of 3.22 eV, which are assigned to the Ag_3PO_4 and the $\text{TiO}_2\text{-P25}$. These band gap values are in good agreement with the literature.²⁸⁷⁻²⁹¹

The UV-Vis absorption spectra of as-prepared cubic and particle Ag_3PO_4 microcrystal were presented in Figure 3.15A. The Ag_3PO_4 microcrystals were dispersed in distilled water for the measurement of UV-vis spectra. The UV-vis absorption spectra reveal that the absorption bands of Ag_3PO_4 cubic (synthesised with 0.15 M of $[\text{NH}_3]$) shift to the longer wavelength (maximum at 527nm) as compared to the particular Ag_3PO_4 (maximum at 516 nm). Hence, the combination of the cubic Ag_3PO_4 microcrystal with $\text{TiO}_2\text{-P25}$ can have a broader wavelength sensitivity allowing harvesting more visible light.

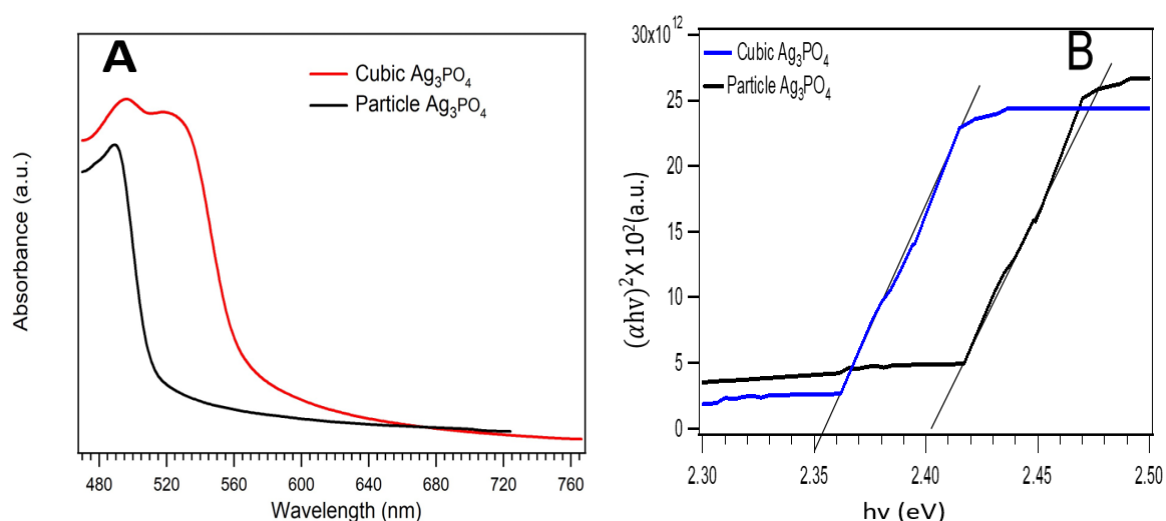


Figure 3.15 (A) UV-Vis absorption spectra of cubic Ag_3PO_4 of (0.15 M $[\text{NH}_3^+]$) microcrystals and particle Ag_3PO_4 and (B) corresponding Tauc plots of Ag_3PO_4 microcrystals.

Figure 3.15B shows the Tauc plots for the cubic and particular Ag_3PO_4 samples. The bandgap energy for the cubic Ag_3PO_4 crystal was found to be 2.353 eV, which was lower than that of the particular Ag_3PO_4 (2.401 eV).

Photoluminescent (PL) emission spectra were measured to probe any alterations in the electronic properties of the prepared photocatalysts: pure Ag_3PO_4 , $\text{Ag}_3\text{PO}_4/\text{TiO}_2$ -P25 (60:40) nanocomposites and $\text{Ag}_3\text{PO}_4/\text{TiO}_2$ -P25 (60:40) physical mixture. For the $\text{Ag}_3\text{PO}_4/\text{TiO}_2$ (60:40) nanocomposite, the PL spectrum in Figure 3.16A shows two distinct emission peaks at 388 nm and ~ 530 nm corresponding to the emission from the TiO_2 and the Ag_3PO_4 , respectively, which is consistent with the double bandgap energies observed from the UV-Vis measurement. The PL signal was measured with the excitation wavelength at 270 nm.

In addition to the emission spectrum, the excitation spectra of different samples were presented in Figure 3.16B. All samples showed an excitation peak at 540 nm, which is determined by the bandgap energy of Ag_3PO_4 . The intensity of the PL signal is associated with the charge recombination. Hence, the higher PL signal will normally give a lower photocatalytic performance.

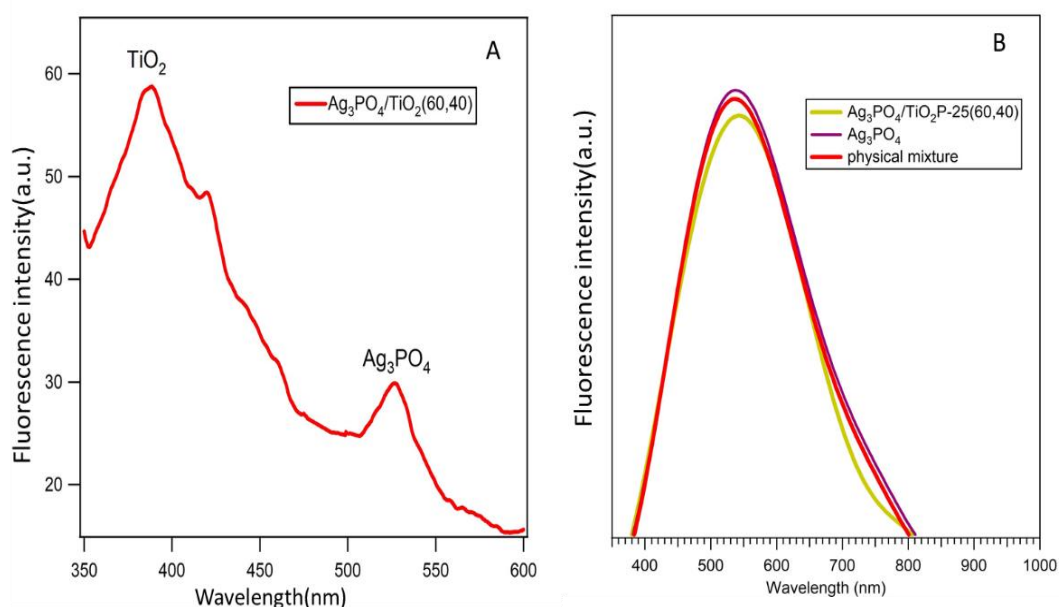


Figure 3.16 (A) PL emission spectrum of $\text{Ag}_3\text{PO}_4/\text{TiO}_2$ P25 (60:40 wt%) nanocomposite under UV-vis irradiation. (B) PL excitation spectra of pure Ag_3PO_4 , $\text{Ag}_3\text{PO}_4/\text{TiO}_2$ P25(60:40 wt%) physical mixture and $\text{Ag}_3\text{PO}_4/\text{TiO}_2$ P25 (60:40 wt%) nanocomposite.

From Figure 3.16B, it can be seen that the PL emission intensity of pure Ag_3PO_4 is higher than that of $\text{Ag}_3\text{PO}_4/\text{TiO}_2$ P25(60:40) physical mixture followed by $\text{Ag}_3\text{PO}_4/\text{TiO}_2$ P25(60:40) nanocomposite. This suggests that pure Ag_3PO_4 exhibits a higher electron-hole recombination rate. This can be explained that for the pure Ag_3PO_4 , there is no built-in electrical field to assist the charge separation. Meanwhile, for the physical mixed $\text{Ag}_3\text{PO}_4/\text{TiO}_2$, the interface between Ag_3PO_4 and TiO_2 is not well defined as the $\text{Ag}_3\text{PO}_4/\text{TiO}_2$ -P25 (60:40 wt%) nanocomposite, due to the weak interactions between the TiO_2 particles and Ag_3PO_4 crystals. In addition, Ag_3PO_4 is easier to be reduced to metallic Ag without the doping of TiO_2 . The high conductivity of the metallic Ag will promote the charge recombination since electrons will be free to move. Therefore, it is understandable that without a good interface between Ag_3PO_4 and TiO_2 , the higher charge recombination rate will result in higher PL intensity. The lower PL emission intensities observed for the $\text{Ag}_3\text{PO}_4/\text{TiO}_2$ -P25 (60:40 wt%) nanocomposite is due to the lower rate of electron-hole recombination, which offers the highest photocatalytic performance, demonstrated later in Figure 3.18.

3.3.6 Effect of $\text{Ag}_3\text{PO}_4/\text{TiO}_2$ Nanocomposite Mix Proportions on Photocatalytic Activity

The effect of relative proportions of Ag_3PO_4 and TiO_2 (both P25 and rutile) on the photocatalytic activity of $\text{Ag}_3\text{PO}_4/\text{TiO}_2$ nanocomposite was investigated by evaluating MB concentrations against irradiation time to calculate the rate of MB photodecomposition under sunlight. MB concentration generally decreased with the increase of irradiation time (Figure 3.17). It was confirmed that in the absence of light, the absorbance remained constant indicating that MB did not undergo decomposition in darkness. Similar observations have been found in the literature also.²⁹² On the other hand, in the absence of a photocatalyst, MB photodegradation was very slow.

This demonstrated UV-light effectively enhanced the photocatalysis of the semiconductor.²⁹²

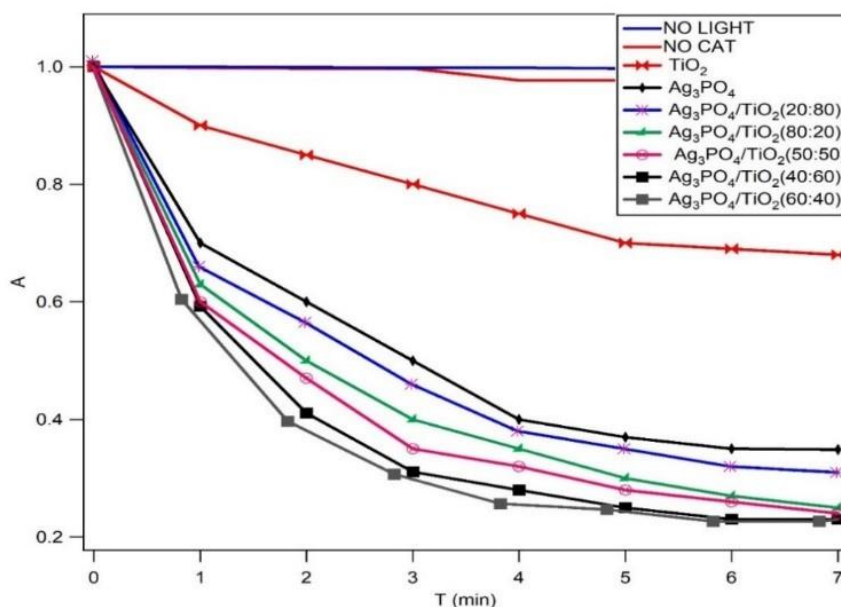


Figure 3.17 Variation of MB absorption against irradiation time using Ag₃PO₄, P25, Ag₃PO₄/P25 nanocomposites, in darkness and without catalyst, under visible light.

When individual catalysts were used, pure Ag₃PO₄ exhibited a greater MB degradation rate than TiO₂. However, by adding TiO₂-P25 in Ag₃PO₄, the MB degradation rate was gradually increased until reach the best performance with the composite contains 60% of Ag₃PO₄ and 40% of P25 (Figure 3.17). Further, increase the content of the TiO₂-P25 causes a decrease in the MB degradation rate.

Figure 3.18 shows the rate constants of the individual pure photocatalysts (Ag₃PO₄ and TiO₂-P25), the Physical mixture of Ag₃PO₄ and TiO₂ -P25 (60:40 weight ratio), and Ag₃PO₄/P25 nanocomposite (60:40 weight ratio). The rate constant of MB photodegradation using pure TiO₂ -P25 was lower ($k = 0.014 \text{ min}^{-1}$) than that of pure Ag₃PO₄ ($k = 0.127 \text{ min}^{-1}$). The rate constant was enhanced to 0.215 min^{-1} using physically mixing Ag₃PO₄ and P25. For the physical mixed sample, Ag₃PO₄ crystal sample was synthesised without the presence P25. It was then mixed with a certain amount of P25 to form the physically mixed catalyst. Hence, we don't expect any

chemical interactions between the Ag_3PO_4 crystals and TiO_2 -P25 powder. Each catalyst will maintain its electronic structure and catalytic performance. Therefore, the enhanced photocatalytic performance from the physically mixed catalyst is likely due to the broadening of the wavelength of the light absorbed. TiO_2 will be responsible for the UV excitation while Ag_3PO_4 is responsible for the visible light absorption. Thus, the overall light absorption became enhanced which resulted in the enhancement of the catalytic activity.

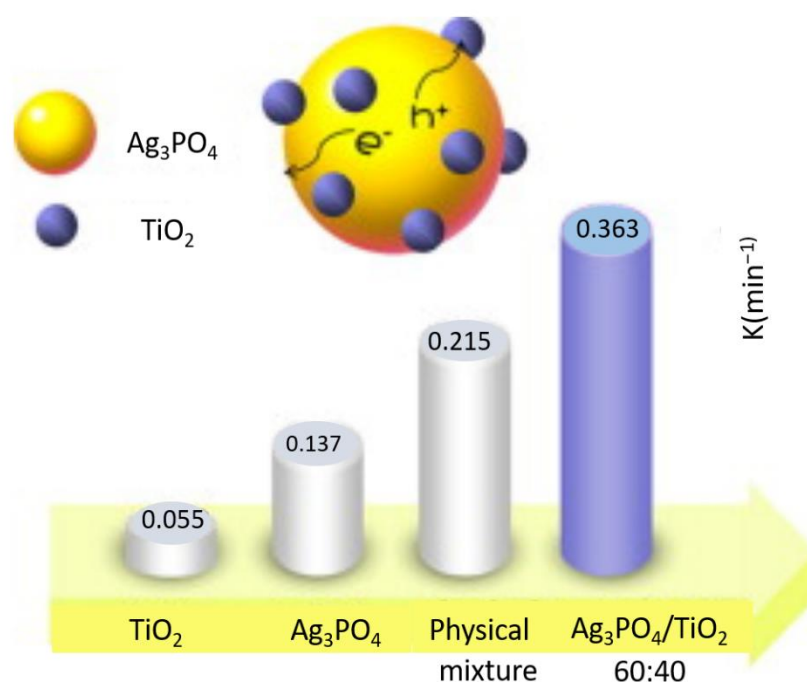


Figure 3.18 The optimised reaction rate constants (k) from different catalysts.

For the $\text{Ag}_3\text{PO}_4/\text{TiO}_2$ -P25 nanocomposites, the photocatalytic performance was further enhanced to a rate constant of 0.363 min^{-1} with the same weight ratio of (60:40). In the comparison with the physically mixed catalyst, the photocatalytic performance was enhanced by 0.148 min^{-1} . This enhanced photocatalytic activity of $\text{Ag}_3\text{PO}_4/\text{TiO}_2$ -P25 nanocomposites can be attributed to two synergetic effects. First, similar to the physically mixed catalyst, the wavelength of the excitation light is greatly broadened. Since the catalyst had the same weight ratio between the Ag_3PO_4 and

TiO₂-P25, the associated catalytic performance enhancement could be similar. Second, the TiO₂ nanoparticles were tightly bonded onto the Ag₃PO₄ microcrystals, which forms interfaces between the two materials. This will create an internal electric field due to the Fermi level alignment and band bending, shown in Figure 3.4. Such internal field will transfer the photoexcited electrons between the conduction bands from the TiO₂ to the Ag₃PO₄ while transferring the holes between the valence bands from the Ag₃PO₄ to the TiO₂. Such processes are important for charge separation and charge usage, and so is the photocatalytic performance.

For further comparison, the effect of TiO₂ crystal structures on the rate of MB photodegradation was investigated using Ag₃PO₄/ TiO₂-rutile nanocomposites. Figure 3.19 shows the photodecomposition of MB by the Ag₃PO₄ / rutile composites containing different proportions of TiO₂-rutile. As the components of TiO₂-rutile decreased gradually, the MB degradation performance was increased monotonically. The best performance was achieved with the lowest TiO₂-rutile concentration of 20 wt% under the experimental conditions. After 1 min of reaction, there were 22% of MB was degraded.

However, for P25, pure Ag₃PO₄, and Ag₃PO₄/P25 (60:40), 10%, 30%, 40% and of MB were degraded, respectively. Hence, the addition of rutile in Ag₃PO₄ has a negative impact to the photocatalytic performance of Ag₃PO₄, while the addition of P25 (~75% anatase) has the positive effects with the optimum contents weight ratio of 60:40.

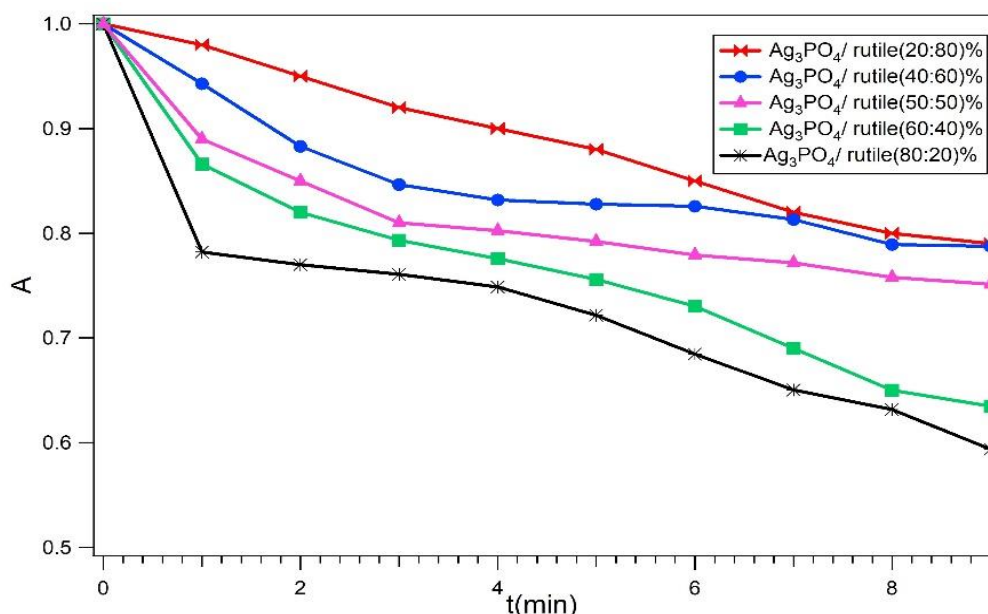


Figure 3.19 Variation of MB absorption against irradiation time using Ag₃PO₄/ rutile composites.

The reason for the negative effects of rutile might be related to the lifetime of the photoexcited electrons in rutile. Since the depth of the electron traps at crystal defects for rutile is much shallower than for anatase, photoexcited electrons have much short lifetime in rutile (~ 1 ps) than in anatase (>1 ms).²⁹³ This suggests that the electron-hole pair in rutile can effectively recombine, resulting in poor photocatalytic performance, even with the presence of Ag₃PO₄. Zhang and his group also revealed that the MB molecules can effectively adsorb on the surface of TiO₂ anatase, which lead to the distortion of surface lattice because of the lattice matching.²⁹⁴ This will increase the depth of the electron trap with improved charge separation. Bojinova and co-workers reported that the k rate increased with the anatase portion increase in a mixture of anatase and rutile catalysts. They found TiO₂-P25 had the higher ability of photodegradation of organic pollutants than both anatase and rutile due to the existence of the interface between anatase and rutile.²⁹⁵

3.3.7 Photocatalytic Activity of Cubic Ag_3PO_4 on MB Degradation

In order to further investigate the effects of the Ag_3PO_4 crystal structures on the rate of MB photodegradation, and the effect of the complex concentration on the cubic Ag_3PO_4 photocatalytic activity was investigated. As shown in Figure 3.20, it can be seen that, except for the Ag_3PO_4 particles (IP), all the cubic Ag_3PO_4 (C1, C2, C3 and C4) photocatalysts exhibited excellent photocatalytic activities for MB degradation.

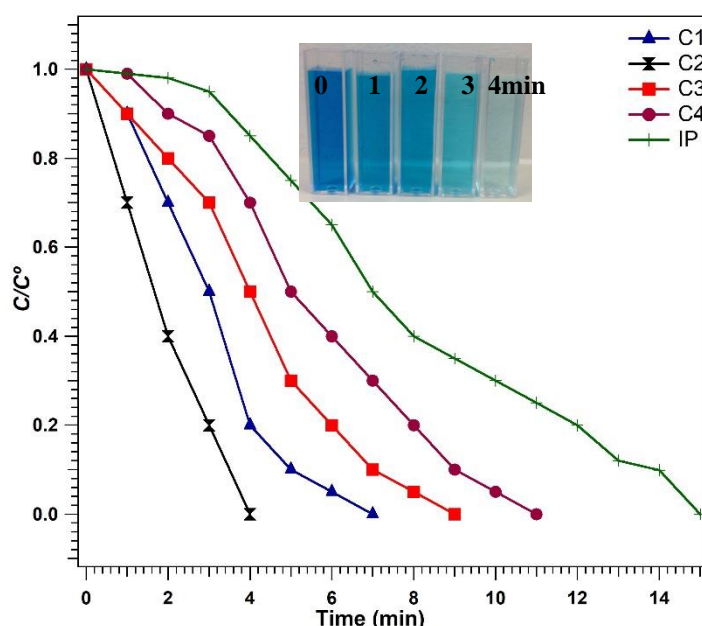


Figure 3.20 Photocatalytic activity of Ag_3PO_4 microcrystals formed at different concentrations of NH_3 , C1 (0.10 M), C2 (0.15 M), C3 (0.20 M), C4 (0.30 M) and IP are the irregular Ag_3PO_4 particles without addition of NH_3 . Inset: photos of MB decomposed by Ag_3PO_4 microcrystals of C2.

The Ag_3PO_4 particles were synthesised without using NH_3 solutions, while C1, C2, C3 and C4 were synthesised with the concentrations of $[\text{NH}_3]$ to be 0.10, 0.15, 0.20, and 0.30 M, respectively. The particle morphologies and size distributions were presented in Figure 3.7 and Table 3.1.

Among them, the C2 catalyst exhibited the highest photocatalytic activity, and can completely degrade MB dye in only 4 min (with a photo of the change of MB colour) followed by the sample C1, C3, and C4. However, the IP catalyst had the lowest photocatalytic activity, which took 15 min to decompose the MB completely. These

results indicate that the photocatalytic properties of cubic Ag_3PO_4 microcrystals can be significantly improved by tailoring their shape and the surface structure, and also the results confirmed that uniform morphologies Ag_3PO_4 microcrystal with a smooth surface, sharp corners and edges had superior photocatalytic activities, which might be due to the exposure of the high energy [100] planes, with respect to the [111] planes.

Table 3.3 The rate constant and half time of cubic Ag_3PO_4 at different concentration of NH_3 and irregular Ag_3PO_4 particles.

No.	Catalyst	k (min^{-1})	$t_{1/2}$ (min)
1	C ₁	0.52	1.3
2	C ₂	0.54	1.2
3	C ₃	0.37	1.9
4	C ₄	0.28	2.4
5	IP	0.17	4.1

The reaction rate constants and the calculated half-lives were summarised in Table 3.3. The highest rate constant and shortest half-life for was achieved from catalyst C₂, while the particular sample had the lowest rate constant and longest half-life. It is expected that the catalyst IP had the highest surface density of defects since Ag^+ and PO_4^{3-} reacted immediately without any time to remove surface defects. Such defects might cause high probably of charge recombination or the reduction of Ag^+ . Hence, either the photoexcited charges cannot be effectively used for the degradation of MB or the photocatalytic performance of the Ag_3PO_4 was rapidly decreased due to the formation of metallic Ag. The cubic crystal morphologies and size distributions were very similar, so were their photocatalytic performances. However, the average size and the size FWHM of the C₄ catalyst were significantly larger than those of C₁ and C₂, caused by the aggregation of the Ag_3PO_4 crystals. Such aggregation will result

in the loss of effective surface area or the density of the [100] facets, which will result in the reduction of the photocatalytic performance.

3.4 Conclusions

By using a simple preparation method, cubic Ag_3PO_4 nanocrystals and Ag_3PO_4 particles were successfully fabricated. Regular cubic Ag_3PO_4 microcrystal was obtained by changing the concentration of ammonia solution. $\text{Ag}_3\text{PO}_4/\text{TiO}_2$ composites were also successfully synthesized by in-situ precipitation techniques using both TiO_2 -P25 and TiO_2 -rutile. The photocatalytic MB decomposition kinetics using the catalysts synthesized with different semiconductor ratios and with different synthesis techniques has been studied. The enhanced decomposition performance from the $\text{Ag}_3\text{PO}_4/\text{TiO}_2$ composites can be attributed to the formation of heterojunctions between the TiO_2 and the Ag_3PO_4 as the result of the attachment of TiO_2 particles across the surface of Ag_3PO_4 . In comparison to the cubic Ag_3PO_4 nanocrystals, the $\text{Ag}_3\text{PO}_4/\text{TiO}_2$ composite samples exhibited higher photocatalytic behaviour for the decomposition of methylene blue (MB) organic dye. The highest photocatalytic activity was achieved from the $\text{Ag}_3\text{PO}_4/\text{TiO}_2$ -P25 (60:40 wt%) nanocomposite. This excellent photoactivity was attributed to the broadening of the wavelength of light absorption and the improved charge separation. The modification with anatase TiO_2 could also help to mitigate the photo-corrosion of Ag_3PO_4 . Perhaps, the unique cubic morphology of Ag_3PO_4 with exposed [100] plane has also contributed to the superior photocatalytic activities, since the random shaped Ag_3PO_4 particles showed much lower photoactivity.

CHAPTER 4 Electrochemical and Photo-Electrochemical Oxidation of Alcohols to Aldehydes

This report demonstrates two-phases electrochemical methods for the oxidative conversion of benzyl alcohol (BA) to benzaldehyde (BAD). The process is selective as it maximizes the yield of BAD. It is also inexpensive and convenient as it can be performed under mild conditions. The electrochemical oxidation (ECO) reaction was further enhanced by photoactivation with a UV light source and photocatalysts, a strategy called photocatalytic electrochemical oxidation (PECO).

4.1 Introduction

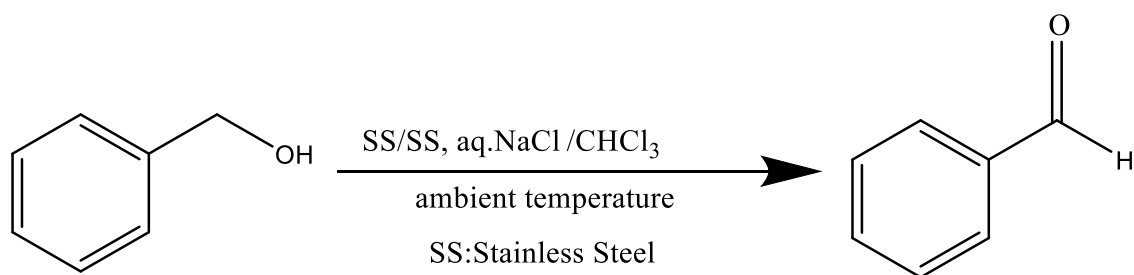
Aldehydes and ketones are essential reagents used in the synthesis of organic compounds for pharmaceutical, synthetic polymers and synthetic dye industries.²⁹⁶ Oxidation of alcohols is a widely used process for the synthesis of aldehydes and ketones.²⁹⁷ The common oxidation method uses stoichiometric oxidants like salts of chromium, manganese, and ruthenium. These chemicals are not environmentally friendly. A relatively greener method is the dehydrogenation of alcohols using molecular oxygen, air, or hydrogen peroxide in the presence of transition metal catalysts (Cu, Ru, Pd, Au, Fe, V, or Ir).²⁹⁸ However, these metals are expensive, and the process usually requires high temperatures.²⁹⁹ Electrochemical oxidation of alcohols with hydrogen release can be run under mild conditions; however, its use has not been utilised so far. Single-phase electrolysis is not efficient due to the formation of chemical waste produced in the reaction.³⁰⁰ However, modifying the electrochemical oxidation with techniques like the use of biphasic electrolyte and photocatalysts can improve the yield of the product.

The selective oxidation of alcohols to their aldehydes or carboxylic acids is critical in organic synthesis for industrial or pharmaceutical production.³⁰¹ Photocatalytic oxidation of alcohols to aldehydes has been reported with high yields in water³⁰² and organic solvent.³⁰³ Photocatalysis is based on the efficiency of the electron-hole pairs ($e^- + h^+$) to generate the highly oxidative hydroxyl radicals (OH^\bullet), which oxidize BA to BAD. However, the photocatalysis must be optimized for improved production of aromatic aldehydes from aromatic alcohols. A few studies have proposed some oxidation strategies to oxidize benzyl alcohol (BA) to benzaldehyde (BAD).^{210,304,305}

Electrochemical strategies have drawn much attention in the literature, on their role in oxidizing primary alcohols to aldehydes, and further to their corresponding carboxylic acids.^{306,307} This strategy converts aliphatic, aromatic, heterocyclic, and other heteroatom-containing alcohols to their respective oxidised products in aqueous solutions at room temperature. The advantage of electrochemical oxidation lies in the possibility of retaining stereochemistry of the substituents that are adjacent to the site of oxidation.³⁰⁶ This requires mild reactor conditions, which can be achieved using a chemical mediator. For instance, 4-acetamido-2,2,6,6-tetramethylpiperidin-1-oxyl (ACT), has been used as an organo-catalyst mediator within the electrochemical oxidation (ECO) of primary alcohols.^{306,307} When performed in a simple electrochemical cell, the electric current passed oxidises the desired species, replacing the chemical oxidant and thereby preventing the formation of undesired chemical waste.³⁰⁷ For instance, Stahl and Badalyan outlined that the electrochemical oxidation of alcohol by using equal mole amounts of catalysts, (2,2'-bipyridine)Cu and TEMPO(2,2,6,6-tetramethyl-1-piperidinyloxy or 2,2,6,6-tetramethylpiperidine-1oxyl) gained half of the electrode potential compared to that used with TEMPO only.³⁰⁸ The

role of an organo-catalyst mediator in ECO is to generate cyclic oxoammonium or nitrosonium ions in situ, by an auxiliary oxidant, upon the application of a small electric potential. For example, cyclic oxoammonium ions are the oxidant species that oxidize the alcohol group to aldehyde, and further to carboxylic acid, upon which it is regenerated electrochemically from the hydroxylamine.³⁰⁷

Electro-organic synthesis allows the sustainable and green production of fine organic chemicals. This technology has the advantage of high product selectivity and mild reaction conditions. The biphasic chloride-mediated ECO of alcohol (Scheme 4.1) performed in this study demonstrates its advantage over the conventional homogeneous and emulsion electrolysis methods of electro-organic synthesis.^{11,309} Homogeneous systems are characterized by lower product (aldehyde) selectivity, due to excessive alcohol oxidation on the surface of the electrodes, producing a mixture of organic products.³¹⁰ On the other hand, the emulsion electrolysis system is disadvantaged by a higher energy consumption due to the passivation of electrodes, which induces high current densities.³¹¹ Moreover, eliminating the spent mediators from these conventional electrolysis systems is problematic. These challenges are addressed in the biphasic chloride-mediated ECO evaluated in the present study.



Scheme 4.1 Selective oxidation of benzyl alcohol to benzaldehyde by two-phase electrolysis.

Using an ECO strategy, Raju *et al.*²¹⁰ oxidized benzylic and substituted benzylic alcohols with two-phase electrolysis resulting in high yields of benzaldehyde (74–96 %). This reaction was carried out in a single compartment cell, with two platinum

electrodes at room temperature, the two phases being organic and aqueous. Chloroform containing alcohol formed the organic phase, and a solution containing 25 wt% sodium bromide and 5% catalytic HBr formed the aqueous phase. This biphasic system was shown to achieve up to four times to higher catalytic efficiency than the conventional single-phase system, in the oxidative conversion of BA. Furthermore, when graphite was used as both electrodes, the high yield of BAD as the product (89%) was observed at 8% of recovered BA. While when a graphite anode and a stainless-steel cathode were used, 85% BAD yield was achieved, confirming the potential of a biphasic photooxidation system.²¹⁰ It is also possible to enhance ECO by combining it with photocatalysis, a strategy called photoelectrochemical oxidation (PECO) using titanium dioxide (TiO_2) as a photocatalyst. Moreover, modifying the microstructures and controlling the electronic structure of TiO_2 can potentially improve the efficiency of photocatalysts.^{312,313} There is an increasing interest in using TiO_2 nanotubes (NTs) for the photocatalytic degradation of organic compounds and the oxidation of alcohols to aldehydes.³¹⁴⁻³¹⁶ Their large specific surface area and highly ordered nanostructures have opened up promising potential applications.³¹⁷ Anodizing a Ti plate is an effective way of creating vertically aligned TiO_2 nanotubular arrays³¹⁸ in a manner similar to the process for fabricating anodic aluminium oxide (AAO),³⁰⁵ however with key differences such as the electrolyte used.³¹³

The biphasic electrolysis system involves the formation of reactive species because of electrolytic oxidation of a mediator (such as NaCl) in the aqueous phase. The mediator selectively reacts with the alcohol to give the products at the interface of the organic and aqueous phases.³¹⁹ Upon completion of electrolysis, the products are afforded by the usual workup of the organic layer.³¹¹ Therefore, it is important to assess the effect of voltage used, redox mediators, type, agitation, and then study the

effect of annealing of TiO₂ NT films on the selective oxidation of BA to BAD using two-phase electrolysis. Selectivity is a crucial issue in photocatalytic processes aimed at the production of functionalized intermediates of interest in fine chemistry. Towards this objective, all steps of the catalytic process must be optimized. The high selectivity of mild photoelectrochemical routes is especially attractive for the manufacture of fine chemicals. The specific objectives were to oxidize BA to BAD using two phases and a mediator and then to optimize TiO₂ photocatalysis by synthesising TiO₂ nanotube, and finally, to compare the efficiency of chloride-mediated ECO to that of PECO (using a TiO₂ nanotube film as a photocatalyst) in the oxidation of BA to BAD.

4.2 Experimental

4.2.1 Chemical Reagents

TiO₂ (Aeroxide[®] P25; formerly Degussa P25), that consists of a mixture of two phases (~75% anatase and ~25% rutile) was commercially obtained from Evonik Industries (Goldschmidtstr, Germany). Sodium chloride (NaCl) (of ≥ 99.5% purity), sodium sulphate (Na₂SO₄) (99+%) and magnesium sulphate (MgSO₄) (62-70%, dried) were purchased from Fisher Scientific (Loughborough, UK). Chloroform (CHCl₃) (≥ 99.8%), was purchased from VWR International (Quebec, Canada). Benzyl alcohol (of 99% purity) was commercially obtained from Acros Organics or fisher Scientific Bvba (Geel, Belgium). Benzaldehyde (of > 99% purity) and 32% aqueous hydrochloric acid were commercially obtained from Sigma-Aldrich (Dorset UK). N-Octadecane (99%) was purchased from BDH (British Drug Houses) chemicals Ltd. Deionized water was prepared in the laboratory using the Suez/Purite Select deionization unit, (Poole Dorset, UK) whereas high purity oxygen gas was purchased from BOC gases (UK). All the chemicals and solvents were of analytical grade, whereas oxygen gas was of

high purity grade. A Philips CDM-T Halogen 150W Metal Halide Lamp was commercially obtained.

4.2.2 Chloride-Mediated ECO of BA to BAD

The batch reactor setup for the chloride-mediated ECO of BA included a pyrex® three-necked round-bottom flask (capacity 120 mL) magnetically stirred and fitted with Liebig condenser on the central open neck. The organic phase was prepared by dissolving 0.2 g octadecane (as an internal standard) in a solution mixture containing 1 mL portion of BA and 20 mL of CHCl_3 . The aqueous phase (0.83 wt% NaCl solution) was prepared by dissolving 0.5 g of NaCl in 60 mL deionized water, followed by the addition of 2 mL of 32 wt% HCl to maintain the medium as acidic. The 60 mL aqueous phase was transferred into the reactor to form the biphasic system with the organic phase. The aqueous phase acted both as an electrolyte and as a source of chlorine radicals.

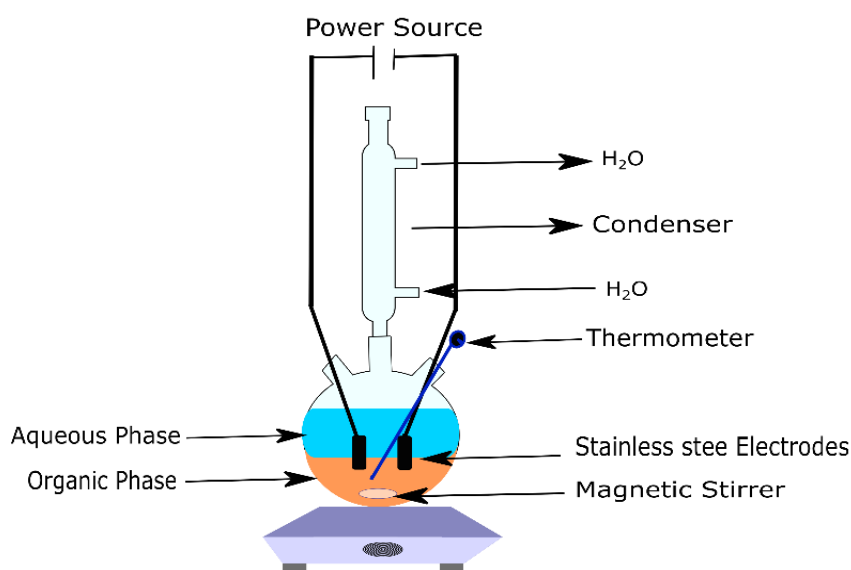


Figure 4.1 The batch reactor assembly for the radical-mediated electrochemical oxidation of BA.

Two stainless-steel electrodes (with equal surface areas of 15 cm²) were used as anode and cathode. The electrodes were placed slanted into the reactor through the two angled side-necks, ensuring they had good contact with the organic phase, close to the inter-phase region. The reactor mixture was stirred with a magnetic stirrer

at a rate of 80 rpm to ensure good mixing of both layers of organic and aqueous phases. The water-cooled condenser fitted at the top was used to prevent the evaporation of chloroform, maintaining the organic phase volume. The electrodes were connected to a DC power supply as shown in Figure 4.1. Ambient temperature was maintained throughout the electrochemical process. Electrolysis was conducted at different values of current densities, ranging from 15 to 230 mA/cm², and voltage ranging from 2.0 to 5.0 V. Samples were drawn periodically from the organic phase and treated with anhydrous MgSO₄ before analysing them using a Hewlett-Packard - HP 6890 Gas Chromatography (HP GC) system equipped with a Flame Ionization Detector (FID) (from Agilent Technologies Inc.). A polar column (Stabilwax 30m x 0.53mmID x 1µm df) was used to separate the reaction products. The organic phase mixtures were analyzed via a manual injection method with an injection volume of 0.06µL. The injector temperature was set and maintained at 250 °C and the oven was kept at a temperature of 180 °C. Calibration curves of the standard BA, BAD and benzoic acid were used to determine the concentration of the reaction products, hence the yield. The procedure was also performed using Na₂SO₄ as the mediator, in the place of NaCl to investigate the effect of mediator type on the reaction.

4.2.3 TiO₂ Nanotube Preparation for PECO of BA to BAD

TiO₂ NT plates were prepared by the anodization of a polished Ti plate (10 mm x 50 mm and 0.25 mm thickness) as described previously by Al-Abdullah *et al.*³²⁰ and Faraji *et al.*³²¹ with a few adjustments. Prior to anodization, the Ti plate was cleaned by ultrasonication in acetone, ethanol, and finally deionized water for 30 min and dried in air at 70 °C. Anodization of the Ti plate was performed by a home-made electrochemical cell using another Ti plate as the cathode. To record the transient

current, a labjack was used, and all the processes were performed at room temperature (Figure 4.2).

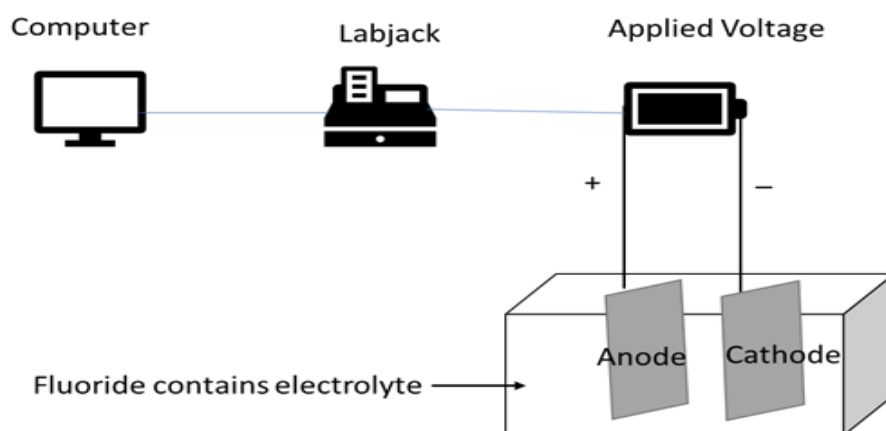


Figure 4.2 The anodization set with two-electrode and applied voltage remotely controlled by a computer.

The voltage and the electrode separation were constant during the anodization. Hydroxide islands were formed (Figure 4.3) when a polished Ti plate was placed in an acidic solution (containing 1 wt% H_3PO_4 and 0.1% HF) for 5 min, and then sonicated in deionized water for 4 min. The H_3PO_4 was used to adjust the pH and F^- to initialize the formation of hydroxide layer. Titanium surface is changed from hydrophobic to hydrophilic due to hydroxide layer.

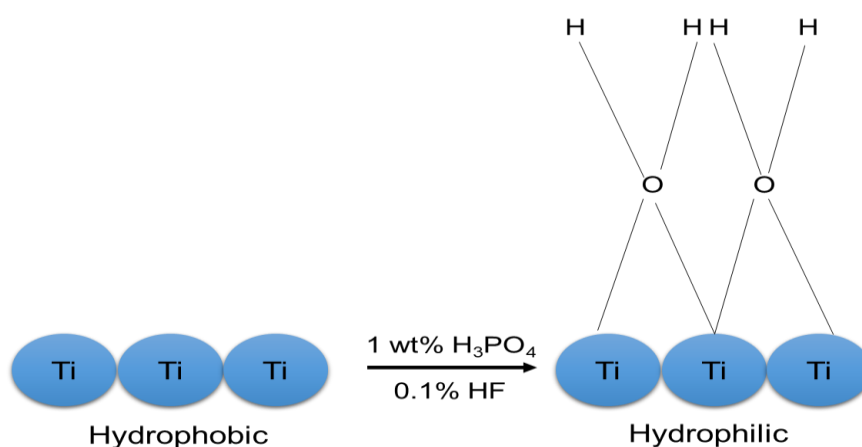


Figure 4.3 The suggested mechanism of the hydroxide islands formation.

The electrolyte contains a solution of 0.6 wt% NH_4F and 2 wt% water in ethylene glycol. Anodization of the Ti plate was constantly performed at 40kV producing a direct current for 45 mins.

The applied DC voltage was monitored and controlled remotely using a computer program (Figure 4.2). This process initially formed Titanium (II) oxide (TiO_2) nanotubes, that were washed using deionized water, dried and further oxidized by calcination at 450°C for 120 mins to form TiO_2 NT plates.

Images of TiO_2 nanotubes were taken by an SEM (JSM 820M, Joel) operating at 30 kV and powder x-ray diffraction (XRD, Siemens D500).

4.2.4 Photoelectrochemical Oxidation Using TiO_2 NT Films

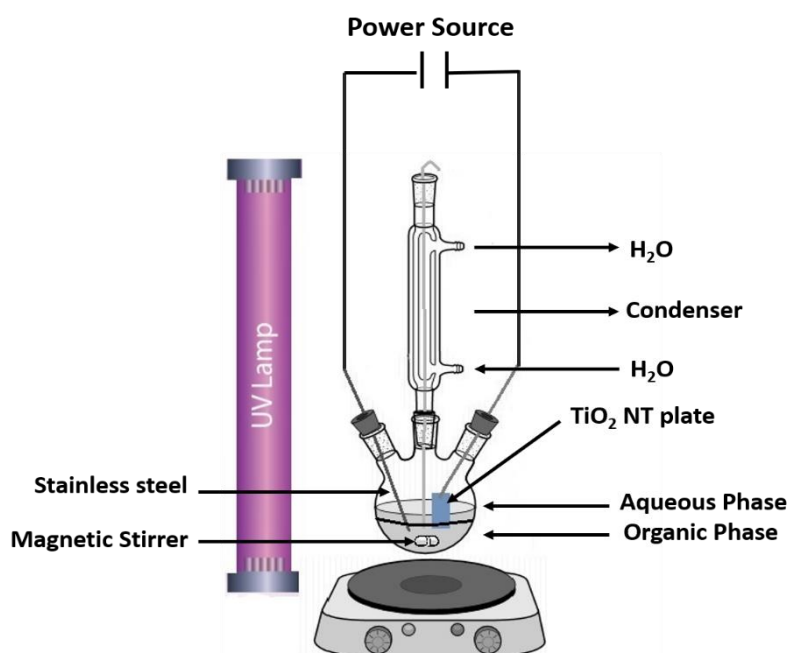


Figure 4.4 The batch reactor assembly for the radical-mediated photocatalytic electrochemical oxidation (PECO) of BA.

The TiO_2 NT was used anode to oxidize BA to BAD using a setup similar to the chloride-mediated ECO of BA, with some modifications. To test the performance of

the TiO₂ NT in photoelectrochemical oxidation (PECO), a UV-lamp was added to the setup, as shown in Figure 4.4. The oxidation was performed using TiO₂ NT film annealed at different temperatures. To test the effectiveness of the photocatalyst, the TiO₂ NT film was excluded from the PECO reactor setup, where only the electrochemical process and UV-irradiation were applied.

The following Equations (4.1)-(4.3) were used to define BA conversion, BAD selectivity and yield respectively for the reaction.³²²

$$\text{BA conversion} = \frac{\text{mole of inlet BA} - \text{mole of outlet BA}}{\text{mole of inlet BA}} \times 100 \% \quad (\text{Eqn 4.1})$$

$$\text{BAD selectivity} = \frac{\text{mole of outlet BAD}}{\text{mole of inlet BA} - \text{mole of outlet BA}} \times 100 \% \quad (\text{Eqn 4.2})$$

$$\text{BAD yield} = \frac{\text{mole of outlet BAD}}{\text{mole inlet of BA}} \times 100 \% \quad (\text{Eqn 4.3})$$

All samples were analysed through manual injection in GC. The compounds were separated using a polar column (Stabilwax 30m x 0.53mmID x 1µm df). The details of the GC-FID setup are described in section 4.2.2. Varian CP- 3800 GC-MS and NMR techniques were also adopted for chemical identification purposes.

4.3 Results and Discussion

4.3.1 Effect of ECO Voltage on Conversion and Selectivity

In order to study the effect of electrical oxidation power in this work, ECO of BA to BAD was performed under different voltages ranging from 2.0 to 5.0 V, yielding current densities from 15 to 230 mA/cm² (Figure 4.5). Clearly, with the rise in voltage and electrical resistance, the current increased almost linearly (straight slope).³²³ The effect of voltage (2.0 to 5.0 V) and indirectly, the quantity the current passed on the concentrations of BA and BAD was evaluated over time.

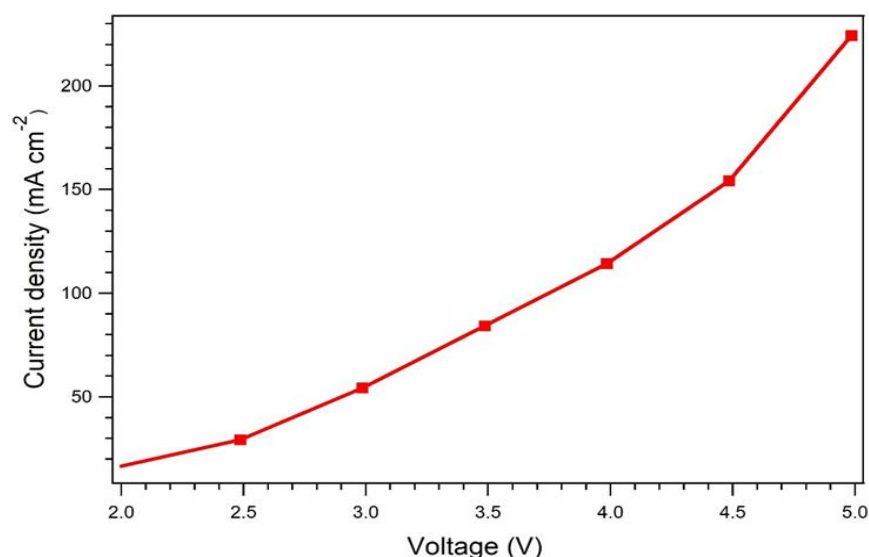


Figure 4.5 The effect of various voltage on the current densities.

At low voltages, it took a longer time (1h) to carry out the oxidation of BA. At higher voltages, however, cell voltage increased towards the end of the reaction above the initial stage values. This was performed to determine the effects on BAD formation and selectivity.

The BA conversion increased with increasing voltage, attaining an optimal conversion rate of 40% at a voltage of 5.0 V (Figure 4.6A). By contrast, the BAD selectivity generally decreased with increasing voltage, whereas its yield increased. Initially, the BAD selectivity increased with voltages from 2.0 to 3.0 V (63.0 - 70.0%) with a yield of up to 8.3%. Beyond 3.0 volts, the selectivity declined sharply to just under 40.0% of that at 5.0 V (Figure 4.6B), while the yield increased to 18.0%. This was contrary to the BA conversion rate, which showed 5.0 V as optimal (40.0%). Thus, the optimal production of BAD was best attained using a voltage of 3.0V, which is consistent with the observations in Figure 4.5, demonstrating 3.0 V (current density of 60 mA/cm²) as the optimal voltage for BA conversion and BAD selectivity. There seems to be a delicate balance between achieving optimal BA conversion and BAD selectivity using voltage.

From this result, it can be deduced that excessively high voltages in ECO generate excess oxidant species, increasing BA conversion whilst resulting in overoxidation of the alcohol group, to produce a mixture of BAD (an aldehyde) and benzoic acid (carboxylic acid). This is evidenced by a sharp drop in BAD selectivity.

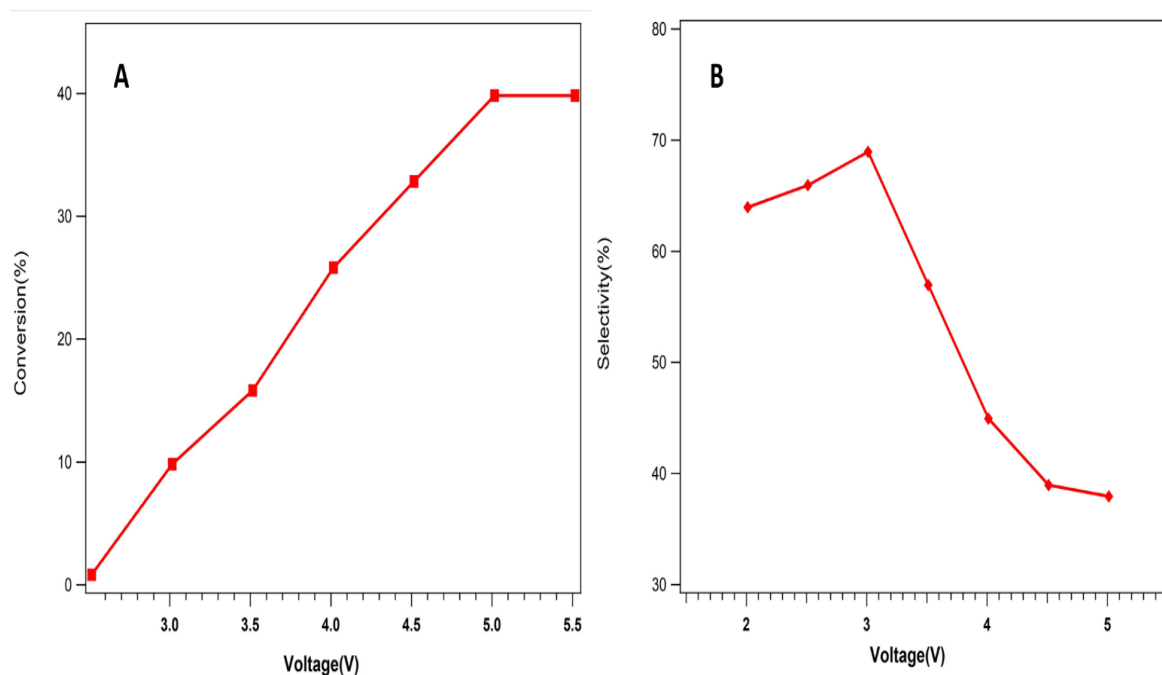


Figure 4.6 (A) The effect of voltage on BA conversion and (B) the effect of voltage on BAD selectivity (reaction time, 2h).

Alternatively, the rate of reduction in BA (BA concentration versus time) increased with a greater quantity of charge passed over a constant time (8 h). As shown in Figure 4.7, the effect of the reaction time was studied as well. The initial conversion of BA increased sharply with increasing the reaction time, while the BAD selectivity decreased over time. No significant change was observed on BA conversion after 8 hours of the reaction, whereas BAD selectivity decreased over time and benzoic acid increased due to the further oxidation of BAD to benzoic acid.

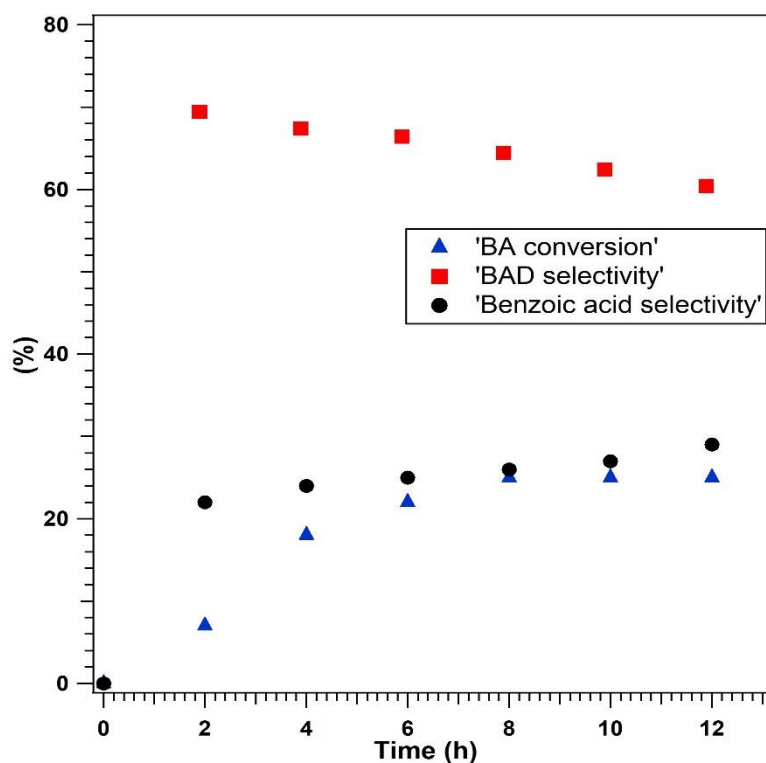


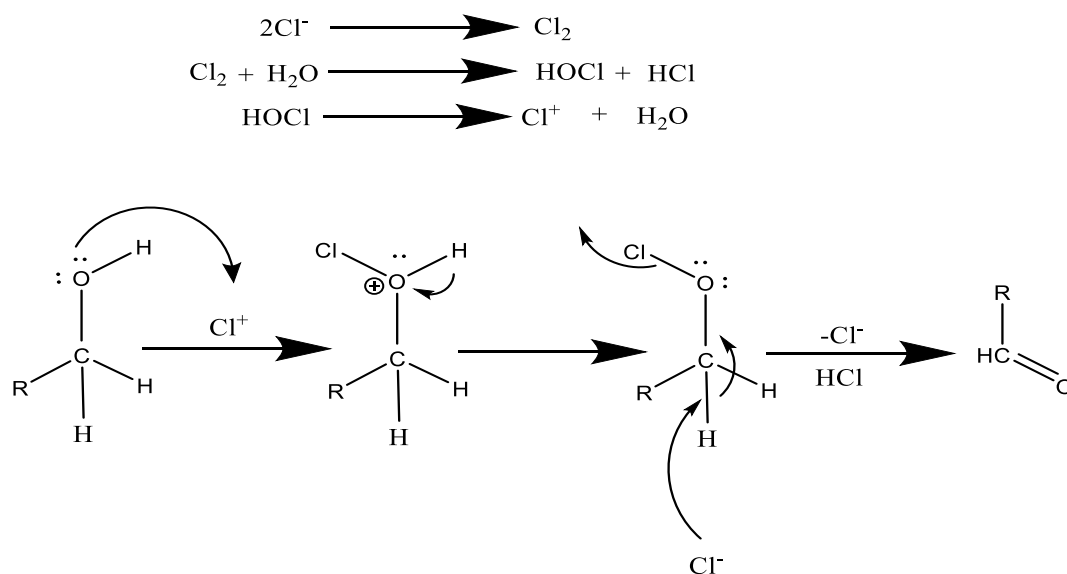
Figure 4.7 Effect of the reaction time on the conversion of BA, the selectivity of BAD and Benzoic acid at 3.0V.

In summary, while a higher voltage of 5.0 V exhibited the highest BA conversion due to greater charge transfer to the solution as well as long reaction time, it resulted in suboptimal selectivity of BAD. The BAD selectivity decreased at voltages above 3.0 V due to over oxidation, and with long reaction time. Similar observations have been found in the literature.^{307,324,325}

4.3.2 Effect of the Mediator Type and Concentration on ECO

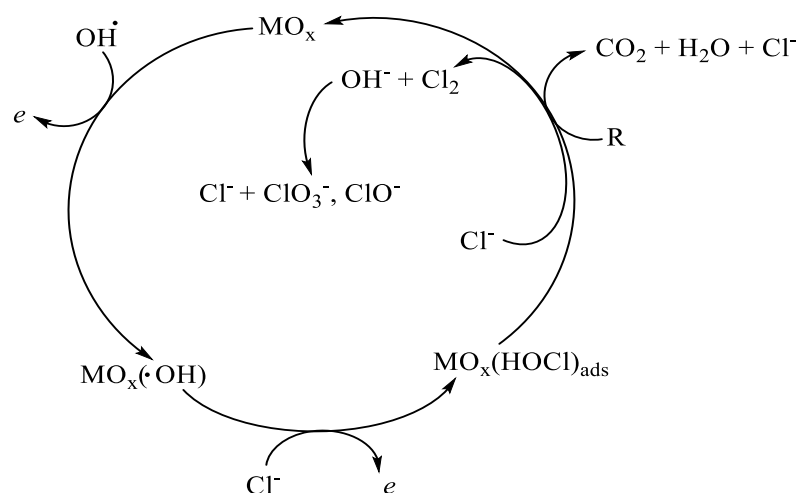
In the present study, the selective oxidation of BA was carried out with various inorganic salt mediators at the optimum electrolysis conditions. Chloride ions, very common inorganic ions frequently present in natural water or anthropogenic wastewater. Since Sodium chloride (NaCl) is a strong electrolyte, it was used as an effective redox mediator for promoting selective ECO of BA into BAD by two-phase electrolysis. In the electrochemical reaction, a chloride ion preferably undergoes

single-electron oxidation to form a chlorine radical, which is known to be an effective hydrogen abstractor for aromatic alcohols scheme 4.2.³¹⁹



Scheme 4.2 The possible mechanism for the mediator biphasic oxidation of BA.³¹⁹

It is the formation of this radical that is believed to initiate the oxidation reaction at the interphase region between organic and aqueous phases. Chlorine and/ or hypochlorite, that generated at the anode, both can be used to oxidize pollutants. In the presence of a sufficient chloride concentration, both inorganic and organic contaminants can be reduced in most cases.^{326,327} A generalized method is presented for the electrochemical conversion/combustion of organics on the oxide anode (MO).³²⁸ In the mechanism of electrochemical destruction, both chloro-and oxychloro-radicals co-generated at the electrode surface have to be considered, thus representing an extension of the model initially proposed by Comninellis *et al.* for direct electrochemical oxidation.³²⁸ De Battisti and his group studied the oxidation of glucose with chlorides and hypothesized HClO to be an oxidizing agent.³²⁹ According to them, instead of form the more commonly cited hydroxyl radicals, and oxygen transfer can be attained through adsorbed oxychloro-species in the case of active chlorine mediation^{329,330} (Scheme 4.3).³²⁸



Scheme 4.3 Extension of the reaction pattern for electrochemical incineration of organics suggested by Comninellis to the case of active chlorine-mediated electrochemical incineration.³²⁸

Given that the chlorine radical is an effective electrochemical mediator, it was important to determine whether its concentration would affect the BA conversion to BAD, or perhaps the yield of BAD. In this study, increasing the chloride increased the BA conversion. With the NaCl concentration between 0.0 to 0.66 wt%, the BAD yield was low, although by increase the NaCl between 0.83 to 3.33 wt% did not seem to affect the yield and the selectivity of BAD, shown in Table 4.1.

Table 4.1 Effect of sodium chloride concentration on BAD yield

Chloride Concentration (NaCl wt%)	BAD yield (%)
0.0-0.66	~1.5-6.0
0.83	~8.3
1-1.66	~8.3
3.33	~8.3

This indicates that sufficient chlorine radical species can be formed with a low amount of chloride mediators in the system. Among the inorganic salts, NaCl is preferred due to its low cost and higher product yield.

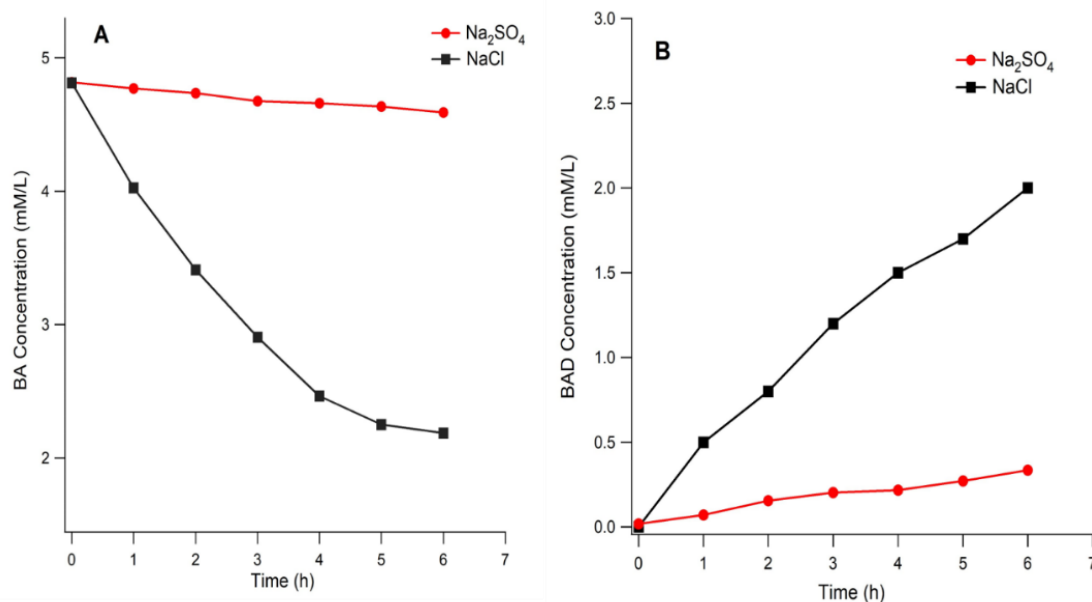


Figure 4.8 The effect of different types of mediators on (A) oxidation of BA and (B) formation of BAD.

Other effective redox mediators for ECO of aromatic alcohols include Na₂SO₄ and NaCl. The comparative effect of the two redox mediators on the oxidation of BA and the formation of BAD is shown in Figure 4.8. As expected, NaCl showed higher efficiency than Na₂SO₄ due to the low effective oxidization potential of SO₄^{•-} in comparison to OH[•] radicals.³³¹ The explanation of this phenomenon is further discussed in chapter 5, section 5.3.5.

4.3.3 Characteristics of The Synthesized TiO₂ NT for PECO

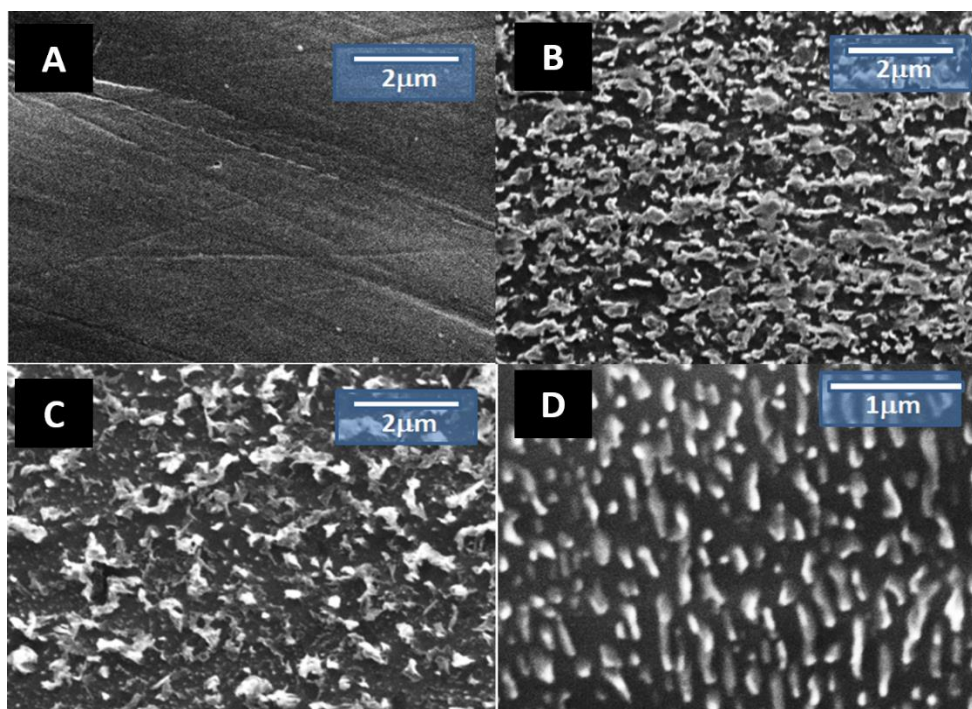


Figure 4.9 SEM images of the Ti plate surface after (A) polishing, (B) 30s acid treatment, (C) 90s acid treatment and (D) after acid treatment for 90 s followed by ultrasonic cleaning in water before anodization.

The physical and microscopic characteristics of the synthesized TiO_2 NTs were studied to assess its photocatalytic value in PECO of BA to BAD. The titanium plates used for anodization were first evaluated using scanning electron microscopy (SEM). Figure 4.9 shows the microscopic surface morphology of polished Ti plate samples before; after 30 and 90 s of acid treatment; and after 90 s of acid treatment followed by ultrasonic cleaning in water. The polished Ti plate surface was smooth with a low density of defects, and the sample was extremely hydrophobic, (Figure 4.9A), while the acid-treated Ti plate surface was rough. The surface roughness increased with increasing the time of acid exposure (B and C). Thus, the surface of the Ti plate acid-treated for the 90s was rougher and more hydrophilic than that which was acid-treated for only 30s. The acid promoted Ti corrosion led to the formation of titanium hydroxide islands on the smooth surface.³²⁰

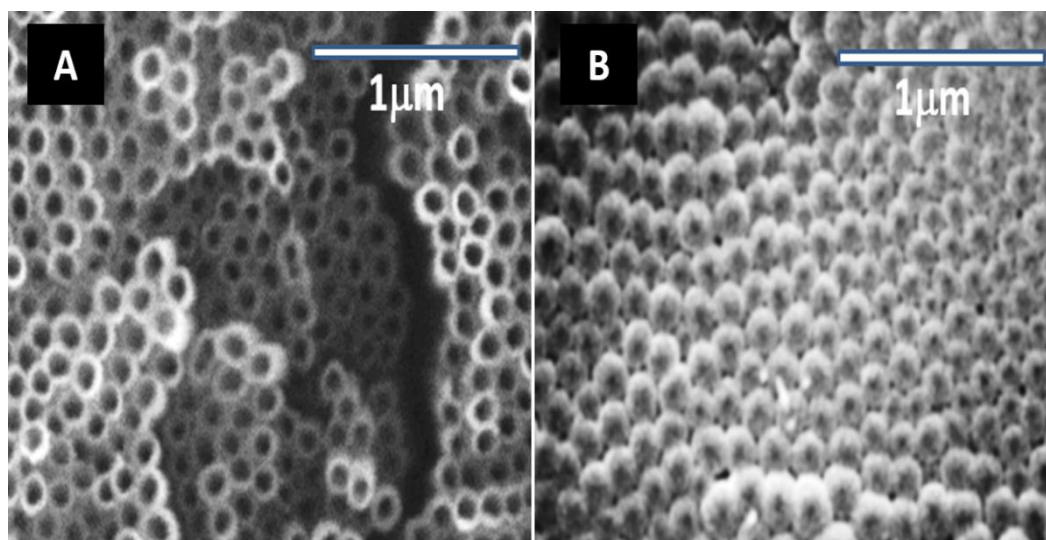


Figure 4.10 SEM images of (A) the top view and (B) the bottom view of TiO_2 nanotubular arrays.

Anodization-prepared TiO_2 nanotubes typically contain some residual organic solvents and are usually amorphous. In order to increase the mobility of the charge carrier and eliminate recombination, the formation of particular crystal phases is important. Therefore, the anodized samples were annealed to a certain temperature. At temperatures above 260°C , the residual organic products are extracted and phase transformation start from temperature from amorphous to anatase from 400 - 500°C .³³² The nanotube arrays were annealed in a tube furnace (CARBOLITE PAT 3081) at 450°C for 2 hours.

The typical morphology of anodized Ti in the electrolyte containing fluoride is shown in Figure 4.10. The SEM images show the circular cross-sections of the nanotubular arrays (A) from the top and (B) from the bottom. The top view of the TiO_2 NT sample shows highly ordered nanotubular arrays, which appeared like a bundle of bamboo sticks. The nanotubes are open from the top and closed at the bottom with an average diameter of 120 nm. A dark region is visible in the centre of each nanotube in the SEM picture in the bottom view, which is possibly due to the presence of the

hollow tubular structure. This image contrast was also observed recently by Chen *et al.*³³³

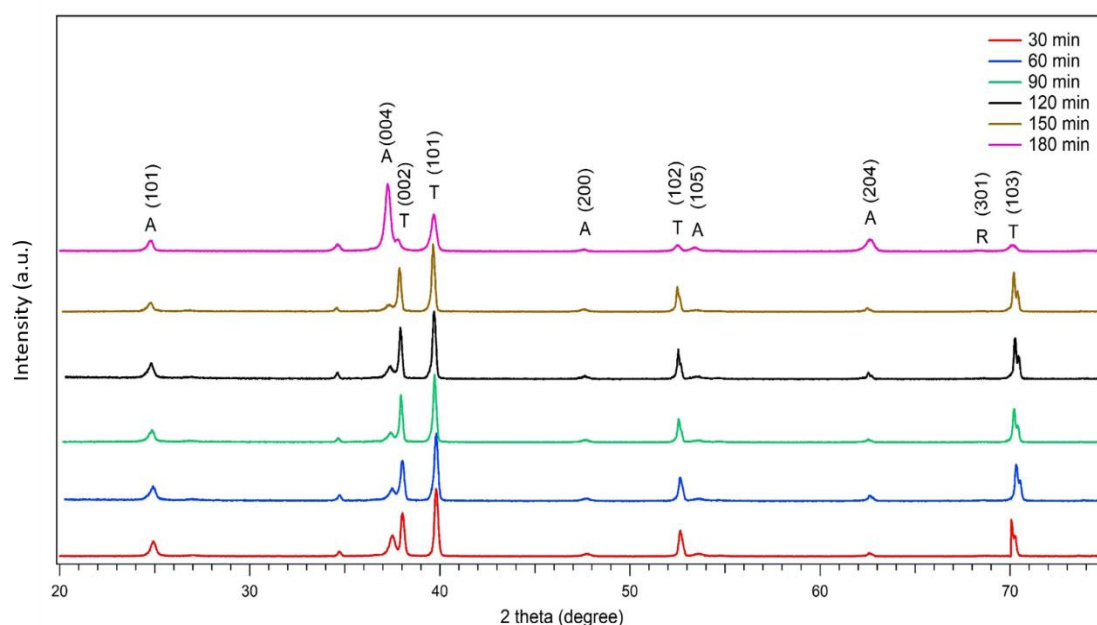


Figure 4.11 XRD pattern of TiO₂ NT films annealed at 450° C for different durations from 30 to 180 mins at time intervals of 30 mins.

The anodization process promotes the creation of an amorphous oxide layer on the surface of the nanotube, as demonstrated by several works on anodized titanium.^{334,335} Therefore, the anodization reduced the growth of Ti (002), (101), (102), (103), (112) peaks.³³⁶ The XRD patterns of TiO₂ NT plates annealed at 450°C for different durations from 30 mins to 180 mins, at time intervals of 30 mins are shown in Figure 4.11. It can be observed that the TiO₂ NT films annealed for 30 mins exhibited diffraction peaks at $2\theta = 25.14^\circ$, 37.76° , 38.28° , 40.06° , 47.34° , 52.42° , 62.82° , and 70.30° corresponding to the Ti (JCPDS No. 44-1294) and anatase which were well indexed to the standard anatase phase (JCPDS No. 21-1272). When the annealing time was increased to 150 mins, no additional peaks were observed. The intensity of the diffraction peaks from the anatase was increased while those of the substrate decreased as the calcination time increases.³³⁷ It was caused by the thermal oxidation

of nanotube. The intensities of the diffraction peaks appeared to be reduced after 180 mins of annealing and a peak from rutile, R (301) appeared, in addition to peaks from the anatase.

4.3.4 Effect of TiO₂ Annealing Time on PECO

From the SEM and XRD data, it can be seen that the TiO₂ had thermal stability and a better ordered structure than without calcination. Thus, TiO₂ NT plates annealed at different durations were used to test the effect of annealing time on BA conversion and BAD selectivity at the optimised potential of 3.0 V (Figure 4.12).

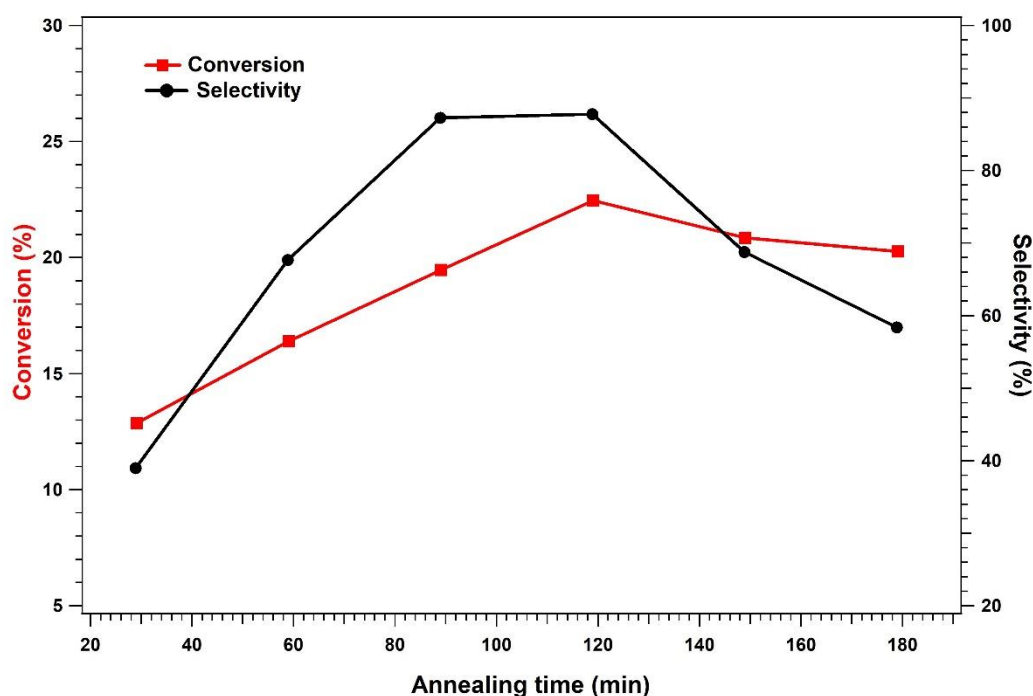


Figure 4.12 Effect of TiO₂ NT annealing time on the BA conversion and BAD yield at constant 3.0 V for 1 h of the reaction time.

The efficiency and stability of TiO₂ nanotube also depend on the calcination time. The BA conversion rate increased with the increase in the duration of annealing, with the optimal rate observed at 120 mins annealing time. The similar result reported by Liang *et al.*, they conclude that TiO₂ nanotube calcined at 500°C for 1 h showed the higher photocatalytic activity than those calcined at 300°C and 800°C.³³⁸ BAD

selectivity also increased almost 2.5 times with annealing time, the optimal rate coming out to be between 90 and 120 mins. Annealing time beyond 120 mins resulted in a decline in both BA conversion and BAD selectivity, which could be attributed to crystal size. The longer the calcination period, the larger TiO_2 crystallites are formed. This may mean that TiO_2 nanotubes that are calcined for a shorter period are more suitable material for photocatalytic treatment (and are composed of smaller crystallites).³³⁷

4.3.5 Effect of Agitation on PECO on BA conversion and BAD selectivity

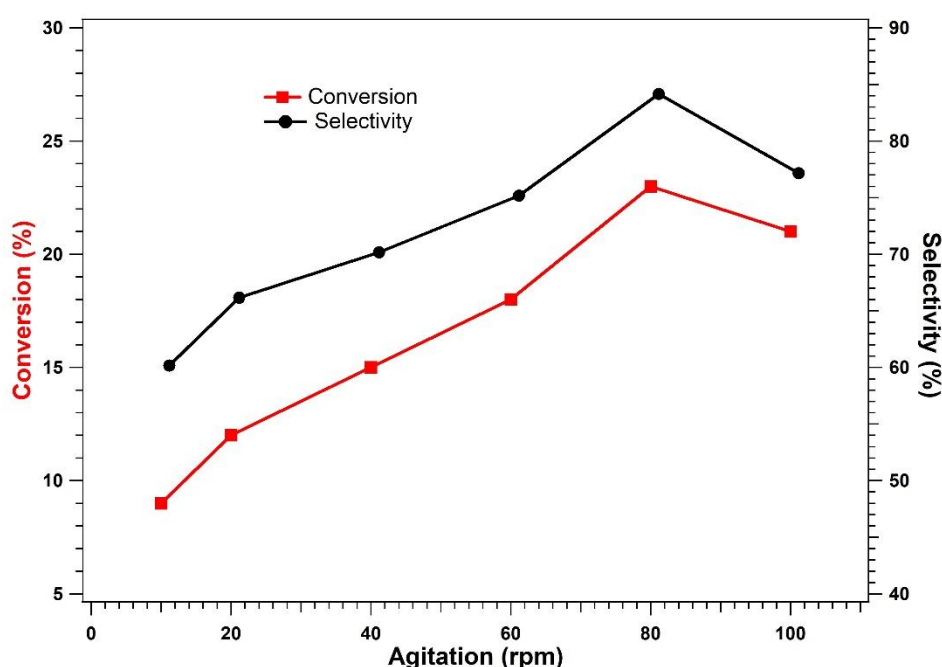


Figure 4.13 The effect of agitation rate on the BA conversion rate (%) and BAD selectivity (%).

TiO_2 nanotubes were selected for the indirect PECO, and based on the above results, we replaced the stain steel anode by TiO_2 nanotube plate which should exhibit higher electrochemical oxidation of BA into BAD. The effect of agitation rate on BA conversion and BAD selectivity on the photoelectrochemical oxidation when varied from 20 to 100 rpm is shown in Figure 4.13 above.

In general, the percentage of BA conversion and BAD selectivity increased with an increase in agitation rate, with optimal rates observed at 80 rpm. Agitation appeared to have increased the mass transfer of the reactants (BA), thus increasing their contact and interaction with the photocatalyst. However, an agitation speed beyond 80 rpm had no significant effect on the rate of the oxidation of BA, while the selectivity of BAD decreased due to overoxidation to benzoic acid.

A similar effect has been reported by Chaudhari *et al.*³³⁹ The study showed no effect of speed of agitation on the catalytic oxidation of BA to BAD by hydrogen peroxide (H_2O_2), indicating the absence of mass transfer limitation,³³⁹ which controls the adsorption kinetic rate. This indicates the limit to which the transport can significantly affect reaction kinetics and change product distributions.³⁴⁰

4.3.6 Comparison Between ECO and PECO Under Various Voltages (1.0-3.0V)

Having determined 3.0 V as the optimal voltage for ECO, it was important to compare BA conversion (Figure 4.14), BAD selectivity and yield (Figure 4.15) using ECO and PECO strategies.

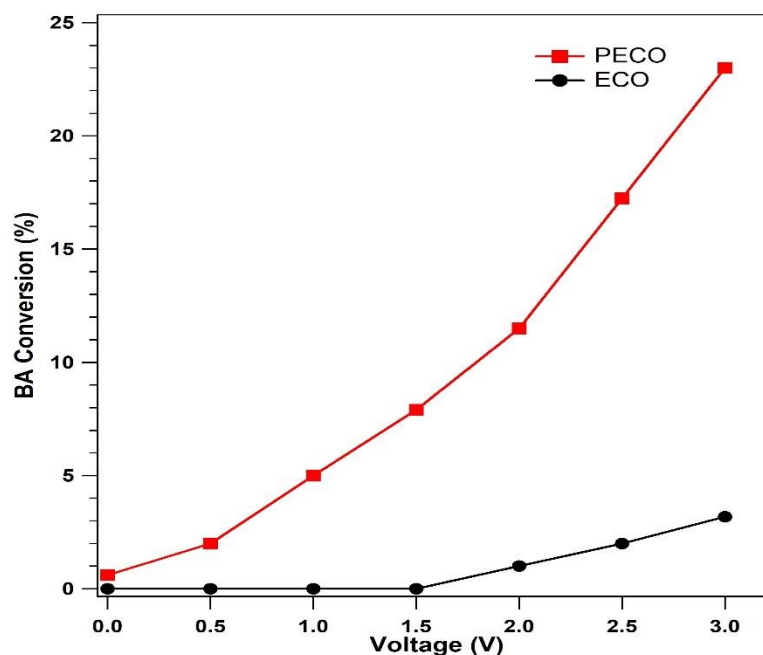


Figure 4.14 Comparison of BA conversion rate (%) using ECO and PECO (reaction time, 1h).

Across all the voltages tested (0.0-3.0V), PECO exhibited the highest BA conversion rate, while ECO exhibited the lowest. As it is shown in Figure 4.14, below 2.0 V (15 mA/cm²) at ECO, the oxidation did not take place in the first hour, and when the voltage increased as well as the current density, the BA conversion increased, a similar effect on BAD selectivity and yield. That could be due to that, increased current density during ECO lead to enhance chlorine generation, which the oxidant radicals.³⁴¹ When BAD selectivity (Figure 4.15A) and yield (Figure 4.15B) was evaluated, PECO still resulted in the highest yields across all voltages from 0.0 to 3.0V. The superiority of PECO strategy can be attributed to photo-activation, electrochemical and photocatalytic synergies. Lack of photo-activation could explain poor selectivity and yield in the case of ECO. However, photo-activation without a photocatalyst did not result in significant improvements. Therefore, the most critical component was the photocatalyst, which is the anodic TiO₂ NT arrays.³¹⁷

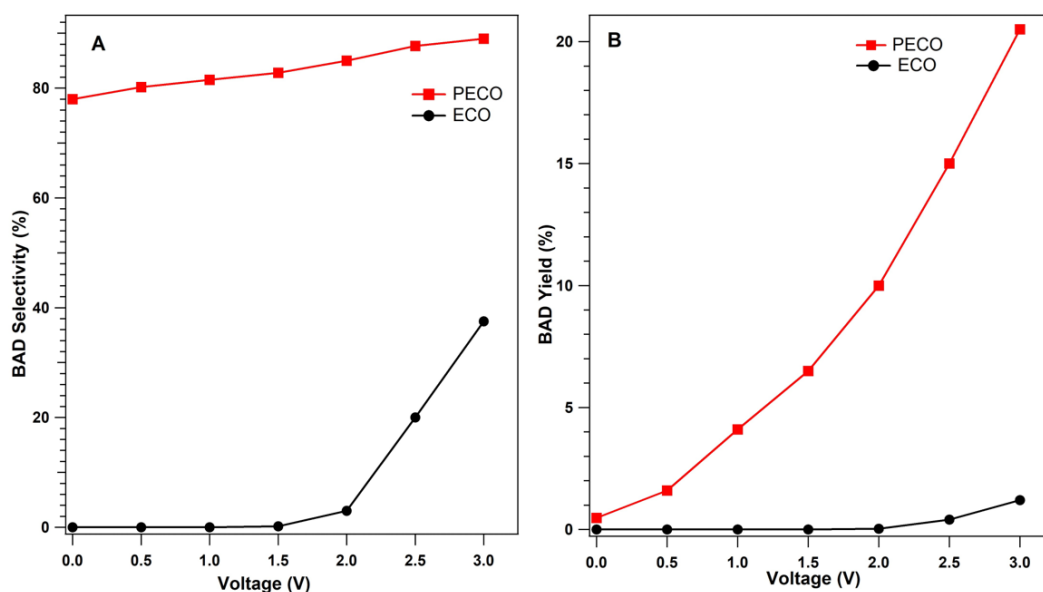


Figure 4.15 Comparison of (A) BAD selectivity (%) and (B) BAD yield produced using ECO and PECO (reaction time, 1 h).

Compared to metal electrodes that are poorly ordered, TiO_2 NTs are highly ordered tubular structures, and therefore, exhibit a significantly higher photocatalytic activity. TiO_2 NTs are widely used in water splitting and photocatalytic degradation of organic compounds due to their strong ion-exchangeability, and low e-h recombination due to relatively long lifetime of the e-h pairs in them.³¹⁷

4.4 Conclusion

The present experiment has demonstrated PECO to be the most efficient strategy in terms of product yield and selectivity in the electrochemical oxidation of BA to BAD. In ECO, voltage seems to be a critical component that influences BA conversion and BAD selectivity. A voltage above 3.0 volts increased the BA conversion rate but resulted in overoxidation. The effect of two mediators has been studied and the conclusion is that the Cl^\cdot radical is the most effective mediator under acidic conditions. The addition of photo-activation slightly increased the BA conversion rate. Significant rates were observed with the addition of TiO_2 NT films as a photocatalyst. TiO_2 NT film

was constructed by using a Ti plate as the substrate of cathode and anode. BA conversion rate and BAD selectivity increased with longer annealing time, with optimal conversion (22%) happening around 120 mins of annealing time and the optimal selectivity of BAD (89%) happening between 90 to 120 mins of annealing with up to 23% of BAD yield.

CHAPTER 5 Highly Selective Photocatalytic Oxidation of Alcohol to Aldehydes with a Radical mediator in Biphasic Reactions

Embracing green chemistry in organic synthesis, the present study explored partial photocatalytic oxidation of benzyl alcohol (BA) to benzaldehyde (BAD) using titanium dioxide as a photocatalyst (TiO_2). This was conducted using aqueous suspensions of different quantities of commercial TiO_2 -P25 within an organic-phase solvent mixture, consisting of chloroform (CHCl_3) and BA. A metal-halide lamp was used as a source of photons. The main photooxidation product was BAD and negligible amount of benzoic acid. The effect of various reaction parameters and conditions on the TiO_2 photo-reactivity were tested. Optimized chloroform proportion and HCl concentration were determined to be 40 vol% and 0.25M, respectively. Higher pH decreased the partial positive charge of the TiO_2 catalytic surface. Nitrate and chloride anions (NO_3^- and Cl^-) increased catalytic reactivity while, SO_4^{2-} led to a lower reactivity. The selective photocatalytic oxidation of BA to BAD was governed by the Hammett relationship. Both meta- and para-substituted phenyl-rings showed electrophilicity, and hence a higher reactivity than the ortho-substituted phenyl-ring.

5.1 Introduction: Synthesis of Carbonyl Compounds

Carbonyl compounds (aldehydes and ketones) have remained key starting materials for the organic synthesis of a range of complex chemical products.³⁴² The electrophilic nature of carbonyl carbon makes carbonyl compounds highly nucleophilic. This allows nucleophilic addition reactions for the interconversion of $\text{C}=\text{O}$ into a wide range of important functional groups.³⁴³ Energy-efficient and environmentally benign selective transformation of organic functional groups is an important step in organic synthesis, yet a challenging endeavour.³⁴⁴

The synthesis of carbonyl compounds requires the selective conversion of alcohol groups, and this is among the most important transformations in organic synthesis.³⁴⁵ This requires partial oxidation of the primary alcohols in air, to prevent further oxidation to carboxylic acids. Several homogeneous heavy metal catalysts such as Palladium (Pd),¹²⁰ Iridium (Ir),³⁴⁶ Ruthenium (Ru),³⁴⁷ and molybdenum (Mo)³⁴⁸ have been used to achieve selective partial oxidation of both aliphatic and aromatic alcohols to their corresponding aldehydes. This has typically required hazardous solvents and/or strong oxidizing reagents such as pyridinium chlorochromate (PCC).³⁴³ However, these homogeneous metal catalysts are not environmentally benign, and therefore, contravene the key principles of green chemistry. However, it is possible to apply green chemistry in homogeneous catalysis by careful selection of the metal catalysts, and optimization of their catalysis.³⁴⁹

Some green pathways have been developed, where homogeneous metal catalysts with low toxicity have been selected, alongside more environmentally benign solvents and oxidants. Selective photocatalytic oxidation of alcohol to aldehydes is an emerging green strategy for the organic synthesis of aldehydes.³⁴³ Benzyl alcohol (BA) is one of the most studied substrates in organic synthesis. Depending on the catalytic strategy, and the reaction conditions (temperature, solvent, and oxygen pressure), BA can be converted into many carbonyl compounds of industrial interest, such as benzaldehyde, benzyl benzoate, benzoic acid and benzyl ether.³⁵⁰ Benzaldehyde (BAD) is a clear, colourless or yellow liquid with a characteristic odour of bitter almonds; it is an important industrially practical intermediate molecule (aromatic aldehyde) widely used in the chemical industry. For example, it is a starting material for the manufacture of various aniline dyes, aliphatic fragrances, flavourings, and pharmaceuticals.³⁵¹ BAD is produced commercially by the oxidation of BA.

The oxidation of BA is traditionally carried out using stoichiometric strong oxidants in organic solvents such as toluene, diethoxyethane, dimethyl sulfoxide (DMSO), and dimethylformamide (DMF).^{352,353} However, the use of strong oxidants in stoichiometric quantities can be expensive, and such processes can produce undesired organic waste.³⁵⁴ Both the toxic oxidants and solvents raise environmental concerns. This has motivated the development of alternative green catalytic processes that use benign and cheap oxidants such as O₂, in combination with supported metal nanoparticles as catalysts.³⁵⁵ This strategy has led to the realization of solvent-free, aerobic oxidation of alcohols to aldehydes.³⁵⁰

Several studies have proposed solvent-free strategies to oxidize BA to BAD.^{210,304,305} A study by Augugliaro *et al.*³⁰⁵ evaluated the photocatalytic oxidation of BA in aqueous suspension of as-synthesised and commercial TiO₂ photocatalysts. Surprisingly, the as-synthesised TiO₂ photocatalyst exhibited a 28% selectivity for BAD production, with yields of up to 50 %, four times higher than the commercial alternative. The replacement of water with small amounts of aliphatic alcohol was shown to decrease the oxidative conversion rate but improve the selectivity for BA conversion by 50%. Increasing the photocatalyst quantity by up to 0.4 g L⁻¹ was also shown to increase the selectivity, but it decreased the conversion.³⁰⁵ The negative effect of photocatalyst loading was also reported previously by Gassim *et al.*³⁰⁴ with an optimal TiO₂ concentration of 0.6 g L⁻¹. From the reviewed literature, it appears that the photocatalytic oxidation of BA to BAD using TiO₂ as the photocatalyst has many factors requiring optimization.³⁰⁴

The present study aimed to develop a photo-efficient, robust, cost-effective and environmentally benign photocatalytic oxidation system for converting alcohols to

aldehydes. This was achieved by studying the effects of various parameters on the oxidation of model alcohol, BA, using photo-catalytic methods.

5.2 Experimental Section

5.2.1 Chemicals Reagents

TiO₂ (Aeroxide® P25; formerly Degussa P25), which consists of a mixture of two phases (~75% anatase and ~25% rutile) was commercially obtained from Evonik Industries (Goldschmidtstr, Germany). BA (benzyl alcohol of 99% purity) were commercially obtained from Sigma-Aldrich (Dorset, UK). Sulphuric acid (98%), sodium chloride (of ≥ 99.5% purity), and magnesium sulfate (62-70%) were purchased from Fisher Scientific (Loughborough, UK). Chloroform (CHCl₃) (99+%), 32% hydrochloric acid and nitric acid were purchased from VWR International (Quebec, Canada). N-Octadecane (of 99 % purity) was sourced from BDH (British Drug Houses) chemicals Ltd. (Poole Dorset, UK), whereas high purity oxygen gas was purchased from BOC gases (UK). All the chemicals and solvents were of analytical grade, whereas oxygen gas was of high purity grade. All chemicals, solvents, and oxygen gas were used as received unless otherwise stated.

5.2.2 Photocatalytic Oxidation of Alcohols to Aldehydes

The photocatalytic oxidation reactions were conducted using aqueous suspensions of different amounts of commercial TiO₂-P25 and an organic-phase solvent mixture consisting of chloroform and BA. P25 was chosen as the catalyst due to its known chemical composition, commercial availability, and its wide acceptance as a benchmark catalyst. The reaction was performed as a single-pot reaction setup, consisting of a three-necked cylindrical batch photo-reactor (Figure 5.1). An immersed lamp was used as a source of photons to drive the photocatalytic reactions with a continuous oxygen supply.

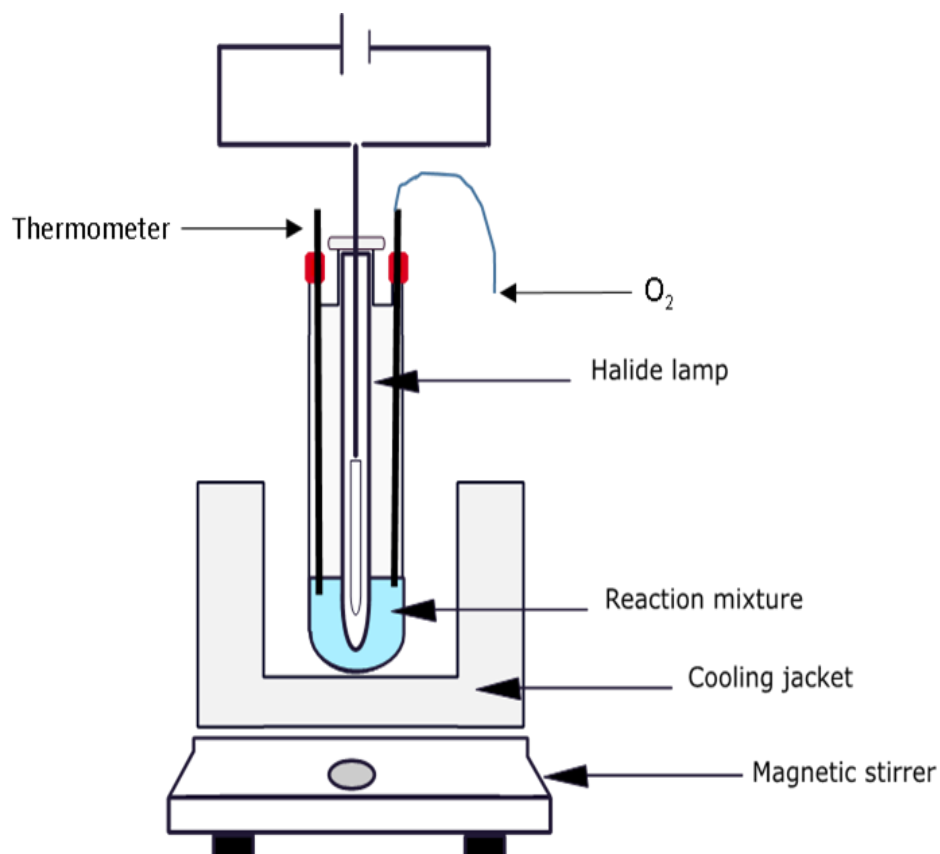


Figure 5.1 A diagram of the reactor setup for the photocatalytic oxidation of benzyl alcohol to aldehyde.

Briefly, 0.075g of P25 catalyst was suspended in a 30 mL mixture containing 18 mL (60 vol %) water, 0.5 mL HCl and 0.15 g NaCl as a mediator, 12 mL (40 vol %) of $CHCl_3$ and, 0.75 mL of BA finally was added to the mixture. Two distinct liquid phase layers were formed, which included an aqueous phase (above) and an organic phase (below). The two liquid phases were continuously mixed using a magnetic stirrer, whilst high purity oxygen gas was bubbled directly into the immiscible liquid mixtures, at a controlled flow rate of 0.9 L/h. Aliquots were analysed to monitor changes in the concentration of BA periodically before illumination. Once equilibrium was attained, the setup was illuminated causing the commencement of the photocatalytic reaction, changes in the concentration of reactants as well as the formation of the products were monitored.

A 150-Watt Ceramic Metal Halide E40 lamp was used as the light source. Samples were collected every 10 minutes and immediately dried with MgSO_4 before instrumental analysis. The run was repeated several times with different amounts of the reacting species. Identification and quantitative measurements of the organic products of the reaction were carried out using a Perkin Elmer gas chromatograph, equipped with a flame ionization detector (FID-GC) (PerkinElmer Instruments, Norwalk, CT, USA), a 0.03 g portion of octadecane was used as an internal standard. Hydrogen (H_2) was used as the GC carrier gas. This gas was chosen because it is easier to obtain and cheaper than helium (He) carrier gas, offering an equivalent level of sensitivity alongside faster speed of analysis. This can lead to an overall improvement in separation performance. Furthermore, H_2 was produced from a Peak Precision Hydrogen Trace Generator, which is significantly safer than high-pressure hydrogen cylinders. All samples were analysed through manual injection and compounds were separated using a polar column (Stabilwax30m x 0.53mmID x 1 μm df). A Varian CP- 3800 with a mass spectrometer detector (GC-MS) and ^1H NMR spectrum were also adopted for identification purposes.

5.3 Results and Discussion

The present study evaluated the reaction conditions that are potentially useful in the optimization, of the photocatalytic oxidation of alcohols to aldehydes. Here, we show that the photocatalytic conversion of BA to BAD can be optimized by controlling the concentration of the TiO_2 photocatalyst, the solvent to water ratio, the pH and the type of acid. Furthermore, this study also explored the reaction kinetics as well as the photocatalytic mechanism involved.

5.3.1 Kinetic Analysis on the Photocatalytic Oxidation of Benzyl Alcohol and its Derivatives

The rate of a chemical reaction can be described as the loss (or production) of a chemical species over a given period of time. Mathematically this is represented according to the rate law shown in Equation (5.1), where v is the rate of the studied chemical reaction, C is the concentration of a reagent chemical species, k is the rate constant of the reaction and n is the order of the reaction.

$$v = \frac{dC}{dt} = -kC^n \quad (\text{Eqn 5.1})$$

The reaction rate constants (k) of photocatalytic oxidation of benzyl alcohol and its derivatives into corresponding benzaldehyde have been evaluated from the first-order rate law in equation (5.2- 5.4)

$$-\frac{dC}{dt} = k \cdot C^n \quad (\text{Eqn 5.2})$$

$$-\int \frac{dC}{C} = \int k dt \quad (\text{Eqn 5.3})$$

$$-kt = \ln \frac{C_t}{C_0} \quad (\text{Eqn 5.4})$$

Whereas C_0 is the initial alcohol concentration and C_t is the alcohol concentration at time t . The reason for the 1st order kinetics is that it is unlikely that the oxidation requires two alcohol to be involved in an elementary reaction steps, which is valid for most of the organic oxidation process.

5.3.2 Catalyst Loading and Catalyst Type

A catalyst typically accelerates a chemical reaction by reducing the activation energy, or by altering the reaction mechanism. Importantly, chemical catalysts are typically effective in small concentrations, therefore, the present study tested the effect of

catalyst loading on the rate of the photocatalytic conversion of BA to BAD. Catalyst loading per liter added to the reacting solution in the range 0.5-5.5 g/L and the corresponding photocatalytic reactivity is shown in Figure 5.2. As seen from the regression study which is greater than 0.91. (Figure 5.2A), thus the photooxidation of benzyl alcohol to benzaldehyde follows the pseudo-first-order rate kinetics. Initially, increasing the loading of TiO₂ photocatalyst increased the photocatalytic reactivity rate, up to a catalyst loading of 4 g/L. At this loading, the peak reactivity was measured to be $62 \times 10^{-3} \text{ h}^{-1}$ (Figure 5.2B). Further catalyst loading resulted in a sharp decline in photocatalytic reactivity to $25 \times 10^{-3} \text{ h}^{-1}$ at a loading of 5 g/L. Thus, the optimum photocatalytic reactivity of TiO₂ photocatalyst can be achieved at a catalyst loading of 4g/L.

This finding suggests that there is an optimal catalyst concentration, which must be determined to optimize photocatalytic efficiency. A study by Marotta *et al.* demonstrated that by using a BA solar photooxidation system, a higher reactivity of the TiO₂ photocatalyst can be achieved at a catalyst concentration of 2.50 mmol/L compared to the initial value of 0.69 mmol/L.³⁰⁹ This is consistent with a study by Spasiano *et al.* in which an optimal TiO₂ concentration of 2.50 mmol/L was determined for the TiO₂/Cu(II) catalyst system, for BA solar photooxidation.³⁵⁶ Furthermore,

Marotta *et al.* tested the effect of increasing TiO_2 concentration beyond 2.50 mmol/L. The higher values beyond this threshold did not increase system reactivity.³⁰⁹

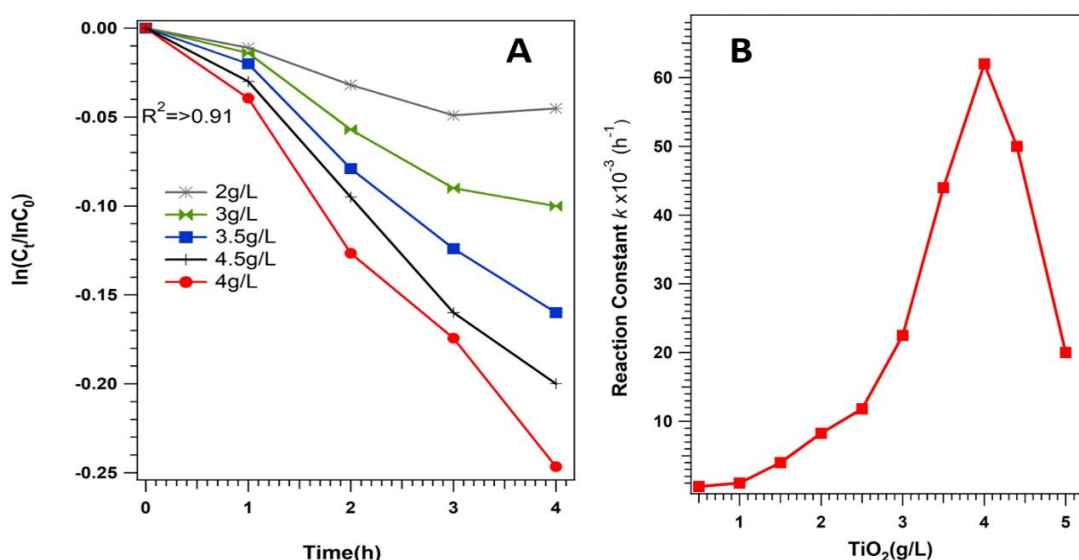


Figure 5.2 (A) Kinetics plot of benzyl alcohol photooxidation following pseudo-first-order. (B) The effect of catalyst loading on the reactivity of the TiO_2 photocatalyst. The system reactivity increased with increasing catalyst loading. An optimal loading was established at 4g/L.

Possible reasons as to why catalytic TiO_2 loads beyond 4g/L do not increase reactivity have been reported. Firstly, this has been attributed to the attenuation of photons due to radiation screening and scattering effects caused by excess TiO_2 particles in the reaction mixture, characteristic of the commercial powder (Degussa P25). Degussa P25 has a smaller crystal size in comparison to commercial Wackherr TiO_2 . TiO_2 -P25 is more active at lower loading while TiO_2 Wackherr is more active at high loading.^{305,357} The excess TiO_2 (Degussa P25) particles in the reaction mixture were shown to mask part of the photosensitive surface of the TiO_2 photocatalyst, thus reducing its reactivity.^{309,356} This negative effect of excess photocatalyst loading was also reported previously by Gassim *et al.* with optimised TiO_2 concentration determined to be 0.6 g L^{-1} . The study demonstrated that increasing substrate (BA) concentration also increased the rate of BA photoconversion. This indicates that there

is an ideal substrate-to-catalyst ratio, deviation from which leads to lower photo-reactivity.³⁰⁴

5.3.3 Effect of Chloroform to Acid Ratio on the photocatalytic oxidation of BA to BAD

TiO₂ is known to exhibit acid-catalytic properties.³⁵⁸ To unravel the nature behind the high catalytic activity of the photooxidation of BA to BAD in the biphasic reaction, further studies were carried out to investigate the effect of the ratio of the organic solvent to water. The present study tested the effect of the chloroform/water volume ratio of starting solvent and increasing the quantity of acid at various volumes of chloroform CHCl₃ solvent (0-90 %) on photocatalytic reactivity. However, after 70% of CHCl₃, the reaction constant (k) remain zero as the reaction did not happen at these ratios which point out the significant role of the two phases system. It was also important to determine what volumes of acid and solvent exhibited optimised reactivity.

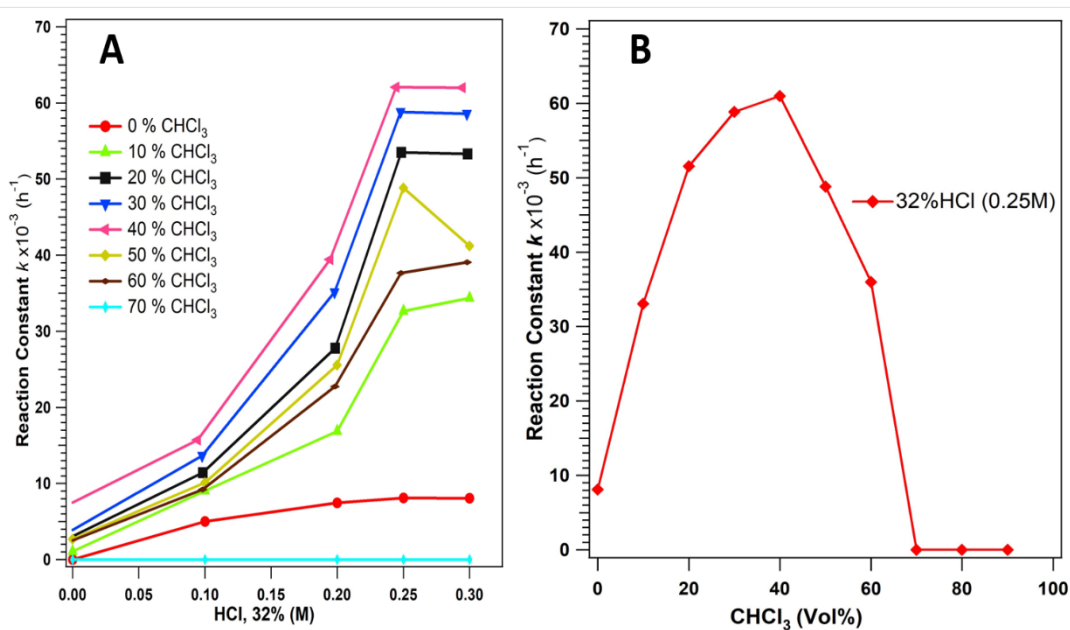


Figure 5.3 (A) Optimisation curves of volume % effects of chloroform and all HCl concentration and (B) Optimisation curves of volume % effects of chloroform at the optimised HCl concentration(0.25M).

Increasing the volume of added HCl generally increased the photocatalytic reactivity (Figure 5.3A). However, when 70% volume CHCl_3 in comparison to the aqueous phase was used, increasing the volume of acid did not change the negligible photocatalytic reactivity. A marginal increase in photocatalytic reactivity was observed in the absence of the solvent (0% CHCl_3). Optimised photocatalytic reactivity was observed at 40 % CHCl_3 , which increased steadily with higher HCl volume, reaching a maximum at 0.25-0.30 M, the same result was found in another study.³¹¹ Thus, the optimized chloroform and HCl volumes were determined to be 40% volume and 0.25-0.30 M, respectively (Figure 5.3A and 5.3B).

Therefore, the interpretation of pH effect on the photocatalytic oxidation was conducted, an increase in pH generally resulted in a decrease in the photocatalytic reactivity of TiO_2 (Figure 5.4). However, an optimal reactivity ($62 \times 10^{-3} \text{ h}^{-1}$) was observed at lower pH values, between 1 and 3. Increasing the pH beyond 3 resulted in a sharp decline in the reactivity, to about $5 \times 10^{-3} \text{ h}^{-1}$ at a neutral pH 7. This is consistent with findings from a similar study by Marotta *et al.*³⁰⁹ which evaluated the photooxidation of BA to BAD.³⁰⁹ In their study, it was demonstrated that increasing the pH from 2.0 to 4.0 resulted in a decrease in BA consumption and BAD formation rates, indicating a reduced reaction rate.

Based on the findings from this experiment, and supported by evidence from Marotta *et al.*,³⁰⁹ it can be deduced that the surface of the TiO_2 photocatalyst can react as both an acid and a base. Thus, the material exhibits amphoteric properties as shown in Equation 5.5 and 5.6. Under acidic conditions, the TiO_2 catalytic surface undergoes protonation, and therefore, acquires a net positive charge (TiOH_2^+).

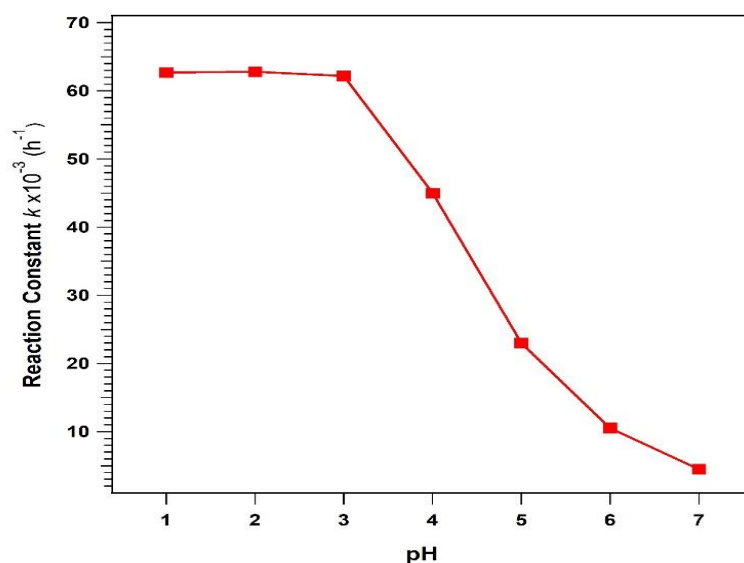
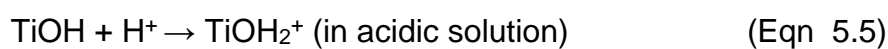


Figure 5.4 The effect of pH on the reactivity of the TiO_2 photocatalyst.

In contrast, under alkaline conditions the TiO_2 catalytic surface undergoes hydroxylation. This results in the loss of a proton, and the catalyst surface acquires a net negative charge (TiO^-).



This partially reduces the adsorptivity of the catalytic TiO_2 surface for Cl^- , and therefore reduces the overall reactivity.^{181,305} This explains why there was a decrease in the BA conversion rate at system pH values above 3.

5.3.4 Effect of Acid-Type

After results in chapter 4 that found the mediator is a major key for two-phase photooxidation. Acid presence is a significant key in the redox-mediated photocatalytic oxidation biphasic system. Different types of acid have varying capabilities to react with positive holes (h^+) at the catalytic surface.

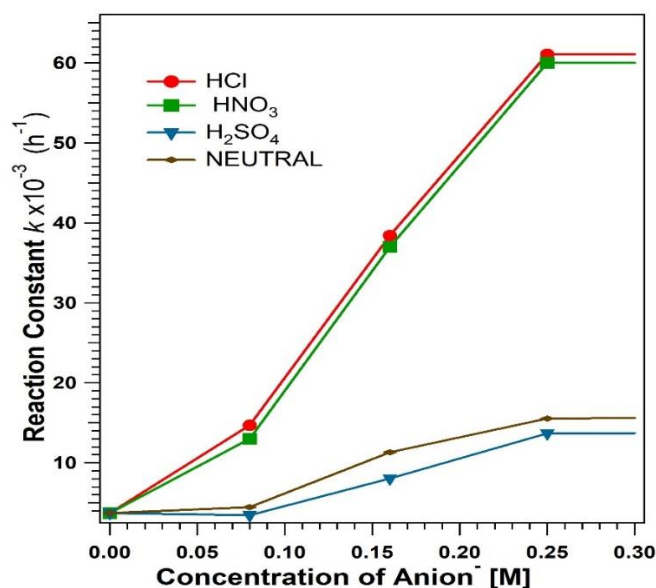


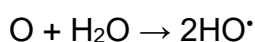
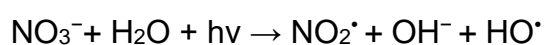
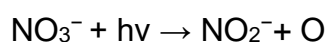
Figure 5.5 The effect of acid-type on the reactivity of TiO₂ with the presence of NaCl. HNO₃, HCl, H₂SO₄ and with no acid.

In the present study, different acid types (HNO₃, H₂SO₄, HCl and no acid) in the presence of NaCl as a mediator, were tested to determine the best acid type that has the best pH-regulating effect (Figure 5.5).

No significant difference was observed in the reactivity rate of the system in the presence of HCl and HNO₃ acids. However, regardless of the acid-type used, increasing anionic concentration also increased the TiO₂ reactivity, with optimised concentration measured at 0.25M. The presence of Cl⁻ and NO₃⁻ anionic acid species were associated with higher photocatalytic reactivity in a concentration-dependent manner. The same result indicated that increasing Cl⁻ ions increasing the photocatalytic degradation of Brilliant Orange K-R by Zhang *et al.*³³¹ Since NaCl is a strong electrolyte, the photocatalytic efficiency of BA would be enhanced noticeably for increasing the increase of free Cl[•] radical concentration. Also a study by Zanoni *et al.*³⁵⁹ found that the photocatalytic oxidation of Remazol Brilliant Orange was more effective in Cl⁻ and NO₃⁻ media.³⁵⁹ However, HCl showed higher efficiency than HNO₃, and that may be due to fewer oxidative species formed in the presence of NO₃⁻. Also,

nitrate ions (NO_3^- from HNO_3), are dissociated by UV light to produce additional hydroxyl.³⁶⁰ The photo-reactive mechanism to generate hydroxyl radical generation from nitrate ions is shown in reaction scheme 5.1.³³¹ The other major difference is possibly depending on the oxidation power of chlorine and hydroxyl radicals for the oxidation of BA

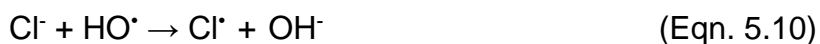
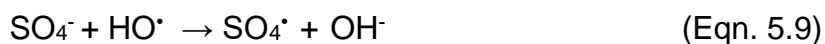
Scheme 5.1: photogeneration of hydroxyl radicals by nitrate ions



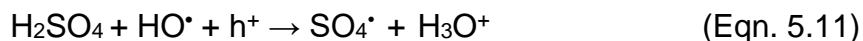
In contrast, SO_4^{2-} acid anions, as well as the pH natural salt solution (NaCl), were associated with lower reactivity. H_2SO_4 and NaCl without acid showed nearly identical reactivity trends throughout the anionic concentration range tested from 0.0 to 0.30 M (Figure 5.5). The lower reactivity of the H_2SO_4 implies that SO_4^{2-} has no positive contribution in the creation of oxidative radicals such as HO^\bullet radicals. Hence only the Cl^- species from the salt react with h^+ to form chlorine radicals, which are responsible for the limited oxidation activities, with or without H_2SO_4 . Meanwhile, the acid-dissociated SO_4^{2-} and the salt-dissociated Cl^- species could behave as HO^\bullet radical scavengers, yielding hydroxyl ions (OH^-) (Equation 5.9 and 5.10). This can form hydroxonium and hydroxide ions respectively (Equation 5.11 and 5.12). SO_4^{2-} was reported to be less reactive than hydroxyl radicals towards organic molecules.^{181,309,331}

Scheme 5.2: The scavenging of hydroxyl radicals by sulphate and chloride ions





Overall equation:



Similarly, Marotta *et al.* demonstrated that phosphoric acid (H_2PO_4) can react with h^+ on the catalytic surface, to produce dihydrogen phosphate radicals, $\text{H}_2\text{PO}_4^\bullet$ (Equation 5.13). This acid was used in literature to adjust the reaction system pH to the optimum range of 2.0 - 4.0. Any decrease in pH beyond this range increased the concentration of $\text{H}_2\text{PO}_4^\bullet$ radicals, which scavenge the hydroxyl radicals, HO^\bullet (Equation 5.14). Since HO^\bullet are pivotal to the oxidation reaction, their accelerated removal from solution (under low pH) results in a marked inhibition of the oxidation of the substrate.³⁰⁹



It is also important to observe that chloride ions are important for the reactivity of TiO_2 photocatalyst for BA conversion to BAD. However, this is only true at low pH. At pH 7, NaCl has a low catalytic effect. As previously identified, pH 7 is not ideal for the photocatalytic reactivity on TiO_2 .^{310,331} A lower pH in the range of 1-3 can be achieved using acids such as HCl, and HNO_3 . All 4 experiments included a NaCl mediator, which produced Cl^\bullet radicals. The adding of HCl increases the concentrations of Cl^\bullet while the addition of HNO_3 , some Cl^\bullet were replaced with OH^\bullet , which offers slightly less reactivity. The enhanced reactivity for TiO_2 under acidic condition is consistent with a study by Wang *et al.*,³⁶¹ which tested the conversion of the photocatalytic oxidation of BA into BAD over TiO_2 with different acids and salts. They found that the

salts had less effect than the acids with the same anions which means that the protons are more effective than counter anions.³⁶¹

5.3.5 Proposed Reaction Mechanism

The photooxidation reaction mechanism, activated by UV-visible light in a single aqueous phase as proposed by Higashimoto *et al.* is summarised in Figure 5.6.³⁶² The proposed photocatalytic mechanism in the single aqueous phase involves the binding of two molecules of TiO₂ photocatalyst via an oxygen bond, and subsequent formation of hydrogen bonds to bind molecules of BA. Upon photooxidation, there is the formation of a carbonyl group (BAD), with the elimination of two water molecules and the regeneration of the TiO₂ photocatalyst. During the photooxidation, the photogenerated h⁺ attacks the aliphatic carbon of the two BA molecules, to form a carbonyl carbon and finally the two molecules of BAD. This reaction terminates by releasing the TiO₂ photocatalyst, which starts the photocatalytic process over again.³⁶²

In a single-phase reaction, the oxidation of BA preceded through two reaction steps: Partial oxidation of BA to BAD and complete oxidation to yield CO₂. This suggests that the molecules of BA may have interacted with the surface of the TiO₂ catalyst in two different ways resulting in their partial oxidation or mineralisation. These findings agree with the report of Augugliaro *et al.*³⁰⁵

Where the oxidation kinetics of aromatic molecules in water using TiO₂ were studied.³⁰⁵ They concluded that molecules of aromatic alcohol are adsorbed onto the partially oxidising sites of the catalyst to produce aldehyde stable intermediates capable of desorbing into the bulk of the solution, while mineralising sites of the catalyst produce CO₂. The mineralisation may occur through a series of intermediates which do not desorb into the solution leaving molecules of both alcohol and aldehyde to the same fate. Another reason could be that since an electron-donating

group/species can increase the hydrophilicity of an aromatic ring, the possibility of the reaction to undergo direct mineralisation to CO_2 is reduced, owing to the increased desorption capacity of the catalyst surface.³⁰⁵

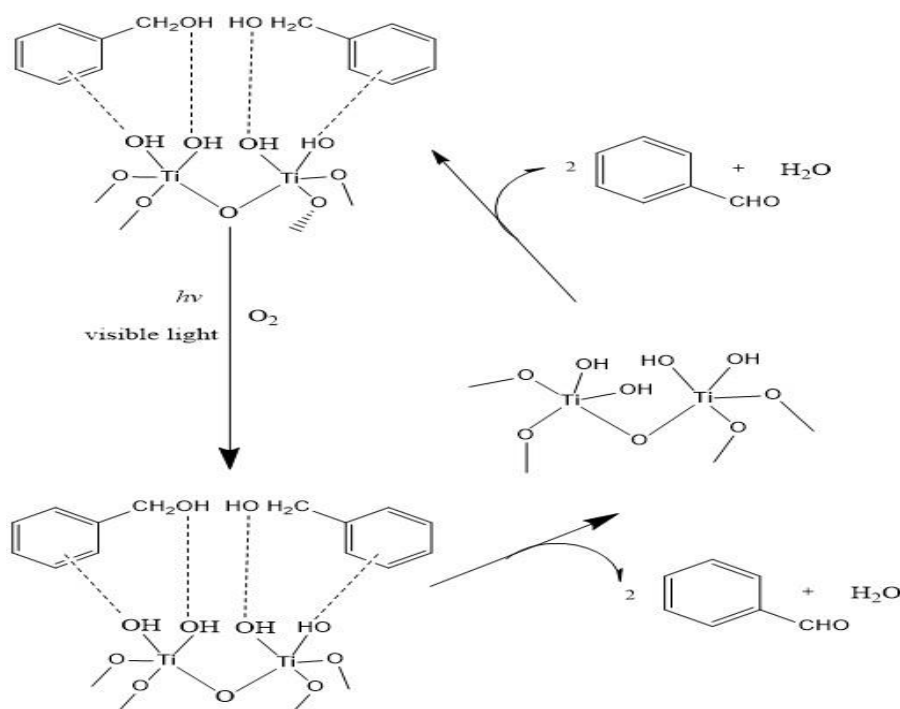


Figure 5.6 The single aqueous phase reaction mechanism proposed by Higashimoto *et al.*³⁶²

However, reports show that for heterogeneous photocatalytic hydroxylation reactions, the partial oxidation pathway is preferential, provided there is an electron-donating group attached to the aromatic ring. Whereas in the case of mineralisation, the presence of an electron-withdrawing group favours this pathway. This same rule is believed to apply to partial oxidation of aromatic alcohols to their corresponding aldehydes in water.

In contrast, the biphasic system is shown in Figure 5.7. where the reactant and the products are isolated from the catalyst. In the entire biphasic system, chloride ions allow the protonation of one oxygen atom for each Ti atom joined by the Ti-O-Ti bond. Two chlorine ions on the photocatalyst surface are attacked by the h^+ of the e-h pair

($e^- + h^+$) to generate two chlorine radicals, forming a chlorine molecule. The chlorine molecules then react with the aqueous phase to produce HCl and hypochlorous acid (HOCl). Upon acidification, HCl and HOCl undergo dissociation to form a monatomic Cl^+ cation, which attacks the oxygen atom on the BA to form a carbonyl group in BAD.³¹⁰ In addition, as it has been discussed in Chapter 4, section 4.3.2, BA could be oxidized by either Cl^+ , HOCl and Cl_2 active species.

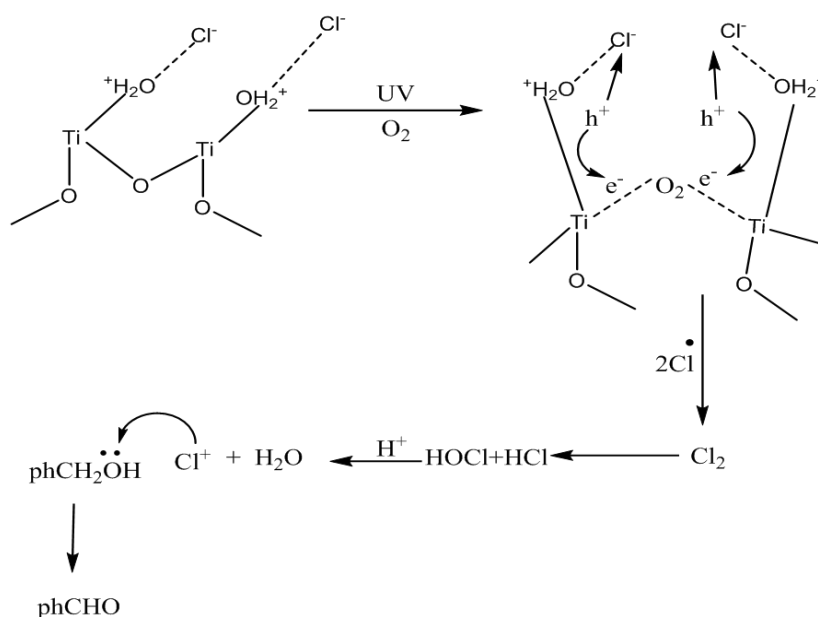


Figure 5.7 The mechanism of biphasic photocatalytic oxidation of BA in the presence of O_2 using TiO_2 under UV light.

It is important to note that primary alcohols are oxidized to the corresponding aldehydes and overoxidation to the corresponding carboxylic acid does not result at early of the reaction time. BA conversion, BAD selectivity and yield were evaluated by the following equations

$$\text{BA conversion} = \frac{\text{mole of inlet BA} - \text{mole of outlet BA}}{\text{mole of inlet BA}} \times 100 \%$$

$$\text{BAD selectivity} = \frac{\text{mole of outlet BAD}}{\text{mole of inlet BA} - \text{mole of outlet BA}} \times 100 \%$$

$$\text{BAD yield} = \frac{\text{mole of outlet BAD}}{\text{mole inlet of BA}} \times 100 \%$$

5.3.6 Change in Concentration of Reactants and Products

Photolysis reaction (without catalysts) showed negligible conversion (<2%) of BA after 4 h of illumination time without any production of BAD which indicates that the light without catalysts has no significant activity towards photooxidation process.

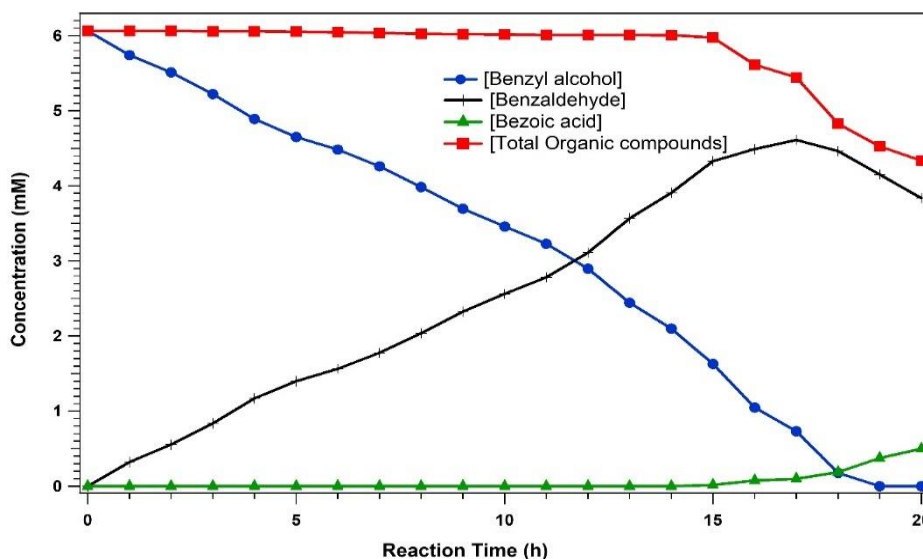


Figure 5.8 The change in concentration of the reactants (BA) and the products (Benzoic acid and BAD) through a 20 hour reaction period.

The changes in concentrations of the reactant (BA) and products (BAD and benzoic acid) were monitored over 20 hours of illumination (Figure 5.8) in the photocatalytic oxidation. The concentration of the BA reduced while the BAD increased steadily over the 20h period. Apart from BAD as the desired product, other organic compounds including benzoic acid and CO₂ gas were produced by the reaction and reported in the literature.³⁰⁵ Other by-products of photocatalytic oxidation of BA to BAD, include hydroxylated and aliphatic compounds.^{305,363} Therefore, it was important to monitor the concentration of BA and BAD along with benzoic acid and total organic compounds during the photocatalysis of BA.

The concentrations of benzoic acid and total organic compounds remained constant for the first 16 hours. After this, (16h - 20h) there was a slight increase in the

concentrations of benzoic acid and a decrease in total organic compounds. This could be attributed to the decrease of BA concentration and therefore BAD started to be oxidized to benzoic acid and then to benzyl benzoate,³⁶⁴ add to that the loss of some solution during the reaction and detection process.

Furthermore, the conversion rate of BA (%), the selectivity and the yield of BAD was monitored over the same 20h period (Figure 5.9). BA exhibited a steady increase in the conversion rate up to 100 % after 20h of illumination with a constant high selectivity BAD was observed in the beginning and started decreasing at 16 h. A maximum yield of benzaldehyde (74%) could be achieved with the unprecedented ~ 90% selectivity after 17 h.

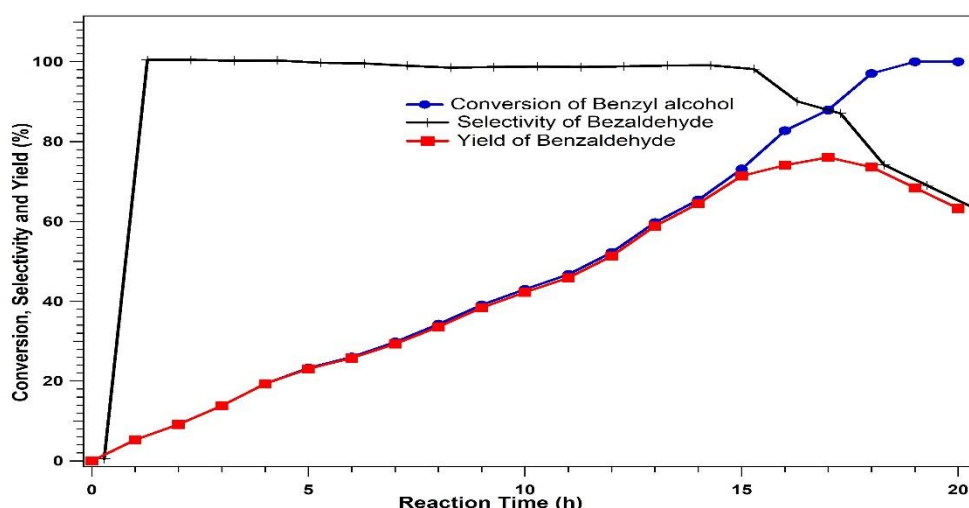


Figure 5.9 The change in percentage conversion of BA, yield and selectivity of BAD through a 20-hour photocatalysis period.

Interestingly, during the last 5 hours BAD selectivity as well as its yield, both started dropping down while BA conversion still increasing. This could be attributed to the saturation BAD and the oxidation of BAD.

5.3.7 Effect of Phenyl-Ring Substitution on BA

The effect of phenyl-ring substitution (substitutions at para-p, meta-m, or ortho-O position) on the photocatalytic oxidation of BA was investigated. Benzyl alcohol and

its derivatives substituted by $-\text{OCH}_3$, $-\text{CH}_3$, $-\text{NO}_2$, $-\text{Cl}$, $-\text{F}$, and $-\text{Br}$ groups were converted to corresponding aldehydes with high conversion and high selectivity on TiO_2 . However, the reaction times needed to achieve 50% conversion of alcohol less in the order $-\text{H} > -\text{CH}_3 > -\text{OCH}_3$, while time was longer from $-\text{H}$ to $-\text{NO}_2$. This order reveals that the reaction rate is enhanced by electron-donating substituents and decelerated by electron-withdrawing substituents. This result suggests that the substituent groups play a crucial role wherefore, the influence of the substituent group on the rate of photocatalytic oxidation of aromatic alcohols can be interpreted in terms of Hammett's relationship.³⁶⁵ The relationship between the reaction constants (k) of BA and its substituent constants (σ) was plotted. The data displays a strong linear trend, as indicated by the solid line shown in Figure 5.10, confirming the Hammett relationship (Equation 5.15). There was an inverse linear relationship between $\text{Log } (k_x/k_H)$ and σ ($\rho = -0.11$). A negative Hammett ρ value is attributed to a developing positive charge on the benzylic carbon, and that has commonly been observed for the alcohol oxidation reactions. On the other hand, large positive ρ values have been reported for enzymatic oxidation reactions of benzyl alcohols and amines, when both carbons from carbonyl and imine on the transition state have been involved.³⁶⁶ there was a linear relationship for free energy. Thus, the selective photocatalytic oxidation of BA to BAD was governed by the Hammett relationship. According to the Hammett rule as σ_x increases, $\text{Log } (k_x/k_H)$ decreases linearly.³⁶⁷⁻³⁶⁹ Hammett study was performed for primary benzyl alcohol.

Within Equation 5.18, σ_x is the Hammett substituent constant and ρ is the reaction constant.

$$\log \frac{k_x}{k_H} = \rho \sigma_x \quad (\text{Eqn 5.15})$$

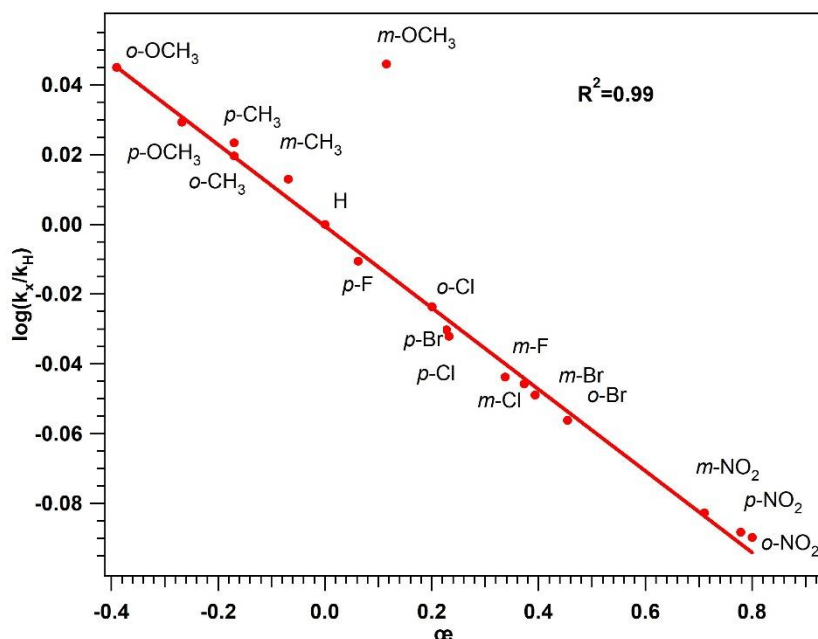


Figure 5.10 A Hammett plot for the oxidation of BA to BAD. Y-axis is the Log (k_x/k_H) while X-axis is the σ is the substituent constant.

The Hammett rule describes the influence of the substituent group on the kinetic constant of partial oxidation of aromatic alcohols to aldehydes. This is based on the assumption, that the electronic properties of the substituent groups are of significant importance than their relative solubilities in the reactant-product mixture. Hammett constants derived from substituents at meta position (σ_m) of the phenyl-ring result in inductive effects due to the movement of electrons via the σ -framework. At para position (σ_p), it results in both inductive and resonance effects due to the movement of electrons in the σ - and π -frameworks. Both meta- and para-substituted phenyl-rings show electrophilicity, and hence a higher reactivity than ortho-substituted phenyl-ring.^{370,371}

The strongly proportional relationship shown in Figure 5.10 confirms the greater influence of the electrophilic nature of the substituent, on the rate of photocatalytic partial oxidation of BA to BAD. However, constituents induce different degrees of electrophilicity and hence photocatalytic reactivity. In the present study, the nitro group in the BA exhibited the lowest while the methoxy group exhibited the strongest

electrophilic effect. Halide substituents such as bromide, chloride, and fluoride exhibited intermediate electrophilicity with fluoride and bromide substituents in the phenyl-ring resulting in the highest and lowest rate constants, respectively.³⁷¹

5.4 Conclusion

Organic synthesis is an important step in the production of crucial compounds especially, aldehydes and ketones. Enthused by the principles of green chemistry, the present study evaluated the efficiency of the photocatalytic oxidation of BA to BAD using a TiO_2 photocatalyst and Cl^- ion as a radical mediator in a biphasic reaction method. From the literature review, it appears that the photocatalytic oxidation of BA to BAD using TiO_2 as a photocatalyst has many factors requiring optimization.

The process conditions, including CHCl_3 /water volume ratio, TiO_2 concentration, pH, and acid types, significantly affected the reactivity and the conversion of BA and the selectivity to BAD. In general, increasing the TiO_2 increased the activity until reaching the optimal concentration, and then the reactivity decreased. The (40/60) CHCl_3 /water volume% ratio and low pH in the range of 1-3 were found to be most effective for TiO_2 reactivity. Using only NaCl as a chlorine source without acid, resulted in poor TiO_2 reactivity as it gave neutral conditions. Lower pH alternately achieved using acids such as H_2SO_4 , HCl, and HNO_3 with varying reactivities. The acid-dissociated SO_4^{2-} species behaved as $\text{HO}\cdot$ radical scavengers, reducing the reactive hydroxyl radical and producing the weak SO_4^{2-} species. The selective photocatalytic oxidation of BA to BAD was also found to be governed by the Hammett rule, where the reaction constants (k) were inversely related to the Hammett constants of its derivatives (σ).

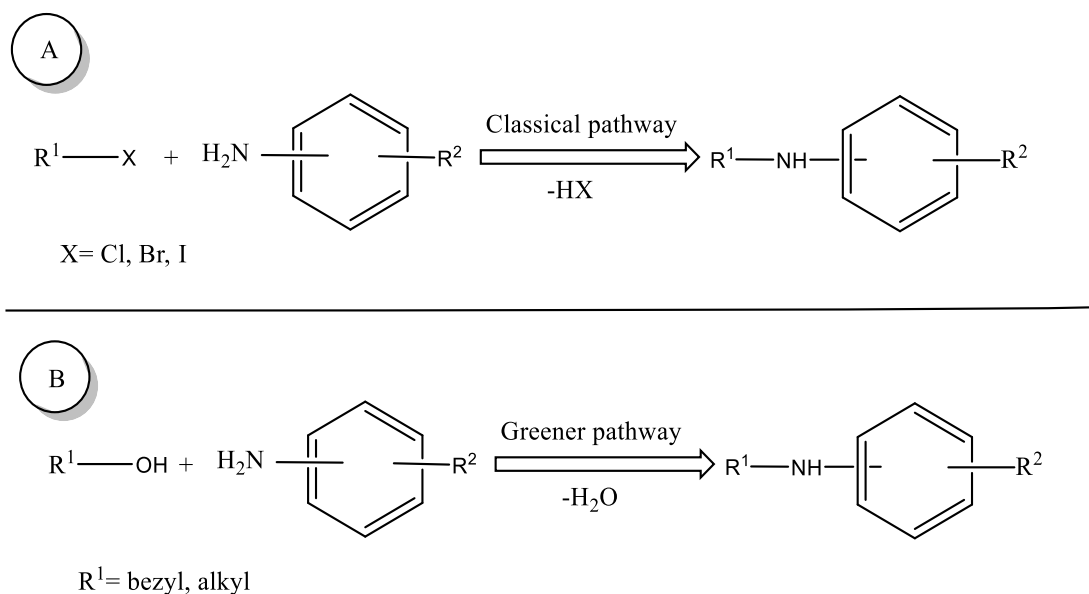
CHAPTER 6 Photocatalytic N-alkylation of Amine with Alcohol

Previous attempts of N-alkylation amines have used transition-metal catalysts in a reaction-cycle concept termed hydrogen autotransfer. This study investigated the feasibility of photocatalysis as an alternative greener process for the N-alkylation of amines. TiO_2 -P25 was used to catalyse the photocatalytic oxidation of benzyl alcohol (BA) into benzaldehyde which reacts with aniline to form imine intermediate product. Gas Chromatograph equipped with Flame Ionized Detector (GC-FID) was used to monitor the reaction progress. Optimization experiments were performed, where a pH 2 was determined to be the optimal condition for the oxidation of BA. The addition of aniline during the reaction using a liquid pump at a flow rate of 0.622 g min^{-1} was used to feed aniline with gradually increase the concentration to match up the rate of BA oxidation. This overcame a reaction limiting protonation of aniline under the acidic condition to produce higher yields of benzylideneaniline intermediate. Finally, by directly injecting H_2 gas into the reaction mixture, the final benzyaniline product was obtained. This is the first report to demonstrate the photocatalytic N-alkylation of an amine using a TiO_2 photocatalyst. Optimization of the reaction conditions described here could provide a large-scale green alternative method for the N-alkylation of amines at industrial levels.

6.1 Introduction

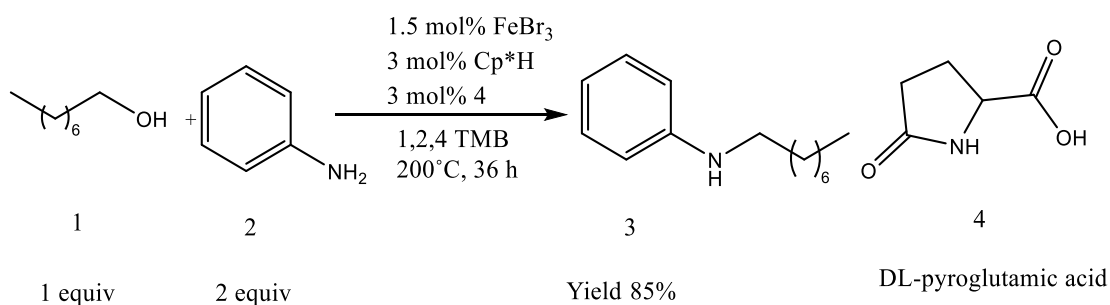
Amines are the organic molecules containing a carbon-nitrogen bond (C-N) and are typically considered to be aliphatic and aromatic derivatives of ammonia. Their acidity and basicity can be manipulated to facilitate the organic synthesis of many drug classes, with a vast majority of drugs containing at least one nitrogen atom.^{372,373}

Typical methods used to synthesize amine compounds include electrophilic alkylation,³⁷⁴ reductive alkylation³⁷⁵ and amination of aryl halides.^{373,376}



Scheme 6.1 C-N bond formation by different methods. A) Traditional method including alkyl halides and B) Greener pathway by borrowing hydrogen.

The atomic-efficient formation of carbon-nitrogen bonds is a crucial stage in the synthesis of the abundance of compounds typically used in life sciences and the chemical industry.³⁷⁷ There are a variety of powerful methods that approach the synthesis of amines because of the importance of these substances. For example, Ullmann reactions³⁷⁸ and hydroaminations³⁷⁹ classic nucleophilic substitutions, as well as Buchwald–Hartwig.³⁸⁰ Most of these more complicated procedures involve catalysts that are focused on particular complexes of (noble metals). While these strategies have shown their efficacy in many cases, they also suffer from the co-production of large quantities of undesired products or waste.¹⁴⁴ which means, these approaches contravene the principles of green chemistry in organic synthesis, because excessive alkylation, which generates large quantities of chemical wastes from the pharmaceutical and chemical industries (Scheme 6.1).³⁸¹

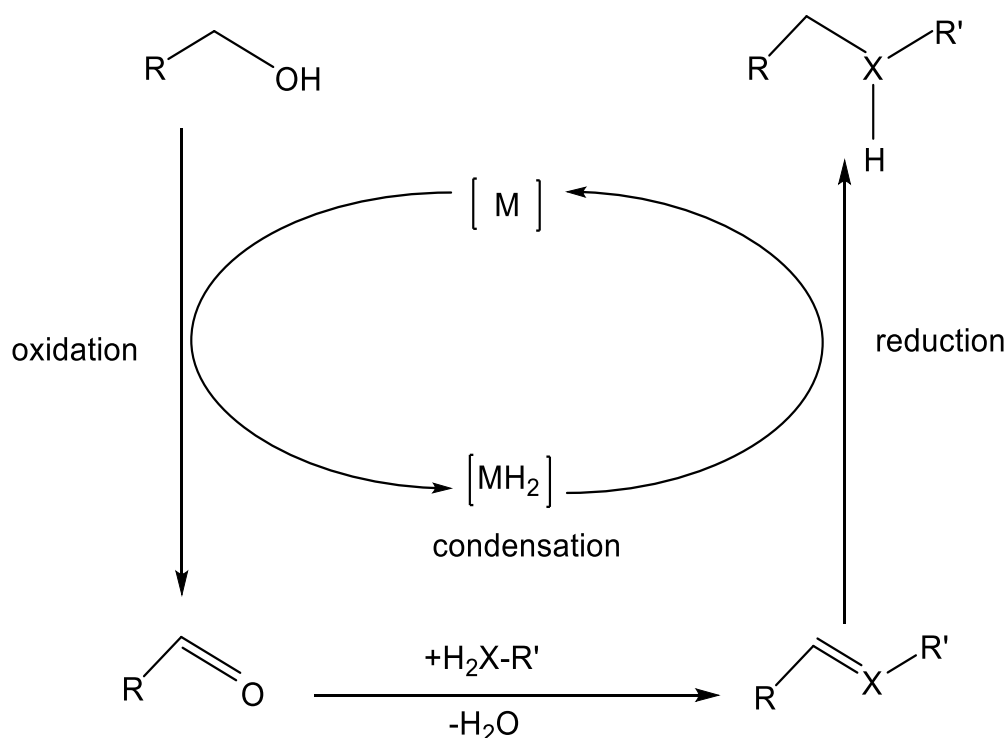


Scheme 6.2 Alcohol N- alkylation using an iron catalyst. Cp*H=1,2,3,4,5-pentamethylcyclopenta-1,3-diene. 1,2,4-TMB = 1,2,4-trimethylbenzene.

In 1901, aniline alkylation with sodium alkoxides was identified.³⁸² This is the first amine-alcohol coupling and reveals that alcohol amination does not actually require a transition metal catalyst.³⁸³ Furthermore, N-alkylation reactions of alcohols could be acid catalysed. These aminations of S_N (a nucleophilic substitution reaction) type alcohol usually involve benzylic, propargylic, or allylic alcohols.³⁸⁴ A very recent example, however, reveals that even non-activated alcohols such as 1-octanol (1) can also be converted to N-alkyl anilines (3) with aniline (2) in good yield³⁸⁵ as shown in Scheme 6.2 Although the temperature of the reaction is high (200° C), some allylic alcohols were successfully converted at 100°C.

This has been solved following the discovery of so-called borrowing hydrogen (BH) or hydrogen autotransfer (HA) methodologies have been established to address this limitation and allowing for more efficient production of amines from alcohols.³⁸⁶⁻³⁹² The terms borrowing hydrogen and hydrogen autotransfer refer to the fact that hydrogen is "borrowed" and "auto" converted to the modified (aminated) aldehyde or ketone by the catalyst. The mechanism of this system is connected to a reaction of transition hydrogenation but has a significant advantage. The oxidised alcohol is no longer waste, but serves as a substrate, as opposed to the hydrogenation of an imine using alcohol as a hydrogen donor. A far higher atomic economy is then achieved.³⁹³ This strategy is based on the borrowing hydrogen (BH) from the activation/oxidation

of the alcohol substrates. The borrowed hydrogen will be used in the reduction of imine which produces water as the only by-product. In principle, the ultimate transition requires a reductive amination as one step. By comparing reductive amination and alcohol amination, it should be remembered that, due to the high concentration of the reactive aldehyde, side reactions, such as aldol condensation, can easily occur in reductive amination. Instead, by using alcohols by borrowing hydrogen, the resulting aldehyde is only present in small quantities, as it is produced and consumed in situ, so that certain side reactions can be reduced.³⁸⁹ Transition metal compounds, such as rhodium (Rh),³⁹⁴ iridium (Ir),³⁹⁵ and ruthenium (Ru),³⁹⁶ used for the N-alkylation of amine with alcohol, must be active for the oxidation of alcohol, and more importantly, be able to store atomic hydrogen atoms for a delayed reduction of imine. Ruthenium compounds exhibited the best performance in this catalytic process.³⁹⁴ The BH process using ruthenium compounds was optimized further by examining the effect of changing the selectivity of amine and alcohol on the overall yield. For instance, a study by Watanabe *et al.* reported that the N-alkylation of aniline 2 with simple alcohol such as ethanol, 1-butanol, and benzyl alcohol using ruthenium catalysts ($\text{RuCl}_2(\text{PPh}_3)_3$), the reactions were carried out efficiently to provide *N,N*-di-substituted aniline in good yield while methanol showed low yield. Aniline conversions were low and only *N*-monoalkylated anilines were obtained at low yields when secondary alcohols, such as 2-propanol and 2-butanol, were used. Therefore, primary alcohols other than methanol are productive for the present reaction.³⁹⁷

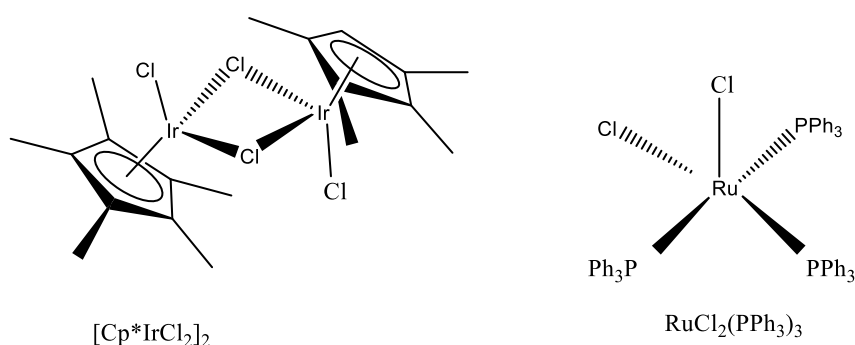


Scheme 6.3 The mechanism of hydrogen autotransfer; X= CH, N; [M] = transition-metal catalyst.

There has been a growing interest in understanding the mechanism of alkylation of amines catalyzed by a transition metal compound. The mechanistic concept termed “hydrogen autotransfer” has been proposed as the novel mechanism.^{373,386,398,399} The details of the N-alkylation with the hydrogen autotransfer mechanism is illustrated in Scheme 6.3. In this mechanistic concept, the selected alcohol initially undergoes catalytic oxidation (by a transition-metal catalyst) to its corresponding aldehyde analogue, which combines with an amine by a condensation reaction to form an imine intermediate (a nitrogen analogue of aldehydes containing a C=N bond). The amine subsequently undergoes reductive hydrogenation to form the final alkylated amine product.³⁹⁹

In the hydrogen autotransfer mechanism, the hydrogen atom abstracted from an alcohol molecule by a transition-metal catalyst (to form an aldehyde) is restored in the final product. The temporary abstraction of hydrogen activates alcohol as an

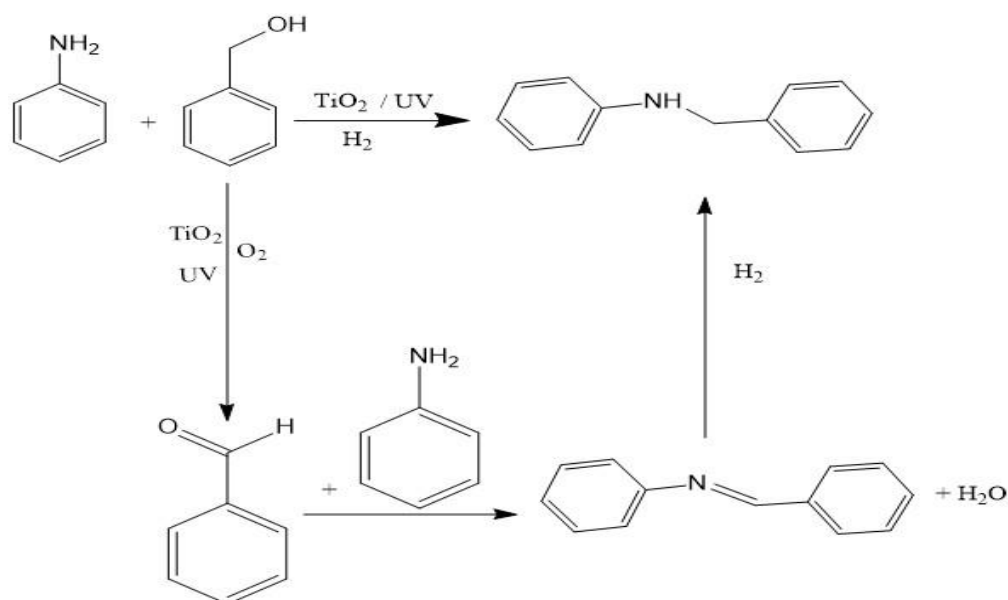
alkylating agent.³⁸⁶ Ruthenium which is the most frequently studied transition-metal catalyst for N-alkylation of amines has been regarded as superior due to its putatively high yields.^{386,398} However, alternative transition metal catalysts have been proposed including iridium, which has been used to produce N-benzylaniline with yields as high as 94%, when the $[\text{Cp}^*\text{IrCl}_2]_2$ complexes were used.^{400,401} here, Cp is the abbreviation for Pentamethylcyclopentadiene (Scheme 6.4).



Scheme 6.4 Chemical structure of two transition-metal complexes catalyst for N-alkylation of amines.

Other metal catalysts including copper (Cu)⁴⁰² cobalt (Co),^{399,403} have also shown high yields to catalyse N-alkylation of amines by alcohol. However, these transition-metal catalysts require high temperatures for extended periods and therefore, which contravenes the principle of designing energy-efficient syntheses routes in green chemistry. This principle requires running reactions at milder temperatures to improve energy efficiency and product selectivity. More importantly, these catalysts are relative expensive with limited stability at high temperature. Thus, further optimizations are warranted to ensure a green N-alkylation of amines by alcohol, ideally at low temperature with relative stable catalysts at low cost. The present study aims to develop a room temperature TiO_2 photocatalytic process for the effective synthesis of benzylaniline by N-alkylation of aniline by benzyl alcohol (Scheme 6.5). The N-alkylation of aniline by benzyl alcohol reaction was performed in

this study through three stages; benzaldehyde was formed as it is discussed in chapter 5, by photooxidation BA. Next, producing the intermediate imine (BDA) by adding aniline after benzaldehyde was formed. Finally, the final product (benzylaniline) was produced after applying H₂ gas to the reaction and reduce of the intermediate (BDA).



Scheme 6.5 Photocatalytic N-alkylation of aniline with benzyl alcohol under various conditions.

The use of photocatalysis for the synthesis of benzylaniline has been investigated, and the photocatalyst P25 was chosen for N-alkylation of aniline by benzyl alcohol. The major downside of the previously studied transition-metal catalytic complexes would be resolved under photocatalytic conditions, as the reaction would not operate for a long period of time under a high temperature. Thus, an alternate method that is more in keeping with the concepts of green chemistry is proposed.

6.2 Experimental

6.2.1 Materials

TiO₂ (Aeroxide® P25; formerly Degussa P25), which consists of a mixture of two phases (~75% anatase and ~25% rutile) was commercially obtained from Evonik

Industries (Goldschmidtstr, Germany). Dry magnesium sulfate (62-70%), sodium hydroxide pellets (of 99 % purity), and sodium chloride (of $\geq 99.5\%$ purity) were commercially obtained from Fischer Scientific (Loughborough, UK). N-benzylideneaniline (of 99% purity), aniline (of 99.8% purity) and benzyl alcohol (of 99% purity) were commercially obtained from Acros Organics or Fisher Scientific Bvba (Geel, Belgium). N-benzylaniline, benzaldehyde (of $> 99\%$ purity) dichloromethane (CH_2Cl_2) (99+%), and 32 % aqueous hydrochloric acid were commercially obtained from Sigma-Aldrich (Dorset UK). N-octadecane (of 99 % purity) was purchased from BDH (British Drug Houses) chemicals (Poole Dorset, UK). Deionized water was prepared in the laboratory using the Suez/Purite Select deionization unit. O_2 , H_2 and N_2 gases of $\geq 99\%$ purity were commercially obtained from BOC gases Ltd. (Middlesbrough, UK). Philips CDM-T Halogen 150W Metal Halide Lamp was obtained commercially obtained from Philips Centre (Guildford, UK). The gearbox used was purchased from the LED group Robus, and the Watson-Marlow peristaltic pump model 501U was sourced from Watson-Marlow Fluid Technology Group.

Gas chromatography analysis was performed using Perkin Elmer Gas Chromatograph equipped with Flame Ionized Detector (GC-FID), The dimensions of the polar column used were $30\text{ m} \times 0.53\text{ mm} \times 1\text{ }\mu\text{m}$. The samples to be analyzed were injected manually into the FID. Injection aliquots of $0.4\text{ }\mu\text{L}$ were used for the analysis of the standard solutions, aniline and benzyl alcohol in reaction samples. A larger injection volume of $1.2\text{ }\mu\text{L}$ was used for the analysis of the benzylideneaniline and benzylaniline, which were anticipated to be present in small quantities. The injector carrier gas used was H_2 , which was delivered at a flow pressure of 20 psi. The injector was maintained at a temperature of 250°C . The analysis was performed at a retention time of 130 seconds. GC temperature was 165°C .

6.2.2 Photocatalytic Reactor Design

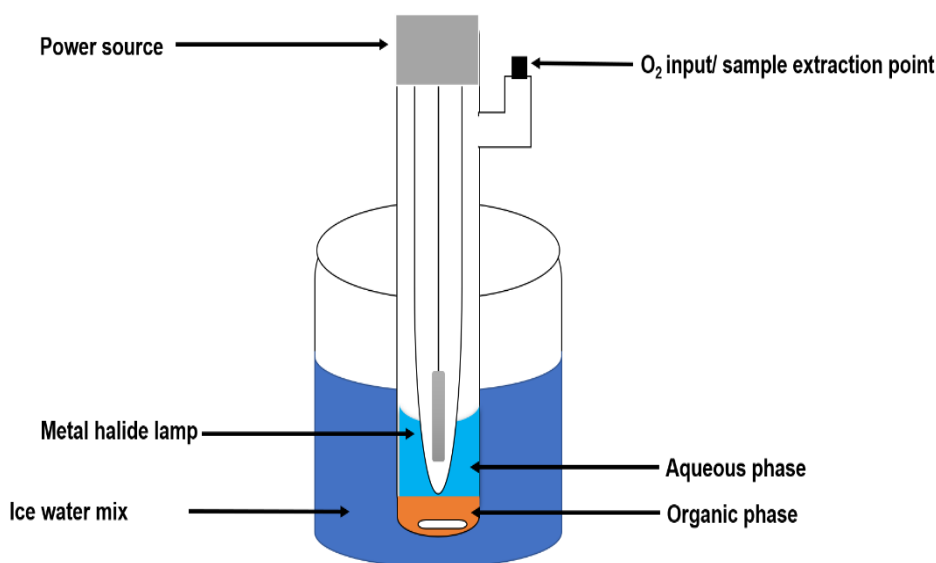


Figure 6.1 A photocatalytic reactor design. The metal halide lamp is enclosed in a water-cooled inner jacket.

A customized photocatalytic reactor was used (Figure 6.1). The metal-halide lamp was jacketed with water in a tube, which was then placed in the reaction flask with an outlet (to allow direct insertion of a metal tube inlet into the reaction mixture) and double inlets on the side. The first inlet allowed the pumping of O₂ gas into the reaction mixture and as a sample extraction point while the second inlet was used to supply a mixture of H₂ and N₂ gases and insertion of the silicone tube (2m x 3.5 mm) for the delivery of the aniline solution. A reflux condenser was fitted to the outlet of the reaction flask to prevent solvent evaporation.

6.2.3 Bi-phasic Photocatalytic Reaction System

A biphasic reaction system was used throughout this experiment with the organic phase containing a mixture of equimolar (7 mmol) solutions of benzyl alcohol (0.75 mL,) and aniline (0.65 mL,) in dichloromethane (12 mL) as a solvent. Aniline, an amine; was chosen because of its high chemical stability in the organic phase due to its

relatively large molecular weight and aromaticity. Dichloromethane was a suitable solvent as it allowed efficient separation of chemical species in the GC-FID spectra. The aqueous phase, on the other hand, contained NaCl (0.15 g) and the TiO_2 catalyst (0.075 g) dispersed in deionized water (18 mL). These biphasic reactants were transferred into a reaction flask (in the photocatalytic reactor), where it was stirred gently in the presence of O_2 gas and UV light from the metal-halide lamp for 60 minutes. The temperature of the reaction mixture was controlled using the water jacket surrounding the metal halide lamp and ice-water outside the reaction flask. Using a syringe, samples were drawn from the organic layer of the reaction mixture at 15 min regular time interval and immediately analyzed with GC-FID to monitor concentration changes in the reactants and products. The initial reaction conditions (a neutral pH and a mol ratio of 1:1 between reactants), there was no benzyaniline peak was detected. Therefore, benzylideneaniline (BDA) intermediate was used instead to measure the reaction progress.

6.2.4 Effect of pH

The effect of pH was monitored for the purpose of optimization of the reaction. The reactants were acidified using drops of 32% HCl to desired pH values of 1, 2 and 3. Alkaline conditions until pH 11 were achieved by the dropwise addition of NaOH. The optimized pH conditions were used to carry out the reaction.

6.2.5 Effect of Aniline Concentration

Using the optimized pH condition, the photocatalytic reaction was further optimized using the concentration of the reactant (aniline). However, aniline was added periodically to the reaction mixture during. At this point, the organic phase contained only 0.75 mL of 7 mmol benzyl alcohol diluted in 12 mL dichloromethane. A solution containing 0.65 mL of 7 mmol aniline in 10mL dichloromethane solvent was prepared

separately and 2.5 mL aliquots added the reaction mixture at an interval 15 minutes while withdrawing samples of the organic layer at the same time. Alternatively, the aniline solution was added to the reaction mixture quantitatively and autonomously at different rates using a liquid pump. The organic layer was drawn from the mixture at 15-minute time intervals to allow the determination of BDA yield. Sample injection rates were first calibrated by measuring the mass of water delivered into a beaker over a period of 1 minute (gmin^{-1}) at different injection rates as dispensed from the liquid pump.

6.2.6 Effect of Hydrogen Injection Rate

The effect of injecting hydrogen into the reaction mixture was also investigated. The hydrogen gas was mixed with a diluent (nitrogen gas) in a ratio of 1:2. The reaction mixture as previously setup and optimized sample injection rate of 0.676 gmin^{-1} as determined previously. The organic layer was drawn at 15 min interval, where they were analyzed through the GC-FID to determine the yield of BDA and benzyaniline. A higher GC-FID temperature of 185°C was used to allow discrimination between the BDA intermediate and the benzyaniline product.

6.2.7 Effect of Injecting Large Volumes of Aniline Solution

The effect of larger solutions of aniline during the reaction was further investigated. A stock solution of aniline (200mL) at the same concentration as the fixed volume solution used previously was prepared. The reaction was carried out as outlined in section 6.2.5, using a liquid pump to smoothly inject aniline solution to the reaction mixture during the 1-hour reaction period. This allowed the comparison of the BDA yield between fixed volume aniline solution and gradual delivery method.

6.3 Results and Discussion

6.3.1 GC-FID Analysis

Chemical constituents of the organic layer of the reaction mixture including benzyaniline as the final product along with by-products (aniline, BA, and BAD) and the intermediate BDA were monitored with GC-FID. The GC-FID data below (Figure 6.2) was interpreted qualitatively based on calibration peaks of known standard solutions for each chemical species.

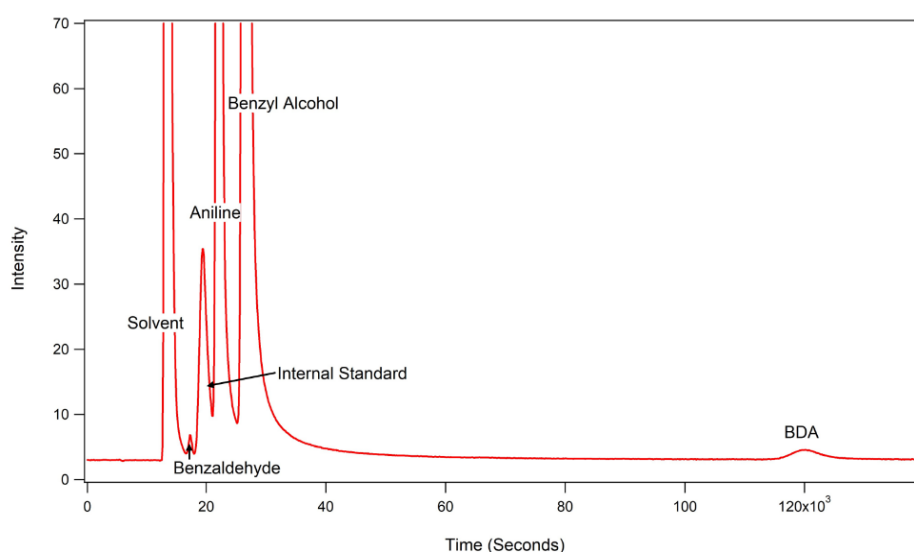


Figure 6.2 A typical GC-FID spectrum of the sample from the organic layer during the reaction.

For quantitative investigations of the above chemical species, octadecane was used as the internal standard. The response factor is calculated using Equation 6.1 with peak intensities obtained from control mixture.

$$RRF = \frac{H_x}{H_{IS}} \times \frac{[IS]}{[x]} \quad (\text{Eqn 6.1})$$

Where RRF is the relative response factor; H_x is the peak height of the chemical species of interest; H_{IS} is the peak height of octadecane; $[IS]$ is the concentration of

the octadecane as the internal standard; $[x]$ is the unknown concentration of the chemical species of interest.

The ratios of peak heights of the unknown chemical species to that of the internal standard; and then divided by the concentration of the standard were calculated. These values were used to generate a calibration curve by plotting on the y-axis against the concentrations of known chemical standards on the x-axis. The gradient of the curve was the RRF. Equation 6.2 below was used to calculate unknown concentrations of the chemical species by substituting RRF and R. The relative yield of the benzyaniline product was determined by predicting a position of 100% yield of the BDA intermediate or benzyaniline product within the calibration graphs. This was used to calculate the yield according to Equation 6.3. Thus, by using a known concentration of the internal standard, it was possible to determine the concentrations of benzyaniline as the final product along with by-products (aniline, BA, and BAD) and the intermediate BDA.

$$[x] = \frac{R}{[IS]} \times \frac{RRF}{1} \quad (\text{Eqn 6.2})$$

Where R is the ratio of a chemical species peak height to the peak height of the internal standard. The yield of the reaction is defined as the ratio of the product concentration and the initial reactant concentration, calculated following Equation 6.3:

$$\% \text{ Yield} = \frac{C_p}{C_0} \times 100 \quad (\text{Eqn 6.3})$$

Where C_p is the concentration of the products of interest; and C_0 is the initial concentration of the benzyl alcohol.

6.3.2 Analysis of the Initial Reaction

Running the photocatalytic reaction initially at a neutral pH, a mol 1:1 ratio of BA and aniline were confirmed to be present in the organic phase at an equimolar quantity of 7mmol. Peaks of the benzaldehyde and BDA intermediate were detected, which confirmed that the oxidation and condensation steps proceeded under TiO₂-mediated photocatalysis according to the hydrogen autotransfer concept. However, benzyaniline as the final product was not observed indicating the insufficiency of the liberated H₂ (within the reaction mixture) to drive the final reduction step via hydrogenation across the C=N double bond to form an amine. The scope of the investigation was changed to monitor the rate of reaction using the BDA intermediate due to the lack of the final benzyaniline. The initial reaction rate was $5.0 \times 10^{-5} \text{ M min}^{-1}$, with a BDA yield of 0.84%. These initial findings demonstrated that N-alkylation of an amine was possible under TiO₂-mediated photocatalysis. However, the poor reaction rate and BDA yield initially observed warranted optimization of the photocatalytic reaction conditions.

6.3.3 pH Optimization

The optimal pH for the photocatalytic reaction was investigated by adjusting using 32% HCl and NaOH. From high pH to the acidic condition, the reaction rate increases and reaches the highest rate at pH of 2 ($10.0 \times 10^{-5} \text{ M min}^{-1}$); which declined upon a further decrease in pH (Figure 6.3A). Similar behaviour was also observed for the BDA yield with its maximum of ~1.8 % (Figure 6.3B) at pH=2. The similar trend between the reaction rate and BDA yield suggests that there is no significant side reaction appearing as the change of reaction pH conditions.

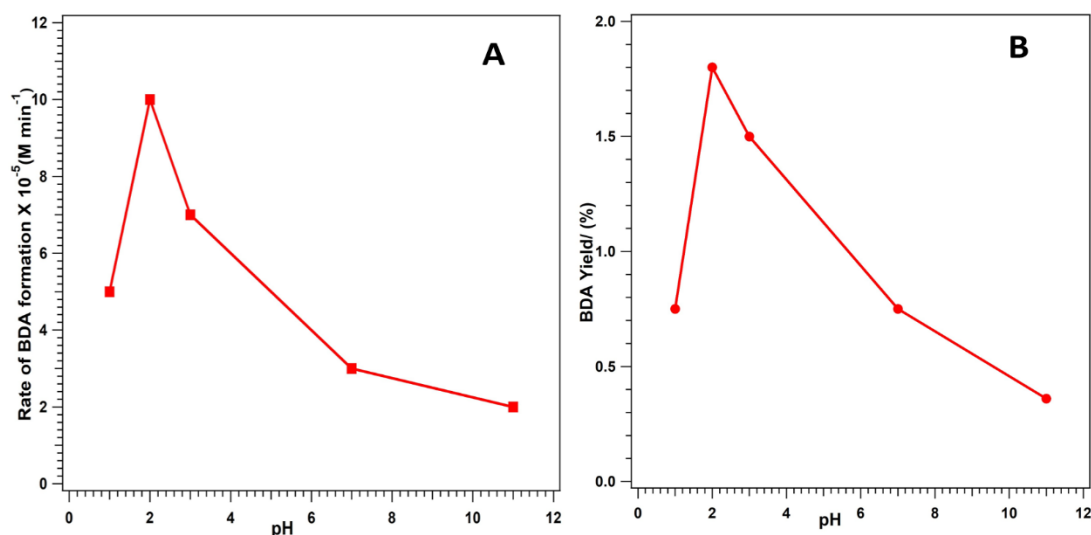


Figure 6.3 (A) Rate and (B) yield of BDA formation at different pH values.

Clearly, the photocatalytic reaction proceeds optimally under acidic conditions, with reaction rate being five times higher than at alkaline pH. It is possible that acidic pH promotes either an oxidation reaction to produce benzaldehyde or condensation reaction to produce BDA intermediate. However, it was clarified that acidic conditions actually favour BA oxidation to form benzaldehyde under enhanced TiO_2 -mediated photocatalysis in chapter 5. Therefore, the rate of intermediate formation is seen to increase to pH 2 optimisation under acidic conditions. This was due to the higher concentration formed in the initial oxidation reaction, which then undergoes a condensation reaction to form the intermediate BDA with aniline.

6.3.4 Effect of Aniline Concentration/Amount

Having optimized the reaction pH (pH 2), the effect of changing the ratio of the reactants (aniline: BA) was also considered for optimization. The experimentally observed relationship between the BDA formation rate and aniline concentration is shown in Figure 6.4A. The optimal reaction rate ($10.0 \times 10^{-5} \text{ M min}^{-1}$) was achieved when aniline quantity was $\sim 7.0 \text{ mmol}$. Further increase in the concentration of aniline resulted in a decline in the reaction rate. The optimal aniline quantity ($\sim 7.0 \text{ mmol}$)

gave a BDA yield of ~1.8 % which is over 3x more than that at an aniline quantity of 14 mmol with a yield reported here of 0.44% (Figure 6.4B).

Clearly, the variation of aniline concentration relative to BA has a significant effect on the TiO_2 -mediated photocatalysis. An upward trend in both the reaction rate and BDA yield was observed when the quantity of aniline was increased from 0.0 to 7.0 mmol. A further increase in aniline quantity resulted in a downward trend. The optimal 7.0 mmol indicates the establishment of equimolar reactants (1:1 molar ratio).

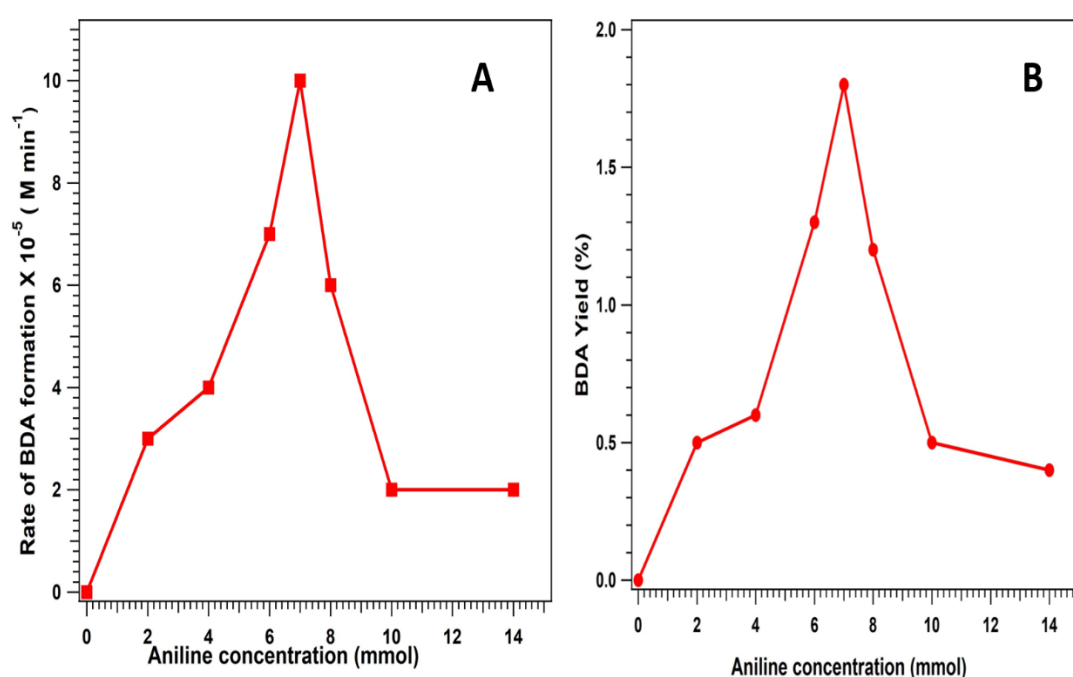


Figure 6.4 (A) Rate and (B) yield of BDA formation against aniline quantity.

With a further rise in aniline quantity above a ratio of 1:1 with benzyl alcohol, a relationship suggestive of a change to benzyl alcohol being the limiting reactant is expected to be observed. A plateau of the reaction rate graph at a quantity that brings the aniline in excess of the benzyl alcohol would explain this. However, this is not observed, but the negative relationship with additional aniline quantity to the rate of reaction suggests a dynamic within the reaction. Therefore, understanding and

overcoming this limiting effect is necessary for the photocatalytic reaction to be further optimized. Further research has been performed to further understand the dynamics at play with aniline. Similarly, to the previous study in which the ratio of aniline: benzyl alcohol was changed by adjusting the amount of aniline present in the reaction mixture, the quantity of aniline is changed but continuously during one reaction run. Therefore, this approach would allow for closer observation of the dynamics of aniline within the reaction mixture than before. During one reaction, changing the aniline concentration will provide data on how aniline acts dynamically.

Interestingly, the effect varying aniline quantity relative to BA on the TiO_2 -mediated photocatalysis to produce BDA was investigated by monitoring BDA yield. There was a linear relationship between aniline quantity and BDA yield (Figure 6.5). This was inconsistent with the earlier demonstration where a negative relationship was observed.

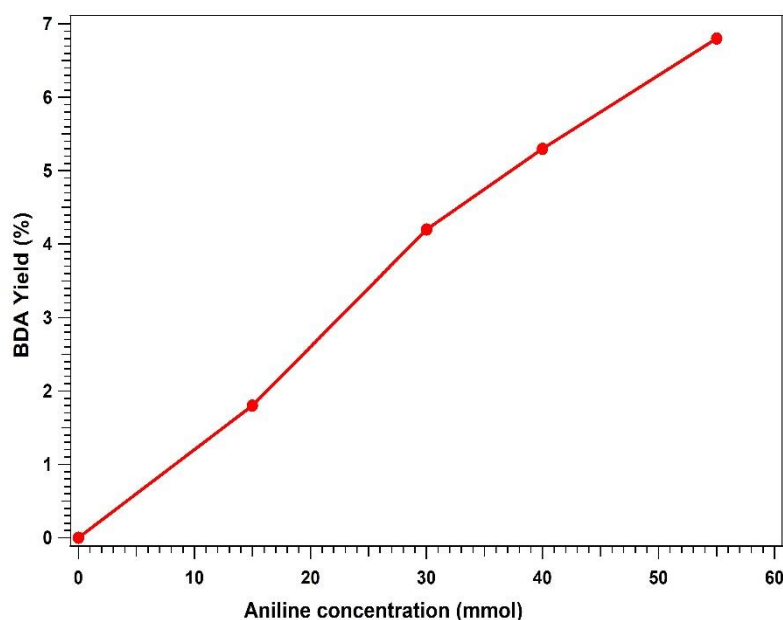


Figure 6.5 The yield of BDA (vs BA) against the injected aniline throughout the reaction period.

In the previous investigation where aniline was added initially, its dynamic acted as a limited factor. Alternatively, the addition of aniline to the reaction mixture following

the initial addition of BA appeared to alter the manner in which aniline reacts with benzaldehyde in the condensation step to form the BDA intermediate. This appears to have overcome the observed limitations of initial aniline addition. This indicated that aniline in the organic phase is unstable under acidic conditions (pH 2), and therefore, preferentially undergoes hydrophilic interactions towards the aqueous phase. By inspecting the GC-FID spectra, subjecting the equimolar reactants at a pH of 2, the 1:1 reactant ratio was not evident (Figure 6.6). The observed small aniline peak indicated a fraction of aniline was protonated and moved to the aqueous phase and therefore, reducing the amount available for reaction with benzaldehyde.

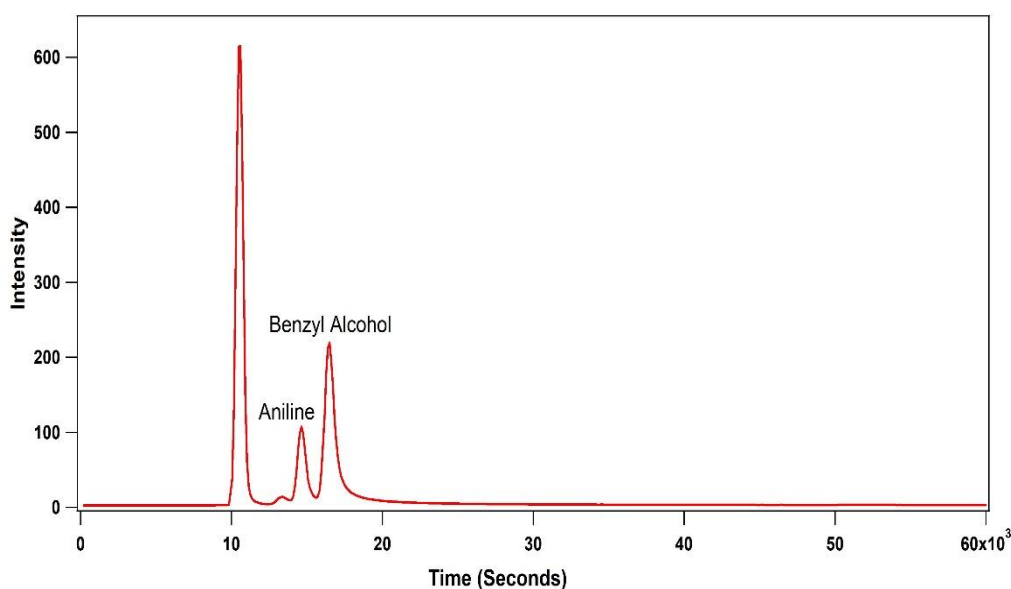


Figure 6.6 GC-FID data of the organic layer under acidic conditions.

As initially observed (Figure 6.4B), the negative relationship between aniline concentration and BDA yield could be due to the loss of aniline to the aqueous phase by protonation. The aniline protonation rate was faster than BA oxidation to benzaldehyde. This was because the aniline was first protonated to the aqueous phase instead of it undergoing a condensation reaction and could thus not react with benzaldehyde. This anomaly can be corrected by adding aniline during the reaction to allow time for the BAD to form. Next, the modality of adding aniline during the reaction

was optimized. 7 mmol aniline was added to the reaction chamber at a regular interval of 15 min during the reaction, with samples being drawn at the same time (Figure 6.7). Improved yield of 2.25% BDA was observed at 7 mmol of the aniline was added stepwise as the reaction proceeded.

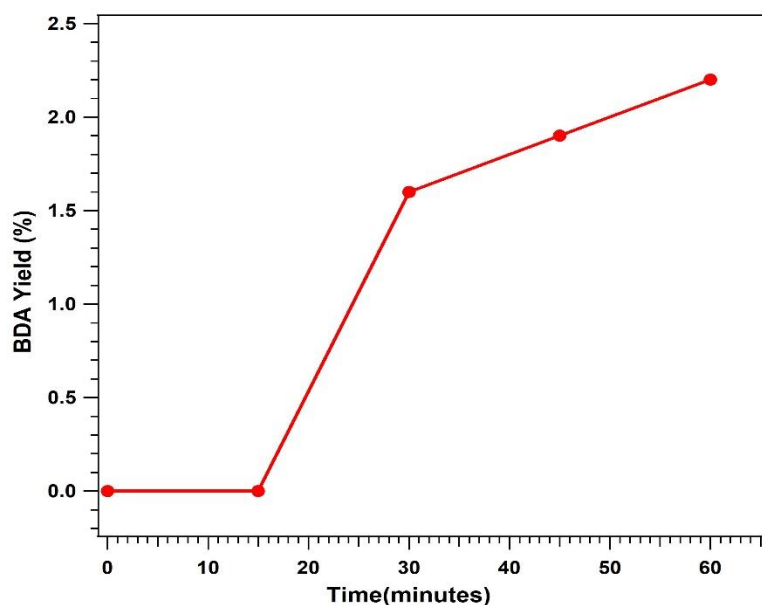


Figure 6.7 BDA yield when an aniline solution was injected autonomously.

This confirmed that the initial presence of aniline at prevailing acidic conditions favoured its protonation and subsequent loss to the aqueous phase, thus a reduced yield. However, the stepwise addition of aniline as demonstrated in the present study is qualitative as it lacks the quantitative aspect of the rate of aniline addition.

The quantitative aspect of aniline addition was developed to work autonomously. This was achieved using a Watson-Marlow 501u liquid pump, which allowed the delivery of aniline in the reaction mixture whilst the reaction was ongoing without any manual adjustments, in a controlled fashion; adjustable in (gmin^{-1}).

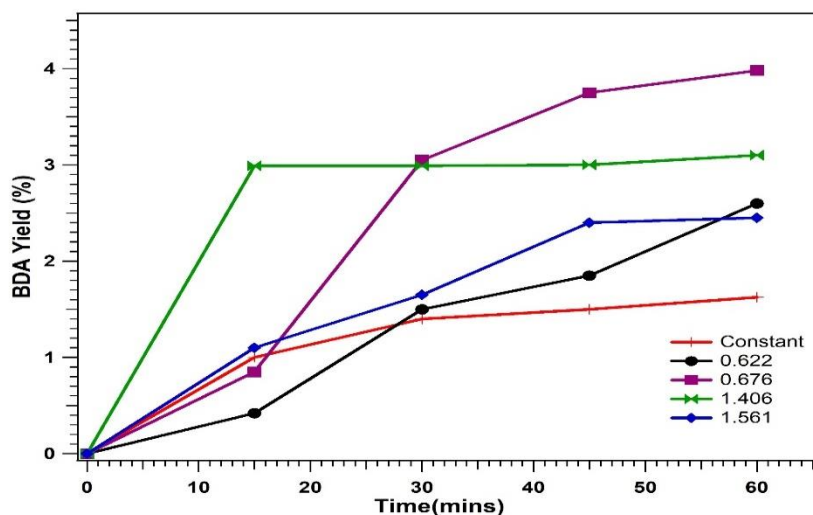


Figure 6.8 BDA yield change over time at different aniline flow rates.

Thus, the effect of different aniline flow rate on BDA yield was monitored (Figure 6.8). Also, the data for when the original 7mmol of aniline was initially introduced is present in the graph. Therefore, the different yield can be compared.

Clearly, aniline flow produced higher BDA yields compared to a constant amount of aniline initially added. The highest yield of 3.9% achieved at an aniline flow rate of 0.676 gmin^{-1} , which was 2.4 times higher than when aniline was initially dosed at a constant amount (Figure 6.9). This feeding rate indicates a balance between being slow enough to allow time for BA oxidation to take place while being efficient enough to resolve any resistive forces present in the given experimental setup that affect aniline solution delivery constantly.

Since the condensation reaction to create the intermediate depends on the benzaldehyde formed reacting directly with aniline delivered into the solution before protonating, it would be expected a higher yield at slower flow rates as there would be a higher concentration of benzaldehyde present in the solution. This is not the case, however since the result at 0.622 gmin^{-1} indicates a decrease in yield, and this is because the reaction run was not adequate to resolve the resistive forces present in the delivery process.

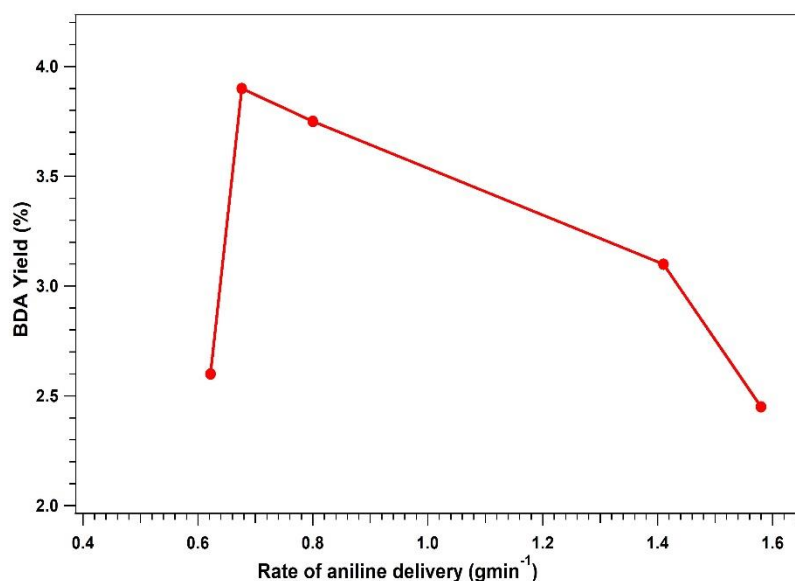


Figure 6.9 BDA yield compared to the different aniline delivery rates.

Due to the location of the silicone tubing and a small pressure building up in the silicone tube from the oxygen gas being poured into the reaction mixture, these resistive forces present include going against gravity. Hence the reliable delivery of aniline at flow rates below 0.676 gmin⁻¹ is a limitation of this experimental process. Conversely, the decrease in yields achieved at 1,406 gmin⁻¹ and 1,561 gmin⁻¹ is due to the flow rate being too rapid to allow an optimal benzaldehyde build-up to take place. A small aniline solution of the fixed volume was produced during the previous investigation to be used for the delivery of aniline at each flow rate, but the impact of using greater volumes in the reaction was not investigated. A large stock of aniline solution of the same concentration as the previous solution was then developed and the investigation was repeated.

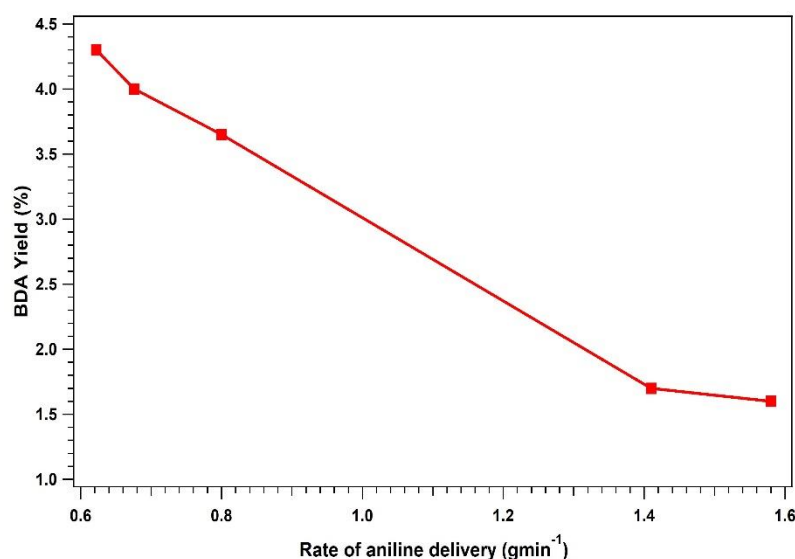


Figure 6.10 BDA Yield compared to the rate of aniline delivery when using a large stock aniline solution.

The investigation was repeated using a larger stock solution where interesting changes in the BDA yields were observed. Initially, the optimization point was between 0.676 gmin^{-1} and 0.622 gmin^{-1} , however, the yield obtained at 0.622 gmin^{-1} was larger with the graph showing an almost linear relationship between flow rate and yield as shown in Figure 6.10. These findings are similar to the hypothetical relationship of slower flow rates leading to higher yields, and these results also indicate that a more reliable distribution at lower flow rates can be accomplished by using a stock solution. Ultimately, however, these findings are again restricted by the liquid pump used, and with the experimental setup provided, consistent delivery of aniline at even lower flow rates is not possible. A more efficient pump will need to be used for further studies into lower flow rates. On the other side of the graph, using a stock solution at the flow rates of 1.406 gmin^{-1} and 1.561 gmin^{-1} leads to a decrease in yields relative to those obtained in Figure 6.9. The explanation for this is that the use of a stock solution at higher flow rates contributes to a significant build-up of solvent dichloromethane, which in turn increases the volume of the organic layer to a volume far greater than the aqueous layer, thus reducing TiO_2 activity and thus the photocatalytic rate.

6.3.5 Reduction of Imine with Hydrogen

To produce the final amine (benzylaniline) product, it was important to investigate the effect of injecting H_2 gas into the reaction mixture. H_2 was mixed with an N_2 diluent at a ratio of 1:2 as a safety precaution. This was based on the hypothesis that delivering an excess amount of H_2 gas into reaction mixture would force the final reduction step to take place. Indeed, benzylaniline peaks were detected allowing the yield to be monitored as a function of time (Figure 6.11).

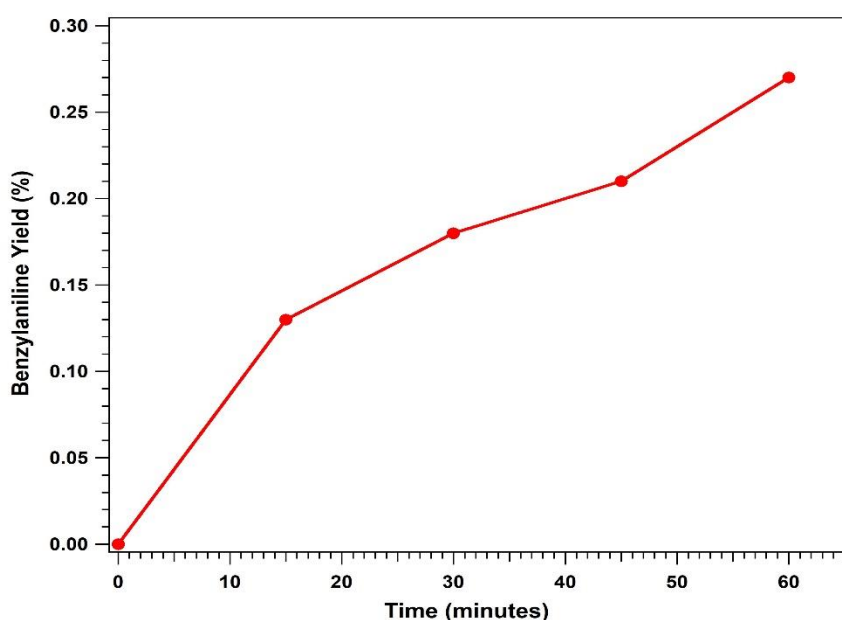


Figure 6.11 The yield of benzylaniline against time.

The results show a linear relationship between the yield of benzylaniline and time, however, it is very low at 0.27 % with the observed yield after 1 hour of reaction time. Comparing this yield to those obtained for the intermediate are very smaller, but this is as expected. The final yield of benzylaniline product depends on, firstly the oxidation of benzyl alcohol, then the condensation reaction between benzaldehyde and aniline and finally the hydrogenation of the imine intermediate. Thus, the low yields are as expected as the final step in the reaction cycle is the reduction reaction to form the benzylaniline. Here the yield is reported after just 1 hour, yields would increase

after longer reaction times as expected. There are no side reactions between the chemical species occurring and the reagents react together in a 1:1 ratio to form the intermediate and finally the product. Therefore, theoretically up to 100% final product yield would be produced after the long run reaction. Which would be agreed with the literature values of yield for this reaction using a transition-metal catalyst as stated in section 6.1.³⁹⁹⁻⁴⁰¹ This result is significantly high as this is the first time the N-alkylation of amines under photocatalytic conditions has been shown to work.

6.4 Conclusion

Photocatalytic N-alkylation of aniline using BA was successful for the synthesis of benzyaniline. GC-FID was useful for tracking the progress of the photocatalytic synthesis process using standard solutions of each of the involved chemical species. However, unoptimized photocatalysis was very slow with no benzyaniline yield. This was improved following optimization of the photocatalyst by carefully selecting the best pH (acidic condition of pH 2) coupled with the equimolar loading of reactants to prevent aniline protonation that was observed to hinder optimal benzyaniline yield. Furthermore, it was demonstrated that the loading of aniline in an ongoing reaction rather than injecting it into the organic layer initially produced better yields. Given aniline protonation rate is faster than BA oxidation, the presence of aniline during the initial phase of the reaction results in preferential protonation before reacting with benzaldehyde. This was solved by adding aniline throughout the reaction to allow it directly to react with the already produced benzaldehyde. The reaction was further optimized by using liquid-pump for a continuous aniline delivery into the reaction mixture, with an optimal flow rate of 0.676 g min^{-1} giving a 3.98 % of benzyldeneaniline intermediate resulting in an increase of yield compared to 1.76 % at constant aniline

concentration. In addition, bubbling of H₂ gas in the 1:2 ratio into the reaction mixture allowed hydrogenation step to occur and produced the final product, benzyaniline; since the lack of H₂ gas evolution initially did not allow hydrogenation of the final product. After 1 hour of reaction, the benzyaniline yield was very low as expected and allowing the reaction to run longer, greater yields were observed. This is the first, report to demonstrate the photocatalytic N-alkylation of an amine using a TiO₂ photocatalyst. Optimization of the reaction conditions as described here could provide a large-scale green alternative method for the N-alkylation of amines at industrial levels.

CHAPTER 7 Synthesis and Photocatalytic Properties of Metal-dopedTiO₂

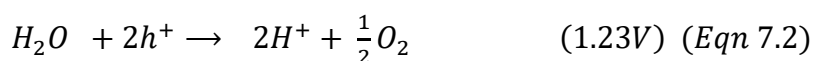
The photocatalytic activity of TiO₂ can be optimized through doping with other metals to lower the bandgap energy and enhance electron trapping, thereby minimizing the recombination of TiO₂ photogenerated electron-hole (e-h) pairs thus improving photocatalytic efficiency. In the present study, Ag-, Fe-, and V- doped TiO₂ nanoparticles (NPs) were synthesized using a controlled hydrolysis technique. The synthesized NPs were subsequently characterized by XRD pattern, BET surface area, photoluminescence emission spectroscopy and UV-Vis diffuse reflectance spectroscopy. Photocatalytic oxidation of benzyl alcohol into aldehyde was performed to evaluate the photocatalytic activity of synthesised NPs and compare it to P25 wherein optimal calcination temperatures for all metal-dopedTiO₂ NPs were found to be 500°C. Evaluation of TiO₂ metal-dopants (mole%) showed that the 0.7% V-doped TiO₂ possessed the lowest bandgap at 2.88 eV and the highest photocatalytic activity of alcohol photooxidation at $62 \times 10^{-3} \text{ min}^{-1}$. This was followed by 0.4 % Fe-doped TiO₂ with a bandgap of 2.92 eV and an alcohol photooxidation rate of $60 \times 10^{-3} \text{ min}^{-1}$. The 0.8% Ag-doped TiO₂ had a bandgap of 3.05 eV, and the lowest rate of alcohol photooxidation with $52 \times 10^{-3} \text{ min}^{-1}$.

7.1 Introduction

7.1.1 Titanium Dioxide as A photocatalyst

Photocatalysis is the process of absorbing light to raise its energy level and supply such energy to a reacting substance for facilitating a chemical reaction.⁴⁰⁴ In a photocatalytic reaction, the photocatalyst is neither consumed nor altered making such reactions sustainable over time. Photocatalysis reactions that use semiconductor particles have been widely due to their potential use in the removal of inorganic and organic contaminants from the environment and in solar energy conversion.⁴⁰⁵ In a semiconductor, free charge carriers such as electrons and electron holes, also known as electron-hole (e-h) pairs, are generated through excitation from the valence band to the conduction band of the electron (e⁻) (Figure 7.1). The excitation of an electron in a photocatalytic reaction occurs when light is absorbed by the atom or molecule causing its movement between the two energy levels - a process referred to as photoexcitation.⁴⁰⁶ The electron-hole is denoted as a positive charge, h⁺, as the lack of an electron at a position where an atom or atomic lattice could exist leaves a net positive charge at the hole's location which balances the negative charge of the electron. An excited electron in the conduction band can fall back to the hole or an empty state in the valence band through a process known as electron-hole recombination.⁴⁰⁷

Titanium dioxide (TiO₂) is a powerful photocatalyst with the ability to photo-generate e-h pairs capable of undergoing redox reactions with water molecules to produce hydrogen from electrons and oxygen gas from holes as shown in Equations 7.1 and 7.2, respectively.⁴⁰⁸



The mechanism of TiO₂-mediated photocatalysis is initiated by the absorption of a photon of energy $h\nu$, which is equal to or greater to the bandgap energy of TiO₂ (~3.3 eV for the anatase crystalline phase of TiO₂). This generates an e-h pair on the surface of the TiO₂ nanoparticles (NPs) as shown in Figure 7.1. An electron (e^-) is promoted to the conductance band (CB), while the positive hole (h^+) is formed in the valence band (VB). The formed h^+ can react with water or oxygen to generate hydroxyl radicals (OH^\bullet) or oxygen radicals ($O_2^{\bullet-}$) with a high redox oxidizing potential which is useful for photocatalytic reactions. However, the excited e-h pairs can undergo recombination, where their energy dissipates as heat, get trapped in metastable surface states or react with electron donors and electron acceptors present on the surface of the semiconductor.⁴⁰⁹ Consequently, the recombined charge carriers cannot participate in the subsequent photocatalytic reactions, thus demonstrating that quick e-h recombination is detrimental to the whole process.⁴¹⁰

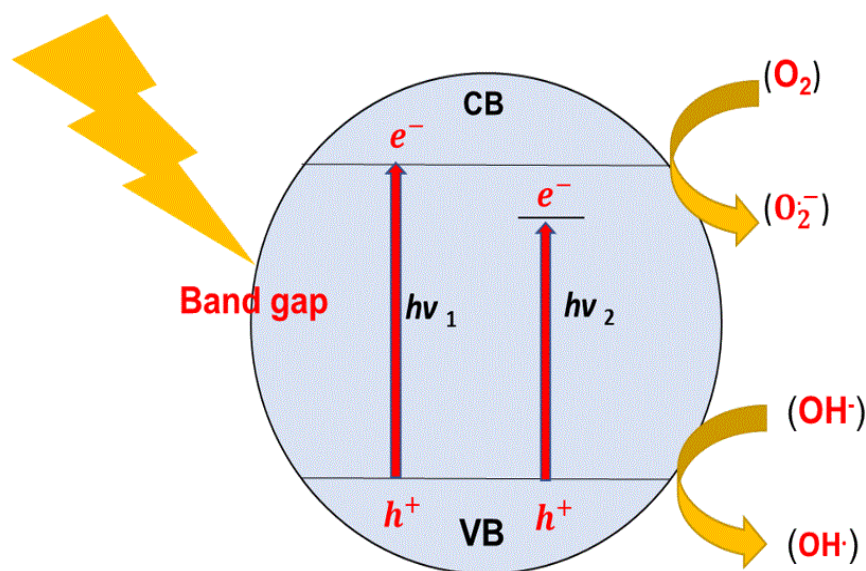


Figure 7.1 Mechanism of TiO₂ photocatalysis: $h\nu_1$: pure TiO₂; $h\nu_2$: metal-doped TiO₂.

The photocatalytic potential of TiO₂ makes it useful for organic synthesis. Also, due to its biological and chemical stability, low cost, nontoxicity and long-term stability

against photo-corrosion and chemical corrosion, TiO_2 has been made the subject of a significant number of studies.⁴¹¹

Despite these attractive advantages, the use of TiO_2 as a photocatalyst has been limited due to the narrow wavelength of light that can effectively photoactivate it. Indeed, the photoactivation of pure TiO_2 is restricted to light sources within the narrow ultraviolet (UV) region (200 - 400 nm), effectively limiting its utilization of sunlight to about 3-5% of the entire solar spectrum.⁴¹¹ This restriction is due to the large bandgap energy of TiO_2 (3.0 eV, rutile),⁴¹² which limits the amount of energy used to achieve photoexcitation. In addition, the photogenerated e-h pairs of TiO_2 are short-lived since they rapidly undergo recombination thus significantly reducing their quantum efficiency. This gives pure TiO_2 a suboptimal photocatalytic efficiency.

7.1.2 Optimization of TiO_2 Photocatalysts

To improve the efficiency of pure TiO_2 , several studies have focused on developing techniques to block or reduce the recombination of TiO_2 -photogenerated e-h pairs thereby enhancing the photocatalytic activity of TiO_2 . Anti-recombination strategies developed for photogenerated e-h pairs from TiO_2 include lowering the bandgap energy of TiO_2 and maximizing its electron lifetime.

7.1.2.1 Lowering of Bandgap Energy

Doping TiO_2 with non-metals or transition metals can lower its bandgap and extend its light absorption to the visible range. During doping with non-metals, the valence band is influenced through interaction with the O 2p electrons, causing the localized states or *p* states of the non-metal dopant to form the impurity levels and lie above the valence band, thereby extending the absorption edge of TiO_2 .⁴¹³ Among the non-metal dopants studied in the literature, surface fluorinated TiO_2 (F- TiO_2) is particularly promising due to its enhanced photocatalytic activity compared to pure TiO_2 . The

addition of a fluorine dopant in F-TiO₂ has also been shown to impart the material with an extended photo-absorption wavelength, beyond the narrow UV region exhibited by pure TiO₂.^{414,415} However, whilst hydroxyl radical (OH•) mediated photooxidation pathways are enhanced by F-TiO₂, reaction pathways that are dependent on hole transfer were found to be inhibited due to the hindered adsorption or complexation of substrates in F-TiO₂.⁴¹⁶ This inhibition of such pathways has led F-TiO₂-mediated photocatalytic reduction reactions, such as dechlorination of trichloroacetate, to proceed with significantly reduced reaction rates in F-TiO₂ when compared to pure TiO₂.⁴¹⁶

7.1.2.2 Increasing Electron Lifetime

Although doping, especially for non-metals, can reduce the bandgap of TiO₂, it could also affect the crystal phase, composition and electronic structure of TiO₂ which are critical for optoelectronic applications.⁴¹⁷ Other ways to improve the photoactive properties of TiO₂ include coupling it with semiconductors or metals. An electronic heterostructure is formed at the interface between TiO₂ and other semiconductors that have a higher conduction band level than TiO₂.⁴¹⁸ This structure can localize holes in the valence band and trap electrons in the conduction band, thereby extending the lifetime of charge carriers.^{413,417} Some of the promising semiconductors that are utilized to improve the efficiency of TiO₂ photocatalysts include graphene,²⁹⁰ Sr₂Nb₂O₇,⁴¹⁹ AgX (X= Cl, Br, I),⁴²⁰ g-C₃N₄,⁴²¹ SnO₂,⁴²² In(OH)₃,⁴²³ CeO₂,⁴²⁴ BiVO₄,⁴²⁵ and Bi₂WO₆.⁴²⁶ In Chapter 3 where synthesis and photocatalytic activities of an Ag₃PO₄/TiO₂ nanocomposite were discussed, it was shown that the Ag₃PO₄/TiO₂ nanocomposite exhibited an increased photocatalytic activity due to increased photoexcitation of Ag₃PO₄ nanoparticles due to a reduction in e-h recombination.

Transition metals and their oxides are also widely studied as TiO₂ dopants.^{409,427} TiO₂ catalysts can be doped with various metal oxides such as Fe, Zn, Cu, Ni, and V,⁴²⁸ reducing the bandgap of TiO₂ for photoexcitation to a lower energy level, $h\nu_2$, as shown in Figure 7.1 The recombination rate of photogenerated e-h pairs can also be reduced simultaneously.⁴²⁸

One of the metals that can be used as a dopant for TiO₂ is silver. Doping of TiO₂ photocatalyst with Ag has been found to reduce the illumination period and make it a more efficient photocatalyst for wastewater treatment.⁴²⁹ He *et al.* noticed that a specific amount of silver dopant can increase the activity of TiO₂ by changing the anatase grain size.⁴³⁰ Aside from Ag, Fe is also one of the most promising transition metals considered as a dopant because of iron's similarity with Ti in terms of size. The ionic radius of Fe³⁺ is 0.69 Å while that of Ti⁴⁺ is 0.745 Å. Hence, Fe³⁺ can ideally integrate into the TiO₂ matrix. The Fe³⁺ electronic configuration is also stable and with half-filled d⁵. Fe³⁺ also inhibits the recombination of photogenerated e-h pairs by acting as a charge carrier trap, thus enhancing the material's photoactivity.^{431,432} Cu-doped TiO₂ NPs were also studied due to their elevated light absorbance coefficients.⁴³³ Bak *et al.* noted that when metal ions such as Fe³⁺ and Cu²⁺ were introduced into TiO₂, the semiconductor's properties changed from an n-type to a p-type semiconductivity.⁴³⁴ Vanadium has also shown promising results as a metal dopant to TiO₂ for improving its photocatalytic efficiency. Doping of TiO₂ with vanadium (V) increases the former's photocatalytic efficiency and also makes it more active in the visible light spectrum.⁴³⁵

Different methods have already been used to synthesize metal-doped TiO₂ catalysts such sol-gel and modified sol-gel methods, wet impregnation, hydrothermal, chemical vapour deposition (CVD), ion-assisted sputtering, metal ion implantation and water in oil (W/O) microemulsion.⁴³⁶ Among these methods, the controlled hydrolysis

technique has been the one widely used for the doping of metal ions in titanium dioxide through the addition of a metal dopant during the hydrolysis of titanium alkoxide.^{437,438}

In this research, TiO₂ nanoparticles (NPs) were doped with metals such as Ag, Fe, and V. The synthesis method utilized was controlled hydrolysis which provides a new approach in the synthesis of NPs that possess better physical and chemical properties.

The present study aims to synthesize metal-doped TiO₂ nanoparticles through the hydrolysis method using various transition metals Ag-, Fe- and V-doped TiO₂. This study also aimed to characterize the metal-doped TiO₂ nanoparticles' morphology and photocatalytic properties using x-ray diffraction, scanning electron microscopy, Brunauer–Emmett–Teller analysis, photoluminescence emission spectroscopy and UV-Vis diffuse reflectance spectroscopy.

7.2 Experiment

7.2.1 Materials and Reagents

The following were used as precursors for the preparation of NPs: ammonium hydroxide (NH₄OH, 30 wt%), titanium (IV) isopropoxide (TTIP, 97% purity), silver nitrate (AgNO₃, > 99 % purity), iron nitrate nonahydrate [Fe(NO₃).9H₂O, ≥99% purity], and vanadium (III) chloride (VCl₃, 97% purity). All reagents were acquired from Sigma-Aldrich except for ammonium hydroxide which was obtained from Fischer Scientific.

7.2.2 Synthesis of Metal Doped TiO₂ Nanoparticles

The TiO₂ was synthesized through a controlled hydrolysis technique using TTIP as a precursor. Thirty drops of 0.2M aqueous ammonia was added dropwise into a glass vial containing 1ml TTIP: 10 ml ethanol solution with continuous stirring. The mixture was stirred for another hour, washed and then oven-dried at 80°C for 12 hours. The dried sample was calcined at 500°C.

The metal doped TiO_2 NPs were synthesized using the controlled hydrolysis method. Undoped metal catalysts were prepared by adding 1 mL of TTIP into 10 mL of ethanol in a glass vial and then stirring the mixture for 20 min. On the other hand, metal dopant solutions of 1 mL were prepared from 0.1 mole% solutions of Ag, Fe, and V precursors in 10 mL of absolute ethanol. The metal dopant solution is added dropwise to the prepared TTIP/EtOH mixture to make Ti/M powders, where M is the transition metal, having a mole ratio of 0.1%.

The doped mixture was stirred using a magnetic stirrer for 30 min after which it was treated with 30 drops of 0.2M ammonium hydroxide solution, dropwise. The mixture was stirred for another hour, then oven-dried at 80°C for 12 hours. The oven-dried metal doped TiO_2 was transferred into a furnace for the calcination process at different temperatures from (400- 600°C) for 2 hours. Metal-doped TiO_2 samples were prepared according to the above-mentioned procedure in the presence of the corresponding metal salt precursors to obtain a doping level range of 0.1 to 1.0 mole % (Figure 7.2).

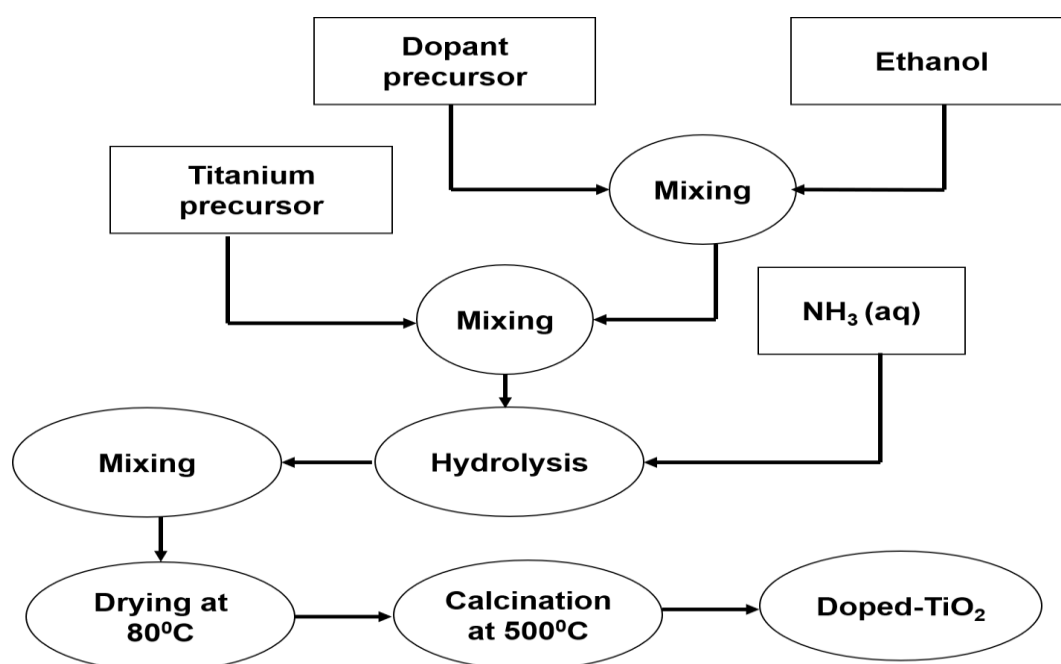


Figure 7.2 Procedure for synthesizing of metal doped TiO_2 photocatalysts.

The photocatalytic activities of the synthesised metal catalysts were evaluated using a method similar to that previously described (Chapter 5) which used the synthesized catalysts rather than P25.

7.2.3 Characterization of metal dopedTiO₂ photocatalysts

In order to determine the composition and crystallite size of the developed photocatalysts, x-ray diffraction measurements were carried out at room temperature using DX-2000 x-ray powder diffractometer (Siemens D500). with Cu K α radiation at an x-ray wavelength of 1.54 Å, a scanning speed of 3°/min, an accelerating voltage of 40 kV and an emission current of 30 mA. Photoluminescence emission spectra were recorded using a fluorescence spectrometer (Perkin Elmer LS 45). The surface area BET measurements were performed using a JWK-B122 surface area and pore size distribution analyser at 77 K. Gas chromatography analysis was performed using a Perkin Elmer Gas Chromatograph equipped with Flame Ionized Detector (GC-FID); the dimensions of the polar column used were 30 m \times 0.53 mm \times 1 μ m. The injector carrier gas used was H₂, which was delivered at a flow pressure of 4.2 psi. The injector was maintained at a temperature of 250°C and the oven was kept at a temperature of 180°C. The analysis was performed at a retention time of 200 seconds.

7.2.4 Photocatalytic Oxidation of Benzyl Alcohol Using Metal-doped TiO₂

The photocatalytic activity of metal-dopedTiO₂ photocatalysts was evaluated according to methods and procedures similar to those described in Chapter 5. TiO₂ P25, synthesised TiO₂ and the metal dopedTiO₂ photocatalysts were used. In order to investigate the influence of doping concentration on the biphasic photocatalytic oxidation of alcohols into aldehydes, the kinetic constants were calculated for each catalyst. To do this, the oxidation performance was considered and described in

(Chapter 5) using pseudo-first-order kinetics described as follows: photocatalytic oxidation depends on the initial substance concentration (C) (Equations (5.1)-(5.4), chapter 5):

$$v = kC$$

where C is the alcohol concentration ($\text{mg}\cdot\text{L}^{-1}$) during irradiation time and k is the kinetic constant in min^{-1} .

$$\frac{dC}{dt} = -kC$$

By integrating the last equation between initial time ($t = 0$) and a generic irradiation time t , the following equation could be established:

$$-kt = \ln \frac{C_t}{C_0}$$

The kinetic constant k value can be calculated by the slope of the straight line attained from plotting $-\ln (C_t/C_0)$ versus t .

7.3 Results and Discussion

7.3.1 Ag-doped TiO_2 NPs Characterization and Evaluation of its Photocatalytic Activity.

The synthesized Ag-doped TiO_2 NPs were characterized using XRD, diffuse reflectance spectroscopy, photoluminescence spectroscopy, and BET.

7.3.1.1 Optimization of Ag-doped TiO₂ NPs

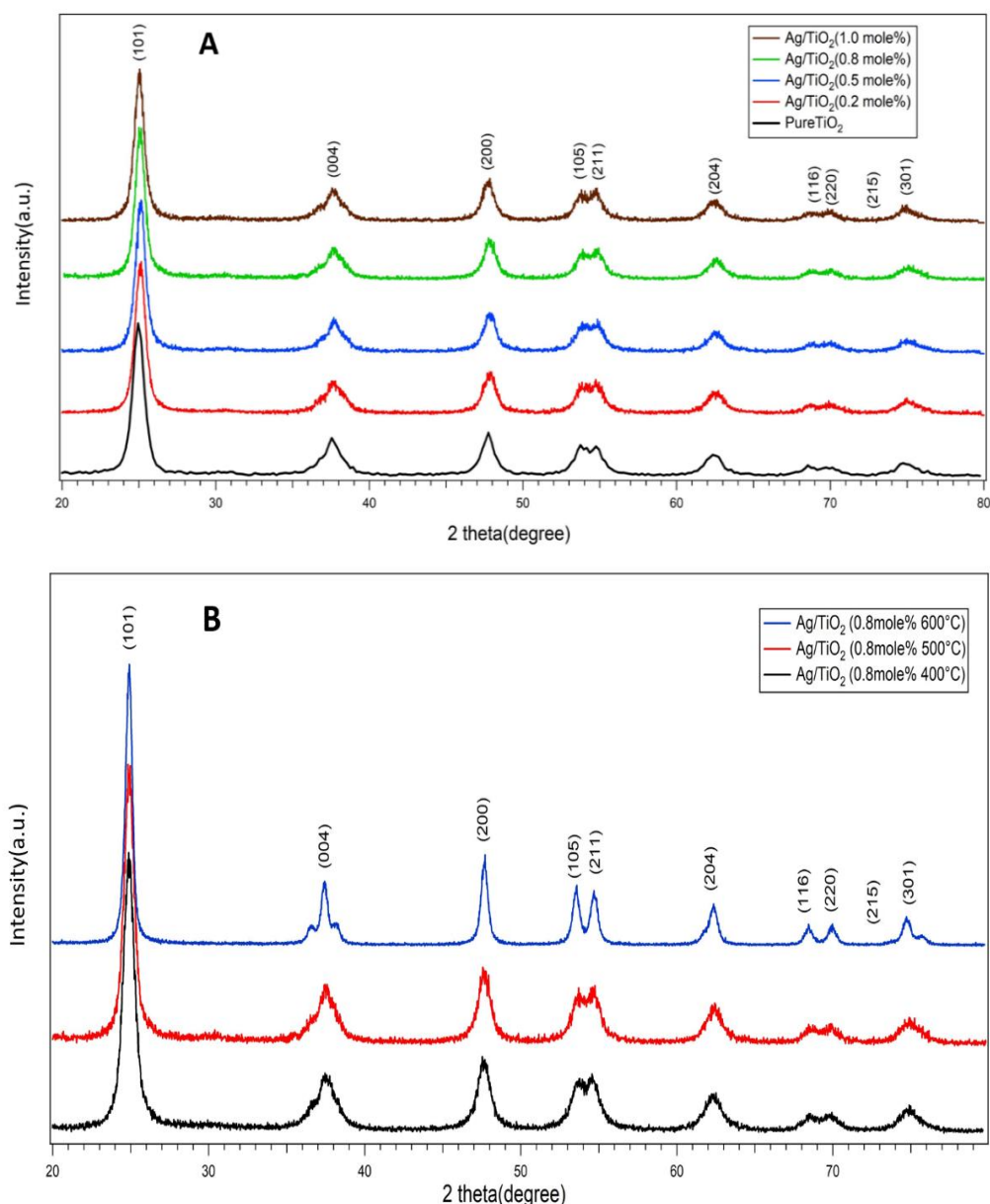


Figure 7.3 XRD patterns of (A) Pure TiO₂, and Ag-doped TiO₂ nanoparticles calcined at 400°C, (B) 0.8mol% Ag-doped TiO₂ nanoparticles calcined at 400, 500 and 600°C.

The XRD patterns of TiO₂ and different ratios of Ag-doped TiO₂ NPs were compared in order to determine the optimal ratio of Ti with a metal dopant and calcination temperature. Figure 7.3 A shows the XRD patterns of pure TiO₂ and Ag-doped TiO₂ NPs at different levels of Ag-doping: 0.2, 0.5, 0.8 and 1.0 mol. (%). For pure TiO₂, the peaks observed at 2θ were 25.50°, 37.75°, 47.80°, 53.75°, 54.90°, 62.50°, 68.80°, 70.50°, and 74.90°, for diffraction of x-rays from (101), (004), (200), (105), (211), (204), (116), (220), and (301),

(116), (220) and (301) crystal planes of the anatase phase (JCPDS Card No.21-1272), respectively. The Ag-doped TiO₂ NPs were found to display the same XRD pattern as that of pure TiO₂ which means that there is no peak related to Ag species even at the highest doping level, and that could be because the anatase phase was not disturbed upon doping and that the dopants in the TiO₂ samples were highly distributed.^{439,440} This means that, without being covalently attached to the crystal lattice, the metal dopants were simply placed on the surface of the crystals. Hence, these metal sites were expected to be below the visibility limit for x-ray analysis. However, with increasing dopant concentration, the major diffraction peaks (101) moved to lower 2θ and became broader. A similar observation was noted in a paper by Ali *et al.*, wherein they reported that the main diffraction peaks became broader and shifted to lower 2θ possibly due to lattice strain.⁴³⁹ The crystallite size was obtained from the diffraction peak broadening using Scherrer's Equation for samples which are displayed in Table 7.1.

The average crystallite size of the samples was calculated using the Debye–Scherrer formula on the anatase (101) diffraction peaks (Equation 2.6, chapter 2):

$$D = k\lambda\beta\cos\theta$$

Where D is the average crystallite size, K is the constant ($=0.89$), λ is the wavelength of the x-ray radiation ($\lambda = 1.5406$ nm), β is the corrected band broadening (full-width at half-maximum (FWHM)) after subtraction of equipment broadening, and θ is the diffraction angle. It is clear from table 7.1, the 0.5% Ag-doped TiO₂ samples had the smallest crystallite size (23 nm) at 500°C. With increasing silver dopant from 0.5 mol. % to 1 mol. %, the crystallite size of the anatase phase in the samples also increased, while decreased with higher calcine temperature and that could be due to the inhabitation of the phase transformation.

The effects of calcination temperature on the 0.8% Ag-dopedTiO₂ NPs were further studied using calcination temperatures of 400, 500 and 600°C for 2 hours. Subsequently, the best amount of dopant for the evaluation of photocatalytic oxidation of benzyl alcohol by Ag-doped TiO₂ NPs was determined to be 0.8mole%. Increasing the temperature from 400 to 500°C increased significantly the peak intensity of (101) peak (Figure 7.3 B). The width of the (101) peak became narrower, demonstrating the growth of the anatase phase and the improvement in crystallinity.⁴⁴¹

It was observed that all peaks were sharp and strong for the anatase phase at $2\Theta = 25.50^\circ$ while no peaks appeared for rutile phase in all of the samples. This demonstrates that phase transformation from anatase to rutile did not take place when 0.8 mol% Ag-dopedTiO₂NPs was calcined below 600°C which means that silver was capable of controlling the phase transformation from anatase to rutile. However, it is well known that the anatase-rutile phase transformation depends on several factors such as synthesis method, heating rate, particle size and doping level. Similar findings have also been reported by other authors.⁴⁴²⁻⁴⁴⁴ However, some articles have reported opposite results regarding the effect of silver doping on phase transformation.⁴⁴⁵

The liquid nitrogen absorption-desorption experimental results from the Brunauer–Emmett–Teller (BET) analysis are presented in Table 7.1. The surface area was highly dependent on the quantity of Ag-doped samples. When the Ag-doped sample amount was 0.0, 0.5, 0.8 and 1.0 %, the SBET of Ag–TiO₂ was found to be 254, 260, 295.5 and 250 m² g⁻¹, respectively. It is interesting to note that the 0.8% Ag-doped TiO₂ displayed the highest BET surface area at 295.5m²/g among the four samples. Since the NPS surface area could be correlated to photocatalytic activity, the Ag-doped NPs can thus be expected to have an enhanced photocatalytic ability.

Table 7.1 BET surface area of Ag-dopedTiO₂

Ag-doping (Mole%)	BET surface area (m²/g)	Crystallite size (nm)
0.0	254	25
0.5	260	23
0.8	295.5	27 (400°C) 25 (500°C) 24 (600°C)
1	250	30

It has been observed that based on the Ag-doping level, BET increased proportionately to a maximum for 0.8% but then decreased when the Ag-doping amount further increased. This is probably due to the sintering of smaller particles into larger particles. Therefore, the higher the Ag-doped amount, the lower the BET surface area. Similar findings have been reported by Li *et al.*⁴⁴⁴

Characterization of Ag-doped TiO₂ NPs compared to pure TiO₂ NPs was also investigated using the obtained photoluminescence (PL) emission spectra (Figure 7.4). PL spectra have been widely used to investigate the efficiency of charge carrier trapping, migration and transfer as well as to determine the fate of e-h pairs in semiconductor particles.⁴⁴⁶

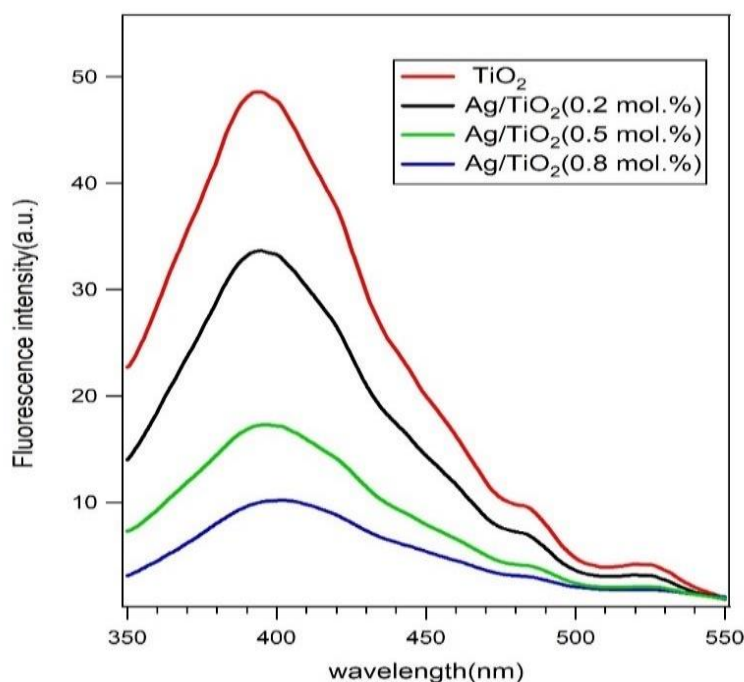


Figure 7.4 Photoluminescent (PL) emission spectra of pure TiO_2 , and Ag-doped TiO_2 (0.2, 0.5, 0.8 mol. %) NPs under UV-vis irradiation.

Pure TiO_2 exhibited the highest PL emission intensity while 0.8% Ag-doped TiO_2 NPs exhibited the lowest PL emission intensity. This high intensity could indicate that the population of photogenerated e-h pairs undergoing recombination is much larger in pure TiO_2 than in Ag-doped TiO_2 , thereby suggesting that Ag-doping effectively inhibits the recombination of electrons and holes in TiO_2 , an effect that could improve the photocatalytic activity of the studied materials. By observing the PL spectra shown in Figure 7.4, it can be noted that the largest degree of inhibition of e-h pairs occurred at a doping level of 0.8% Ag. Indeed, when the Ag content was too small, the recombination rate of e-h pairs tended to be higher due to the absence of adequate traps. A similar quenching effect on luminescence intensity has been observed in other studies wherein V-, Fe-, W-, Zr-, Cu-, Ni-, Ga-, Cd-, Ag-, Al- and Pb- were used for doping TiO_2 .⁴⁴⁷⁻⁴⁴⁹

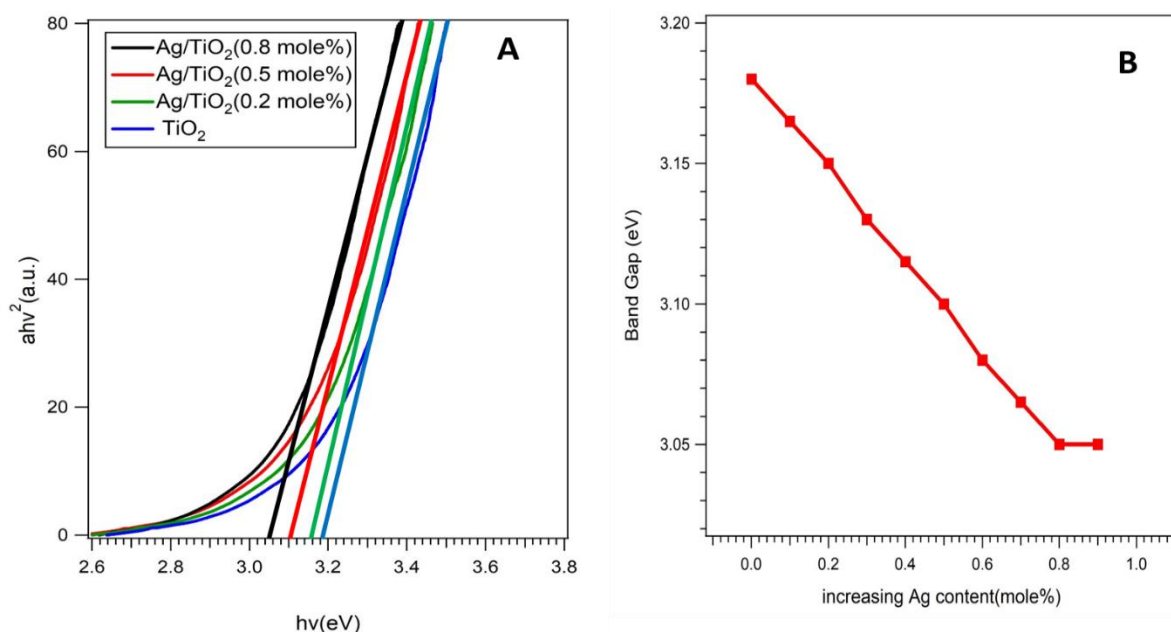


Figure 7.5 (A) Band gaps obtained from Tauc plots calculated from diffuse reflectance spectra of pure and Ag-doped TiO₂ NPS. (B) Effect of increasing Ag content on the bandgap energy.

The Tauc plot, generated from the UV-Vis reflectance spectra of pure TiO₂ and Ag-doped TiO₂ NPs which can be used to determine the most optimal Ag-doped TiO₂ based on bandgap reduction, is presented in Figure 7.5. The obtained spectrum for TiO₂ contains a single absorption peak, just below 370 nm, which is attributed to the charge transfer from the valence band - formed by the $2p$ orbitals of oxide anions - to the conduction band.⁴⁵⁰ The addition of Ag ions and the UV irradiation caused large changes to the shift of TiO₂ absorption in the UV-vis region. As can be observed in Figure 7.5, an increase in Ag-dopant resulted in a steady decrease in the bandgap of the Ag-doped TiO₂ NPs from 3.18 eV, at 0.0% Ag, to 3.05 eV, at 0.8% Ag. Further increases in the amount of the Ag dopant were found to be constant. Consequently, it was determined that 0.8 mol% was the dopant concentration which allowed the maximum reduction in bandgap and therefore expected to have the highest photoactivity. Mogal.S *et al.* have reported similar observations regarding the bandgap of Ag-doped TiO₂.⁴⁵¹

7.3.1.2 Photocatalytic Activity of Ag-doped TiO₂

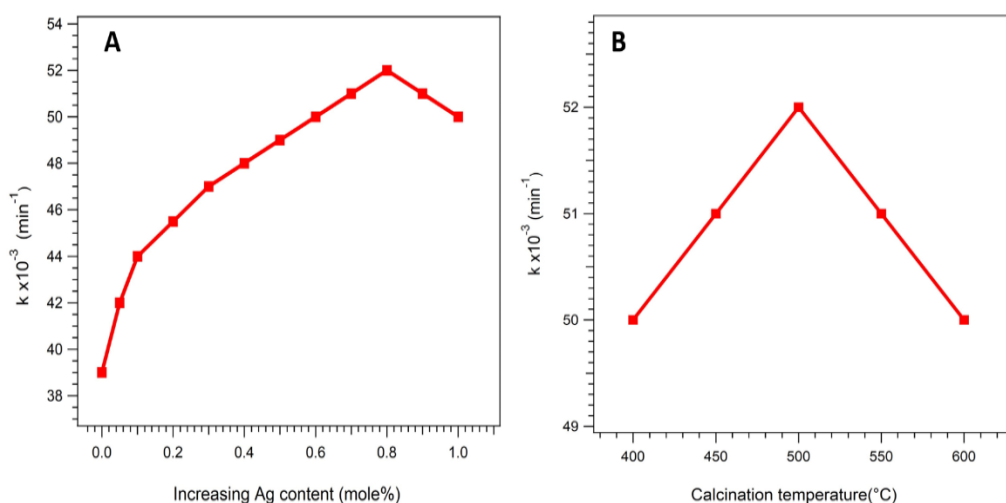


Figure 7.6 Photocatalytic activity of Ag-doped TiO₂ at different Ag concentrations (A) and various calcination temperatures of 0.8%Ag-dopedTiO₂ (B).

In order to optimize the Ag-doped TiO₂ NPs with respect to the quantity of the Ag-dopant (0.8%) and calcination temperature (500°C), the photocatalytic activity of the synthesized nanoparticles was investigated. The photocatalytic activity of Ag-doped TiO₂ NPs (Figure 7.6 A) was noted to increase steadily as the amount of the Ag dopant increased from 39 x 10⁻³ min⁻¹ for pure TiO₂ to 52 x 10⁻³ min⁻¹ for 0.8 % Ag-doped TiO₂ NPs. The improved photocatalytic activity of Ag-doped TiO₂, when compared to the synthesised TiO₂, can be attributed to the silver ion acting as an electron trap and hindering the electron-hole recombination.⁴⁵² Further addition of the Ag dopant to the NPs was seen to decrease the photocatalytic activity to 50 x 10⁻³ min⁻¹ for 1.0 % Ag-doped TiO₂ NPs. This could be since Ag particles can cover the TiO₂ surface thus causing a decrease in the concentration of photogenerated charge carriers and the photocatalytic activity.⁴⁵³ Previously, Huan *et al.* has noted that an increase in doping quantity decreases the light absorption and generation of electrons and holes.⁴¹³ As Figure 7.6 B shown that 500°C optimal calcination temperature and that could be due to the stability of anatase phase at this temperature.⁴³⁶

7.1.2.3 The mechanism of the enhanced activity of Ag-TiO₂ nanoparticles

The Fermi level of TiO₂ is higher than that of silver.⁴⁵⁴ As a result, silver ions can act as an accumulation site for the photogenerated electrons of TiO₂. When the silver aggregation is minimal and the photogenerated electrons are transferred to the silver aggregation effectively, a greater separation of electrons and holes can be reached by increasing the level of silver loading up to an optimum amount (Equation 7.3). These electrons either react with adsorbed molecular oxygen or with the Ti⁴⁺ surface to form reactive O₂⁻ species and reactive centre surface Ti³⁺, respectively (Equation 7.4 and Equation 7.5). This extends the electron lifetime thus slowing the e-h recombination process. The formation of O₂⁻ and surface Ti³⁺ increased proportionately with the number of h⁺. As the number and size of silver aggregates within the TiO₂ increased, the electrical properties of bulk silver became more dominant, causing the silver clusters within the NPs to become independent recombination sites for photogenerated e-h pairs (Equation 7.6). The reactions that occurred in the system are shown as follows.⁴⁵³



7.3.2 Fe-doped TiO₂ NPs Characterization and Evaluation of its Photocatalytic Activity.

7.3.2.1 Optimization of Fe-doped TiO₂ NPs

The XRD patterns of TiO₂ and different ratios of Fe-doped TiO₂ NPs were compared in order to determine the most optimal dopant concentration and most effective

calcination temperature. The optimal photocatalytic activity of Fe-doped TiO_2 NPs was observed at 0.4% mole at a calcination temperature of 500°C .

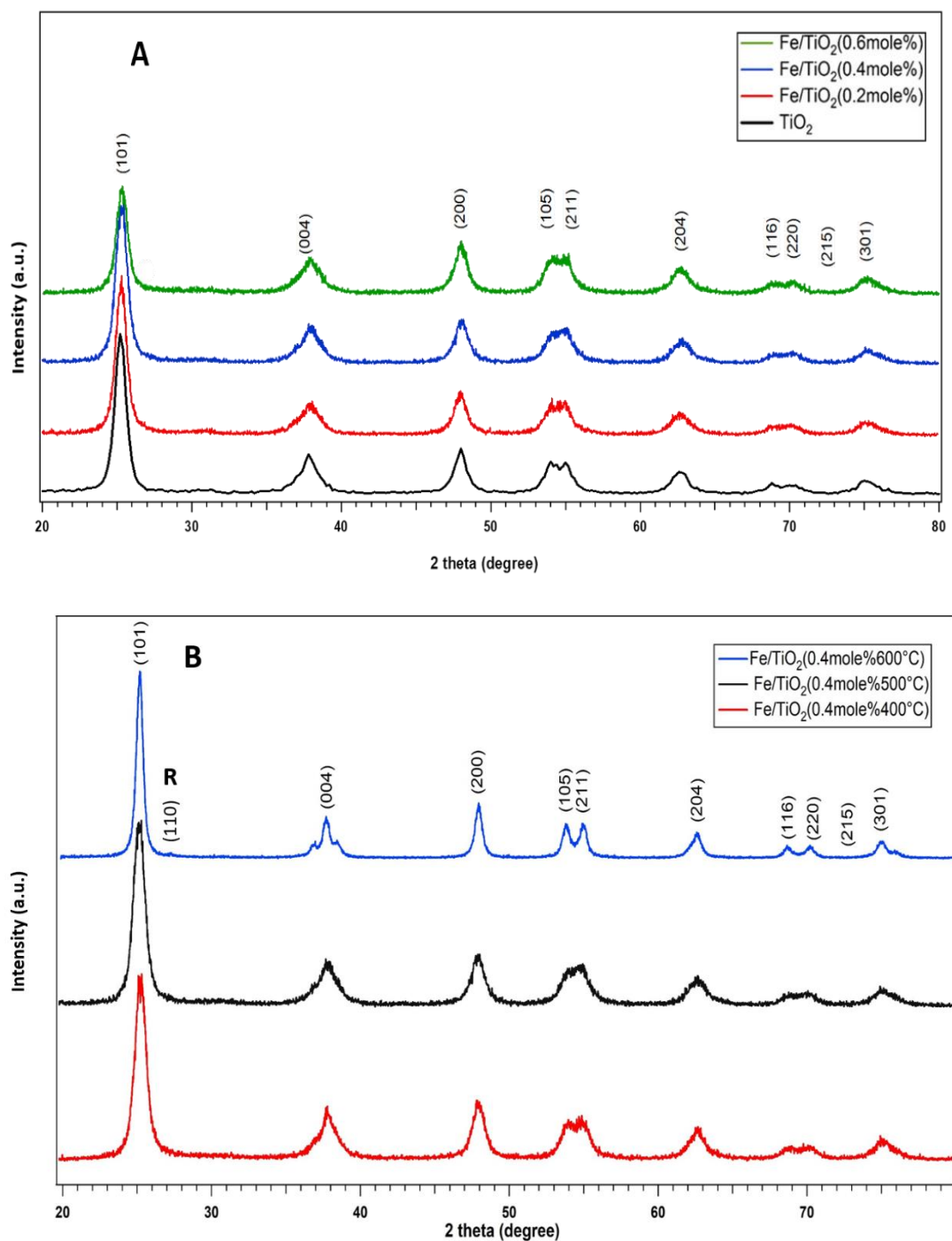


Figure 7.7 The XRD patterns of (A) TiO_2 , and Fe-doped TiO_2 nanoparticles calcined at 400°C , (B) 0.4mol% Fe-doped TiO_2 nanoparticles calcined at 400, 500 and 600°C

Figure 7.7A shows the XRD patterns of TiO₂ and Fe-doped TiO₂ NPs at 0.2, 0.4 and 0.6 mole % and range of $2\Theta = 20-80^\circ$. The diffraction peaks were indexed to (101), (004), (200), (105), (211), (204), (116), (220), (215) and (301) planes of anatase phase of TiO₂ and their XRD patterns matched well with JCPDS Card No.21-1272 and published literature.⁴⁵⁵ It is worth noting that no peak for iron oxide was detected and this could be due to low Fe content that is beyond XRD detection or due to the introduction of Fe³⁺ with an ionic radius = 64 pm into TiO₂ crystals to replace Ti⁴⁺ having an ionic radius = 68 pm, as a result of their radii proximity.^{441,456,457} Further optimization of 0.4 % Fe-doped TiO₂ NPs was done by investigating the calcination temperature. Figure 7.7B shows that increasing the temperature from 400 to 600°C, the peak intensity could be increased and made narrower. A peak was observed at $2\Theta = 27.30$ corresponding to (110) rutile phase when 0.4mole% Fe-dopedTiO₂ was calcined at 600°C. The average crystallite sizes were estimated using the Scherrer equation (Table 7.2).

It has been demonstrated by Li *et al.*⁴⁵⁸ that transformation of anatase phase to rutile happens only at temperatures that range from 700 to 800°C, and that increasing the temperature increases the particle size of both the anatase and rutile phases. However, the growth rate was different; a much higher growth rate was noted in the rutile phase compared to that in the anatase phase. The anatase phase transformation to rutile phase accelerated after doping by iron, shifting the transformation to lower temperatures.⁴⁵⁹ This is in accordance with the result of this current research wherein the transformation of anatase to rutile phase was found to occur at 600 °C during doping of TiO₂ with 0.4mole% Fe.

Table 7.2 Crystallite size and BET surface area of TiO₂ and Fe-doped TiO₂

Entry	Fe loading (mole%)	Crystallite size (nm)	SBET (m ² /g)
1	0.0	25	254
2	0.4	20 (400°C) 22 (500°C) 24 (600°C)	138
3	0.6	17	109

As shown in Table 7.2, there was a decrease in the crystallinity of the Fe-doped TiO₂ nanoparticles, when compared with the undoped TiO₂, accompanied by a decrease in the intensity of TiO₂ peaks. This result indicates that doping Fe³⁺ reduces the size of TiO₂ crystals as has been reported by other researchers.^{460,461} This is understandable because the addition of Fe³⁺ could occupy the regular lattice site of TiO₂ and distort the crystal structure of the host compound. The crystallite sizes of TiO₂, calculated through the Scherrer formula, decreased from 25 to 17 nm when the Fe content increased from 0.0% to 0.6mole%. On the other hand, the crystallite size of the 0.4% mole dopant increased from 20 to 24 nm with increasing calcination temperature.

The PL emission spectra of the Fe-doped TiO₂ were compared to that of pure TiO₂ NPs (Figure 7.8). Six emission peaks can be observed at around 390, 422, 452, 469, 483 and 493 nm from an excitation wavelength of 320 nm. All the peaks of Fe-doped TiO₂ corresponded with those of pure TiO₂, indicating that iron doping did not significantly change the material's photon emission as has been reported previously by Meng *et al.*⁴⁶²

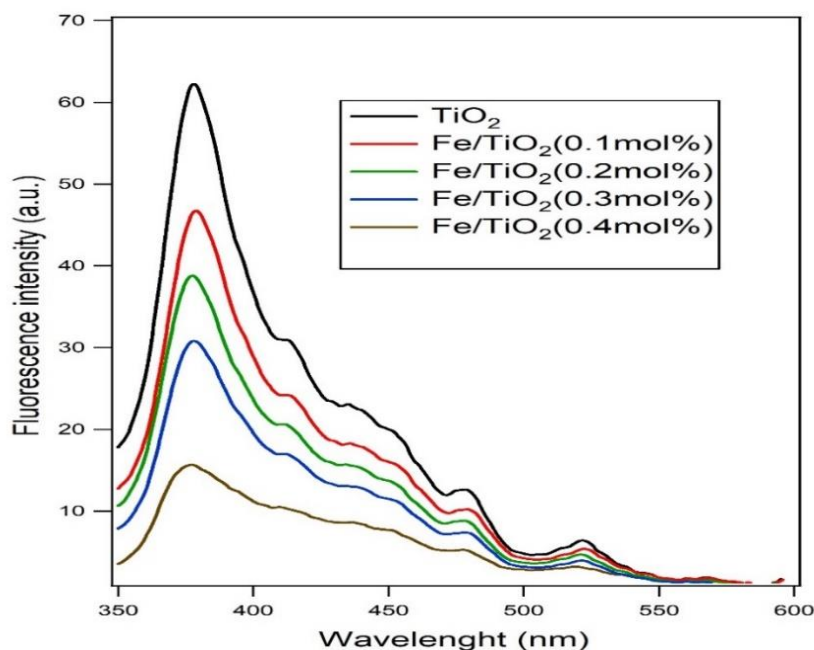


Figure 7.8 Photoluminescence spectra of pure and Fe-doped TiO_2 nanoparticles at different dopant concentrations calcined at 500°C .

The higher energy peaks observed in the PL spectrum can be attributed to the band edge luminescence of TiO_2 particles, while the lower energy peaks can be attributed to the oxygen vacancies present in the material.⁴⁶³ Pure TiO_2 exhibited a higher PL emission spectrum compared to that of Fe-doped TiO_2 NPs which could be caused by the impurity levels formed by the dopant that improved the nonradioactive recombination of excited e-h pairs.⁴⁴⁷ However, a lower amount of Fe dopant, at 0.1 %, in Fe-doped TiO_2 NPs was found to exhibit a higher intensity of PL emission spectrum compared to that of greater amounts of the dopant, from 0.2-0.4 %. This indicates that when the Fe amount is small, the recombination rate of e-h pairs remains substantially high due to the absence of adequate traps. When the doping quantity is increased, on the other hand, the absorption of light and the generation of e-h are both reduced.⁴¹¹

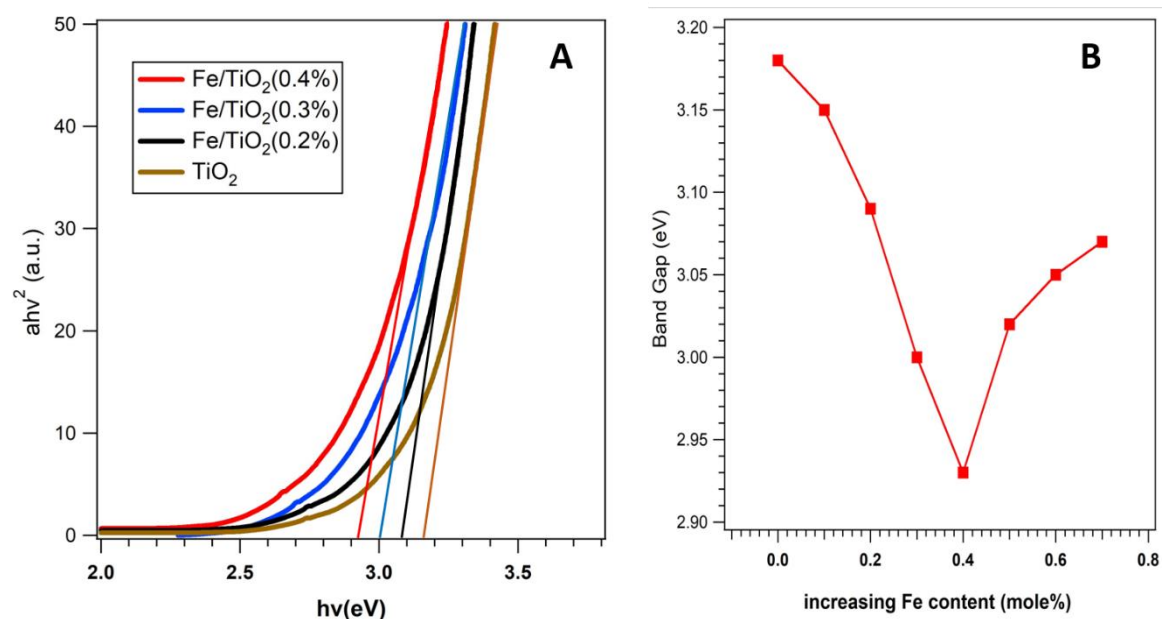


Figure 7.9 (A) Band gaps obtained from Tauc plots calculated from diffuse reflectance spectra of pure and Fe-doped TiO₂ NPS. (B) Effect of increasing Fe content on the bandgap energy.

Tauc plots derived from diffuse reflectance spectra of pure TiO₂ and Fe-doped TiO₂ NPS are shown in Figure 7.9. Increasing the proportion of the Fe-dopant in the Fe-doped TiO₂ NPs resulted in a steady decrease in the bandgap of the Fe-doped TiO₂ NPs from 3.18 eV, at 0.0% Fe, which is close to the reported value of anatase at 3.18 eV,^{444,464} to 2.92 eV, at 0.4 % Fe. The redshift of the spectra could be due to the generation of a dopant energy level in the TiO₂ band gap.⁴⁶⁵ The Fe³⁺ impurities had bands close to the TiO₂ valence band. Allowing electrons to transfer from the Fe³⁺ impurities rather than from the valence band to the conduction band because of the lower excitation energy induces a redshift in the NPs' light absorption.⁴⁴⁷ Further increases in the amount of the Fe dopant resulted in a steady increase in the bandgap to 3.07 eV at 0.7 % Fe, an effect that can be attributed to a Moss-Burstein shift.⁴⁶⁶ The Moss-Burstein effect arises when increased doping causes semiconductors degeneration. Degenerate semiconductors gain conductive properties, which means their e-h recombination rate can become very rapid, potentially reducing photocatalytic

performance. Thus, the optimal proportion of Fe dopant in the Fe-doped TiO₂ NPs was determined to be 0.4 %.

7.3.2.2 Photocatalytic Activity of Fe-doped TiO₂

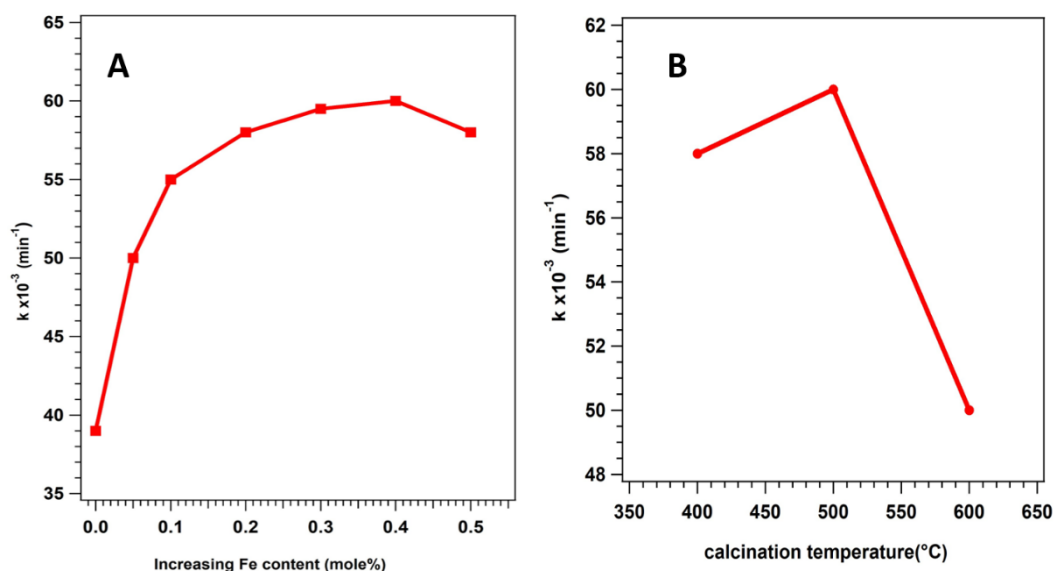
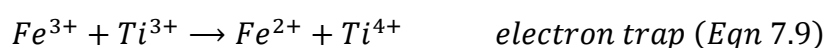
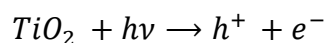


Figure 7.10 Photocatalytic activity of (A) Fe-doped TiO₂ at different Fe concentrations and (B) various calcination temperatures of 0.4%Fe-dopedTiO₂.

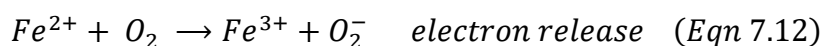
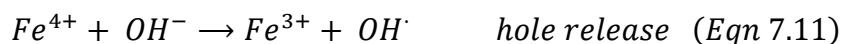
The photocatalytic pseudo-first-order oxidation rate of alcohol into aldehyde over Fe-doped TiO₂, k values are shown in Figure 7.10A. The photocatalytic activity of Fe-doped TiO₂ NPs increased steadily with the increasing amount of the Fe dopant from $39 \times 10^{-3} \text{ min}^{-1}$, for pure TiO₂, to $\sim 60 \times 10^{-3} \text{ min}^{-1}$, for 0.4% Fe-doped TiO₂ NPs. Further additions of the Fe dopant slightly reduced the reactivity to $58 \times 10^{-3} \text{ min}^{-1}$, for 0.5 % Fe-doped TiO₂ NPs. The optimized 0.4% Fe-doped TiO₂ NPs were evaluated at different calcination temperatures, from 400 to 600°C (Figure 7.10 B), indicating that the optimal photocatalytic activity was at a calcination temperature of 500°C.

A small amount of dopant Fe ions are believed to act as mediators that can affect the charge separation process, e-h recombination rate and interfacial charge transfer of TiO₂-doped catalysts.⁴⁶⁷ In Fe-doped TiO₂, the relatively unstable d⁶ orbital of Fe²⁺ could be oxidized to half-filled spin d⁵ of Fe³⁺ by the transport of electrons to

the Ti^{4+} surface or to the adsorption of O_2 on the TiO_2 surface which causes the interfacial electron transfer.⁴⁶⁷ Thus, accelerated photogenerated carrier transfer and effective charge separation can be achieved, leading to enhancements in the NPs photocatalytic activity.^{468,469}



Fe^{4+} and Fe^{2+} ions are relatively unstable, from the point of view of crystal field theory, compared to Fe^{3+} ions with half-filled d orbital ions. Therefore, the generation of the following reactions tends to result from the transfer of the trapped charges from Fe^{4+} or Fe^{2+} to the interface.⁴⁷⁰



However, Fe^{3+} can also serve as the recombination centre for photogenerated e-h⁺ pairs. When the doping concentration was increased, the distance between trapping sites decreased thereby increasing the rate of recombination while lowering the rate of the redox reaction,⁴⁷¹ thus resulting in the reduction in efficiency of the photocatalytic activity. Calcination temperature was further investigated and demonstrated that at 400°C, the NPs showed obvious photocatalytic activity which could be due to the formation of anatase. With increasing calcination temperature, the photocatalytic activity of the NPs was observed to increase and reach a maximum value at 500°C. Then, the photocatalytic activity decreased steadily as the calcination temperature further increased to 600°C.

7.3.3 V-doped TiO₂ NPs Characterization

7.3.3.1 Optimization of V-doped-TiO₂ NPs

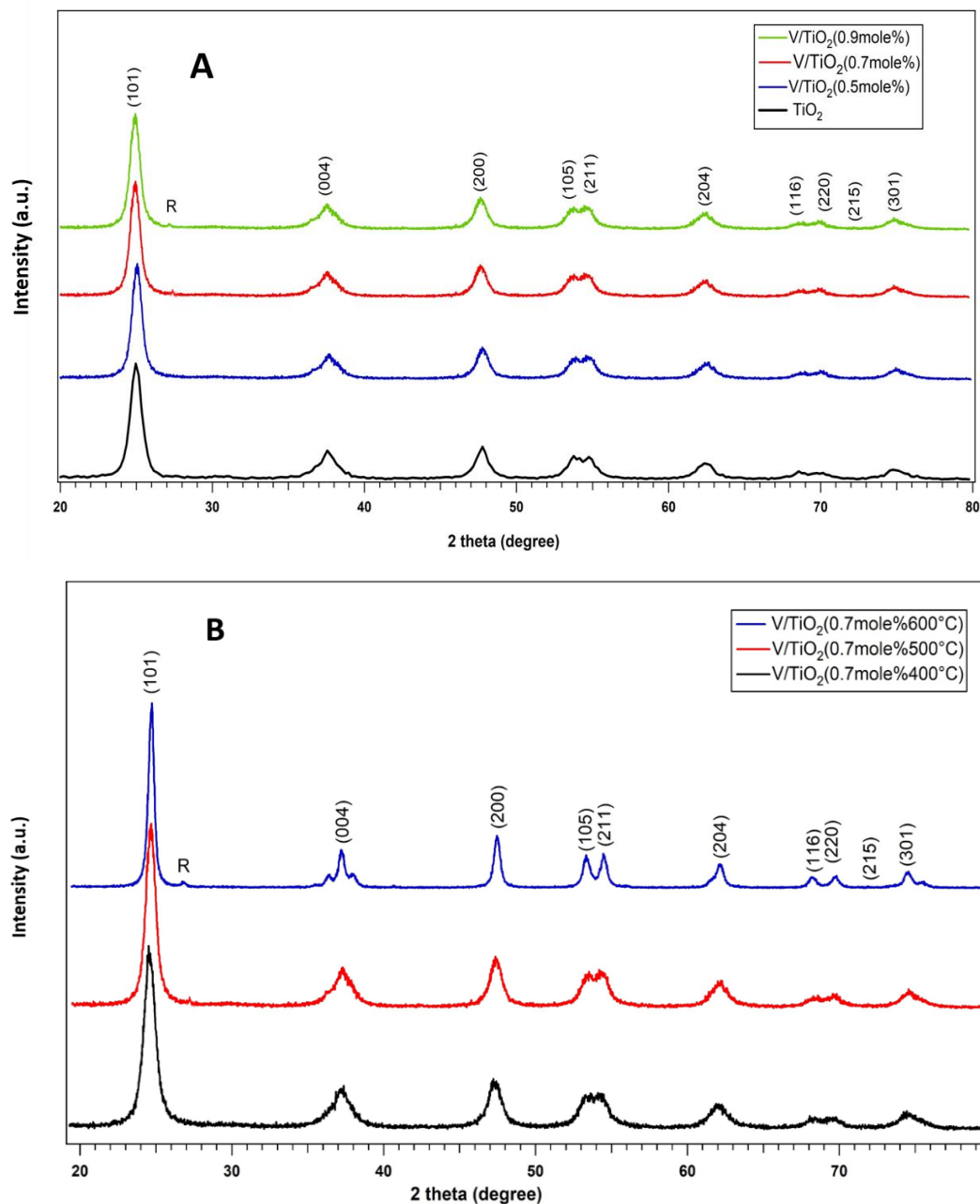


Figure 7.11 The XRD patterns of (A) TiO₂ and V-doped TiO₂ nanoparticles, and (B) 0.7mole%V-doped TiO₂ nanoparticles at different calcination temperatures.

The XRD patterns of pure TiO₂ and V-doped TiO₂ at varying ratios calcined at different temperatures are presented in Figure 7.11. The peak at $2\theta = 25.2^\circ$ is representative of the (101) anatase phase reflections and $2\theta = 27.3^\circ$ is representative of the (110) rutile

phase reflections. The rutile phase appeared at 500°C with 0.7% mole of dopant amount. An increase in V dopant amount and an increase in temperature increased in the rutile phase. Ding *et al.* have found that doping metal oxides with a melting point higher than that of TiO₂ can inhibit the transformation of anatase phase to rutile phase.⁴⁷² However, the opposite was reported by Zhou *et al.*, noting that the melting point of the doping metal oxide is lower than that of TiO₂. Zhou *et al.* have found that the promotional effect of V doping on the phase transformation was due to the fact that the melting point of V₂O₅, at 750°C, is lower than that of TiO₂, at 1720°C.⁴⁷³

By comparing the XRD patterns of pure TiO₂ and V-doped TiO₂ NPs, it was found that the addition of V to the NPs (Figure 7.11 A) did not produce any characteristic peak from V₂O₅. This means that either the V ions introduced in the NPs were well dispersed into the TiO₂ matrix or the V oxide concentrations were very low such that they cannot be detected through XRD which has a detection limit of ~1% vol. Besides, there was no peak observed for vanadium oxides such as V₂O₅ or VO₂.⁴⁷⁴ Similar results have been reported in other previous studies.⁴⁷⁵ To obtain further insight into the effects of calcining temperature, 0.7mole% V-TiO₂ was calcined at different temperatures: 400, 500 and 600°C. It was found that 500°C enabled higher activity of photocatalytic oxidation of benzyl alcohol with a crystal size of 21 nm and a bandgap of 2.88 (Figure 7.11 B).

Table 7.3 shows the bandgap and the average crystallite size of the catalysts calculated using the Scherrer formula on the anatase (101) diffraction peaks at different ratios of the V dopant as well as different calcine temperatures of 0.7%V-dopedTiO₂.

Table 7.3 Band gaps and average crystallite size of pure TiO₂ and V-doped TiO₂ from XRD analysis.

Entry	V loading (Mole%)	Bandgap (eV)	Crystallite size (nm)
1	0	3.18	25
2	0.5	2.96	21
3	0.7	2.88	20 (400°C) 21 (500°C) 22 (600°C)
4	0.9	2.60	19

As shown in Table 7.3, the crystallite size of V–dopedTiO₂ is smaller than that of pure TiO₂. In addition, values indicate that the crystallite size increases with the increase in calcination temperature because of the mixing of the anatase and the rutile phases.⁴⁷⁶

The band gaps of NPs were calculated from their diffuse reflectance spectra (Table 7.3). Pure TiO₂ exhibited the highest bandgap energy at 3.18 eV, implying a lower photocatalysis rate compared to V-doped TiO₂. The bandgap was observed to decrease steadily as the concentration of V dopant increased, with the smallest energy gap observed for 0.9 % V-doped TiO₂ at 2.60 eV.

It was found that pure TiO₂ exhibited a higher PL emission spectrum compared to V-doped TiO₂ (Figure 7.12) and, therefore, was highly susceptible to e-h recombination. The PL intensity was considerably higher when a low amount of V dopant, such as 0.3 mole %, was used compared to when higher amounts, such as 0.5 and 0.7 mole %, were used. This indicates that when the V dopant amount is too small, the recombination rate of e-h pairs remains substantially high due to the absence of adequate traps.

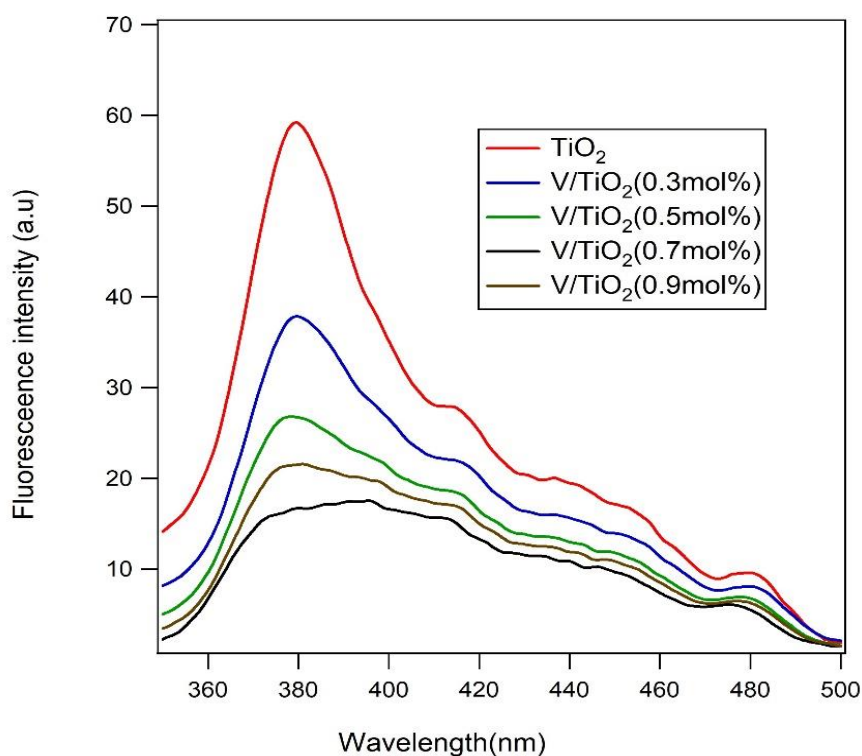


Figure 7.12 Photoluminescence spectra of pure and V-doped TiO₂ nanoparticles at different dopant concentrations.

With the following conclusions, the reduction in the strength of PL spectra for the V-doped samples can be clarified. Firstly, some of the electrons excited by UV-light passed from the TiO₂ CB to the V⁵⁺ species on the TiO₂ surface. Secondly, the other visible-light excited electrons were collected by the new energy levels (V3d (V⁴⁺)) produced within the TiO₂ bandgap,^{477,478} and then transferred to V⁵⁺ species. Then, all of these photo-generated electrons reacted on the photocatalyst surface with the adsorbed oxygen molecules. Therefore, the PL intensity decreased, thus increasing the photocatalytic activity. On the other hand, the PL intensity increased with increasing dopant amount, from 0.7% to 0.9%. This could mean that the excess dopant amount above the optimal concentration caused e-h recombination which led to a decrease in the photocatalytic efficiency. Similar results have been reported by other researchers as well.⁴⁷⁹

7.3.3.2 Photocatalytic Activity of V-doped TiO₂

Based on the k values shown in Figure 7.13, the photocatalytic oxidation efficiencies were first increased and then decreased in relation to the concentration of the V dopant in the NPs. All V-doped TiO₂ photocatalysts showed higher photocatalytic oxidation efficiency compared to pure TiO₂. However, a maximum dopant concentration was found to exist, beyond which the photocatalytic activity no longer improved.

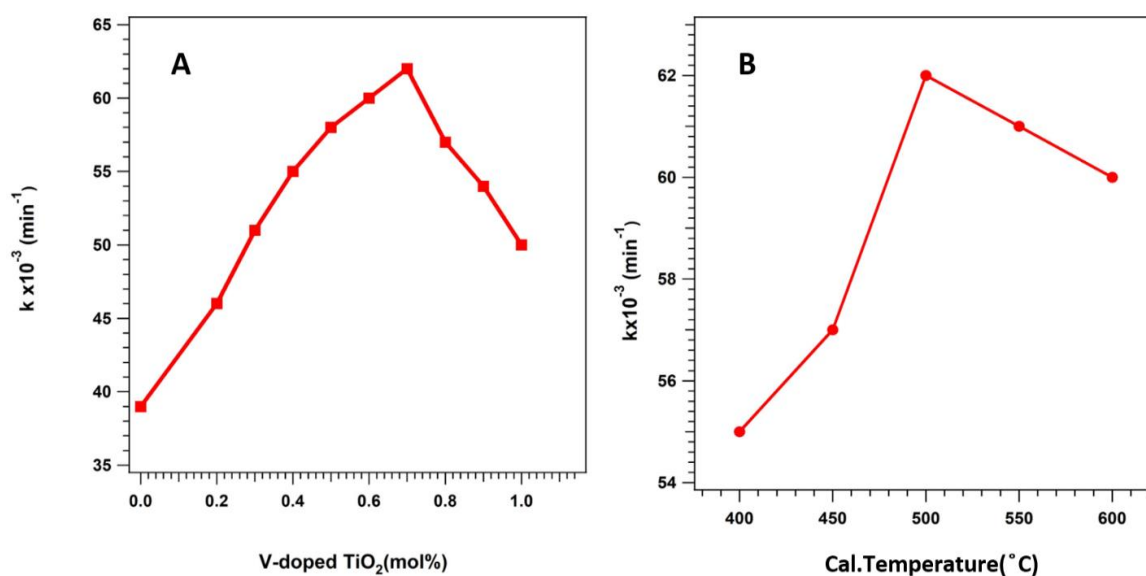


Figure 7.13 Photocatalytic activity of (A) V-doped TiO₂ at different V concentrations and (B) different calcination temperatures.

A V dopant content of 0.7% was found to achieve the highest photocatalytic oxidation efficiency. The photocatalytic activity of V-doped TiO₂ NPs increased steadily as the amount of V dopant increased from $39 \times 10^{-3} \text{ min}^{-1}$, for pure TiO₂, to $62 \times 10^{-3} \text{ min}^{-1}$, for 0.7 % V-doped TiO₂ NPs. Further increase of V dopant to 1.0 % reduced the reactivity to $50 \times 10^{-3} \text{ min}^{-1}$ (Figure 7.13). This could be due to the excess V⁵⁺ ions which became the recombination centres of electron-hole pairs in TiO₂ crystal lattices, directly affecting the photocatalytic oxidation efficiency of TiO₂.⁴⁸⁰ From Figure 7.13 B, the optimal temperature was 500°C and that could be because of right mixture phase of anatase and rutile.

7.3.4 Comparison Between P25 and Ag-, Fe- and V- doped TiO₂ NPs

Photocatalytic oxidation of benzyl alcohol into benzaldehyde under P25, synthesised-pureTiO₂ and metal dopedTiO₂ was investigated.

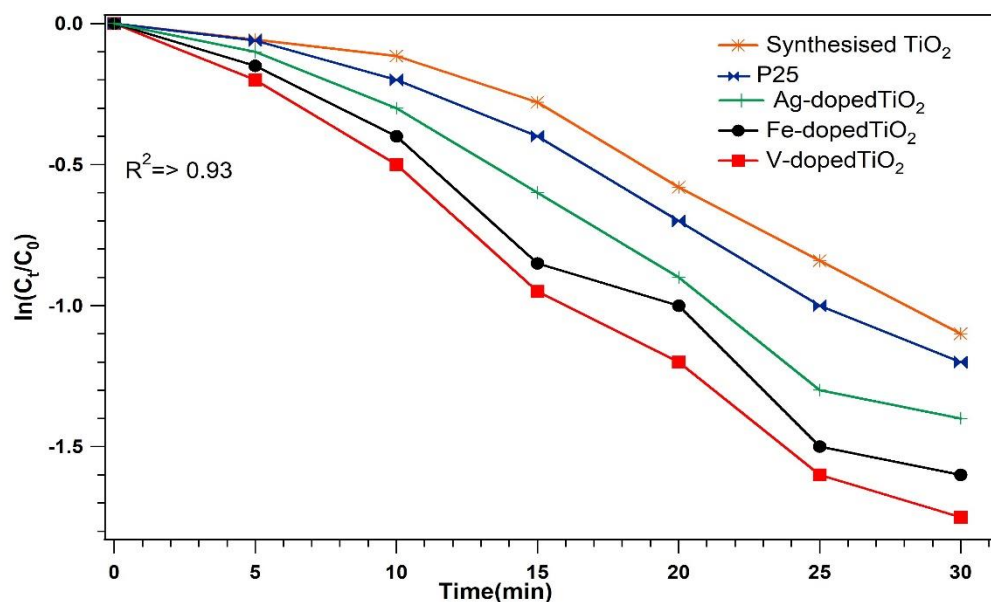


Figure 7.14 Kinetics plot of benzyl alcohol photooxidation by P25, synthesised TiO₂, 0.8Ag-dopedTiO₂, 0.4Fe-dopedTiO₂ and 0.7V-dopedTiO₂.

Figure 7.14 shows that photooxidation BA rate by P25 ($45 \times 10^{-3} \text{ min}^{-1}$) was faster than that of the synthesised TiO₂ ($39 \times 10^{-3} \text{ min}^{-1}$) but slower than the optimal metal-dopedTiO₂. The metal dopedTiO₂, showed the higher surface area and smaller band gaps, also the preparation method could potentially affect the photoactivity. From the data, which was already discussed, the optimized metal doped were; 0.8% Ag-, 0.4% Fe- and 0.7% V-doped TiO₂ with $52 \times 10^{-3} \text{ min}^{-1}$, $60 \times 10^{-3} \text{ min}^{-1}$ and $62 \times 10^{-3} \text{ min}^{-1}$ of photocatalytic activity, respectively. This means that the Ag-dopedTiO₂ NPs had the lowest efficiency, this could have been due to several reasons. First, all Ag-dopedTiO₂ NPs only displayed the anatase phase, while with Fe-dopedTiO₂ NPs as well as V-dopedTiO₂NPs showed mixed structures between anatase and rutile which might have affected their activity.⁴⁸¹ Second, increasing the dopant in Ag-TiO₂NPs

increased the crystallite size and caused broadening of the XRD, which can be attributed to the silver placed on the surface of TiO₂. Mogae *et al.* have reported that the Ag⁺ ion radius of ~126 pm is much larger than that of the Ti⁴⁺ ion, which is ~68 pm, therefore the Ag⁺ ions cannot enter the lattice of TiO₂ to form a stable solid solution. Hence, Ag⁺ ions can migrate from the grains to the TiO₂ surface during crystallization.⁴⁵¹ Also, excessive Ag can cover the surface of TiO₂, leading to a decrease in photogenerated charge carrier concentration and catalyst activity.⁴⁸² Moreover, the amount of Ag can prevent light absorption and TiO₂ adsorption of reactant molecules.⁴⁸² Third, the optimized mole ratio of Ag dopant at 0.8% resulted in bigger crystallite size compared to that in optimized Fe and V with sizes of 25 > 22 > 21 nm respectively. This could have affected the efficiency⁴⁸³ even though Ag-doped NPs showed the higher surface area and less activity, probably due to that the other dopant catalysts having mixed-phase anatase-rutile structures.⁴⁸⁴ Fourth, according to the fluorescence data, 0.8%Ag-dopedTiO₂ had higher intensity than 0.4%Fe- and 0.7%V-dopedTiO₂ when compared to that of pure TiO₂, which means the charge-carrier recombination was faster in 0.8%Ag and slower in 0.7%V catalysts. Fifth, pure TiO₂ was characterized by a sharp absorption edge with an energy band gap of ~3.18 eV whereas all metal-dopedTiO₂ showed extended absorption spectra into the visible-light region. The lowest bandgap of metal-doped NPs was for dopant V at 2.60-2.88 eV, followed by that of Fe-dopedTiO₂ which was higher at 2.96 eV, while the highest was for Ag dopant at 3.05 eV. It is a well-known fact that the reduction potential of the silver ion is sufficiently positioned to reduce photocatalytic Ag⁺ ion to Ag⁰, thus producing metallic silver on the surface of the TiO₂ nanoparticles.⁴⁸⁵

7.4 Conclusions

Although pure TiO_2 is a powerful photocatalyst of organic synthesis, its photocatalytic efficiency is low due to its high bandgap energy, at 3.18 eV, and due to its relatively large particle size. By investigating the effect of doping Ag, Fe and V to TiO_2 , the optimal calcination temperature for metal doped TiO_2 NPs were found to be 500°C. During PL characterization, it was observed that metal doped TiO_2 has a lower PL emission spectrum compared to pure TiO_2 , indicating minimal susceptibility to e-h recombination. The obtained diffuse reflectance spectra showed a reduction in bandgap energy compared to pure TiO_2 bandgap. However, it was noted that there is a limit to the amount of metal dopant that can be added and that beyond this limit, photocatalytic efficiency and activity are reduced. Excess metal dopant was found capable of accumulating and serving as centres for e-h pair recombination, thereby reducing the mass transport on the surface of the photocatalyst. Of the evaluated TiO_2 transition metal-dopants, 0.7% V-doped TiO_2 possessed the lowest bandgap, at 2.88 eV, and the highest photocatalytic activity at $62 \times 10^{-3} \text{ min}^{-1}$. It was followed by 0.4 % Fe-doped TiO_2 with a 2.93 eV bandgap and a $59 \times 10^{-3} \text{ min}^{-1}$ photocatalytic activity and then by 0.8% Ag-doped TiO_2 with a 3.05 eV bandgap and a $52 \times 10^{-3} \text{ min}^{-1}$ photocatalytic activity.

CHAPTER 8 Photocatalytic Asymmetric Epoxidation of Styrene

Photocatalytic epoxidation of styrene has the potential to enhance conversion rate, selectivity toward styrene oxide (as opposed to benzaldehyde (BAD)). The present study investigated photocatalytic epoxidation of styrene with TiO_2 photocatalyst containing NaCl as a chlorine radical source. Catalyst loading effects on the styrene conversion, reaction products and product selectivities were investigated by GC-MS and it was found that neutral pH favours the selectivity of the epoxide enantiomers. The photocatalytic epoxidation of styrene was also investigated using various concentration of NaCl as a Cl^\bullet radical source.

8.1 Introduction

8.1.1 Photocatalytic Epoxidation

Styrene, which contains an alkene attached to a benzene ring, is an important precursor for key starting material for organic synthesis. Epoxidation of styrene gives styrene oxide, which is a key intermediate required for the synthesis of fine aromatic organic chemicals and pharmaceuticals.^{486,487} Conventional dehydrochlorination of styrene to styrene oxide or styrene epoxidation by homogeneous catalysis is environmentally unfriendly due to the generation of chemical wastes.⁴⁸⁸ Industrial examples include epoxidation of styrene oxide and α -pinene oxide, which yield key carbonyl compounds such as phenylacetaldehyde and campholenic aldehyde, respectively. These chemicals are key starting materials for the synthesis of fragrances or flavours and polymers.⁴⁸⁹

Epoxides are one of the many of alkenes reactivities, also it is known as oxiranes which versatile intermediates in organic synthesis. Epoxides are cyclic ethers containing three atoms to form a triangle. Their basic chemical structure is made up of two carbon atoms from hydrocarbon molecules connected to an oxygen atom as shown in Figure 8.1.

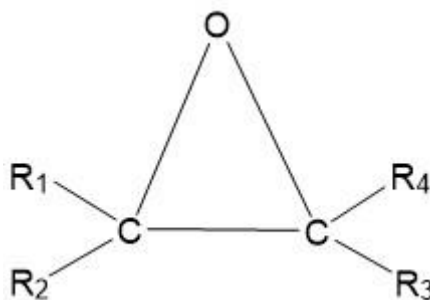


Figure 8.1 Epoxide chemical structure.

Conventional production of styrene oxide involves dehydrochlorination of styrene chlorohydrin with a base or organic peracids, H_2O_2 , or urea- H_2O_2 , which are oxidants. While organic peracids are effective in the oxidation of organic compounds, they are very expensive, hazardous to handle, non-selective for epoxidation reaction, and also result in the production of appreciable quantities of undesirable epoxidation by-products.^{490,491} In addition, styrene epoxidation based on homogeneous catalysis using transition metal complexes yields large quantities of chemical wastes due to a technical challenge in the separation of the chemicals.⁴⁹² Such challenges are being circumvented by using environmentally friendly re-usable heterogeneous catalysts, TiO_2 dispersed in silicon dioxide (SiO_2 ; silica), Titanium Silicalite-1 (TS-1), Ti-MCM-41 nanoparticles 80–160nm in diameter (Ti-MCM-41 NP), iron (Fe) or Vanadium (V) dispersed on silica (Fe or V/ SiO_2), and MgO and other alkaline earth oxides. These catalysts are used in the presence of an oxidizing agent, such as t-Butyl hydroperoxide (TBHP), H_2O_2 , or urea- H_2O adduct.⁴⁸⁷

Epoxidation of styrene produces several products, depending on the epoxidation agent and catalyst used. Peroxidative epoxidation of styrene using aqueous 30 % H_2O_2 or TBHP as an oxidizing agent in the presence of vanadium catalysts gives styrene oxide and benzaldehyde (BAD) as major products. The process also produces 1-phenylethane-1, 2-diol, phenylacetaldehyde, and benzoic acid as minor products.⁴⁹³ While styrene conversion rates using anhydrous H_2O_2 as an oxidizing agent are high, the selectivity of styrene is very poor. On the other hand, under optimized reaction conditions, TBHP or urea- H_2O adduct as oxidizing agents gives a lower conversion rate (~ 10-18 %) but exhibits higher selectivities towards styrene oxide (> 80%), than towards BAD (6–13%).⁴⁹⁴ Other minor epoxidation products particularly benzoic acid, phenylacetaldehyde, and 1-phenylethane-1, 2-diol are produced with very low selectivities in decreasing order. These reactions also demand the use of an anhydrous H_2O_2 (as the oxidizing agent) and also large heterogeneous catalyst load as high as 20-wt % of the styrene.^{495,496}

Organic solvents that are used in the epoxidation of styrene influence the selectivities of BAD. For instance, when a mixture of substrate styrene (20 mL), H_2O_2 (75 mL, 36%), Titanium Silicalite-1 (TS-1) catalyst (2.5 g) and an organic solvent (40 mL methanol, acetone or t-butyl alcohol) was stirred at 80 °C; the selectivities to BAD were as high as 90 % with styrene conversion being as high as 95 %.^{487,497} Molecular oxygen is the most desirable oxidant for the epoxidation of alkenes for environmental and economic considerations. Catalytic epoxidation of styrene with molecular oxygen has been achieved using cobalt-exchanged zeolite X in the presence of alkali metal cations (Na^+) as promoters (NaCo_x) as the catalyst. Previous studies indicate that the styrene conversion rate was very high > 99 %; though the selectivity of the styrene oxide was moderate (68 %).⁴⁸⁷ Photocatalytic epoxidation of styrene has the potential

to yield styrene oxide with even higher conversion and selectivity rates. For instance, a highly selective photocatalytic epoxidation of styrene by molecular oxygen activation under mild conditions was achieved using a highly dispersed TiO_2 photocatalyst on silica ($\text{TiO}_2/\text{SiO}_2$ nanoparticles).⁴⁹⁸ Metal-free TiO_2 catalysts can convert alkenes to epoxides under mild conditions (room temperature, O_2 , light source) in solution, as shown in Figure 8.2. Nonetheless, the selectivity is quite low to be commercially viable.⁴⁹⁹

According to literature, one of the most effective methodology to obtain enantiopure epoxides is enantioselective epoxidation produced by chiral salen Mn(III) ligand.⁵⁰⁰⁻⁵⁰⁴ Enantioselective Mn (III) salen complexes in heterogeneous and homogenous reactions have been studied.⁵⁰⁵⁻⁵⁰⁷ Heterogenized Mn(III) salen compounds have great attention due to ease of separating the products and recovering the catalysts.^{183,235,508} Furthermore, research indicates that the heterogenized Mn(III) chiral salen complexes display a great efficiency in the asymmetric epoxidation of unfunctionalized olefins.⁵⁰⁹⁻⁵¹¹

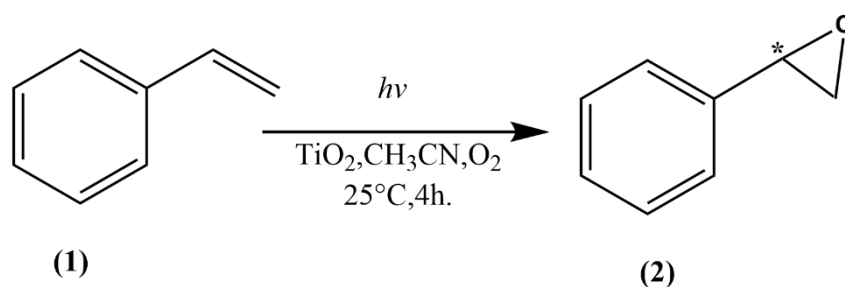


Figure 8.2 General reaction scheme for the photocatalytic epoxidation of styrene using a TiO_2 catalyst and O_2 gas under mild conditions with continuous illumination from a light source. Benzaldehyde is not seen but contains side products of the reaction.

8.1.2 Asymmetric Photocatalytic Epoxidation

In the preceding section, the epoxidation of styrene using different catalysts was undertaken. This section will cover asymmetric photocatalytic epoxidation of an

alkene. Chirality is basically a geometric property of a molecule or object that makes it non-superimposable on its mirror image either by translation or by rotation. Chirality is also referred to as stereoisomerism or enantiomeric. This property describes the handedness of a molecule. In chemistry, a chiral molecule and its mirror image have a similar chemical structure. The two enantiomers also have similar physical properties. Nonetheless, their chemical properties are very different.

Chirally pure epoxides have important uses in organic synthesis, this includes the production of enantiopure drugs.⁵¹² As a result, unlike racemic mixtures, the synthesis of pure epoxides is of great interest medicinal chemistry. Although enantiopure drugs have the same chemical structure, these drugs have different pharmacological effects that are absorption, distribution, metabolism, excretion and toxicity in the human body.⁵¹² Thus, the scientific community is interested in finding ways of the economic and affordable way of synthesizing chiral epoxides from achiral alkenes. This is important to improve the accessibility of enantiopure drugs.

There are two distinct ways of asymmetric epoxidation of an alkene. The first approach is via chiral organic peracids. Nonetheless, this method has a very low enantiomeric excess (ee) values.⁵¹³ In commercial production systems, asymmetric epoxidation is carried out via organometallic reagents either using the Sharpless⁵¹⁴ or Jacobsen⁵¹⁵ asymmetric epoxidation reactions as shown in Figure 8.3. Epoxidation reactions using Sharpless or Jacobsen methods have high enantiomeric excesses values (99%). Metal oxides and atoms lack chirality hence these reagents are used together with dialkyltartrate to locate the stereochemical pathway of the epoxidation reaction.⁵¹³

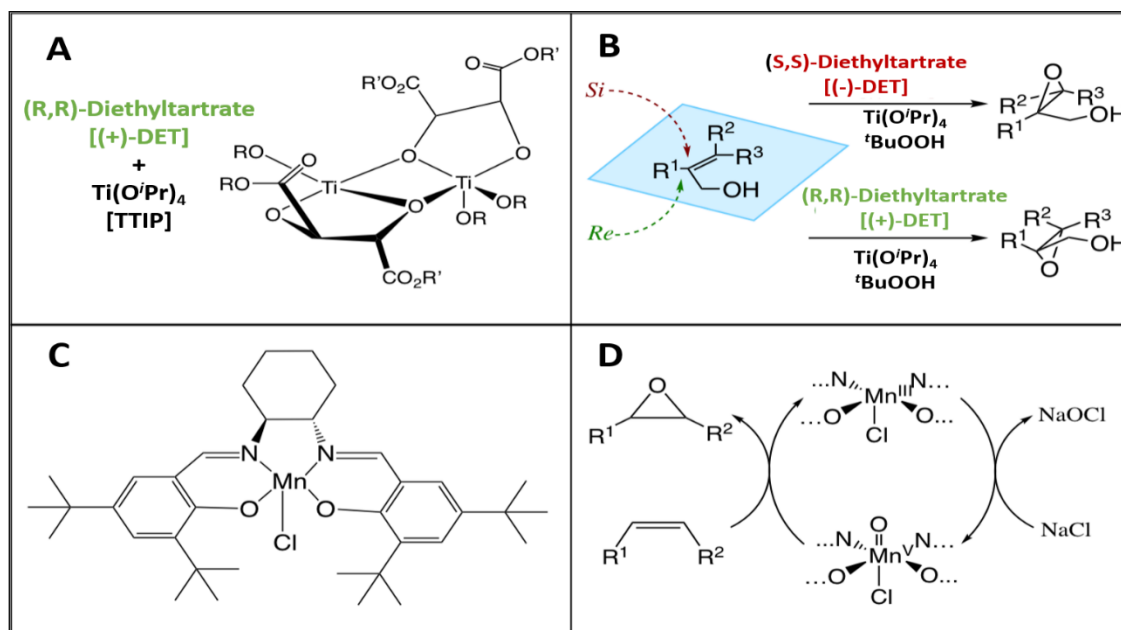


Figure 8.3 (A) Chemical structure of the catalyst produced by the Sharpless method. (B) Mechanism of Sharpless asymmetric epoxidation depicting the origin of the stereo-selectivity. (C) Chemical structure of the Jacobsen's catalyst. (D) Mechanism of the Jacobsen's asymmetric epoxidation.⁵¹⁴⁻⁵¹⁶

The Sharpless asymmetric epoxidation method is widely used in research and pharmaceutical industry, however; its major drawback is its reliance on an allylic alcohol starting material. The Sharpless method does not use an alkene functional group.^{513,514} As a result, the process has limited versatility. Nonetheless, Sharpless asymmetric epoxidation has an excellent yield and enantiomeric excess. In addition, the process makes use of cheap reagents and its predictions are spot-on. On the other hand, the Jacobsen method converts cis-alkene groups into epoxide enantiomers.⁵¹⁷ The process have an excellent enantiomeric excess however, Jacobsen method cannot achieve the same results if terminal and trans-alkenes are used.⁵¹⁷

Organometallic catalysts have been used extensively in the asymmetric epoxidation of alkenes nonetheless; research indicates that there is no pure metal oxide that can be used as a catalyst for the asymmetric epoxidation of alkenes.⁵¹⁸ A metal oxide is likely to improve the versatility of the reaction because of its apparent lack of selectivity with respect to cis- and trans- alkenes.⁵¹⁸

The present work aims to investigate photocatalytic epoxidation of styrene using Jacobson catalyst with TiO_2 photocatalyst containing NaCl as a chlorine radical source. The specific objectives are to determine the effect of various factors including TiO_2 catalysts loading, pH, and concentration of the chlorine radical source (NaCl) on the styrene conversion, styrene oxide selectivity, and styrene oxide purity in terms of enantiomeric excess (ee).

8.2 Experimental

This section describes the materials and equipment that were used in the present study. Also, the design of the photocatalytic reactor is discussed in this section.

8.2.1 Materials and Equipment

TiO_2 (Aeroxide® P25, 21 nm particle size, $\geq 99.9\%$ trace metals basis) was purchased from Evonik Industries. (R)-styrene oxide (95%, 95% ee), benzaldehyde ($\geq 99\%$), dodecane ($\geq 99\%$) and Dichloromethane, DCM ($\geq 99.5\%$), Jacobsen's catalyst (R, R) were purchased from Sigma-Aldrich. Styrene (stabilized with 10-15 ppm of 4-tert-butylcatechol, 99%) and (\pm)-styrene oxide ($\geq 98\%$) were sourced from Alfa Aesar, O_2 gas ($\geq 99.5\%$) was obtained from BOC. All chemicals were used without further purification. The metal halide UVC ConstantColor™ CMH G12 lamp was purchased from General Electric (GE) and the gearbox was purchased from LED Group Robus.

8.2.2 Photocatalytic Reactor Design

The photocatalytic reactor as shown in Figure 8.4, was handmade supplied from Hamilton Glass with two-jackets: a glass outer jacket for the reaction mixture and a cooling water glass inner jacket for the metal-halide lamp. To avoid evaporation of the solvent the glass outer jacket was extra cooled using a 2000 mL beaker filled with ice water. There are three outer jacket ports: (i) a reflux condenser was fitted to avoid

solvent evaporation issues. (ii) a cannula was fitted to extract aliquots and add more solvent (iii) a cannula was fitted to bubble O_2 through the solution. Figure 8.4 shows a custom-built photocatalytic reactor. The reactor is used in photocatalytic reactions. The setup consists of a metal halide lamp that is enclosed in a water-cooled jacket. The outer jacket contains the reaction mixture that is cooled by a beaker that is filled with water.

The experimental set-up for the photocatalytic epoxidation of styrene is as follows. The reaction mixture is comprised of an organic layer and an aqueous layer. The organic layer was prepared by mixing 50 mL of dichloromethane (DCM), 0.01 mL of dodecane (as an internal standard), 0.025 mL of styrene, and 0.03g Jacobsen's catalyst (R, R).

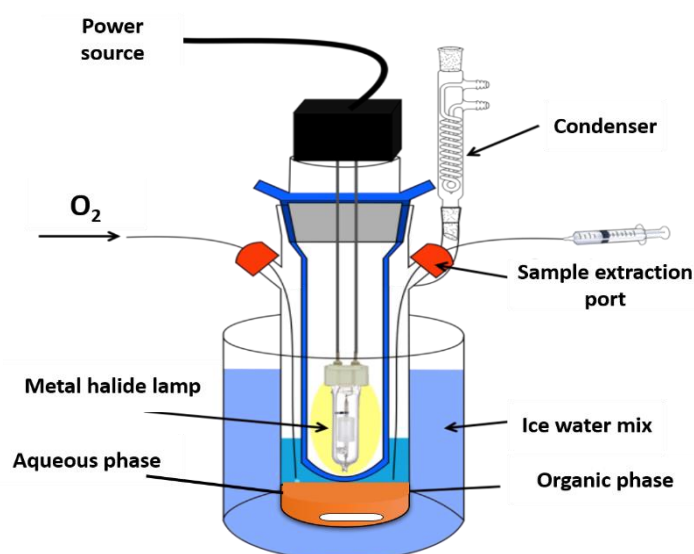


Figure 8.4 Custom-built photocatalytic reactor.

The aqueous layer was prepared by mixing 0.2 g of TiO_2 containing a chlorine radical source (NaCl), in 50 mL deionized distilled water. Gas Chromatography-Mass Spectrometry (GC-MS) analysis was performed using a Varian CP-3800 gas chromatograph with a Saturn 2200 mass spectrometer. The GC was equipped with a Restek™ β DEXse chiral capillary column (30 m length, 0.25 mm internal diameter, 0.25- μ m film thickness). A suitable method was developed for the analysis, which gave

good separation of the reaction products. The organic phase mixtures were analysed via a manual split injection method (split ratio: 100) with an injection volume of 0.6 μ L. Helium served as the carrier gas, which was set at a flow rate of 1.4 ml/min. The injector temperature was set to 250 $^{\circ}$ C and maintained at this temperature. The samples were injected into the machine using a manual method. The MS was performed through Electron Ionization (EI), scanned between 10 and 250 m/z for 11 min with an initial solvent delay of 2 min.

The effect of TiO₂ catalyst loading and reaction mixture pH on the conversion of styrene and purity of the styrene oxide for ee % were also evaluated. The effect of pH on the selectivity of the product was also assessed since styrene oxide and benzaldehyde are the major products of photocatalytic epoxidation of styrene.

The following mathematical relationships were used to calculate conversion, enantiomeric excess and yield respectively:

$$\text{Styrene conversion (\%)} = \frac{S_0 - S_f}{S_0} \times 100 \quad (\text{Eqn 8.1})$$

Where S_0 is the mole amount of styrene in the reaction mixture before irradiation and S_f is the mole amount of styrene in the reaction mixture after irradiation.

$$\text{ee(\%)} = \frac{(R - S)}{(R + S)} \times 100 \quad (\text{Eqn 8.2})$$

$$\text{BAD yield(\%)} = \frac{\text{mole of outlet of BAD}}{\text{mole inlet of styrene}} \times 100 \quad (\text{Eqn 8.3})$$

Whereas R and S refer to the arrangement of a chirality centre, R (Rectus) and it is Latin means right, S (Sinister) means left.

8.3 Results and Discussion

8.3.1 GC-MS Analysis

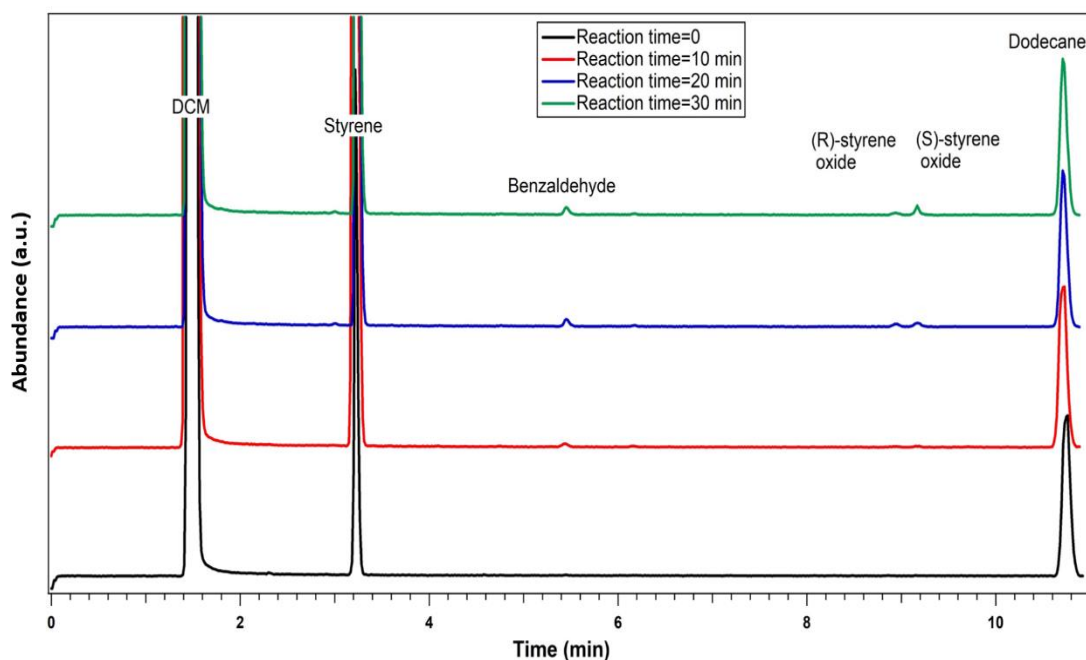
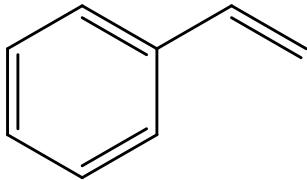
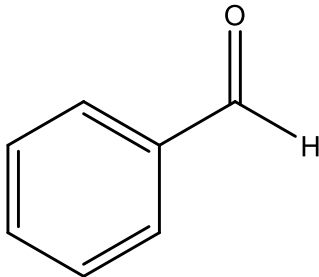
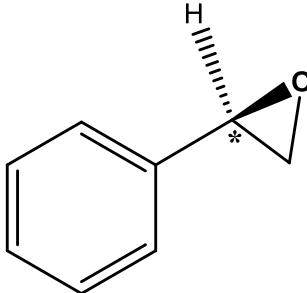
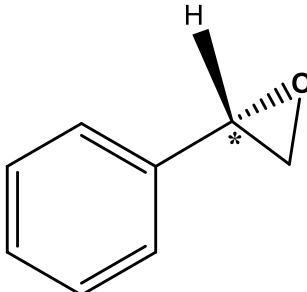
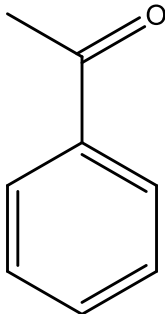


Figure 8.5 GC-MS chromatography of the final reaction mixture after 30 min from the photocatalytic reaction.

In the present study, the outputs from the photocatalytic reaction were determined using the Gas Chromatography-Mass Spectrometry (GC-MS). Figure 8.5 shows the GC-MS Chromatograph of the final photocatalytic reaction. This was obtained after a photocatalytic reaction that was carried out for 30 minutes. The reactants were a standard TiO_2 -P25 catalyst, molecular O_2 and styrene.

The chromatograph shows the same retention times and mass spectra at different peak points that is 1.5 min for DCM, 3.2 min for styrene, 5.5 min for benzaldehyde, 8.9 min for (R) -styrene oxide, 9.2 min for (S) -styrene and 10.8 min for dodecane. The retention times at various peak points are shown in Table 8.1.

Table 8.1 Overview of the retention times GC-MS signals and their corresponding compounds obtained from the final mixture in the photo-epoxidation of styrene using P25 in DCM.

Retention Time(min)	Identity	Structure	Mass form MS spectrum (m/z)
3.2	Styrene		104
5.5	Benzaldehyde		106
8.9	(R)-Styrene oxide		120
9.2	(S)-Styrene oxide		120
10.4	Acetophenone		120

8.3.2 The Effect of Catalysts (TiO₂) Loading

The number of catalysts loaded in the solution affect the photocatalytic reaction rate. At lower loading, there are not enough TiO₂ particles to be excited, so the overall reaction rate will be low. At higher loading, catalysts might block the light and will result in insufficient illumination. As a result, the reaction rate will also be reduced. Hence, an optimum catalyst loading exists which balances the light illumination and the catalyst contact with reactants. In order to find the optimum loading, the reaction rate was measured as a function of TiO₂ loading. TiO₂ was used as a photocatalyst under a normal laboratory lighting condition. The effect of TiO₂ photocatalyst loading on the styrene epoxidation conversion was evaluated to determine an optimal catalyst load for optimal conversion rate and purity (ee %). This was evaluated at a photocatalyst load ranging from 0.00 to 0.30 g (Figure 8.6).

Styrene epoxidation conversion increased with increasing catalyst load from 0.00 to 0.20 g. The optimal TiO₂ photocatalyst load was 0.20 g, where further loading did not increase the conversion rate. This optimal catalyst load corresponds to a 40 % conversion rate. This finding indicates that TiO₂ photocatalyst concentration influences the photocatalytic conversion of styrene, such that its photocatalytic activity increases with increasing photocatalyst load until a certain optimal load. This finding is consistent with those by Ghosh *et al.*, who evaluated catalytic epoxidation of styrene with Ag nanoparticles immobilized mesoporous TiO₂. The study reported that, under the same conditions, when the catalyst loading was 10mg the conversion of styrene was 75.8% and selectivity styrene oxide 89.3%. The conversion and the selectivity increased as well when the concentration of nanoparticles (25 mg) was increased to 98.1 and 94.5% respectively. At 50 mg loading the conversion dropped again and the selectivity of styrene oxide to 93.2 and 87.2 respectively.⁵¹⁹

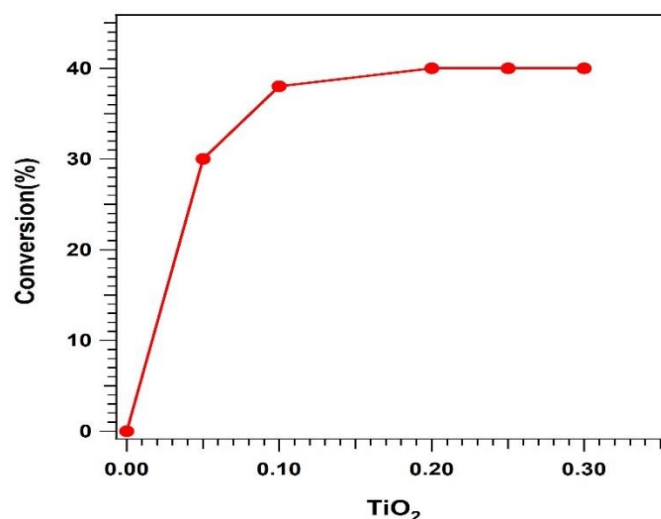


Figure 8.6 The effect of TiO₂ photocatalyst loading on the styrene conversion. Styrene conversion increased with increasing TiO₂ loading, with an optimal conversion rate (40 %) corresponding to an optimal photocatalyst load of 0.20 g. Further TiO₂ loading beyond 0.20 g did not increase the conversion rate.

The main reason why TiO₂ photocatalyst has an optimal load or concentration is due to the attenuation of photons due to radiation screening and scattering by the excess TiO₂ particles in the reaction mixture. This is especially observed with the commercial TiO₂ (Degussa P25), which has tiny crystals; where their high concentrations in reaction system provide lower photocatalytic surface area as it masks part of the photosensitive surface, thus reducing their overall photocatalytic reactivity.^{309,356}

Photocatalytic conversion of styrene yields two main products (BAD and styrene oxide), with styrene oxide exhibiting chirality due to the presence of a chiral centre at the benzylic carbon atom. Thus, styrene oxide has two possible enantiomers including (R)-styrene oxide and (S)-styrene oxide.

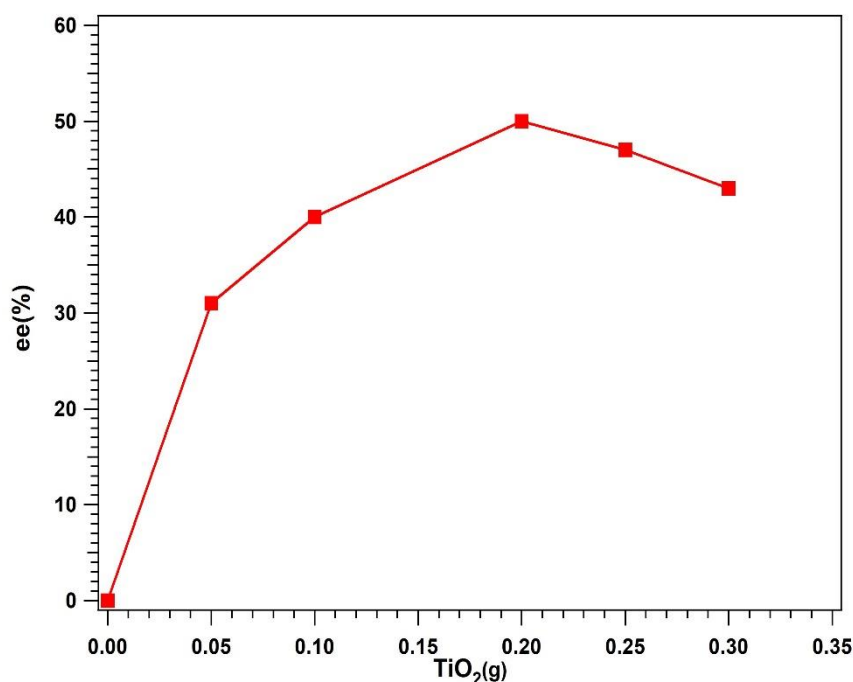


Figure 8.7 The effect of TiO₂ photocatalyst load on enantiomeric excess(ee). A photocatalyst load of 0.2 g was determined to be optimal for an optimal ee of 50 %.

If an optically pure reagent is used, only one optically pure compound will be obtained. In the present study, it was important to determine the effect of catalyst loading on the ee %, which is the difference between the relative abundance of the two enantiomers (R- and S-styrene oxides) and a measure of purity in these chiral substances. A TiO₂ photocatalyst load of 0.20g, which was determined to be optimal for styrene epoxidation conversion also resulted in an optimal ee of 50 % (Figure 8.7). Further catalyst load beyond 0.20 g resulted in a sharp decline in ee%, which implied the loss of purity of the enantiomeric mixture of styrene oxide. A lower load of TiO₂ photocatalyst implies a lower rate of photocatalysis, which results in lower purity of the styrene oxide characterized by a mixture of enantiomers forming racemic (50-50) mixture. Increasing catalyst load, which increased photocatalysis rate also appeared to have increased the purity to an optimum ee% of 50 %. These findings indicate that the purity of the styrene oxide produced was influenced by the conversion rate of styrene, such that a higher degree of conversion produced styrene oxide of high purity

while lower conversion rate resulted in styrene oxide of low purity (racemic mixture of R- and S-styrene oxides).

8.3.3 The Effect of Reactor pH Conditions

Photocatalytic is influenced by the surface properties of the catalyst (TiO_2), molecular charge and also the concentration of hydroxyl ions. Nonetheless, these factors are affected by pH. The attraction or repulsion of catalyst and an organic molecule depends on whether the organic compound is an anion or cation.

TiO_2 is known to exhibit acid-catalytic properties, meaning that both acidic pH and acidity strength affect its catalytic activity.^{209,358} Therefore, the effect of pH on TiO_2 -mediated photocatalytic conversion of styrene to R, S-styrene oxide and BAD was investigated.

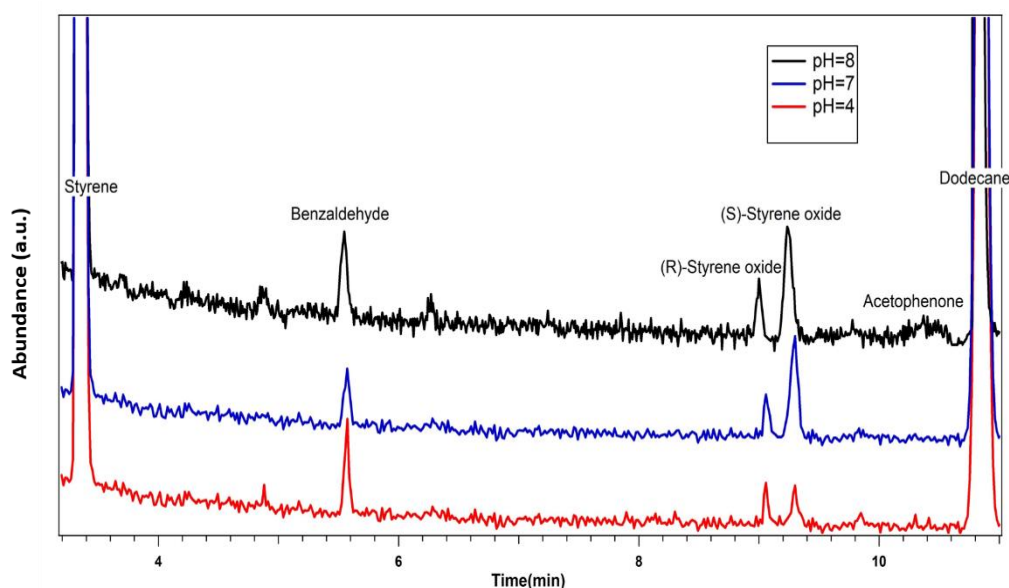


Figure 8.8 The GC-MS chromatography of the photoepoxidation reaction in acidic, neutral and basic mediums.

As shown in Figure 8.8, at pH 8, a new peak was observed at a retention time of 10.4 min. The mass spectrum of the new peak is indicated in Table 8.1. An analysis of this peak did not yield any conclusive results. Taking into consideration the chemical

structure of styrene and the molecular peak at $m/z = 120$, two probable compounds are phenylacetaldehyde and acetophenone. In this case, since the molecular peak gives rise to two different compounds there is no valid conclusion from this information. Nonetheless, the observation can be a result of peak tailing generated by the (S)-styrene oxide peak at 9.2 min. It certainly not due to co-elution of phenylacetaldehyde and acetophenone. Thus, according to Table 8.1, the peak at 10.4 min corresponds to acetophenone. The products obtained from the photocatalytic process were assigned following the findings of Fox⁵²⁰ and Ohno *et al.*⁵²¹ When the medium was acidic, more BAD was detected and equal R, S- styrene oxide.

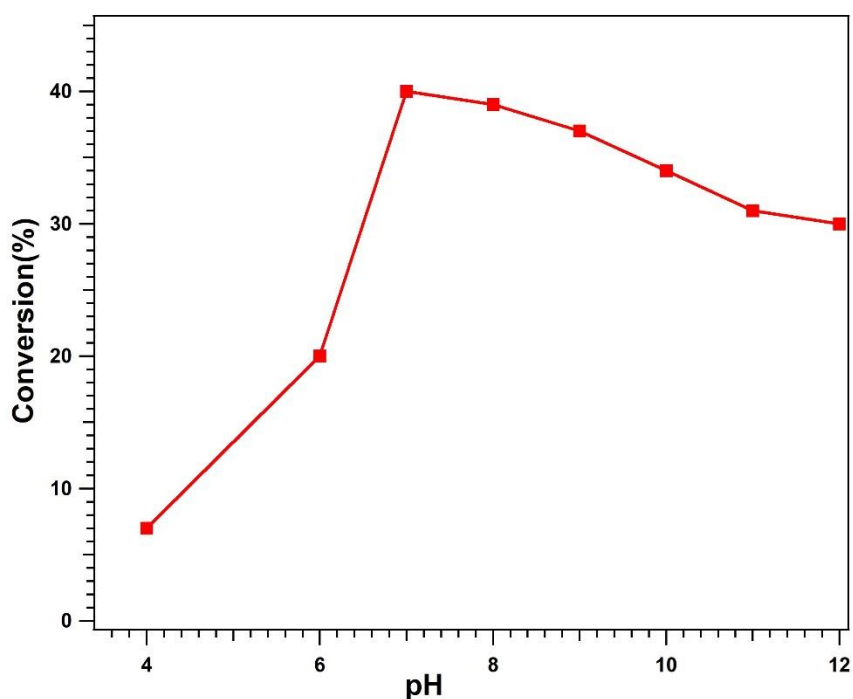


Figure 8.9 The effect of pH (pH 4-12) on the styrene epoxidation conversion rate. Styrene conversion increased with increasing pH with an optimal conversion rate (40 %) corresponding to the neutral pH 7. Alkaline pH (pH > 7-14) resulted in a decline in the styrene conversion rate to 30 %.

However, when the medium was neutral less BAD was observed and higher ee. Moreover, at pH 4, more unknown peaks were detected and less in acidic while almost clean in pH 7 beside BAD. Of the tested pH range of 4-12, a neutral pH (pH

7.0) resulted in the highest photocatalytic epoxidation of styrene, with a conversion rate of 40 % (Figure 8.9).

At acidic conditions (pH 4-6), the TiO₂-mediated photocatalytic conversion of styrene was lowest (7-20 %) followed by alkaline conditions (pH 8-12), which gave 40-30 % conversion rate. A similar finding reported by Lin *et al.* Lin and his group studied the effect of pH (6-8) on styrene conversion and they reported that the styrene conversion increased when the pH increased from 6 to 6.5- 7 and then decreased when the pH higher to 8.⁵²² Conversely, an optimal ee of 40 % was also observed at neutral pH. Under acidic conditions (pH 4 and 6), the ee was 0% implying that the styrene oxide existed as a racemic mixture containing a 50-50 mixture of both enantiomers (Figure 8.8).

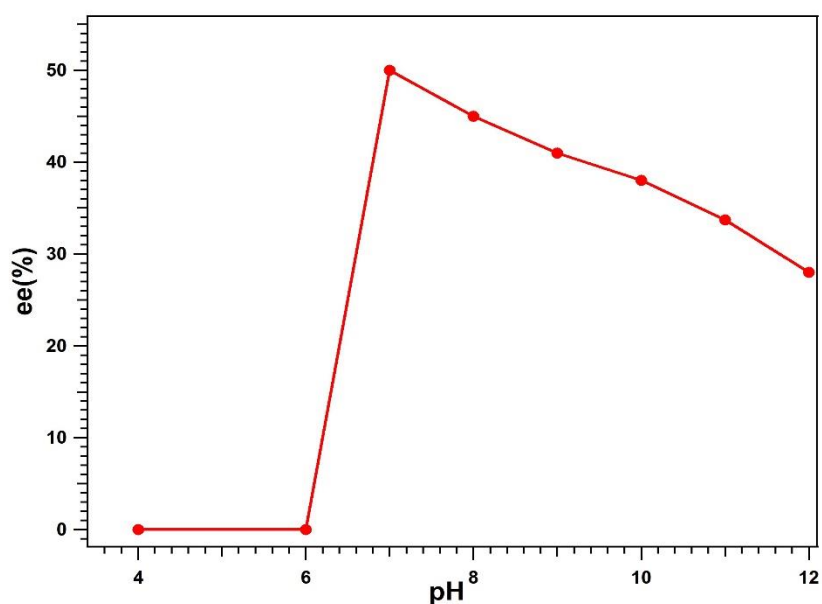


Figure 8.10 The effect of pH (pH 4-12) on the purity of styrene oxide. Enantiomeric excess (ee%) of styrene oxide was lowest (0%) at pH 4 to 6. This indicated there was a racemic mixture of styrene oxide enantiomers, which reflects low purity.

Furthermore, alkaline conditions (pH 8-12) resulted in a steady decline in ee%, which were calculated to be 45% at pH 8 to 28 % at pH 12 (Figure 8.10). Given that BAD is one of the major products of photocatalytic epoxidation of styrene, it was

important to determine the effect of pH on the yield of the unwanted BAD. Acidic reaction condition (pH 4-6) generally resulted in higher BAD yields (7-11%), followed by neutral (pH 7) condition (pH 4.8 %) and finally alkaline (pH >7-12) conditions (4.6-2.8%).

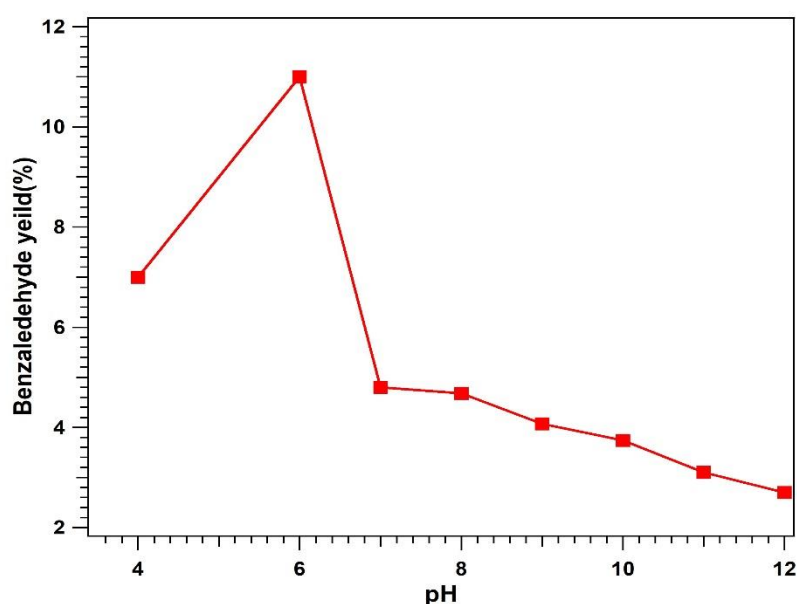


Figure 8.11 The effect of pH condition on benzaldehyde yield. The BAD yield was high (7-11%) at lower acidic pH range (4-6), which declined from pH 7-12 (4.8 - 2.8 %). Thus, lower pH conditions favoured BAD while higher pH conditions did not favour BAD.

The highest BAD yield of 11 % was observed at a mild acidic condition (pH 6) (Figure 8.11). This finding is consistent with findings previously reported in Chapter 5; which evaluated photooxidation of BA to BAD. In chapter 5, it was demonstrated that TiO₂-catalysed photoconversion of BA to BAD was optimal under acidic photoreactor condition with a pH range of 1-3, beyond which the conversion and selectivity declined. This was consistent with a study by *Marotta et al.*, which also demonstrated that increasing reactor pH from 2 to 4 resulted in a marked decrease in BA consumption and BAD formation rates, indicating reduced reaction rate.³⁰⁹ Therefore, it can be deduced that acidic photoreactor pH condition favours styrene conversion to BAD while a neutral pH favours styrene oxide formation with high purity.

8.3.4 The Effect of Radical Concentration

Sodium chloride was chosen as a cheaper and effective redox mediator to carry out the epoxidation of styrene in biphasic reactions. In this section, the effect of concentration of NaCl as a source of Cl^\bullet radical on the conversion of styrene and ee% as well as the BAD yield is presented. The conversion rate of styrene was analysed at different NaCl concentrations. As shown in Figure 8.12 at low concentration of NaCl, the rate of styrene conversion is high. An increase in NaCl from 0.0 to about 1 M NaCl reduces styrene conversion rate from 54% to less than 40% (Figure 8.12).

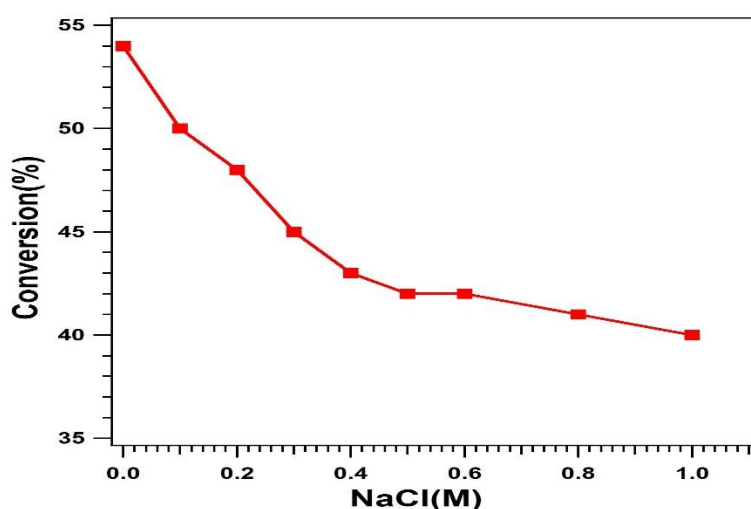


Figure 8.12 The effect of radical source concentration on styrene conversion. Styrene conversion decreased with increasing NaCl concentration from 54% (at 0.0 NaCl) to 40% (at 1 M NaCl).

The highest styrene conversion rate (54%) was observed in the absence of NaCl (0 M). Correspondingly, the conversion rate decreased with increasing NaCl concentration, with the lowest conversion (40%) observed at a molar concentration of 1 M. In comparison, the concentration of NaCl has a positive effect on the purity of styrene oxide. The relationship between NaCl concentration and ee is shown in Figure 8.13. It is evident from Figure 8.13 that the purity of styrene oxide is affected by an increase in the concentration of NaCl. A plot of NaCl against ee (%) shows that optimal

purity of 50 % ee was achieved at a NaCl concentration of 0.6 M. Above that concentration there is no further increase of ee%.

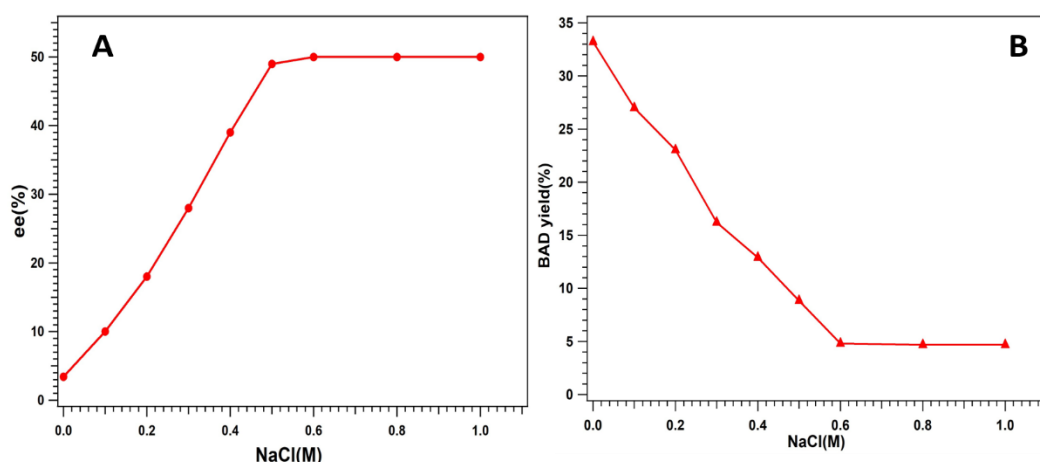


Figure 8.13 The effect of chlorine radical concentration on (A) The purity of styrene oxide and (B) Benzaldehyde yield.

The conversion decreased steadily with increasing molar concentration of NaCl (Figure 8.12). This finding indicates that the presence of a chlorine radical source decreases the styrene conversion rate in a concentration-dependent manner. The ee of styrene oxide was lowest at a molar NaCl concentration of 0.0 %. The highest ee (50 %) was achieved at a molar NaCl concentration of 0.6 M (Figure 8.13A).

The production of the undesirable BAD was also affected by NaCl concentration. The BAD yield was highest (33%) in the absence of NaCl as a Cl radical source (0 M NaCl). BAD concentration decreased steadily with increasing NaCl concentration, until a molar concentration of 0.6 M beyond, which BAD yield remained constant at 5% (Figure 8.13B).

8.3.5 Reaction Mechanism

A lot has been written about the epoxidation of alkenes by the use of TiO_2 -P25 in a single aqueous phase through a photocatalytic reaction. In an experimental study that was carried out by Ohno *et al.*, the authors reported that the photocatalytic process using TiO_2 proceed by a cationic radical olefin and O^- anion (rather than superoxide

ion O_2^-) on the surface of the TiO_2 particles (Figure 8.14).⁵²¹ In a related study, Fox, however, argued that by using TiO_2 , the oxidative cleavage of alkenes to form aldehyde and ketones go through various intermediate reaction (dioxetane).⁵²⁰

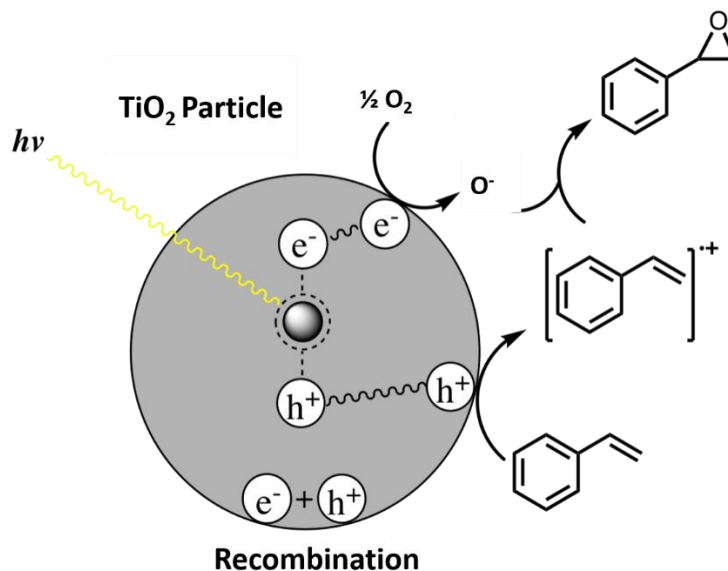


Figure 8.14 Representation of photocatalytic mechanism for the epoxidation of styrene using TiO_2 and molecular oxygen anion proposed by Ohno *et al.*⁵²¹

For the strongly enantioselective asymmetric epoxidation of olefins, Mn(III) salen complexes are excellent catalysts.⁵²³ However, The actual mechanism of epoxide production in this catalytic reaction is unclear.⁵²⁴ Various studies noted that the effect of the solvent, reaction temperature as well as the co-catalyst properties are important determinants of the activity and selectivity of the Jacobsen catalyst. Moreover, the reaction pathways are very sensitive to the process conditions.^{192,525}

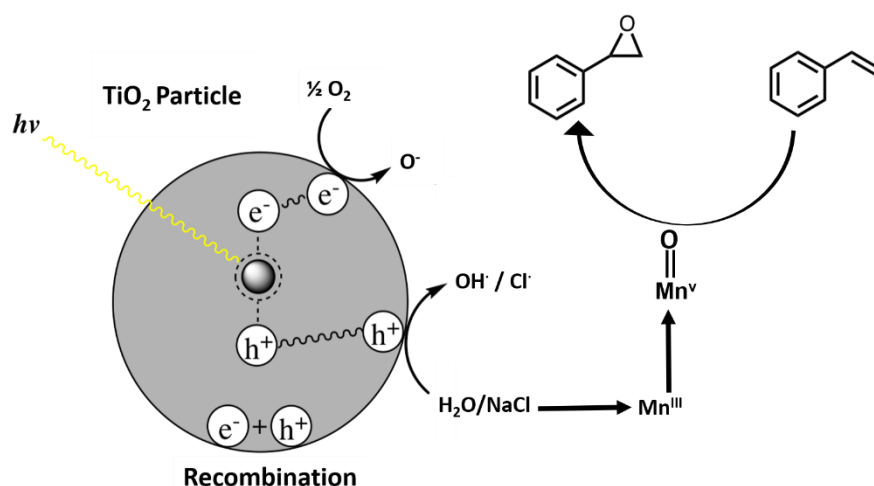


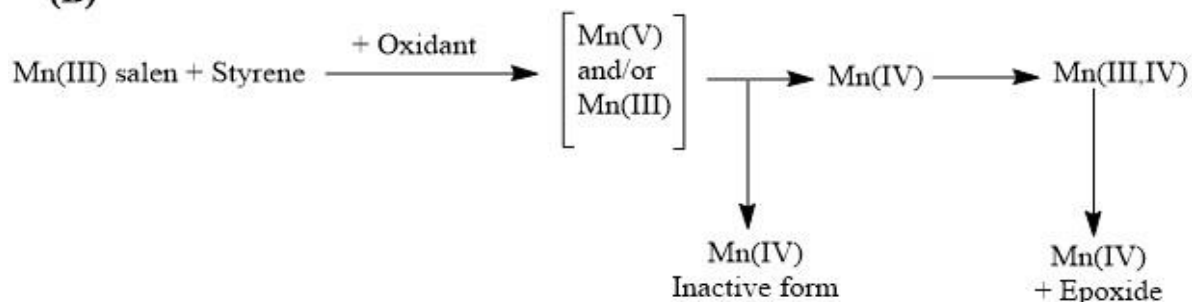
Figure 8.15 Representation of photocatalytic epoxidation mechanism of styrene in a biphasic system.

The preceding figure shows a representation of the photocatalytic epoxidation mechanism of styrene in the biphasic system (Figure 8.15). As it has proposed in chapter 4 and 5, the chlorine radical is the responsibility of the oxidation (Scheme 8.1A) the chlorine ion is oxidized by h^+ to form chlorine molecule, which upon hydrolysis results in the formation of hypochlorous acid and HCl and then produced either Cl^+ , Cl^- , ClO^- species.^{319,328}

(A)



(B)



Scheme 8.1 A) The chloride species formed in the aqueous phase.^{319,328} B) The epoxidation reaction mechanism includes the Mn species.⁵²⁴

The chloride species would oxidize Mn^{III} at the interphase region to either Mn^{III} or Mn^{V} (Scheme 8.1B). It is assumed that the $\text{Mn}(\text{III})$ salen complex is initially oxidized to $\text{Mn}(\text{V})=\text{O}$ species,⁵²⁶ for conjugated olefins, which subsequently participates in the transfer of oxygen atoms to the olefin through either direct substrate attack on the oxo ligand in a stepwise radical intermediate process⁵²⁷ or through a substrate attack on both the centre of Mn and the oxo ligand (via an oxametallic intermediate $\text{Mn}(\text{IV})$).⁵²⁸

8.4 Conclusion

The purpose of this study was to investigate photocatalytic epoxidation of styrene using Jacobson catalyst with TiO_2 photocatalyst containing NaCl as a chlorine radical source. The other objectives are to determine the effect of various factors including TiO_2 catalysts loading, pH, and concentration of the chlorine radical source (NaCl) on the styrene conversion, styrene oxide selectivity, and styrene oxide purity in terms of enantiomeric excess (ee). The study revealed that styrene epoxidation conversion increased with increasing catalyst load from 0.0 to 0.20 g. The optimal TiO_2 photocatalyst load was 0.20 g, where further loading did not increase the conversion rate. In addition, a neutral pH (pH 7.0) resulted in the highest photocatalytic epoxidation of styrene, with a conversion rate of 40 %. Moreover, the concentration of NaCl as a radical source appears to have a direct correlation with product purity (yield of unwanted BAD) and an inverse relationship with the styrene conversion rate. Nonetheless, photocatalytic epoxidation of styrene to styrene oxide is a potentially efficient and green approach to organic synthesis.

CHAPTER 9 Conclusions and Further Work

9.1 Conclusions

In this thesis, the synthesis and modification of titanium dioxide (TiO_2) nanostructures with different morphologies, optical and electrical properties were performed for enhancing their applications in photocatalytic oxidation of organic pollutants.

Ag_3PO_4 nanocrystals (cubic and particles) were synthesised via in-situ precipitation and modified for the application in photocatalytic water purification. $\text{Ag}_3\text{PO}_4/\text{TiO}_2$ composites were also successfully synthesized by in-situ precipitation techniques using both TiO_2 P25 and TiO_2 -rutile in order to enhance the photocatalytic activity of Ag_3PO_4 . In comparison to the cubic Ag_3PO_4 nanocrystals, the $\text{Ag}_3\text{PO}_4/\text{TiO}_2$ composite samples exhibited higher photocatalytic behaviour for the decomposition of methylene blue (MB) organic dye. The results indicated that the photocatalytic oxidation of the synthesised catalysts is mainly affected by their morphology, electronic structure and stability.

Biphasic selective oxidation of benzyl alcohol (BA) to benzaldehyde (BAD) using the electrolysis method in the presence of a chloride mediator presents an efficient alternative to the conventional method, was investigated in both electrochemical (ECO) and photocatalytic electrochemical oxidation (PECO). TiO_2 nanotube was synthesised by anodization method using clean Ti plates as a cathode and anode and then used it as a photoanode in PECO. The oxidation was selective towards the desired product due to the biphasic method. Various parameters have been studied toward optimization for both ECO and PECO. The conversion of BA and the yield or selectivity of BAD was higher in PECO than that in ECO, which could be

because of TiO₂ NTs are highly ordered tubular structures, and therefore, exhibit a significantly higher photocatalytic activity.

Organic synthesis is an important step in the production of crucial compounds especially, aldehydes and ketones. Enthused by the principles of green chemistry, partial photocatalytic oxidation of benzyl alcohol (BA) to benzaldehyde (BAD) using TiO₂ as a photocatalyst was improved. This was conducted using aqueous suspensions of different quantities of commercial TiO₂-P25 and (NaCl) as a mediator within an organic-phase solvent mixture, consisting of chloroform (CHCl₃) and BA. The process conditions, including TiO₂ concentration, CHCl₃/water volume ratio, pH, and acid types, significantly affected the reactivity and the conversion of BA and the selectivity to BAD. In general, the concentration of catalyst exhibited enhanced selectivity values for the production of aldehyde, the optimal was found to be 4g/L. The (40/60) CHCl₃/water volume% ratio and low pH in the range of 1-3 were found to be most effective for TiO₂ reactivity. The type of acid and mediators play a significant influence on the photocatalytic oxidation BA. It was also found that the selective photocatalytic oxidation of BA to BAD was regulated by the Hammett rule, where the reaction constants (*k*) were inversely related to that of its derivatives (σ). A possible mechanism of photocatalytic oxidation BA to BAD in two phases was proposed.

The photocatalytic N-alkylation of aniline by benzyl alcohol was successful for the synthesis of benzyaniline. This was accomplished by using standard solutions of each chemical species present within the reaction cycle, as verified by the use of GC-FID to monitor the progress of the reaction, leading to a clear assignment of the peaks in the GC-FID results. Although the reaction rate was initially slow with no benzyaniline produced, higher reaction yields were achieved by optimization of the photocatalytic reaction. The optimal reaction conditions for the oxidation of benzyl

alcohol to benzaldehyde were determined to be an acidic pH 2. However, it was found that under these conditions, the reaction was ultimately limited as aniline protonation inhibited the yield of the reaction. Furthermore, it was demonstrated that the loading of aniline in an ongoing reaction rather than injecting it into the organic layer initially produced better yields. Aniline protonation is faster than benzyl alcohol oxidation, so when aniline is present from the start of the reaction, it is first protonated before it can react with benzaldehyde, but when it is added in the reaction, it reacts with the benzaldehyde that has already been formed. This was solved by adding aniline throughout the reaction to allow it directly react with the already produced benzaldehyde. The reaction was further optimized by using liquid-pump for a continuous aniline delivery into the reaction mixture, with an optimal flow rate of 0.676 g min^{-1} giving a 3.98% of benzylideneaniline intermediate resulting in an increase of yield compared to 1.76% at constant aniline concentration. During the reaction, bubbling H_2 gas into the reaction mixture in a 1:2 ratio with N_2 produced an excess of hydrogen that forced the final step of hydrogenation to occur. After 1 hour of reaction, the benzyaniline yield was very low as expected and allowing the reaction to run longer, greater yields were observed. This is the first, report to demonstrate the photocatalytic N-alkylation of an amine using a TiO_2 photocatalyst.

Metal-doped TiO_2 catalysts with three doping metal of Ag, Fe and V were synthesized through a controlled hydrolysis method followed by a post-annealing process. XRD, BET surface area, diffuse reflectance and visible-light photoactivity were measured to characterize the physical properties of the synthesized NPs particles. By investigating the effect of doping Ag, Fe and V to TiO_2 , the optimal calcination temperature for metal-doped TiO_2 NPs were found to be 500°C . Ag doping could control the transformation of titanium from anatase to rutile while Fe doping

could reduce the temperature to form rutile. However, with V doping, the rutile phase showed when both the dopant and the temperature increased. Ag-doped NPs have the highest BET as well as the crystallite size comparing to Fe and V dopant. The evaluated TiO₂ transition metal-dopants, 0.7% V-doped TiO₂ possessed the lowest bandgap, at 2.88 eV, and the highest photocatalytic activity rate at $62 \times 10^{-3} \text{ min}^{-1}$. It was followed by 0.4 % Fe-doped TiO₂ with a 2.93 eV bandgap and a $59 \times 10^{-3} \text{ min}^{-1}$ photocatalytic activity rate and then by 0.8% Ag-doped TiO₂ with a 3.05 eV bandgap and a $52 \times 10^{-3} \text{ min}^{-1}$ photocatalytic activity.

The biphasic photo-epoxidation of styrene using a TiO₂ as a photocatalyst and NaCl as a chlorine source was investigated under mild reaction conditions. The effect of catalyst loading, NaCl concentration and pH were investigated. The study revealed that styrene epoxidation conversion increased with increasing catalyst load from 0.0 to 0.20 g. The optimal TiO₂ photocatalyst load was 0.20 g, where further loading did not increase the conversion rate. In addition, a neutral pH (pH 7.0) resulted in the highest photocatalytic epoxidation of styrene, with a conversion rate of 40 %. Moreover, the concentration of NaCl as a radical source appears to have a direct correlation with product purity (yield of unwanted BAD) and an inverse relationship with the styrene conversion rate. Nonetheless, photocatalytic epoxidation of styrene to styrene oxide is a potentially efficient and green approach to organic synthesis.

9.2 Further work

Many optimization methods will greatly assist in selecting the best conditions for optimal performance. Such optimisations should include different solvent, temperature, light source position and sufficient catalyst. Further future studies will involve further photocatalytic reactions using all the different synthesized catalysts to

obtain direct proof of the effects on the photocatalytic activity of the synthetic procedures. With the initial photocatalytic reactors design, several problems were discovered and had to be completely re-designed and ordered, reducing the number of photocatalytic reactions that could be investigated. There are still some flaws with the reactor set-up, with the evaporation of the solvent and probably the reactants during the reaction being the most significant. A further investigation that can be explored is using various other types of semiconductors and synthesis more catalyst using different methods and different morphology.

In order to determine if this has a beneficial impact on the benzyaniline yield, more work on the use of various volumes of H_2 gas flow should be investigated and investigated different sources of H_2 . For example, molybdenum disulphide complexes (MoS_2) have shown great promise for the production of hydrogen by electrochemical and photochemical water splitting. The MoS_2 complexes can be integrated into the aqueous layer with the TiO_2 photocatalyst, this could be of great impact on this photocatalytic investigation.

More work on photoepoxidation of styrene such as, synthesise chiral catalyst as well as Jacobsen's catalyst, investigate different solvent and run the reaction for a longer time. Few difficulties I faced with epoxidation of styrene, the reaction cannot run for longer than 30 minutes because of Jacobsen's catalyst was oxidized in this time. Due to the short time, we couldn't investigate more.

Bibliography

1. Campos, K.R., P.J. Coleman, J.C. Alvarez, S.D. Dreher, R.M. Garbaccio, N.K. Terrett, R.D. Tillyer, M.D. Truppo, E.R. Parmee, *The importance of synthetic chemistry in the pharmaceutical industry*. Science, 2019. **363**(6424): p. eaat0805.
2. Dighe, N.S., S.R. Pattan, D.S. Musmade, V.M. Gaware, M.B. Hole, S.R. Butle, and D.A. Nirmal, *Convergent synthesis: A strategy to synthesize compounds of biological interest*. ChemInform, 2011. **42**(29). <https://doi.org/10.1002/chin.201129232>.
3. Li, C.-J. and B.M. Trost, *Green chemistry for chemical synthesis*. Proceedings of the National Academy of Sciences, 2008. **105**(36): p. 13197-13202.
4. Rashed, M.N., *Adsorption technique for the removal of organic pollutants from water and wastewater*, in *Organic pollutants-monitoring, risk and treatment*. 2013, IntechOpen. <http://dx.doi.org/10.5772/54048>.
5. Barnabé, S., S. Brar, R. Tyagi, I. Beauchesne, and R. Surampalli, *Pre-treatment and bioconversion of wastewater sludge to value-added products—Fate of endocrine disrupting compounds*. Science of the total environment, 2009. **407**(5): p. 1471-1488.
6. Pal, A., Y. He, M. Jekel, M. Reinhard, and K.Y.-H. Gin, *Emerging contaminants of public health significance as water quality indicator compounds in the urban water cycle*. Environment international, 2014. **71**: p. 46-62.
7. Yan, S., S.B. Subramanian, R. Tyagi, R.Y. Surampalli, and T.C. Zhang, *Emerging contaminants of environmental concern: source, transport, fate, and treatment*. Practice Periodical of Hazardous, Toxic, and Radioactive Waste Management, 2010. **14**(1): p. 2-20.
8. Farrington, J.W. and H. Takada, *Persistent organic pollutants (POPs), polycyclic aromatic hydrocarbons (PAHs), and plastics: Examples of the status, trend, and cycling of organic chemicals of environmental concern in the ocean*. Oceanography, 2014. **27**(1): p. 196-213.
9. Zacharia, J.T., *Degradation Pathways of Persistent Organic Pollutants (POPs) in the Environment*, in *Persistent Organic Pollutants*. 2019, IntechOpen. <http://dx.doi.org/10.5772/intechopen.79645>
10. Chemat, F. and M.A. Vian, *Alternative solvents for natural products extraction*. 2014: Springer. <http://www.springer.com/series/11661>
11. Lohr, T.L., A.R. Mouat, N.M. Schweitzer, P.C. Stair, M. Delferro, and T.J. Marks, *Efficient catalytic greenhouse gas-free hydrogen and aldehyde formation from*

- aqueous alcohol solutions*. Energy & Environmental Science, 2017. **10**(7): p. 1558-1562.
12. Mason, B.P., K.E. Price, J.L. Steinbacher, A.R. Bogdan, and D.T. McQuade, *Greener approaches to organic synthesis using microreactor technology*. Chemical reviews, 2007. **107**(6): p. 2300-2318.
 13. Anastas, P.T. and E.S. Beach, *Green chemistry: the emergence of a transformative framework*. Green Chemistry Letters and Reviews, 2007. **1**(1): p. 9-24.
 14. *Basics of Green Chemistry*. United States Environmental Protection Agency 2017; Available from: <https://www.epa.gov/greenchemistry/basics-green-chemistry#twelve>.
 15. Anastas, P.T., M.M. Kirchhoff, and T.C. Williamson, *Catalysis as a foundational pillar of green chemistry*. Applied Catalysis A: General, 2001. **221**(1-2): p. 3-13.
 16. Sheldon, R.A., *Fundamentals of green chemistry: efficiency in reaction design*. Chemical Society Reviews, 2012. **41**(4): p. 1437-1451.
 17. Khare, R., A. Kulshrestha, J. Pandey, and N. Singh, *Importance of Green chemistry in oxidation and reduction*. International Journal of Engineering and Technical Research. **7**(7).
 18. Anastas, P.T. and J.C. Warner, *Green chemistry : theory and practice*. Print book : English ed. 1998: Oxford [England] ; New York : Oxford University Press, 1998.
 19. Trost, B.M., *The atom economy--a search for synthetic efficiency*. Science, 1991. **254**(5037): p. 1471-1477.
 20. Anastas, P. and J. Zimmerman, *The twelve principles of green engineering as a foundation for sustainability*, in *Sustainability Science and Engineering*. 2006, Elsevier. p. 11-32.
 21. Sheldon, R.A., *The E factor 25 years on: the rise of green chemistry and sustainability*. Green Chemistry, 2017. **19**(1): p. 18-43.
 22. Anastas, N.D. and J.C. Warner, *The incorporation of hazard reduction as a chemical design criterion in green chemistry*. Chemical Health and Safety, 2005. **2**(12): p. 9-13.
 23. DeVito, S.C. and R.L. Garrett, *Designing safer chemicals: Green chemistry for pollution prevention*. 1996: ACS Publications. doi: 10.1021/bk-1996-0640.ch010
 24. Dunn, P.J., *The importance of green chemistry in process research and development*. Chemical Society Reviews, 2012. **41**(4): p. 1452-1461.
 25. Centi, G. and S. Perathoner, *Catalysis and sustainable (green) chemistry*. Catalysis Today, 2003. **77**(4): p. 287-297.
 26. Anastas, P.T., L.B. Bartlett, M.M. Kirchhoff, and T.C. Williamson, *The role of catalysis in the design, development, and implementation of green chemistry*. Catalysis Today, 2000. **55**(1-2): p. 11-22.

27. Cole-Hamilton, D.J. and R.P. Tooze, *Catalyst separation, recovery and recycling: chemistry and process design*. Vol. 30. 2006: Springer Science & Business Media.
28. Shen, Y., H. Tang, and S. Ding, *Catalyst separation in atom transfer radical polymerization*. Progress in polymer science, 2004. **29**(10): p. 1053-1078.
29. Pinault, N. and D.W. Bruce, *Homogeneous catalysts based on water-soluble phosphines*. Coordination chemistry reviews, 2003. **241**(1-2): p. 1-25.
30. Hájek, M., F. Skopal, L. Čapek, M. Černoch, and P. Kutálek, *Ethanolysis of rapeseed oil by KOH as homogeneous and as heterogeneous catalyst supported on alumina and CaO*. Energy, 2012. **48**(1): p. 392-397.
31. Grisel, R., P. Kooyman, and B. Nieuwenhuys, *Influence of the preparation of Au/Al₂O₃ on CH₄ oxidation activity*. Journal of Catalysis, 2000. **191**(2): p. 430-437.
32. Jia, J., K. Haraki, J.N. Kondo, K. Domen, and K. Tamaru, *Selective hydrogenation of acetylene over Au/Al₂O₃ catalyst*. The Journal of Physical Chemistry B, 2000. **104**(47): p. 11153-11156.
33. Berndt, H., I. Pitsch, S. Evert, K. Struve, M.-M. Pohl, J. Radnik, and A. Martin, *Oxygen adsorption on Au/Al₂O₃ catalysts and relation to the catalytic oxidation of ethylene glycol to glycolic acid*. Applied Catalysis A: General, 2003. **244**(1): p. 169-179.
34. Galeano, C., R. Güttel, M. Paul, P. Arnal, A.H. Lu, and F. Schüth, *Yolk-Shell Gold Nanoparticles as Model Materials for Support-Effect Studies in Heterogeneous Catalysis: Au, @ C and Au, @ ZrO₂ for CO Oxidation as an Example*. Chemistry–A European Journal, 2011. **17**(30): p. 8434-8439.
35. Prati, L. and F. Porta, *Oxidation of alcohols and sugars using Au/C catalysts: Part 1. Alcohols*. Applied Catalysis A: General, 2005. **291**(1-2): p. 199-203.
36. Hutchings, G.J., S. Carrettin, P. Landon, J.K. Edwards, D. Enache, D.W. Knight, . . . A.F. Carley, *New approaches to designing selective oxidation catalysts: Au/C a versatile catalyst*. Topics in catalysis, 2006. **38**(4): p. 223-230.
37. Kumar, P.S.S., R. Sivakumar, S. Anandan, J. Madhavan, P. Maruthamuthu, and M. Ashokkumar, *Photocatalytic degradation of Acid Red 88 using Au–TiO₂ nanoparticles in aqueous solutions*. water research, 2008. **42**(19): p. 4878-4884.
38. Lee, I., J.B. Joo, Y. Yin, and F. Zaera, *A yolk@ shell nanoarchitecture for Au/TiO₂ catalysts*. Angewandte Chemie International Edition, 2011. **50**(43): p. 10208-10211.
39. Khan, M.M., J. Lee, and M.H. Cho, *Au@ TiO₂ nanocomposites for the catalytic degradation of methyl orange and methylene blue: an electron relay effect*. Journal of Industrial and Engineering Chemistry, 2014. **20**(4): p. 1584-1590.
40. Tian, T., Y. Liu, and X. Zhang, *Bimetallic synergistic Au/CuO-hydroxyapatite catalyst for aerobic oxidation of alcohols*. Chinese Journal of Catalysis, 2015. **36**(8): p. 1358-1364.

41. Gamboa-Rosales, N., J. Ayastuy, Z. Boukha, N. Bion, D. Duprez, J. Perez-Omil, E. del Río, M. Gutierrez-Ortiz, *Ceria-supported Au–CuO and Au–Co₃O₄ catalysts for CO oxidation: An 18O/16O isotopic exchange study*. Applied Catalysis B: Environmental, 2015. **168**: p. 87-97.
42. Jia, Q., D. Zhao, B. Tang, N. Zhao, H. Li, Y. Sang, N. Bao, X. Zhang, X. Xu, H. Liu, *Synergistic catalysis of Au–Cu/TiO₂ 2-NB nanopaper in aerobic oxidation of benzyl alcohol*. Journal of Materials Chemistry A, 2014. **2**(38): p. 16292-16298.
43. Enache, D.I., J.K. Edwards, P. Landon, B. Solsona-Espriu, A.F. Carley, A.A. Herzing, M. Watanabe, C.J. Kiely, D.W. Knight, G.J. Hutchings, *Solvent-free oxidation of primary alcohols to aldehydes using Au-Pd/TiO₂ catalysts*. Science, 2006. **311**(5759): p. 362-365.
44. Bowker, M., C. Morton, J. Kennedy, H. Bahruji, J. Greves, W. Jones, P.R. Davies, C. Brookes, P.P. Wells, N. Dimitratos, *Hydrogen production by photoreforming of biofuels using Au, Pd and Au–Pd/TiO₂ photocatalysts*. Journal of Catalysis, 2014. **310**: p. 10-15.
45. Hong, Y., X. Jing, J. Huang, D. Sun, T. Odoom-Wubah, F. Yang, M. Du, Q. Li, *Biosynthesized bimetallic Au–Pd nanoparticles supported on TiO₂ for solvent-free oxidation of benzyl alcohol*. ACS Sustainable Chemistry & Engineering, 2014. **2**(7): p. 1752-1759.
46. Lee, J., J.C. Park, and H. Song, *A nanoreactor framework of a Au@ SiO₂ yolk/shell structure for catalytic reduction of p-nitrophenol*. Advanced Materials, 2008. **20**(8): p. 1523-1528.
47. Lee, J., J.C. Park, J.U. Bang, and H. Song, *Precise tuning of porosity and surface functionality in Au@ SiO₂ nanoreactors for high catalytic efficiency*. Chemistry of Materials, 2008. **20**(18): p. 5839-5844.
48. Lu, Y., Y. Yin, Z.-Y. Li, and Y. Xia, *Synthesis and self-assembly of Au@ SiO₂ core-shell colloids*. Nano Letters, 2002. **2**(7): p. 785-788.
49. Ali, M.E., M.M. Rahman, S.M. Sarkar, and S.B.A. Hamid, *Heterogeneous metal catalysts for oxidation reactions*. Journal of Nanomaterials, 2014. **2014**: p. 209.
50. Westermann, T. and T. Melin, *Flow-through catalytic membrane reactors—Principles and applications*. Chemical Engineering and Processing: Process Intensification, 2009. **48**(1): p. 17-28.
51. Degenstein, N., R. Subramanian, and L. Schmidt, *Partial oxidation of n-hexadecane at short contact times: Catalyst and washcoat loading and catalyst morphology*. Applied Catalysis A: General, 2006. **305**(2): p. 146-159.
52. Keller, N., C. Pham-Huu, S. Roy, M. Ledoux, C. Estournes, and J. Guille, *Influence of the preparation conditions on the synthesis of high surface area SiC for use as a*

- heterogeneous catalyst support*. Journal of materials science, 1999. **34**(13): p. 3189-3202.
53. Clacens, J.-M., Y. Pouilloux, and J. Barrault, *Selective etherification of glycerol to polyglycerols over impregnated basic MCM-41 type mesoporous catalysts*. Applied Catalysis A: General, 2002. **227**(1-2): p. 181-190.
 54. Dapurkar, S.E., A. Sakthivel, and P. Selvam, *Novel mesoporous (Cr) MCM-48 molecular sieves: Promising heterogeneous catalysts for selective oxidation reactions*. New Journal of Chemistry, 2003. **27**(8): p. 1184-1190.
 55. Sakthivel, A. and P. Selvam, *Mesoporous (Cr) MCM-41: A mild and efficient heterogeneous catalyst for selective oxidation of cyclohexane*. Journal of Catalysis, 2002. **211**(1): p. 134-143.
 56. Song, Y., D. Johnson, R. Peng, D.K. Hensley, P.V. Bonnesen, L. Liang, . . . R. Qiao, *A physical catalyst for the electrolysis of nitrogen to ammonia*. Science advances, 2018. **4**(4): p. e1700336.
 57. Licht, S., B. Cui, B. Wang, F.-F. Li, J. Lau, and S. Liu, *Ammonia synthesis by N₂ and steam electrolysis in molten hydroxide suspensions of nanoscale Fe₂O₃*. Science, 2014. **345**(6197): p. 637-640.
 58. Onuegbu, T.O., Adaora & Ekeoma, Moses, *THE ROLE OF CATALYSTS IN GREEN SYNTHESIS OF CHEMICALS FOR SUSTAINABLE FUTURE*. Journal of Basic Physical Research 41-8411 ONLINE 2011. **2**: p. pp 86-92.
 59. Te, M., C. Fairbridge, and Z. Ring, *Oxidation reactivities of dibenzothiophenes in polyoxometalate/H₂O₂ and formic acid/H₂O₂ systems*. Applied Catalysis A: General, 2001. **219**(1-2): p. 267-280.
 60. Bolm, C. and F. Bienewald, *Asymmetric sulfide oxidation with vanadium catalysts and H₂O₂*. Angewandte Chemie International Edition in English, 1996. **34**(23-24): p. 2640-2642.
 61. Muruganandham, M. and M. Swaminathan, *Photochemical oxidation of reactive azo dye with UV-H₂O₂ process*. Dyes and pigments, 2004. **62**(3): p. 269-275.
 62. Gutscher, M., M.C. Sobotta, G.H. Wabnitz, S. Ballikaya, A.J. Meyer, Y. Samstag, and T.P. Dick, *Proximity-based protein thiol oxidation by H₂O₂-scavenging peroxidases*. Journal of Biological Chemistry, 2009. **284**(46): p. 31532-31540.
 63. Szpyrkowicz, L., C. Juzzolino, and S.N. Kaul, *A comparative study on oxidation of disperse dyes by electrochemical process, ozone, hypochlorite and Fenton reagent*. Water research, 2001. **35**(9): p. 2129-2136.
 64. Benitez, F.J., J.L. Acero, and F.J. Real, *Degradation of carbofuran by using ozone, UV radiation and advanced oxidation processes*. Journal of hazardous materials, 2002. **89**(1): p. 51-65.

65. Hosokawa, S. and S. Ichimura, *Ozone jet generator as an oxidizing reagent source for preparation of superconducting oxide thin film*. Review of scientific instruments, 1991. **62**(6): p. 1614-1619.
66. Kim, M.-J. and J. Nriagu, *Oxidation of arsenite in groundwater using ozone and oxygen*. Science of the total environment, 2000. **247**(1): p. 71-79.
67. Schröder, H.F. and R.J. Meesters, *Stability of fluorinated surfactants in advanced oxidation processes—A follow up of degradation products using flow injection–mass spectrometry, liquid chromatography–mass spectrometry and liquid chromatography–multiple stage mass spectrometry*. Journal of Chromatography A, 2005. **1082**(1): p. 110-119.
68. Chambers, R.D., D. Holling, A.J. Rees, and G. Sandford, *Microreactors for oxidations using fluorine*. Journal of fluorine chemistry, 2003. **119**(1): p. 81-82.
69. Liang, A., J. Peng, Q. Liu, G. Wen, Z. Lu, and Z. Jiang, *Highly sensitive and selective determination of fluorine ion by graphene oxide/nanogold resonance Rayleigh scattering-energy transfer analytical platform*. Food chemistry, 2015. **181**: p. 38-42.
70. Sharma, V.K., *Oxidative transformations of environmental pharmaceuticals by Cl₂, ClO₂, O₃, and Fe (VI): kinetics assessment*. Chemosphere, 2008. **73**(9): p. 1379-1386.
71. Lierse, C., J.C. Sullivan, and K.H. Schmidt, *Rates of oxidation of selected actinides by Cl₂*. Inorganic Chemistry, 1987. **26**(9): p. 1408-1410.
72. Hirao, T., M. Mori, and Y. Ohshiro, *VO (OR) Cl₂-induced oxidative aromatization of alpha.,. beta.-unsaturated cyclohexenones*. The Journal of Organic Chemistry, 1990. **55**(1): p. 358-360.
73. Michalski, G., M. Kolanowski, and K.M. Riha, *Oxygen and nitrogen isotopic composition of nitrate in commercial fertilizers, nitric acid, and reagent salts*. Isotopes in environmental and health studies, 2015. **51**(3): p. 382-391.
74. Ghorbani-Choghamarani, A., M. Nikoorazm, H. Goudarziafshar, L. Shiri, and Z. Chenani, *Oxidation of Hantzsch 1, 4-dihydropyridines using supported nitric acid on silica gel and poly vinyl pyrrolidone (PVP) under mild and heterogeneous conditions*. Bulletin of the Korean Chemical Society, 2009. **30**(4): p. 972-974.
75. Heravi, M.M., P. Kazemian, H.A. Oskooie, and M. Ghassemzadeh, *HNO₃/Silica gel supported CAN; oxidative deprotection of benzylic tetrahydropyranyl ethers under solvent-free conditions using microwaves*. Journal of Chemical Research, 2005. **2005**(2): p. 105-106.
76. Montazerozohori, M., B. Karami, and M. Azizi, *Molybdate sulfuric acid (MSA): a novel and efficient solid acid reagent for the oxidation of thiols to symmetrical disulfides*. Arkivoc, 2007. **1**: p. 99-104.

77. Ma, Y., X. Jin, M. Zhou, Z. Zhang, X. Teng, and H. Chen, *Chemiluminescence behavior based on oxidation reaction of rhodamine B with cerium (IV) in sulfuric acid medium*. *Analytica chimica acta*, 2003. **489**(2): p. 173-181.
78. AliáZolfigol, M. and A. GhorbaniáChoghamarani, *Silica modified sulfuric acid/NaNO₂ as a novel heterogeneous system for the oxidation of 1, 4-dihydropyridines under mild conditions*. *Green Chemistry*, 2002. **4**(6): p. 562-564.
79. Nielsen, A.T., R.L. Atkins, W.P. Norris, C.L. Coon, and M.E. Sitzmann, *Synthesis of polynitro compounds. Peroxydisulfuric acid oxidation of polynitroarylamines to polynitro aromatics*. *The Journal of Organic Chemistry*, 1980. **45**(12): p. 2341-2347.
80. Hach, C.C., S.V. Brayton, and A.B. Kopelove, *A powerful Kjeldahl nitrogen method using peroxymonosulfuric acid*. *Journal of Agricultural and Food Chemistry*, 1985. **33**(6): p. 1117-1123.
81. Mounsey, D.M. and D.B. Mobbs, *Separation of cobalt and nickel by oxidative precipitation with peroxymonosulfuric acid*. 1983, Google Patents.
82. Damm, J.H., C. Hardacre, R.M. Kalin, and K.P. Walsh, *Kinetics of the oxidation of methyl tert-butyl ether (MTBE) by potassium permanganate*. *Water Research*, 2002. **36**(14): p. 3638-3646.
83. Sorlini, S. and F. Gialdini, *Conventional oxidation treatments for the removal of arsenic with chlorine dioxide, hypochlorite, potassium permanganate and monochloramine*. *Water Research*, 2010. **44**(19): p. 5653-5659.
84. Demir, A.S. and H. Findik, *Potassium permanganate/carboxylic acid/organic solvent: a powerful reagent for enone oxidation and aryl coupling reactions*. *Tetrahedron*, 2008. **64**(27): p. 6196-6201.
85. Aizpurua, J., M. Juaristi, B. Lecea, and C. Palomo, *Reagents and synthetic methods—40: halosilanes/chromium trioxide as efficient oxidizing reagents*. *Tetrahedron*, 1985. **41**(14): p. 2903-2911.
86. Lou, J.-D. and Z.-N. Xu, *Selective oxidation of primary alcohols with chromium trioxide under solvent free conditions*. *Tetrahedron letters*, 2002. **43**(35): p. 6095-6097.
87. Borkar, S.D. and B.M. Khadilkar, *A convenient method for the synthesis of benzophenones using silica gel supported chromium trioxide reagent*. *Synthetic communications*, 1999. **29**(23): p. 4295-4298.
88. Tamami, B. and N. Goudarzian, *Poly (vinylpyridine N-oxide) supported dichromates as new effective, mild and versatile oxidizing reagents for various organic compounds*. *European polymer journal*, 1992. **28**(9): p. 1035-1038.
89. Seo, H.-B., H.-J. Kim, O.-K. Lee, J.-H. Ha, H.-Y. Lee, and K.-H. Jung, *Measurement of ethanol concentration using solvent extraction and dichromate oxidation and its*

- application to bioethanol production process*. Journal of industrial microbiology & biotechnology, 2009. **36**(2): p. 285-292.
90. Hajipour, A.R., I. Mohammadpoor-Baltork, and K. Niknam, *Benzyltriphenylphosphonium dichromate as a mild reagent for the oxidation of organic compounds*. Organic preparations and procedures international, 1999. **31**(3): p. 335-341.
 91. Ashdown, B., D. Stricof, M. May, S.J. Sherman, and R.F. Carmody, *Hydrogen peroxide poisoning causing brain infarction: neuroimaging findings*. AJR. American journal of roentgenology, 1998. **170**(6): p. 1653-1655.
 92. Sagripant, J. and K. Kraemer, *Site-specific oxidative DNA damage at polyguanosines produced by copper plus hydrogen peroxide*. Journal of Biological Chemistry, 1989. **264**(3): p. 1729-1734.
 93. Lacey, R. and G. Walker, *Provision and control of water for healthcare purposes*, in *Decontamination in Hospitals and Healthcare*. 2014, Elsevier. p. 254-298.
 94. Fiessinger, F., Y. Richard, A. Montiel, and P. Musquere, *Advantages and disadvantages of chemical oxidation and disinfection by ozone and chlorine dioxide*. Science of the Total Environment, 1981. **18**: p. 245-261.
 95. Rice, R.G. and M. Gomez-Taylor, *Occurrence of by-products of strong oxidants reacting with drinking water contaminants--scope of the problem*. Environmental health perspectives, 1986. **69**: p. 31-44.
 96. Jones, C.W., *Applications of hydrogen peroxide and derivatives*. 2007: Royal Society of Chemistry. ISBN 0-85404-536-8.
 97. Smith, A.H. and C.M. Steinmaus, *Health effects of arsenic and chromium in drinking water: recent human findings*. Annual review of public health, 2009. **30**: p. 107-122.
 98. Abbas, H.H. and F.K. Ali, *Study the effect of hexavalent chromium on some biochemical, citotoxicological and histopathological aspects of the Oreochromis spp. fish*. Pak. J. Biol. Sci, 2007. **10**: p. 3973-3982.
 99. Liang, Y., H. Wang, P. Diao, W. Chang, G. Hong, Y. Li, M. Gong, Li. Xie, J. Zhou, J. Wang, *Oxygen reduction electrocatalyst based on strongly coupled cobalt oxide nanocrystals and carbon nanotubes*. Journal of the American Chemical Society, 2012. **134**(38): p. 15849-15857.
 100. Sakai, H., T. Nakagawa, Y. Tokita, T. Hatazawa, T. Ikeda, S. Tsujimura, and K. Kano, *A high-power glucose/oxygen biofuel cell operating under quiescent conditions*. Energy & Environmental Science, 2009. **2**(1): p. 133-138.
 101. Demirel, S., K. Lehnert, M. Lucas, and P. Claus, *Use of renewables for the production of chemicals: Glycerol oxidation over carbon supported gold catalysts*. Applied Catalysis B: Environmental, 2007. **70**(1-4): p. 637-643.

102. Erhart, P., A. Klein, and K. Albe, *First-principles study of the structure and stability of oxygen defects in zinc oxide*. Physical Review B, 2005. **72**(8): p. 085213.
103. Shin, H., Y. Luo, A. Benali, and Y. Kwon, *Diffusion Monte Carlo study of O₂ adsorption on single layer graphene*. Physical Review B, 2019. **100**(7): p. 075430.
104. Cao, R., R. Thapa, H. Kim, X. Xu, M.G. Kim, Q. Li, N. Park, M. Liu, J. Cho, *Promotion of oxygen reduction by a bio-inspired tethered iron phthalocyanine carbon nanotube-based catalyst*. Nature communications, 2013. **4**(1): p. 1-7.
105. Marcus, P., *On some fundamental factors in the effect of alloying elements on passivation of alloys*. Corrosion science, 1994. **36**(12): p. 2155-2158.
106. Hay, P.J. and T.H. Dunning Jr, *Geometries and energies of the excited states of O₃ from abinitio potential energy surfaces*. The Journal of Chemical Physics, 1977. **67**(5): p. 2290-2303.
107. Tarchouna, Y., M. Bahri, N. Jaidane, Z. Ben Lakhdar, and J. Flament, *Ab initio transition state theory calculation of the rate constant for the hydrogen abstraction reaction H₂O₂ + H → H₂ + HO₂*. The Journal of chemical physics, 2003. **118**(3): p. 1189-1195.
108. Mason, N., J. Gingell, J. Davies, H. Zhao, I. Walker, and M. Siggel, *VUV optical absorption and electron energy-loss spectroscopy of ozone*. Journal of Physics B: Atomic, Molecular and Optical Physics, 1996. **29**(14): p. 3075.
109. Blint, R.J. and M.D. Newton, *Ab initio studies of interoxygen bonding in O₂, HO₂, H₂O₂, O₃, HO₃, and H₂O₃*. The Journal of Chemical Physics, 1973. **59**(12): p. 6220-6228.
110. Liotta, L., M. Gruttadauria, G. Di Carlo, G. Perrini, and V. Librando, *Heterogeneous catalytic degradation of phenolic substrates: catalysts activity*. Journal of hazardous materials, 2009. **162**(2-3): p. 588-606.
111. Trawczyński, J., *Noble metals supported on carbon black composites as catalysts for the wet-air oxidation of phenol*. Carbon, 2003. **41**(8): p. 1515-1523.
112. Li, G. and Z. Tang, *Noble metal nanoparticle@ metal oxide core/yolk-shell nanostructures as catalysts: recent progress and perspective*. Nanoscale, 2014. **6**(8): p. 3995-4011.
113. Steele, A., J. Zhu, and S. Tsang, *Noble metal catalysed aerial oxidation of alcohols to aldehydes in supercritical carbon dioxide*. Catalysis letters, 2001. **73**(1): p. 9-13.
114. Gopiraman, M., H. Bang, G. Yuan, C. Yin, K.-H. Song, J.S. Lee, I. Chung, R. Karvembu, I.S. Kim, *Noble metal/functionalized cellulose nanofiber composites for catalytic applications*. Carbohydrate polymers, 2015. **132**: p. 554-564.

115. Vamathevan, V., R. Amal, D. Beydoun, G. Low, and S. McEvoy, *Photocatalytic oxidation of organics in water using pure and silver-modified titanium dioxide particles*. Journal of Photochemistry and Photobiology A: Chemistry, 2002. **148**(1-3): p. 233-245.
116. Lathasree, S., A.N. Rao, B. SivaSankar, V. Sadasivam, and K. Rengaraj, *Heterogeneous photocatalytic mineralisation of phenols in aqueous solutions*. Journal of Molecular Catalysis A: Chemical, 2004. **223**(1-2): p. 101-105.
117. Tacchini, I., E. Terrado, A. Anson, and M. Martinez, *Preparation of a TiO₂–MoS₂ nanoparticle-based composite by solvothermal method with enhanced photoactivity for the degradation of organic molecules in water under UV light*. Micro & Nano Letters, 2011. **6**(11): p. 932-936.
118. Mallat, T. and A. Baiker, *Selectivity enhancement in heterogeneous catalysis induced by reaction modifiers*. Applied Catalysis A: General, 2000. **200**(1-2): p. 3-22.
119. Lee, I., R. Morales, M.A. Albiter, and F. Zaera, *Synthesis of heterogeneous catalysts with well shaped platinum particles to control reaction selectivity*. Proceedings of the National Academy of Sciences, 2008. **105**(40): p. 15241-15246.
120. Besson, M. and P. Gallezot, *Selective oxidation of alcohols and aldehydes on metal catalysts*. Catalysis Today, 2000. **57**(1-2): p. 127-141.
121. Iwasawa, T., M. Tokunaga, Y. Obora, and Y. Tsuji, *Homogeneous palladium catalyst suppressing Pd black formation in air oxidation of alcohols*. Journal of the American Chemical Society, 2004. **126**(21): p. 6554-6555.
122. Dijkstra, A., A. Marino-Gonzalez, A. Mairata i Payeras, I.W. Arends, and R.A. Sheldon, *Efficient and selective aerobic oxidation of alcohols into aldehydes and ketones using ruthenium/TEMPO as the catalytic system*. Journal of the American Chemical Society, 2001. **123**(28): p. 6826-6833.
123. Ley, S.V. and A. Madin, *Oxidation adjacent to oxygen of alcohols by chromium reagents*. Oxidation: Selectivity, Strategy & Efficiency in Modern Organic Chemistry, 1992: p. 251.
124. Liotta, L., A. Venezia, G. Deganello, A. Longo, A. Martorana, Z. Schay, and L. Guzzi, *Liquid phase selective oxidation of benzyl alcohol over Pd–Ag catalysts supported on pumice*. Catalysis today, 2001. **66**(2-4): p. 271-276.
125. Mallat, T. and A. Baiker, *Oxidation of alcohols with molecular oxygen on platinum metal catalysts in aqueous solutions*. Catalysis Today, 1994. **19**(2): p. 247-283.
126. Hermans, I., E.S. Spier, U. Neuenschwander, N. Turrà, and A. Baiker, *Selective oxidation catalysis: opportunities and challenges*. Topics in catalysis, 2009. **52**(9): p. 1162-1174.

127. Ali, A.H. and F. Zaera, *Kinetic study on the selective catalytic oxidation of 2-propanol to acetone over nickel foils*. Journal of Molecular Catalysis A: Chemical, 2002. **177**(2): p. 215-235.
128. Natarajan, P., V.D. Vagicherla, and M.T. Vijayan, *Indirect electrochemical oxidation of substituted polycyclic aromatic hydrocarbons to corresponding para-quinones with potassium bromide in water–chloroform medium*. Tetrahedron letters, 2014. **55**(42): p. 5817-5821.
129. M Heravi, M., A. Fazeli, and Z. Faghihi, *Recent Advances in Application of Pyridinium Chlorochromate (PCC) in Organic Synthesis*. Current Organic Synthesis, 2016. **13**(2): p. 220-254.
130. Ravelli, D., D. Dondi, M. Fagnoni, and A. Albini, *Photocatalysis. A multi-faceted concept for green chemistry*. Chemical Society Reviews, 2009. **38**(7): p. 1999-2011.
131. Fagnoni, M., D. Dondi, D. Ravelli, and A. Albini, *Photocatalysis for the Formation of the C–C Bond*. Chemical Reviews, 2007. **107**(6): p. 2725-2756.
132. Narayanam, J.M. and C.R. Stephenson, *Visible light photoredox catalysis: applications in organic synthesis*. Chemical Society Reviews, 2011. **40**(1): p. 102-113.
133. Hoffmann, N., *Homogeneous Photocatalytic Reactions with Organometallic and Coordination Compounds—Perspectives for Sustainable Chemistry*. ChemSusChem, 2012. **5**(2): p. 352-371.
134. Wang, X., S. Goeb, Z. Ji, N.A. Pogulaichenko, and F.N. Castellano, *Homogeneous photocatalytic hydrogen production using π -conjugated platinum (II) arylacetylide sensitizers*. Inorganic chemistry, 2011. **50**(3): p. 705-707.
135. Linsebigler, A.L., G. Lu, and J.T. Yates Jr, *Photocatalysis on TiO₂ surfaces: principles, mechanisms, and selected results*. Chemical reviews, 1995. **95**(3): p. 735-758.
136. Herrmann, J.-M., *Heterogeneous photocatalysis: fundamentals and applications to the removal of various types of aqueous pollutants*. Catalysis today, 1999. **53**(1): p. 115-129.
137. Kumar, K. and A. Chowdhury, *Use of Novel Nanostructured Photocatalysts for the Environmental Sustainability of Wastewater Treatments*. 2018.
138. Li, C.-H., M.-C. Liu, C.-L. Chiang, J.-Y. Li, S.-P. Chen, T.-C. Hsieh, Y.-I. Chou, Y.-P. Lin, P.-H. Wang, M.-S. Chun, *Discharge and photo-luminescence properties of a parallel plates electron emission lighting device*. Optics express, 2011. **19**(101): p. A51-A56.
139. Janczarek, M. and E. Kowalska, *On the origin of enhanced photocatalytic activity of copper-modified titania in the oxidative reaction systems*. Catalysts, 2017. **7**(11): p. 317.

140. Liu, B., X. Wang, G. Cai, L. Wen, Y. Song, and X. Zhao, *Low temperature fabrication of V-doped TiO₂ nanoparticles, structure and photocatalytic studies*. Journal of hazardous materials, 2009. **169**(1-3): p. 1112-1118.
141. Jaiswal, R., J. Bharambe, N. Patel, A. Dashora, D. Kothari, and A. Miotello, *Copper and Nitrogen co-doped TiO₂ photocatalyst with enhanced optical absorption and catalytic activity*. Applied Catalysis B: Environmental, 2015. **168**: p. 333-341.
142. Ohno, T., M. Akiyoshi, T. Umebayashi, K. Asai, T. Mitsui, and M. Matsumura, *Preparation of S-doped TiO₂ photocatalysts and their photocatalytic activities under visible light*. Applied Catalysis A: General, 2004. **265**(1): p. 115-121.
143. Ohno, T., T. Mitsui, and M. Matsumura, *Photocatalytic activity of S-doped TiO₂ photocatalyst under visible light*. Chemistry letters, 2003. **32**(4): p. 364-365.
144. Li, M., P. Li, K. Chang, T. Wang, L. Liu, Q. Kang, S. Ouyang, J. Ye, *Highly efficient and stable photocatalytic reduction of CO₂ to CH₄ over Ru loaded NaTaO₃*. Chemical Communications, 2015. **51**(36): p. 7645-7648.
145. Corma, A. and H. Garcia, *Photocatalytic reduction of CO₂ for fuel production: Possibilities and challenges*. Journal of catalysis, 2013. **308**: p. 168-175.
146. Nikokavoura, A. and C. Trapalis, *Alternative photocatalysts to TiO₂ for the photocatalytic reduction of CO₂*. Applied Surface Science, 2017. **391**: p. 149-174.
147. Williams, G., B. Seger, and P.V. Kamat, *TiO₂-graphene nanocomposites. UV-assisted photocatalytic reduction of graphene oxide*. ACS nano, 2008. **2**(7): p. 1487-1491.
148. Sayama, K. and H. Arakawa, *Photocatalytic decomposition of water and photocatalytic reduction of carbon dioxide over zirconia catalyst*. The Journal of Physical Chemistry, 1993. **97**(3): p. 531-533.
149. Selishchev, D., N. Kolobov, A. Pershin, and D. Kozlov, *TiO₂ mediated photocatalytic oxidation of volatile organic compounds: Formation of CO as a harmful by-product*. Applied Catalysis B: Environmental, 2017. **200**: p. 503-513.
150. Muggli, D.S., J.T. McCue, and J.L. Falconer, *Mechanism of the photocatalytic oxidation of ethanol on TiO₂*. Journal of catalysis, 1998. **173**(2): p. 470-483.
151. Muggli, D.S. and J.L. Falconer, *Role of lattice oxygen in photocatalytic oxidation on TiO₂*. Journal of Catalysis, 2000. **191**(2): p. 318-325.
152. Machulek Jr, A., S.C. Oliveira, M.E. Osugi, V.S. Ferreira, F.H. Quina, R.F. Dantas, S.L. Oliveira, G.A. Casagrande, F.J. Silva, V.O. Silva, *Application of different advanced oxidation processes for the degradation of organic pollutants*, in *Organic pollutants-Monitoring, risk and treatment*. 2013, IntechOpen.
153. Stasinakis, A., *Use of selected advanced oxidation processes (AOPs) for wastewater treatment—a mini review*. Global NEST journal, 2008. **10**(3): p. 376-385.

154. Khin, M.M., A.S. Nair, V.J. Babu, R. Murugan, and S. Ramakrishna, *A review on nanomaterials for environmental remediation*. Energy & Environmental Science, 2012. **5**(8): p. 8075-8109.
155. Suri, R.P., J. Liu, D.W. Hand, J.C. Crittenden, D.L. Perram, and M.E. Mullins, *Heterogeneous photocatalytic oxidation of hazardous organic contaminants in water*. Water Environment Research, 1993. **65**(5): p. 665-673.
156. Kaan, C.C., A.A. Aziz, S. Ibrahim, M. Matheswaran, and P. Saravanan, *Heterogeneous photocatalytic oxidation an effective tool for wastewater treatment—a review*. Studies on water management issues. INTECH, 2012: p. 219-236.
157. Rahimi, N., R.A. Pax, and E.M. Gray, *Review of functional titanium oxides. I: TiO₂ and its modifications*. Progress in Solid State Chemistry, 2016. **44**(3): p. 86-105.
158. Rimoldi, L., D. Meroni, E. Falletta, V. Pifferi, L. Falciola, G. Cappelletti, and S. Ardizzone, *Emerging pollutant mixture mineralization by TiO₂ photocatalysts. The role of the water medium*. Photochemical & Photobiological Sciences, 2017. **16**(1): p. 60-66.
159. Paz, Y., *Application of TiO₂ photocatalysis for air treatment: Patents' overview*. Applied Catalysis B: Environmental, 2010. **99**(3-4): p. 448-460.
160. Fujishima, A., X. Zhang, and D. Tryk, *Surf. Sci. Rep.* 2008.
161. Portela, R., S. Suárez, S.B. Rasmussen, N. Arconada, Y. Castro, A. Durán, P. Avila, J.M. Coronado, B. Sánchez, *Photocatalytic-based strategies for H₂S elimination*. Catalysis Today, 2010. **151**(1-2): p. 64-70.
162. Sajjad, A.K.L., S. Shamaila, B. Tian, F. Chen, and J. Zhang, *One step activation of WO_x/TiO₂ nanocomposites with enhanced photocatalytic activity*. Applied Catalysis B: Environmental, 2009. **91**(1-2): p. 397-405.
163. Pfeifer, V., P. Erhart, S. Li, K. Rachut, J. Morasch, J. Brötz, P. Reckers, T. Mayer, S. Ruhle, A. Zaban, *Energy band alignment between anatase and rutile TiO₂*. The Journal of physical chemistry letters, 2013. **4**(23): p. 4182-4187.
164. Di Paola, A., M. Bellardita, R. Ceccato, L. Palmisano, and F. Parrino, *Highly active photocatalytic TiO₂ powders obtained by thermohydrolysis of TiCl₄ in water*. The Journal of Physical Chemistry C, 2009. **113**(34): p. 15166-15174.
165. Su, R., R. Bechstein, L. Sør, R.T. Vang, M. Sillassen, B. Esbjornsson, A. Palmqvist, F. Besenbacher, *How the anatase-to-rutile ratio influences the photoreactivity of TiO₂*. The journal of physical chemistry C, 2011. **115**(49): p. 24287-24292.
166. Le, T.K., D. Flahaut, H. Martinez, H.K.H. Nguyen, and T.K.X. Huynh, *Study of the effects of surface modification by thermal shock method on photocatalytic activity of TiO₂ P25*. Applied Catalysis B: Environmental, 2015. **165**: p. 260-268.

167. Ohtani, B., O. Prieto-Mahaney, D. Li, and R. Abe, *What is Degussa (Evonik) P25? Crystalline composition analysis, reconstruction from isolated pure particles and photocatalytic activity test*. Journal of Photochemistry and Photobiology A: Chemistry, 2010. **216**(2-3): p. 179-182.
168. Yu, J., W. Wang, B. Cheng, and B.-L. Su, *Enhancement of photocatalytic activity of mesoporous TiO₂ powders by hydrothermal surface fluorination treatment*. The Journal of Physical Chemistry C, 2009. **113**(16): p. 6743-6750.
169. López-Tenllado, F., A. Marinas, F. Urbano, J. Colmenares, M. Hidalgo, J. Marinas, and J. Moreno, *Selective photooxidation of alcohols as test reaction for photocatalytic activity*. Applied Catalysis B: Environmental, 2012. **128**: p. 150-158.
170. Veronovski, N., P. Andreozzi, C. La Mesa, and M. Sfiligoj-Smole, *Stable TiO₂ dispersions for nanocoating preparation*. Surface and Coatings Technology, 2010. **204**(9-10): p. 1445-1451.
171. Ohno, T., K. Sarukawa, K. Tokieda, and M. Matsumura, *Morphology of a TiO₂ photocatalyst (Degussa, P-25) consisting of anatase and rutile crystalline phases*. Journal of Catalysis, 2001. **203**(1): p. 82-86.
172. Colodrero, S., A. Mihi, L. Häggman, M. Ocana, G. Boschloo, A. Hagfeldt, and H. Miguez, *Porous one-dimensional photonic crystals improve the power-conversion efficiency of dye-sensitized solar cells*. Advanced Materials, 2009. **21**(7): p. 764-770.
173. Cho, I.S., Z. Chen, A.J. Forman, D.R. Kim, P.M. Rao, T.F. Jaramillo, and X. Zheng, *Branched TiO₂ nanorods for photoelectrochemical hydrogen production*. Nano letters, 2011. **11**(11): p. 4978-4984.
174. Liu, B. and E.S. Aydil, *Growth of oriented single-crystalline rutile TiO₂ nanorods on transparent conducting substrates for dye-sensitized solar cells*. Journal of the American Chemical Society, 2009. **131**(11): p. 3985-3990.
175. Bavykin, D.V., J.M. Friedrich, and F.C. Walsh, *Protonated titanates and TiO₂ nanostructured materials: synthesis, properties, and applications*. Advanced materials, 2006. **18**(21): p. 2807-2824.
176. Peng, Z., H. Tang, Y. Tang, K.F. Yao, and H.H. Shao, *Synthesis and photocatalytic activity of magnetically recoverable core-shell nanoparticles*. International Journal of Photoenergy, 2014. **2014**.
177. Gupta, S.M. and M. Tripathi, *A review of TiO₂ nanoparticles*. Chinese Science Bulletin, 2011. **56**(16): p. 1639.
178. Nakamura, R., T. Okamura, N. Ohashi, A. Imanishi, and Y. Nakato, *Molecular mechanisms of photoinduced oxygen evolution, PL emission, and surface roughening at atomically smooth (110) and (100) n-TiO₂ (rutile) surfaces in aqueous acidic solutions*. Journal of the American Chemical Society, 2005. **127**(37): p. 12975-12983.

179. Daneshvar, N., D. Salari, and A. Khataee, *Photocatalytic degradation of azo dye acid red 14 in water on ZnO as an alternative catalyst to TiO₂*. Journal of photochemistry and photobiology A: chemistry, 2004. **162**(2-3): p. 317-322.
180. Lin, X.H., Y. Miao, and S.F.Y. Li, *Location of photocatalytic oxidation processes on anatase titanium dioxide*. Catalysis Science & Technology, 2017. **7**(2): p. 441-451.
181. Furukawa, S., T. Shishido, K. Teramura, and T. Tanaka, *Photocatalytic oxidation of alcohols over TiO₂ covered with Nb₂O₅*. Acs Catalysis, 2011. **2**(1): p. 175-179.
182. Schneider, J., M. Matsuoka, M. Takeuchi, J. Zhang, Y. Horiuchi, M. Anpo, and D.W. Bahnemann, *Understanding TiO₂ photocatalysis: mechanisms and materials*. Chemical reviews, 2014. **114**(19): p. 9919-9986.
183. Fujishima, A. and K. Honda, *Electrochemical photolysis of water at a semiconductor electrode*. nature, 1972. **238**(5358): p. 37-38.
184. Wang, C.M. and T.E. Mallouk, *New photochemical method for selective fluorination of organic molecules*. Journal of the American Chemical Society, 1990. **112**(5): p. 2016-2018.
185. Magalhaes, P., L. Andrade, O.C. Nunes, and A. Mendes, *TITANIUM DIOXIDE PHOTOCATALYSIS: FUNDAMENTALS AND APPLICATION ON PHOTOINACTIVATION*. Reviews on Advanced Materials Science, 2017. **51**(2).
186. Humayun, M., F. Raziq, A. Khan, and W. Luo, *Modification strategies of TiO₂ for potential applications in photocatalysis: a critical review*. Green Chemistry Letters and Reviews, 2018. **11**(2): p. 86-102.
187. Ashoka, S., G. Nagaraju, C. Tharamani, and G. Chandrappa, *Ethylene glycol assisted hydrothermal synthesis of flower like ZnO architectures*. Materials Letters, 2009. **63**(11): p. 873-876.
188. Altstädt, V., J.-H. Keller, and A. Fathi. *Front Matter for Volume 1593*. in *AIP Conference Proceedings*. 2014. American Institute of Physics.
189. Pan, K., Y. Dong, W. Zhou, Q. Pan, Y. Xie, T. Xie, G. Tian, G. Wang, *Facile fabrication of hierarchical TiO₂ nanobelt/ZnO nanorod heterogeneous nanostructure: an efficient photoanode for water splitting*. ACS applied materials & interfaces, 2013. **5**(17): p. 8314-8320.
190. Mane, R.S., W.J. Lee, H.M. Pathan, and S.-H. Han, *Nanocrystalline TiO₂/ZnO thin films: fabrication and application to dye-sensitized solar cells*. The journal of physical chemistry B, 2005. **109**(51): p. 24254-24259.
191. Hanaor, D.A. and C.C. Sorrell, *Review of the anatase to rutile phase transformation*. Journal of Materials science, 2011. **46**(4): p. 855-874.

192. Mattsson, A. and L. Osterlund, *Adsorption and photoinduced decomposition of acetone and acetic acid on anatase, brookite, and rutile TiO₂ nanoparticles*. The Journal of Physical Chemistry C, 2010. **114**(33): p. 14121-14132.
193. Li, W., Z. Wu, J. Wang, A.A. Elzatahry, and D. Zhao, *A perspective on mesoporous TiO₂ materials*. Chemistry of Materials, 2013. **26**(1): p. 287-298.
194. Augustynski, J., *The role of the surface intermediates in the photoelectrochemical behaviour of anatase and rutile TiO₂*. Electrochimica Acta, 1993. **38**(1): p. 43-46.
195. Sclafani, A. and J. Herrmann, *Comparison of the photoelectronic and photocatalytic activities of various anatase and rutile forms of titania in pure liquid organic phases and in aqueous solutions*. The Journal of Physical Chemistry, 1996. **100**(32): p. 13655-13661.
196. Sumita, T., T. Yamaki, S. Yamamoto, and A. Miyashita, *Photo-induced surface charge separation of highly oriented TiO₂ anatase and rutile thin films*. Applied Surface Science, 2002. **200**(1-4): p. 21-26.
197. Scanlon, D.O., C.W. Dunnill, J. Buckeridge, S.A. Shevlin, A.J. Logsdail, S.M. Woodley, . . . I.P. Parkin, *Band alignment of rutile and anatase TiO₂*. Nature materials, 2013. **12**(9): p. 798.
198. Rehman, S., R. Ullah, A. Butt, and N. Gohar, *Strategies of making TiO₂ and ZnO visible light active*. Journal of hazardous materials, 2009. **170**(2-3): p. 560-569.
199. Bickley, R.I., T. Gonzalez-Carreno, J.S. Lees, L. Palmisano, and R.J. Tilley, *A structural investigation of titanium dioxide photocatalysts*. Journal of Solid State Chemistry, 1991. **92**(1): p. 178-190.
200. Yamada, Y., S. Shikano, T. Akita, and S. Fukuzumi, *Synergistic effects of Ni and Cu supported on TiO₂ and SiO₂ on photocatalytic H₂ evolution with an electron donor-acceptor linked molecule*. Catalysis Science & Technology, 2015. **5**(2): p. 979-988.
201. Choi, H., M. Carboni, Y.K. Kim, C.H. Jung, S.Y. Moon, M.M. Koebel, and J.Y. Park, *Synthesis of High Surface Area TiO₂ Aerogel Support with Pt Nanoparticle Catalyst and CO Oxidation Study*. Catalysis Letters, 2018. **148**(5): p. 1504-1513.
202. Yamaguchi, Y., T. Shimodo, S. Usuki, K. Torigoe, C. Terashima, K.-i. Katsumata, M. Ikekita, A. Fujishima, H. Sakai, K. Nakata, *Different hollow and spherical TiO₂ morphologies have distinct activities for the photocatalytic inactivation of chemical and biological agents*. Photochemical & Photobiological Sciences, 2016. **15**(8): p. 988-994.
203. Zhang, D. and J. Wang, *In situ photoactivated plasmonic Ag₃PO₄@ silver as a stable catalyst with enhanced photocatalytic activity under visible light*. Materials Research, 2017. **20**(3): p. 702-711.
204. Asahi, R., T. Morikawa, T. Ohwaki, K. Aoki, and Y. Taga, *Visible-light photocatalysis in nitrogen-doped titanium oxides*. science, 2001. **293**(5528): p. 269-271.

205. Fu, G., P.S. Vary, and C.-T. Lin, *Anatase TiO₂ nanocomposites for antimicrobial coatings*. The Journal of Physical Chemistry B, 2005. **109**(18): p. 8889-8898.
206. Blanco-Galvez, J., P. Fernández-Ibáñez, and S. Malato-Rodríguez, *Solar photocatalytic detoxification and disinfection of water: recent overview*. 2006.
207. Inturi, S.N.R., T. Boningari, M. Suidan, and P.G. Smirniotis, *Flame aerosol synthesized Cr incorporated TiO₂ for visible light photodegradation of gas phase acetonitrile*. The Journal of Physical Chemistry C, 2013. **118**(1): p. 231-242.
208. Barndöck, H., D. Hermosilla, C. Han, D.D. Dionysiou, C. Negro, and Á. Blanco, *Degradation of 1, 4-dioxane from industrial wastewater by solar photocatalysis using immobilized NF-TiO₂ composite with monodisperse TiO₂ nanoparticles*. Applied Catalysis B: Environmental, 2016. **180**: p. 44-52.
209. Tsega, M. and F. Dejene, *Influence of acidic pH on the formulation of TiO₂ nanocrystalline powders with enhanced photoluminescence property*. Heliyon, 2017. **3**(2): p. e00246.
210. Raju, T., S. Manivasagan, B. Revathy, K. Kulangiappar, and A. Muthukumaran, *A mild and efficient method for the oxidation of benzylic alcohols by two-phase electrolysis*. Tetrahedron letters, 2007. **48**(21): p. 3681-3684.
211. Lee, R.E., *Scanning electron microscopy and X-ray microanalysis*. 1993.
212. Zachariasen, W., *A general theory of X-ray diffraction in crystals*. Acta Crystallographica, 1967. **23**(4): p. 558-564.
213. Holt, D.B. and D.C. Joy, *SEM microcharacterization of semiconductors*. Vol. 12. 1989: Academic Press.
214. Bragg, W., *X-ray diffraction and crystal structure*. Proc. Roy. Soc. A, 1913. **89**: p. 248-77.
215. Waterhouse, G.I. and M.R. Waterland, *Opal and inverse opal photonic crystals: fabrication and characterization*. Polyhedron, 2007. **26**(2): p. 356-368.
216. Hargreaves, J., *Some considerations related to the use of the Scherrer equation in powder X-ray diffraction as applied to heterogeneous catalysts*. Catalysis, Structure & Reactivity, 2016. **2**(1-4): p. 33-37.
217. Swinehart, D., *The beer-lambert law*. Journal of chemical education, 1962. **39**(7): p. 333.
218. Tahir, A.A., M.A. Ehsan, M. Mazhar, K.U. Wijayantha, M. Zeller, and A. Hunter, *Photoelectrochemical and photoresponsive properties of Bi₂S₃ nanotube and nanoparticle thin films*. Chemistry of Materials, 2010. **22**(17): p. 5084-5092.
219. Kumar, V., S.K. Sharma, T. Sharma, and V. Singh, *Band gap determination in thick films from reflectance measurements*. Optical materials, 1999. **12**(1): p. 115-119.

220. Tauc, J., *Amorphous and liquid semiconductors*. 1974, London: Springer Science & Business Media.
221. Bartle, K.D. and P. Myers, *History of gas chromatography*. TrAC Trends in Analytical Chemistry, 2002. **21**(9-10): p. 547-557.
222. McNair, H.M., J.M. Miller, and N.H. Snow, *Basic gas chromatography*. 2019: John Wiley & Sons.
223. Pedersen-Bjergaard, S. and T. Greibrokk, *On-column bromine-and chlorine-selected detection for capillary gas chromatography using a radio frequency plasma*. Analytical Chemistry, 1993. **65**(15): p. 1998-2002.
224. Dolia, S., R. Sharma, M. Sharma, and N. Saxena, *Synthesis, X-ray diffraction and optical band gap study of nanoparticles of NiFe₂O₄*. 2006.
225. Würth, C., M. Grabolle, J. Pauli, M. Spieles, and U. Resch-Genger, *Relative and absolute determination of fluorescence quantum yields of transparent samples*. Nature protocols, 2013. **8**(8): p. 1535.
226. Berne, B.J. and R. Pecora, *Dynamic light scattering: with applications to chemistry, biology, and physics*. 2000: Courier Corporation.
227. Zero, K. and R. Pecora, *Dynamic depolarized light scattering*, in *Dynamic Light Scattering*. 1985, Springer. p. 59-83.
228. International Organization for Standardization. Technical Committee ISO/TC 24. Particle characterization including sieving, S.S., Particle characterization, *Determination of the Specific Surface Area of Solids by Gas Adsorption: BET Method*. 2010: ISO.
229. Buccini, J., *The development of a global treaty on persistent organic pollutants (POPs)*, in *Persistent organic pollutants*. 2003, Springer. p. 13-30.
230. Wong, M.H., A. Leung, J. Chan, and M. Choi, *A review on the usage of POP pesticides in China, with emphasis on DDT loadings in human milk*. Chemosphere, 2005. **60**(6): p. 740-752.
231. Manahan, S.E., *Environmental chemistry*. 2017: CRC press.
232. Legrini, O., E. Oliveros, and A. Braun, *Photochemical processes for water treatment*. Chemical reviews, 1993. **93**(2): p. 671-698.
233. Chong, M.N., B. Jin, C.W. Chow, and C. Saint, *Recent developments in photocatalytic water treatment technology: a review*. Water research, 2010. **44**(10): p. 2997-3027.
234. Miranda-García, N., S. Suárez, B. Sánchez, J. Coronado, S. Malato, and M.I. Maldonado, *Photocatalytic degradation of emerging contaminants in municipal wastewater treatment plant effluents using immobilized TiO₂ in a solar pilot plant*. Applied Catalysis B: Environmental, 2011. **103**(3-4): p. 294-301.

235. Carp, O., C.L. Huisman, and A. Reller, *Photoinduced reactivity of titanium dioxide*. Progress in solid state chemistry, 2004. **32**(1-2): p. 33-177.
236. Herrmann, J.-M., C. Duchamp, M. Karkmaz, B.T. Hoai, H. Lachheb, E. Puzenat, and C. Guillard, *Environmental green chemistry as defined by photocatalysis*. Journal of hazardous materials, 2007. **146**(3): p. 624-629.
237. Zhou, L., W. Zhang, L. Chen, and H. Deng, *Z-scheme mechanism of photogenerated carriers for hybrid photocatalyst Ag₃PO₄/g-C₃N₄ in degradation of sulfamethoxazole*. Journal of colloid and interface science, 2017. **487**: p. 410-417.
238. Ghazalian, E., N. Ghasemi, and A. Amani-Ghadim, *Effect of gadollunium doping on visible light photocatalytic performance of Ag₃PO₄: evaluation of activity in degradation of an anthraquinone dye and mechanism study*. Journal of Molecular Catalysis A: Chemical, 2017. **426**: p. 257-270.
239. Labaali, Z., S. Kholtei, and J. Naja, *Valorization of phosphate waste rocks to Ag₃PO₄/hydroxyapatite for photocatalytic degradation of Rhodamine B under visible light irradiation*. Water Science and Technology, 2020.
240. Garg, R., S. Mondal, L. Sahoo, C.P. Vinod, and U.K. Gautam, *Nanocrystalline Ag₃PO₄ for sunlight and ambient air driven oxidation of amines: high photocatalytic efficiency and a facile catalyst regeneration strategy*. ACS Applied Materials & Interfaces, 2020.
241. Bi, Y., H. Hu, S. Ouyang, Z. Jiao, G. Lu, and J. Ye, *Selective growth of metallic Ag nanocrystals on Ag₃PO₄ submicro-cubes for photocatalytic applications*. Chemistry–A European Journal, 2012. **18**(45): p. 14272-14275.
242. Zhao, F.-M., L. Pan, S. Wang, Q. Deng, J.-J. Zou, L. Wang, and X. Zhang, *Ag₃PO₄/TiO₂ composite for efficient photodegradation of organic pollutants under visible light*. Applied surface science, 2014. **317**: p. 833-838.
243. Rawal, S.B., S. Do Sung, and W.I. Lee, *Novel Ag₃PO₄/TiO₂ composites for efficient decomposition of gaseous 2-propanol under visible-light irradiation*. Catalysis Communications, 2012. **17**: p. 131-135.
244. Clive, T., *Persistent Organic Pollutants: Are we close to a solution*. Published by the Canadian Arctic Resources Committee, 2000. **26**(1).
245. Safe, S., *Polychlorinated biphenyls (PCBs), dibenzo-p-dioxins (PCDDs), dibenzofurans (PCDFs), and related compounds: environmental and mechanistic considerations which support the development of toxic equivalency factors (TEFs)*. Critical reviews in toxicology, 1990. **21**(1): p. 51-88.
246. Chrysikou, L.P., P.G. Gemenetzi, and C.A. Samara, *Wintertime size distribution of polycyclic aromatic hydrocarbons (PAHs), polychlorinated biphenyls (PCBs) and organochlorine pesticides (OCPs) in the urban environment: Street-vs rooftop-level measurements*. Atmospheric Environment, 2009. **43**(2): p. 290-300.

247. Theron, J., J. Walker, and T. Cloete, *Nanotechnology and water treatment: applications and emerging opportunities*. Critical reviews in microbiology, 2008. **34**(1): p. 43-69.
248. Padmanabhan, P., K. Sreekumar, T. Thiyagarajan, R. Satpute, K. Bhanumurthy, P. Sengupta, G. Dey, K. Warriar, *Nano-crystalline titanium dioxide formed by reactive plasma synthesis*. Vacuum, 2006. **80**(11-12): p. 1252-1255.
249. Dong, H., X. Guan, D. Wang, C. Li, X. Yang, and X. Dou, *A novel application of H₂O₂-Fe (II) process for arsenate removal from synthetic acid mine drainage (AMD) water*. Chemosphere, 2011. **85**(7): p. 1115-1121.
250. Oller, I., S. Malato, and J. Sánchez-Pérez, *Combination of advanced oxidation processes and biological treatments for wastewater decontamination—a review*. Science of the total environment, 2011. **409**(20): p. 4141-4166.
251. Zhou, Y., L. Tang, G. Zeng, J. Chen, Y. Cai, Y. Zhang, G. Yang, Y. Liu, C. Zhang, W. Tang, *Mesoporous carbon nitride based biosensor for highly sensitive and selective analysis of phenol and catechol in compost bioremediation*. Biosensors and Bioelectronics, 2014. **61**: p. 519-525.
252. Houas, A., H. Lachheb, M. Ksibi, E. Elaloui, C. Guillard, and J.-M. Herrmann, *Photocatalytic degradation pathway of methylene blue in water*. Applied Catalysis B: Environmental, 2001. **31**(2): p. 145-157.
253. Farghali, A.A., W.M. El Rouby, and A. Hamdedein, *Effect of hydrothermal conditions on microstructures of pure and doped CeO₂ nanoparticles and their photo-catalytic activity: degradation mechanism and pathway of methylene blue dye*. Research on Chemical Intermediates, 2017. **43**(12): p. 7171-7192.
254. Ikehata, K. and M. Gamal El-Din, *Aqueous pesticide degradation by ozonation and ozone-based advanced oxidation processes: a review (Part I)*. Ozone: science and engineering, 2005. **27**(2): p. 83-114.
255. Khataee, A. and M.B. Kasiri, *Photocatalytic degradation of organic dyes in the presence of nanostructured titanium dioxide: influence of the chemical structure of dyes*. Journal of Molecular Catalysis A: Chemical, 2010. **328**(1-2): p. 8-26.
256. Kočí, K., K. Matějů, L. Obalová, S. Krejčíková, Z. Lacný, D. Plachá, L. Capek, A. Hospodkova, O. Šolcová, *Effect of silver doping on the TiO₂ for photocatalytic reduction of CO₂*. Applied Catalysis B: Environmental, 2010. **96**(3-4): p. 239-244.
257. Yang, J., X. Zhang, H. Liu, C. Wang, S. Liu, P. Sun, L. Wang, Y. Liu, *Heterostructured TiO₂/WO₃ porous microspheres: preparation, characterization and photocatalytic properties*. Catalysis today, 2013. **201**: p. 195-202.
258. Zhang, X., H. Cui, M. Humayun, Y. Qu, N. Fan, X. Sun, and L. Jing, *Exceptional performance of photoelectrochemical water oxidation of single-crystal rutile TiO₂*

- nanorods dependent on the hole trapping of modified chloride*. Scientific reports, 2016. **6**(1): p. 1-8.
259. Bessegato, G.G., J.C. Cardoso, and M.V.B. Zanoni, *Enhanced photoelectrocatalytic degradation of an acid dye with boron-doped TiO₂ nanotube anodes*. Catalysis Today, 2015. **240**: p. 100-106.
 260. Yao, W., B. Zhang, C. Huang, C. Ma, X. Song, and Q. Xu, *Synthesis and characterization of high efficiency and stable Ag₃PO₄/TiO₂ visible light photocatalyst for the degradation of methylene blue and rhodamine B solutions*. Journal of Materials Chemistry, 2012. **22**(9): p. 4050-4055.
 261. Chen, Z., J. Zeng, J. Di, D. Zhao, M. Ji, J. Xia, and H. Li, *Facile microwave-assisted ionic liquid synthesis of sphere-like BiOBr hollow and porous nanostructures with enhanced photocatalytic performance*. Green Energy & Environment, 2017. **2**(2): p. 124-133.
 262. Lim, Y.W.L., Y. Tang, Y.H. Cheng, and Z. Chen, *Morphology, crystal structure and adsorption performance of hydrothermally synthesized titania and titanate nanostructures*. Nanoscale, 2010. **2**(12): p. 2751-2757.
 263. Ma, X., B. Lu, D. Li, R. Shi, C. Pan, and Y. Zhu, *Origin of photocatalytic activation of silver orthophosphate from first-principles*. The Journal of Physical Chemistry C, 2011. **115**(11): p. 4680-4687.
 264. Masson, M., *Standard potentials in aqueous solution:: AJ Bard, R. Parsons and J. Jordan (eds.), Dekker, New York, 1985. Pages xii+ 834. \$29.95. 1986, Elsevier*.
 265. Chen, X., Y. Dai, and X. Wang, *Methods and mechanism for improvement of photocatalytic activity and stability of Ag₃PO₄: a review*. Journal of Alloys and Compounds, 2015. **649**: p. 910-932.
 266. Siraj, K., K. Javaid, J. Pedarnig, M. Bodea, and S. Naseem, *Electron beam induced nanostructures and band gap tuning of ZnO thin films*. Journal of alloys and compounds, 2013. **563**: p. 280-284.
 267. Martin, D.J., G. Liu, S.J. Moniz, Y. Bi, A.M. Beale, J. Ye, and J. Tang, *Efficient visible driven photocatalyst, silver phosphate: performance, understanding and perspective*. Chemical Society Reviews, 2015. **44**(21): p. 7808-7828.
 268. Li, Y., H. Yu, W. Song, G. Li, B. Yi, and Z. Shao, *A novel photoelectrochemical cell with self-organized TiO₂ nanotubes as photoanodes for hydrogen generation*. international journal of hydrogen energy, 2011. **36**(22): p. 14374-14380.
 269. Bi, Y., H. Hu, S. Ouyang, G. Lu, J. Cao, and J. Ye, *Photocatalytic and photoelectric properties of cubic Ag₃PO₄ sub-microcrystals with sharp corners and edges*. Chemical Communications, 2012. **48**(31): p. 3748-3750.

270. Al Kausor, M., S.S. Gupta, and D. Chakraborty, *Ag₃PO₄-based nanocomposites and their applications in photodegradation of toxic organic dye contaminated wastewater: review on material design to performance enhancement*. Journal of Saudi Chemical Society, 2020. **24**(1): p. 20-41.
271. Yi, Z., J. Ye, N. Kikugawa, T. Kako, S. Ouyang, H. Stuart-Williams, H. Yang, J. Cao, W. Luo, Z. Li, *An orthophosphate semiconductor with photooxidation properties under visible-light irradiation*. Nature materials, 2010. **9**(7): p. 559-564.
272. Teng, W., X. Li, Q. Zhao, and G. Chen, *Fabrication of Ag/Ag₃PO₄/TiO₂ heterostructure photoelectrodes for efficient decomposition of 2-chlorophenol under visible light irradiation*. Journal of Materials Chemistry A, 2013. **1**(32): p. 9060-9068.
273. Rashid, J. and M. Barakat, *Facile in situ synthesis and characterization of Ag₃PO₄ supported TiO₂ nanocomposite for visible light photocatalysis*. DESALINATION AND WATER TREATMENT, 2018. **101**: p. 193-202.
274. Lopez, L., W.A. Daoud, D. Dutta, B.C. Panther, and T.W. Turney, *Effect of substrate on surface morphology and photocatalysis of large-scale TiO₂ films*. Applied Surface Science, 2013. **265**: p. 162-168.
275. Li, Y. and W. Shen, *Morphology-dependent nanocatalysts: Rod-shaped oxides*. Chemical Society Reviews, 2014. **43**(5): p. 1543-1574.
276. Ma, X.-Y., Y. Chen, H. Wang, Q.-X. Li, W.-F. Lin, and W.-B. Cai, *Electrocatalytic oxidation of ethanol and ethylene glycol on cubic, octahedral and rhombic dodecahedral palladium nanocrystals*. Chemical Communications, 2018. **54**(20): p. 2562-2565.
277. Yao, J. and C. Wang, *Decolorization of methylene blue with sol via UV irradiation photocatalytic degradation*. International Journal of Photoenergy, 2010. **2010**.
278. Ma, X., H. Li, Y. Wang, H. Li, B. Liu, S. Yin, and T. Sato, *Substantial change in phenomenon of "self-corrosion" on Ag₃PO₄/TiO₂ compound photocatalyst*. Applied Catalysis B: Environmental, 2014. **158**: p. 314-320.
279. Jacobs, J.F., I. Van de Poel, and P. Osseweijer, *Sunscreens with titanium dioxide (TiO₂) nano-particles: a societal experiment*. Nanoethics, 2010. **4**(2): p. 103-113.
280. Liu, Y., Y. Liu, J. Lin, H. Tan, and C. Zhang, *UV-protective treatment for Vectran® fibers with hybrid coatings of TiO₂/organic UV absorbers*. Journal of Adhesion Science and Technology, 2014. **28**(18): p. 1773-1782.
281. Colbeau-Justin, C., M. Kunst, and D. Huguenin, *Structural influence on charge-carrier lifetimes in TiO₂ powders studied by microwave absorption*. Journal of materials science, 2003. **38**(11): p. 2429-2437.

282. Xu, M., Y. Gao, E.M. Moreno, M. Kunst, M. Muhler, Y. Wang, H. Adriss, C. Wöll, *Photocatalytic activity of bulk TiO₂ anatase and rutile single crystals using infrared absorption spectroscopy*. Physical Review Letters, 2011. **106**(13): p. 138302.
283. Wilson, J.N. and H. Idriss, *Structure sensitivity and photocatalytic reactions of semiconductors. Effect of the last layer atomic arrangement*. Journal of the American Chemical Society, 2002. **124**(38): p. 11284-11285.
284. Wilson, J. and H. Idriss, *Effect of surface reconstruction of TiO₂ (001) single crystal on the photoreaction of acetic acid*. Journal of Catalysis, 2003. **214**(1): p. 46-52.
285. Komaguchi, K., H. Nakano, A. Araki, and Y. Harima, *Photoinduced electron transfer from anatase to rutile in partially reduced TiO₂ (P-25) nanoparticles: An ESR study*. Chemical Physics Letters, 2006. **428**(4-6): p. 338-342.
286. Zhang, J., Q. Xu, Z. Feng, M. Li, and C. Li, *Importance of the relationship between surface phases and photocatalytic activity of TiO₂*. Angewandte Chemie, 2008. **120**(9): p. 1790-1793.
287. Liu, R., P. Hu, and S. Chen, *Photocatalytic activity of Ag₃PO₄ nanoparticle/TiO₂ nanobelt heterostructures*. Applied Surface Science, 2012. **258**(24): p. 9805-9809.
288. Zhu, H. and J.M. Liu, *First-principle study of electronic structures and optical properties of chromium and carbon co-doped anatase TiO₂*. Ceramics International, 2016. **42**(12): p. 13900-13908.
289. Yang, X., H. Cui, Y. Li, J. Qin, R. Zhang, and H. Tang, *Fabrication of Ag₃PO₄-graphene composites with highly efficient and stable visible light photocatalytic performance*. Acs Catalysis, 2013. **3**(3): p. 363-369.
290. Liang, Q., Y. Shi, W. Ma, Z. Li, and X. Yang, *Enhanced photocatalytic activity and structural stability by hybridizing Ag₃PO₄ nanospheres with graphene oxide sheets*. Physical Chemistry Chemical Physics, 2012. **14**(45): p. 15657-15665.
291. Wang, P., Y. Li, Z. Liu, J. Chen, Y. Wu, M. Guo, and P. Na, *In-situ deposition of Ag₃PO₄ on TiO₂ nanosheets dominated by (001) facets for enhanced photocatalytic activities and recyclability*. Ceramics International, 2017. **43**(15): p. 11588-11595.
292. Pan, L., T. Muhammad, L. Ma, Z.-F. Huang, S. Wang, L. Wang, J.-J. Zou, X. Zhang, *MOF-derived C-doped ZnO prepared via a two-step calcination for efficient photocatalysis*. Applied Catalysis B: Environmental, 2016. **189**: p. 181-191.
293. Yamakata, A., J.J.M. Vequizo, and H. Matsunaga, *Distinctive behavior of photogenerated electrons and holes in anatase and rutile TiO₂ powders*. The Journal of Physical Chemistry C, 2015. **119**(43): p. 24538-24545.
294. Zhang, J., Y. Zhang, Y. Lei, and C. Pan, *Photocatalytic and degradation mechanisms of anatase TiO₂: a HRTEM study*. Catalysis Science & Technology, 2011. **1**(2): p. 273-278.

295. Bojinova, A., R. Kralchevska, I. Poullos, and C. Dushkin, *Anatase/rutile TiO₂ composites: Influence of the mixing ratio on the photocatalytic degradation of Malachite Green and Orange II in slurry*. Materials Chemistry and Physics, 2007. **106**(2-3): p. 187-192.
296. Machado, L.L., J.S.N. Souza, M.C. de Mattos, S.K. Sakata, G.A. Cordell, and T.L. Lemos, *Bioreduction of aldehydes and ketones using Manihot species*. Phytochemistry, 2006. **67**(15): p. 1637-1643.
297. Tojo, G. and M.I. Fernandez, *Oxidation of alcohols to aldehydes and ketones: a guide to current common practice*. 2006: Springer Science & Business Media.
298. Shi, Z., C. Zhang, C. Tang, and N. Jiao, *Recent advances in transition-metal catalyzed reactions using molecular oxygen as the oxidant*. Chemical Society Reviews, 2012. **41**(8): p. 3381-3430.
299. Wang, D., P. Wang, S. Wang, Y.-H. Chen, H. Zhang, and A. Lei, *Direct electrochemical oxidation of alcohols with hydrogen evolution in continuous-flow reactor*. Nature communications, 2019. **10**(1): p. 1-8.
300. Oturan, M., *An ecologically effective water treatment technique using electrochemically generated hydroxyl radicals for in situ destruction of organic pollutants: application to herbicide 2, 4-D*. Journal of Applied Electrochemistry, 2000. **30**(4): p. 475-482.
301. Xie, F., Y. Zhang, X. He, H. Li, X. Qiu, W. Zhou, S. Huo, Z. Tang, *First achieving highly selective oxidation of aliphatic alcohols to aldehydes over photocatalysts*. Journal of Materials Chemistry A, 2018. **6**(27): p. 13236-13243.
302. Palmisano, L., V. Augugliaro, M. Bellardita, A. Di Paola, E. García López, V. Loddo, G. Marci, G. Palmisano, S. Yurdakal, *Titania photocatalysts for selective oxidations in water*. ChemSusChem, 2011. **4**(10): p. 1431-1438.
303. Colmenares, J.C., W. Ouyang, M. Ojeda, E. Kuna, O. Chernyayeva, D. Lisovytskiy, S. De, R. Luque, A.M. Balu, *Mild ultrasound-assisted synthesis of TiO₂ supported on magnetic nanocomposites for selective photo-oxidation of benzyl alcohol*. Applied Catalysis B: Environmental, 2016. **183**: p. 107-112.
304. Gassim, F.A.-Z.G., A.N. Alkhateeb, and F.H. Hussein, *Photocatalytic oxidation of benzyl alcohol using pure and sensitized anatase*. Desalination, 2007. **209**(1-3): p. 342-349.
305. Augugliaro, V., H. Kisch, V. Loddo, M.J. López-Muñoz, C. Márquez-Álvarez, G. Palmisano, L. Palmisano, F. Parrino, S. Yurdakal, *Photocatalytic oxidation of aromatic alcohols to aldehydes in aqueous suspension of home-prepared titanium dioxide: 1. Selectivity enhancement by aliphatic alcohols*. Applied Catalysis A: General, 2008. **349**(1-2): p. 182-188.

306. Rafiee, M., Z.M. Konz, M.D. Graaf, H.F. Koolman, and S.S. Stahl, *Electrochemical Oxidation of Alcohols and Aldehydes to Carboxylic Acids Catalyzed by 4-Acetamido-TEMPO: An Alternative to "Anelli" and "Pinnick" Oxidations*. ACS Catalysis, 2018. **8**(7): p. 6738-6744.
307. Ciriminna, R., M. Ghahremani, B. Karimi, and M. Pagliaro, *Electrochemical Alcohol Oxidation Mediated by TEMPO-like Nitroxyl Radicals*. ChemistryOpen, 2017. **6**(1): p. 5-10.
308. Badalyan, A. and S.S. Stahl, *Cooperative electrocatalytic alcohol oxidation with electron-proton-transfer mediators*. Nature, 2016. **535**(7612): p. 406-410.
309. Marotta, R., I. Di Somma, D. Spasiano, R. Andreozzi, and V. Caprio, *Selective oxidation of benzyl alcohol to benzaldehyde in water by TiO₂/Cu (II)/UV solar system*. Chemical engineering journal, 2011. **172**(1): p. 243-249.
310. Bosco, A.J., S. Lawrence, C. Christopher, S. Radhakrishnan, A.A. Joseph Rosario, S. Raja, and D. Vasudevan, *Redox-mediated oxidation of alcohols using Cl⁻/OCl⁻ redox couple in biphasic media*. Journal of Physical Organic Chemistry, 2015. **28**(9): p. 591-595.
311. Christopher, C., S. Lawrence, A.J. Bosco, N. Xavier, and S. Raja, *Selective oxidation of benzyl alcohol by two phase electrolysis using nitrate as mediator*. Catalysis Science & Technology, 2012. **2**(4): p. 824-827.
312. Kim, D., A. Ghicov, S.P. Albu, and P. Schmuki, *Bamboo-type TiO₂ nanotubes: improved conversion efficiency in dye-sensitized solar cells*. Journal of the American Chemical Society, 2008. **130**(49): p. 16454-16455.
313. Grimes, C.A., *Synthesis and application of highly ordered arrays of TiO₂ nanotubes*. Journal of Materials Chemistry, 2007. **17**(15): p. 1451-1457.
314. Tan, J., L. Yang, Q. Kang, and Q. Cai, *In situ ATR-FTIR and UV-visible spectroscopy study of photocatalytic oxidation of ethanol over TiO₂ nanotubes*. Analytical letters, 2011. **44**(6): p. 1114-1125.
315. Wu, Z., J. Wang, Z. Zhou, and G. Zhao, *Highly selective aerobic oxidation of biomass alcohol to benzaldehyde by an in situ doped Au/TiO₂ nanotube photonic crystal photoanode for simultaneous hydrogen production promotion*. Journal of Materials Chemistry A, 2017. **5**(24): p. 12407-12415.
316. Quang, D.A., T.T.T. Toan, T.Q. Tung, T.T. Hoa, T.X. Mau, and D.Q. Khieu, *Synthesis of CeO₂/TiO₂ nanotubes and heterogeneous photocatalytic degradation of methylene blue*. Journal of environmental chemical engineering, 2018. **6**(5): p. 5999-6011.
317. Ge, M., Q. Li, C. Cao, J. Huang, S. Li, S. Zhang, Z. Chen, K. Zhang, S. Al-Deyab, Y. Lai, *One-dimensional TiO₂ nanotube photocatalysts for solar water splitting*. Advanced Science, 2017. **4**(1): p. 1600152.

318. Bella, F., A. Lamberti, A. Sacco, S. Bianco, A. Chiodoni, and R. Bongiovanni, *Novel electrode and electrolyte membranes: towards flexible dye-sensitized solar cell combining vertically aligned TiO₂ nanotube array and light-cured polymer network*. Journal of membrane science, 2014. **470**: p. 125-131.
319. Bosco, A.J., S. Lawrence, C. Christopher, M. Balaganesh, M. Easuraja, and S. Raja, *A novel biphasic electrolysis method for the oxidation of 4-methylbenzyl alcohol by in-situ generated hypochlorous acid using NaCl as electro catalytic mediator*. Int. J. Pharm. Pharm. Sci, 2013. **5**: p. 531-535.
320. Al-Abdullah, Z.T., Y. Shin, R. Kler, C.C. Perry, W. Zhou, and Q. Chen, *The influence of hydroxide on the initial stages of anodic growth of TiO₂ nanotubular arrays*. Nanotechnology, 2010. **21**(50): p. 505601.
321. Faraji, M., M. Amini, and A.P. Anbari, *Preparation and characterization of TiO₂-nanotube/Ti plates loaded Cu₂O nanoparticles as a novel heterogeneous catalyst for the azide-alkyne cycloaddition*. Catalysis Communications, 2016. **76**: p. 72-75.
322. Ning, X., S. Meng, X. Fu, X. Ye, and S. Chen, *Efficient utilization of photogenerated electrons and holes for photocatalytic selective organic syntheses in one reaction system using a narrow band gap CdS photocatalyst*. Green Chemistry, 2016. **18**(12): p. 3628-3639.
323. He, S., Q. Huang, Y. Zhang, L. Wang, and Y. Nie, *Investigation on direct and indirect electrochemical oxidation of ammonia over Ru-Ir/TiO₂ anode*. Industrial & Engineering Chemistry Research, 2015. **54**(5): p. 1447-1451.
324. Palmisano, G., R. Ciriminna, and M. Pagliaro, *Waste-Free Electrochemical Oxidation of Alcohols in Water*. Advanced Synthesis & Catalysis, 2006. **348**(15): p. 2033-2037.
325. Luo, J., H. Yu, H. Wang, H. Wang, and F. Peng, *Aerobic oxidation of benzyl alcohol to benzaldehyde catalyzed by carbon nanotubes without any promoter*. Chemical Engineering Journal, 2014. **240**: p. 434-442.
326. Naumczyk, J., L. Szpyrkowicz, and F. Zilio-Grandi, *Electrochemical treatment of textile wastewater*. Water Science and Technology, 1996. **34**(11): p. 17-24.
327. Szpyrkowicz, L., J. Naumczyk, and F. Zilio-Grandi, *Application of electrochemical processes for tannery wastewater treatment*. Toxicological & Environmental Chemistry, 1994. **44**(3-4): p. 189-202.
328. Comninellis, C., *Electrocatalysis in the electrochemical conversion/combustion of organic pollutants for waste water treatment*. Electrochimica Acta, 1994. **39**(11-12): p. 1857-1862.
329. Bonfatti, F., S. Ferro, F. Lavezzo, M. Malacarne, G. Lodi, and A. De Battisti, *Electrochemical incineration of glucose as a model organic substrate. II. Role of active chlorine mediation*. Journal of the Electrochemical Society, 2000. **147**(2): p. 592.

330. Bonfatti, F., A. De Battisti, S. Ferro, G. Lodi, and S. Osti, *Anodic mineralization of organic substrates in chloride-containing aqueous media*. *Electrochimica Acta*, 2000. **46**(2-3): p. 305-314.
331. Zhang, W., T. An, M. Cui, G. Sheng, and J. Fu, *Effects of anions on the photocatalytic and photoelectrocatalytic degradation of reactive dye in a packed-bed reactor*. *Journal of Chemical Technology & Biotechnology: International Research in Process, Environmental & Clean Technology*, 2005. **80**(2): p. 223-229.
332. Li, G., Z.-Q. Liu, J. Lu, L. Wang, and Z. Zhang, *Effect of calcination temperature on the morphology and surface properties of TiO₂ nanotube arrays*. *Applied surface science*, 2009. **255**(16): p. 7323-7328.
333. Chen, Y., X.-M. Wang, S.-S. Lu, and X. Zhang, *Formation of titanium oxide nanogrooves island arrays by anodization*. *Electrochemistry communications*, 2010. **12**(1): p. 86-89.
334. Berger, S., A. Ghicov, Y.-C. Nah, and P. Schmuki, *Transparent TiO₂ nanotube electrodes via thin layer anodization: fabrication and use in electrochromic devices*. *Langmuir*, 2009. **25**(9): p. 4841-4844.
335. Macak, J.M., M. Zlamal, J. Krysa, and P. Schmuki, *Self-organized TiO₂ nanotube layers as highly efficient photocatalysts*. *small*, 2007. **3**(2): p. 300-304.
336. Pak, D., *Ti plate with TiO₂ nanotube arrays as a novel cathode for nitrate reduction*. *Chemosphere*, 2019. **228**: p. 611-618.
337. Nischk, M., P. Mazierski, M. Gazda, and A. Zaleska, *Ordered TiO₂ nanotubes: The effect of preparation parameters on the photocatalytic activity in air purification process*. *Applied Catalysis B: Environmental*, 2014. **144**: p. 674-685.
338. Liang, H.-c. and X.-z. Li, *Effects of structure of anodic TiO₂ nanotube arrays on photocatalytic activity for the degradation of 2, 3-dichlorophenol in aqueous solution*. *Journal of hazardous materials*, 2009. **162**(2-3): p. 1415-1422.
339. Chaudhari, M.P. and S.B. Sawant, *Kinetics of heterogeneous oxidation of benzyl alcohol with hydrogen peroxide*. *Chemical engineering journal*, 2005. **106**(2): p. 111-118.
340. Madon, R.J. and M. Boudart, *Experimental criterion for the absence of artifacts in the measurement of rates of heterogeneous catalytic reactions*. *Industrial & Engineering Chemistry Fundamentals*, 1982. **21**(4): p. 438-447.
341. Deng, Y. and J.D. Englehardt, *Electrochemical oxidation for landfill leachate treatment*. *Waste management*, 2007. **27**(3): p. 380-388.
342. McCooey, S.H. and S.J. Connon, *Readily accessible 9-epi-amino cinchona alkaloid derivatives promote efficient, highly enantioselective additions of aldehydes and ketones to nitroolefins*. *Organic letters*, 2007. **9**(4): p. 599-602.

343. Kokel, A. and C. Schäfer, *Chapter 3.11 - Application of Green Chemistry in Homogeneous Catalysis*. Green Chemistry, 2018: p. 375-414.
344. Qamar, M., M. Fawakhiry, A.-M. Azad, M. Ahmed, A. Khan, and T. Saleh, *Selective photocatalytic oxidation of aromatic alcohols into aldehydes by tungsten blue oxide (TBO) anchored with Pt nanoparticles*. RSC Advances, 2016. **6**(75): p. 71108-71116.
345. Anderson, R., K. Griffin, P. Johnston, and P.L. Alsters, *Selective oxidation of alcohols to carbonyl compounds and carboxylic acids with platinum group metal catalysts*. Advanced Synthesis & Catalysis, 2003. **345**(4): p. 517-523.
346. Kawahara, R., K.i. Fujita, and R. Yamaguchi, *Cooperative catalysis by iridium complexes with a bipyridonate ligand: versatile dehydrogenative oxidation of alcohols and reversible dehydrogenation–hydrogenation between 2-propanol and acetone*. Angewandte Chemie, 2012. **124**(51): p. 12962-12966.
347. Wolfson, A., S. Wuyts, D.E. De Vos, I.F. Vankelecom, and P.A. Jacobs, *Aerobic oxidation of alcohols with ruthenium catalysts in ionic liquids*. Tetrahedron letters, 2002. **43**(45): p. 8107-8110.
348. Nagaraju, P., M. Balaraju, K.M. Reddy, P.S. Prasad, and N. Lingaiah, *Selective oxidation of allylic alcohols catalyzed by silver exchanged molybdovanado phosphoric acid catalyst in the presence of molecular oxygen*. Catalysis Communications, 2008. **9**(6): p. 1389-1393.
349. Polshettiwar, V. and R.S. Varma, *Green chemistry by nano-catalysis*. Green Chemistry, 2010. **12**(5): p. 743-754.
350. Chan-Thaw, C.E., A. Savara, and A. Villa, *Selective benzyl alcohol oxidation over Pd catalysts*. Catalysts, 2018. **8**(10): p. 431.
351. Dionísio, A.P., G. Molina, D.S. de Carvalho, R. Dos Santos, J. Bicas, and G. Pastore, *Natural flavourings from biotechnology for foods and beverages*, in *Natural food additives, ingredients and flavourings*. 2012, Elsevier. p. 231-259.
352. Steinhoff, B.A. and S.S. Stahl, *Mechanism of Pd (OAc)₂/DMSO-catalyzed aerobic alcohol oxidation: mass-transfer-limitation effects and catalyst decomposition pathways*. Journal of the American Chemical Society, 2006. **128**(13): p. 4348-4355.
353. Huin, C., Z. Eskandani, N. Badi, A. Farcas, V. Bennevault-Celton, and P. Guégan, *Anionic ring-opening polymerization of ethylene oxide in DMF with cyclodextrin derivatives as new initiators*. Carbohydrate polymers, 2013. **94**(1): p. 323-331.
354. Jia, A., L.-L. Lou, C. Zhang, Y. Zhang, and S. Liu, *Selective oxidation of benzyl alcohol to benzaldehyde with hydrogen peroxide over alkali-treated ZSM-5 zeolite catalysts*. Journal of Molecular Catalysis A: Chemical, 2009. **306**(1-2): p. 123-129.
355. Vayssilov, G.N., Y. Lykhach, A. Migani, T. Staudt, G.P. Petrova, N. Tsud, T. Nataliya, T. Skala, A. Bruix, F. Illas, K.C. Prince, *Support nanostructure boosts oxygen transfer*

- to catalytically active platinum nanoparticles. *Nature materials*, 2011. **10**(4): p. 310-315.
356. Spasiano, D., L.d.P.P. Rodriguez, J.C. Olleros, S. Malato, R. Marotta, and R. Andreozzi, *TiO₂/Cu (II) photocatalytic production of benzaldehyde from benzyl alcohol in solar pilot plant reactor*. *Applied Catalysis B: Environmental*, 2013. **136**: p. 56-63.
 357. Vione, D., C. Minero, V. Maurino, M.E. Carlotti, T. Picatotto, and E. Pelizzetti, *Degradation of phenol and benzoic acid in the presence of a TiO₂-based heterogeneous photocatalyst*. *Applied Catalysis B: Environmental*, 2005. **58**(1-2): p. 79-88.
 358. Akizuki, M. and Y. Oshima, *Effects of water density on acid-catalytic properties of TiO₂ and WO₃/TiO₂ in supercritical water*. *The Journal of Supercritical Fluids*, 2013. **84**: p. 36-42.
 359. Zanoni, M.V.B., J.J. Sene, and M.A. Anderson, *Photoelectrocatalytic degradation of Remazol Brilliant Orange 3R on titanium dioxide thin-film electrodes*. *Journal of Photochemistry and Photobiology A: chemistry*, 2003. **157**(1): p. 55-63.
 360. Zepp, R.G. and N.L. Wolfe, *Abiotic transformation of organic chemicals at the particle/water interface*. NTIS, SPRINGFIELD, VA(USA). 1987., 1987.
 361. Wang, Q., M. Zhang, C. Chen, W. Ma, and J. Zhao, *Photocatalytic aerobic oxidation of alcohols on TiO₂: the acceleration effect of a Brønsted acid*. *Angewandte Chemie International Edition*, 2010. **49**(43): p. 7976-7979.
 362. Higashimoto, S., N. Kitao, N. Yoshida, T. Sakura, M. Azuma, H. Ohue, and Y. Sakata, *Selective photocatalytic oxidation of benzyl alcohol and its derivatives into corresponding aldehydes by molecular oxygen on titanium dioxide under visible light irradiation*. *Journal of Catalysis*, 2009. **266**(2): p. 279-285.
 363. Amadelli, R., L. Samiolo, A. Maldotti, A. Molinari, and D. Gazzoli, *Selective Photooxidation and Photoreduction Processes at International Journal of Photoenergy*, 2011. **2011**.
 364. Choudhary, V.R., R. Jha, and P. Jana, *Solvent-free selective oxidation of benzyl alcohol by molecular oxygen over uranium oxide supported nano-gold catalyst for the production of chlorine-free benzaldehyde*. *Green Chemistry*, 2007. **9**(3): p. 267-272.
 365. Hammett, L.P., *The effect of structure upon the reactions of organic compounds. Benzene derivatives*. *Journal of the American Chemical Society*, 1937. **59**(1): p. 96-103.
 366. Kageyama, Y. and S. Murata, *Oxidative formation of thioesters in a model system of the pyruvate dehydrogenase complex*. *The Journal of Organic Chemistry*, 2005. **70**(8): p. 3140-3147.

367. Joshi, S.R., K.L. Kataria, S.B. Sawant, and J.B. Joshi, *Kinetics of oxidation of benzyl alcohol with dilute nitric acid*. Industrial & engineering chemistry research, 2005. **44**(2): p. 325-333.
368. Fristrup, P., L.B. Johansen, and C.H. Christensen, *Mechanistic investigation of the gold-catalyzed aerobic oxidation of alcohols*. Catalysis Letters, 2008. **120**(3-4): p. 184-190.
369. Bijudas, K., *Kinetics and mechanism of the selective oxidation of benzyl alcohols by acidified dichromate in aqueous acetic acid medium*. Oriental journal of chemistry, 2014. **30**(3): p. 1391-1396.
370. Lewis, M., C. Bagwill, L.K. Hardebeck, and S. Wireduaah, *The use of Hammett constants to understand the non-covalent binding of aromatics*. Computational and structural biotechnology journal, 2012. **1**(1): p. e201204004.
371. Yurdakal, S., G. Palmisano, V. Loddo, O. Alagöz, V. Augugliaro, and L. Palmisano, *Selective photocatalytic oxidation of 4-substituted aromatic alcohols in water with rutile TiO₂ prepared at room temperature*. Green Chemistry, 2009. **11**(4): p. 510-516.
372. Newman, D.J. and G.M. Cragg, *Natural products as sources of new drugs over the 30 years from 1981 to 2010*. Journal of natural products, 2012. **75**(3): p. 311-335.
373. Guillena, G., D.J. Ramon, and M. Yus, *Hydrogen autotransfer in the N-alkylation of amines and related compounds using alcohols and amines as electrophiles*. Chemical reviews, 2009. **110**(3): p. 1611-1641.
374. Salvatore, R.N., C.H. Yoon, and K.W. Jung, *Synthesis of secondary amines*. Tetrahedron, 2001. **57**(37): p. 7785-7812.
375. Jonathan Clayden, N.G., and Stuart Warren, *Organic Chemistry Second Edition*. 2012: OUP Higher Education Division.
376. Schlummer, B. and U. Scholz, *Palladium-Catalyzed C–N and C–O Coupling—A Practical Guide from an Industrial Vantage Point*. Advanced Synthesis & Catalysis, 2004. **346**(13-15): p. 1599-1626.
377. Amines, S.L., *Synthesis, Properties, and Application*. 2004, Cambridge University Press, Cambridge.
378. Sperotto, E., G.P. van Klink, G. van Koten, and J.G. de Vries, *The mechanism of the modified Ullmann reaction*. Dalton Transactions, 2010. **39**(43): p. 10338-10351.
379. Huang, L., M. Arndt, K.t. Gooßen, H. Heydt, and L.J. Goossen, *Late transition metal-catalyzed hydroamination and hydroamidation*. Chemical Reviews, 2015. **115**(7): p. 2596-2697.

380. Magano, J. and J.R. Dunetz, *Large-scale applications of transition metal-catalyzed couplings for the synthesis of pharmaceuticals*. Chemical Reviews, 2011. **111**(3): p. 2177-2250.
381. Elangovan, S., J. Neumann, J.-B. Sortais, K. Junge, C. Darcel, and M. Beller, *Efficient and selective N-alkylation of amines with alcohols catalysed by manganese pincer complexes*. Nature communications, 2016. **7**(1): p. 1-8.
382. Nef, J., *Dissociationsvorgänge bei den einatomigen alkoholen, aethern und salzen*. Justus Liebigs Annalen der Chemie, 1901. **318**(2-3): p. 137-230.
383. Martínez, R., D.J. Ramón, and M. Yus, *Selective N-monoalkylation of aromatic amines with benzylic alcohols by a hydrogen autotransfer process catalyzed by unmodified magnetite*. Organic & biomolecular chemistry, 2009. **7**(10): p. 2176-2181.
384. Hellal, M., F.C. Falk, E. Wolf, M. Dryzhakov, and J. Moran, *Breaking the dichotomy of reactivity vs. chemoselectivity in catalytic SN 1 reactions of alcohols*. Organic & biomolecular chemistry, 2014. **12**(31): p. 5990-5994.
385. Zhao, Y., S.W. Foo, and S. Saito, *Iron/amino acid catalyzed direct N-alkylation of amines with alcohols*. Angewandte Chemie International Edition, 2011. **50**(13): p. 3006-3009.
386. Yang, Q., Q. Wang, and Z. Yu, *Substitution of alcohols by N-nucleophiles via transition metal-catalyzed dehydrogenation*. Chemical Society Reviews, 2015. **44**(8): p. 2305-2329.
387. Dobereiner, G.E. and R.H. Crabtree, *Dehydrogenation as a substrate-activating strategy in homogeneous transition-metal catalysis*. Chemical reviews, 2010. **110**(2): p. 681-703.
388. Hamid, M.H.S., P.A. Slatford, and J.M. Williams, *Borrowing hydrogen in the activation of alcohols*. Advanced Synthesis & Catalysis, 2007. **349**(10): p. 1555-1575.
389. Bähn, S., S. Imm, L. Neubert, M. Zhang, H. Neumann, and M. Beller, *The catalytic amination of alcohols*. ChemCatChem, 2011. **3**(12): p. 1853-1864.
390. Guillena, G., D.J. Ramon, and M. Yus, *Hydrogen autotransfer in the N-alkylation of amines and related compounds using alcohols and amines as electrophiles*. Chemical reviews, 2010. **110**(3): p. 1611-1641.
391. Gunanathan, C. and D. Milstein, *Applications of acceptorless dehydrogenation and related transformations in chemical synthesis*. Science, 2013. **341**(6143).
392. Leonard, J., A.J. Blacker, S.P. Marsden, M.F. Jones, K.R. Mulholland, and R. Newton, *A survey of the borrowing hydrogen approach to the synthesis of some pharmaceutically relevant intermediates*. Organic Process Research & Development, 2015. **19**(10): p. 1400-1410.

393. Trost, B.M., *Atom economy—a challenge for organic synthesis: homogeneous catalysis leads the way*. Angewandte Chemie International Edition in English, 1995. **34**(3): p. 259-281.
394. Grigg, R., T. Mitchell, S. Sutthivaiyakit, and N. Tongpenyai, *Transition metal-catalysed N-alkylation of amines by alcohols*. Journal of the Chemical Society, Chemical Communications, 1981(12): p. 611-612.
395. Fujita, K.-i., K. Yamamoto, and R. Yamaguchi, *Oxidative cyclization of amino alcohols catalyzed by a Cp* Ir complex. Synthesis of indoles, 1, 2, 3, 4-tetrahydroquinolines, and 2, 3, 4, 5-tetrahydro-1-benzazepine*. Organic letters, 2002. **4**(16): p. 2691-2694.
396. Hamid, M.H.S., C.L. Allen, G.W. Lamb, A.C. Maxwell, H.C. Maytum, A.J. Watson, and J.M. Williams, *Ruthenium-catalyzed N-alkylation of amines and sulfonamides using borrowing hydrogen methodology*. Journal of the American Chemical Society, 2009. **131**(5): p. 1766-1774.
397. Watanabe, Y., Y. Tsuji, H. Ige, Y. Ohsugi, and T. Ohta, *Ruthenium-catalyzed N-alkylation and N-benzylation of aminoarenes with alcohols*. The Journal of Organic Chemistry, 1984. **49**(18): p. 3359-3363.
398. Hamid, M.H.S. and J.M. Williams, *Ruthenium catalysed N-alkylation of amines with alcohols*. Chemical communications, 2007(7): p. 725-727.
399. Rösler, S., M. Ertl, T. Irrgang, and R. Kempe, *Cobalt-Catalyzed Alkylation of Aromatic Amines by Alcohols*. Angewandte Chemie International Edition, 2015. **54**(50): p. 15046-15050.
400. Gnanamgari, D., E.L. Sauer, N.D. Schley, C. Butler, C.D. Incarvito, and R.H. Crabtree, *Iridium and ruthenium complexes with chelating N-heterocyclic carbenes: efficient catalysts for transfer hydrogenation, β -alkylation of alcohols, and N-alkylation of amines*. Organometallics, 2008. **28**(1): p. 321-325.
401. Fujita, K.-i., Y. Enoki, and R. Yamaguchi, *Cp* Ir-catalyzed N-alkylation of amines with alcohols. A versatile and atom economical method for the synthesis of amines*. Tetrahedron, 2008. **64**(8): p. 1943-1954.
402. Li, F., H. Shan, Q. Kang, and L. Chen, *Regioselective N-alkylation of 2-aminobenzothiazoles with benzylic alcohols*. Chemical Communications, 2011. **47**(17): p. 5058-5060.
403. Yin, Z., H. Zeng, J. Wu, S. Zheng, and G. Zhang, *Cobalt-catalyzed synthesis of aromatic, aliphatic, and cyclic secondary amines via a "hydrogen-borrowing" strategy*. ACS Catalysis, 2016. **6**(10): p. 6546-6550.
404. Oshida, Y., *Bioscience and bioengineering of titanium materials*. 2010: Elsevier.
405. Linden, K. and M. Mohseni, *Advanced oxidation processes: applications in drinking water treatment*. 2014.

406. Hemond, H. F. and E. J. Fechner, *Chemical fate and transport in the environment*. 2014: Elsevier.
407. Kuik, M., L. Koster, G. Wetzelaer, and P. Blom, *Trap-assisted recombination in disordered organic semiconductors*. Physical review letters, 2011. **107**(25): p. 256805.
408. Jafari, T., E. Moharreri, A.S. Amin, R. Miao, W. Song, and S.L. Suib, *Photocatalytic water splitting—the untamed dream: a review of recent advances*. Molecules, 2016. **21**(7): p. 900.
409. Zaleska, A., *Doped-TiO₂: a review*. Recent patents on engineering, 2008. **2**(3): p. 157-164.
410. Kang, X., S. Liu, Z. Dai, Y. He, X. Song, and Z. Tan, *Titanium dioxide: from engineering to applications*. Catalysts, 2019. **9**(2): p. 191.
411. Jinfeng, Z., Y. Yunguang, and L. Wei, *Preparation, characterization, and activity evaluation of CuO/F-TiO₂ photocatalyst*. International Journal of Photoenergy, 2012. **2012**.
412. Pesci, F.M., G. Wang, D.R. Klug, Y. Li, and A.J. Cowan, *Efficient suppression of electron–hole recombination in oxygen-deficient hydrogen-treated TiO₂ nanowires for photoelectrochemical water splitting*. The Journal of Physical Chemistry C, 2013. **117**(48): p. 25837-25844.
413. Huang, F., A. Yan, and H. Zhao, *Influences of doping on photocatalytic properties of TiO₂ photocatalyst*. Semiconductor Photocatalysis—Materials, Mechanisms and Applications; Cao, W., Ed, 2016: p. 31-80.
414. Sivapatarnkun, J., K. Hathaisamit, and S. Pudwat, *High photocatalytic activity of F-TiO₂ on activated carbon*. Materials Today: Proceedings, 2017. **4**(5): p. 6495-6501.
415. Chen, Y., Y. Jiang, X. Wang, and Q. Deng. *Preparation And Photocatalytic Performance Of F-TiO₂ Photocatalyst*. in *IOP Conference Series: Earth and Environmental Science*. 2018. IOP Publishing.
416. Park, H. and W. Choi, *Effects of TiO₂ surface fluorination on photocatalytic reactions and photoelectrochemical behaviors*. The Journal of Physical Chemistry B, 2004. **108**(13): p. 4086-4093.
417. Fakhouri, H., F. Arefi-Khonsari, A. Jaiswal, and J. Pulpytel, *Enhanced visible light photoactivity and charge separation in TiO₂/TiN bilayer thin films*. Applied Catalysis A: General, 2015. **492**: p. 83-92.
418. Zhang, X., L. Zhang, T. Xie, and D. Wang, *Low-temperature synthesis and high visible-light-induced photocatalytic activity of BiOI/TiO₂ heterostructures*. The Journal of Physical Chemistry C, 2009. **113**(17): p. 7371-7378.
419. Guo, J., H. Zhou, S. Ouyang, T. Kako, and J. Ye, *An Ag₃PO₄/nitridized Sr₂Nb₂O₇ composite photocatalyst with adjustable band structures for efficient elimination of*

- gaseous organic pollutants under visible light irradiation*. *Nanoscale*, 2014. **6**(13): p. 7303-7311.
420. Wang, W.-S., H. Du, R.-X. Wang, T. Wen, and A.-W. Xu, *Heterostructured Ag₃PO₄/AgBr/Ag plasmonic photocatalyst with enhanced photocatalytic activity and stability under visible light*. *Nanoscale*, 2013. **5**(8): p. 3315-3321.
 421. Xiu, Z., H. Bo, Y. Wu, and X. Hao, *Graphite-like C₃N₄ modified Ag₃PO₄ nanoparticles with highly enhanced photocatalytic activities under visible light irradiation*. *Applied Surface Science*, 2014. **289**: p. 394-399.
 422. Zhang, L., H. Zhang, H. Huang, Y. Liu, and Z. Kang, *Ag₃PO₄/SnO₂ semiconductor nanocomposites with enhanced photocatalytic activity and stability*. *New Journal of Chemistry*, 2012. **36**(8): p. 1541-1544.
 423. Guo, J., S. Ouyang, H. Zhou, T. Kako, and J. Ye, *Ag₃PO₄/In (OH)₃ composite photocatalysts with adjustable surface-electric property for efficient photodegradation of organic dyes under simulated solar-light irradiation*. *The Journal of Physical Chemistry C*, 2013. **117**(34): p. 17716-17724.
 424. Yang, Z.-M., G.-F. Huang, W.-Q. Huang, J.-M. Wei, X.-G. Yan, Y.-Y. Liu, C. Jiao, Z. Wan, A. Pan, *Novel Ag₃PO₄/CeO₂ composite with high efficiency and stability for photocatalytic applications*. *Journal of Materials Chemistry A*, 2014. **2**(6): p. 1750-1756.
 425. Li, C., P. Zhang, R. Lv, J. Lu, T. Wang, S. Wang, H. Haifeng, J. Gong, *Selective deposition of Ag₃PO₄ on monoclinic BiVO₄ (040) for highly efficient photocatalysis*. *Small*, 2013. **9**(23): p. 3951-3956.
 426. Fu, G., G. Xu, S. Chen, L. Lei, and M. Zhang, *Ag₃PO₄/Bi₂WO₆ hierarchical heterostructures with enhanced visible light photocatalytic activity for the degradation of phenol*. *Catalysis Communications*, 2013. **40**: p. 120-124.
 427. Bhatia, V. and A. Dhir, *Transition metal doped TiO₂ mediated photocatalytic degradation of anti-inflammatory drug under solar irradiations*. *Journal of environmental chemical engineering*, 2016. **4**(1): p. 1267-1273.
 428. Khairy, M. and W. Zakaria, *Effect of metal-doping of TiO₂ nanoparticles on their photocatalytic activities toward removal of organic dyes*. *Egyptian Journal of Petroleum*, 2014. **23**(4): p. 419-426.
 429. Sökmen, M. and A. Özkan, *Decolourising textile wastewater with modified titania: the effects of inorganic anions on the photocatalysis*. *Journal of Photochemistry and Photobiology A: Chemistry*, 2002. **147**(1): p. 77-81.
 430. He, C., Y. Yu, X. Hu, and A. Larbot, *Influence of silver doping on the photocatalytic activity of titania films*. *Applied Surface Science*, 2002. **200**(1-4): p. 239-247.

431. Zhou, M., J. Yu, and B. Cheng, *Effects of Fe-doping on the photocatalytic activity of mesoporous TiO₂ powders prepared by an ultrasonic method*. Journal of hazardous materials, 2006. **137**(3): p. 1838-1847.
432. Zhang, Z., C.-C. Wang, R. Zakaria, and J.Y. Ying, *Role of particle size in nanocrystalline TiO₂-based photocatalysts*. The Journal of Physical Chemistry B, 1998. **102**(52): p. 10871-10878.
433. Li, C.W. and M.W. Kanan, *CO₂ reduction at low overpotential on Cu electrodes resulting from the reduction of thick Cu₂O films*. Journal of the American Chemical Society, 2012. **134**(17): p. 7231-7234.
434. Bak, T., J. Nowotny, M. Rekas, and C. Sorrell, *Photo-electrochemical hydrogen generation from water using solar energy. Materials-related aspects*. International journal of hydrogen energy, 2002. **27**(10): p. 991-1022.
435. Wu, J.C.-S. and C.-H. Chen, *A visible-light response vanadium-doped titania nanocatalyst by sol-gel method*. Journal of Photochemistry and Photobiology A: Chemistry, 2004. **163**(3): p. 509-515.
436. Mogal, S.I., M. Mishra, V.G. Gandhi, and R.J. Tayade. *Metal doped titanium dioxide: synthesis and effect of metal ions on physico-chemical and photocatalytic properties*. in *Materials Science Forum*. 2013. Trans Tech Publ. **734**: p. 364-378.
437. Chen, X., H. Sun, J. Zhang, Y. Guo, and D.-H. Kuo, *Cationic S-doped TiO₂/SiO₂ visible-light photocatalyst synthesized by co-hydrolysis method and its application for organic degradation*. Journal of Molecular Liquids, 2019. **273**: p. 50-57.
438. Tong, T., J. Zhang, B. Tian, F. Chen, and D. He, *Preparation of Fe³⁺-doped TiO₂ catalysts by controlled hydrolysis of titanium alkoxide and study on their photocatalytic activity for methyl orange degradation*. Journal of Hazardous Materials, 2008. **155**(3): p. 572-579.
439. Ali, T., A. Ahmed, U. Alam, I. Uddin, P. Tripathi, and M. Muneer, *Enhanced photocatalytic and antibacterial activities of Ag-doped TiO₂ nanoparticles under visible light*. Materials Chemistry and Physics, 2018. **212**: p. 325-335.
440. Santos, L.M., W.A. Machado, M.D. França, K.A. Borges, R.M. Paniago, A.O. Patrocínio, and A.E. Machado, *Structural characterization of Ag-doped TiO₂ with enhanced photocatalytic activity*. RSC advances, 2015. **5**(125): p. 103752-103759.
441. Lei, J., X. Li, W. Li, F. Sun, D. Lu, and Y. Lin, *Photocatalytic degradation of methyl orange on arrayed porous iron-doped anatase TiO₂*. Journal of Solid State Electrochemistry, 2012. **16**(2): p. 625-632.
442. Park, J.-Y., J.-J. Yun, C.-H. Hwang, and I.-H. Lee, *Influence of silver doping on the phase transformation and crystallite growth of electrospun TiO₂ nanofibers*. Materials Letters, 2010. **64**(24): p. 2692-2695.

443. Subramanian, V., E. Wolf, and P.V. Kamat, *Semiconductor– Metal composite nanostructures. To what extent do metal nanoparticles improve the photocatalytic activity of TiO₂ films?* The Journal of Physical Chemistry B, 2001. **105**(46): p. 11439-11446.
444. Li, Y., M. Ma, W. Chen, L. Li, and M. Zen, *Preparation of Ag-doped TiO₂ nanoparticles by a miniemulsion method and their photoactivity in visible light illuminations.* Materials Chemistry and Physics, 2011. **129**(1-2): p. 501-505.
445. Chao, H., Y. Yun, H. Xingfang, and A. Larbot, *Effect of silver doping on the phase transformation and grain growth of sol-gel titania powder.* Journal of the European Ceramic Society, 2003. **23**(9): p. 1457-1464.
446. Ravishankar, T., M.d.O. Vaz, and S. Teixeira, *The effects of surfactant in the sol–gel synthesis of CuO/TiO₂ nanocomposites on its photocatalytic activities under UV-visible and visible light illuminations.* New Journal of Chemistry, 2020. **44**(5): p. 1888-1904.
447. Nagaveni, K., M. Hegde, and G. Madras, *Structure and photocatalytic activity of Ti_{1-x}M_xO_{2±δ} (M= W, V, Ce, Zr, Fe, and Cu) synthesized by solution combustion method.* The Journal of Physical Chemistry B, 2004. **108**(52): p. 20204-20212.
448. Zhou, J., Y. Zhang, X. Zhao, and A.K. Ray, *Photodegradation of benzoic acid over metal-doped TiO₂.* Industrial & engineering chemistry research, 2006. **45**(10): p. 3503-3511.
449. Rahman, M., K. Krishna, T. Soga, T. Jimbo, and M. Umeno, *Optical properties and X-ray photoelectron spectroscopic study of pure and Pb-doped TiO₂ thin films.* Journal of Physics and Chemistry of Solids, 1999. **60**(2): p. 201-210.
450. Gerischer, H. and A. Heller, *The role of oxygen in photooxidation of organic molecules on semiconductor particles.* The Journal of Physical Chemistry, 1991. **95**(13): p. 5261-5267.
451. Mogal, S.I., V.G. Gandhi, M. Mishra, S. Tripathi, T. Shripathi, P.A. Joshi, and D.O. Shah, *Single-step synthesis of silver-doped titanium dioxide: influence of silver on structural, textural, and photocatalytic properties.* Industrial & Engineering Chemistry Research, 2014. **53**(14): p. 5749-5758.
452. Nainani, R., P. Thakur, and M. Chaskar, *Synthesis of silver doped TiO₂ nanoparticles for the improved photocatalytic degradation of methyl orange.* Journal of Materials Science and Engineering B, 2012. **2**(1): p. 52-58.
453. Cao, Y., H. Tan, T. Shi, T. Tang, and J. Li, *Preparation of Ag-doped TiO₂ nanoparticles for photocatalytic degradation of acetamiprid in water.* Journal of Chemical Technology & Biotechnology: International Research in Process, Environmental & Clean Technology, 2008. **83**(4): p. 546-552.

454. Hernandez, J.V., *Structural and Morphological modification of TiO₂ doped metal ions and investigation of photo-induced charge transfer processes*. 2017. <https://tel.archives-ouvertes.fr/tel-01954392>.
455. Li, X., P.-L. Yue, and C. Kotal, *Synthesis and photocatalytic oxidation properties of iron doped titanium dioxide nanosemiconductor particles*. New journal of chemistry, 2003. **27**(8): p. 1264-1269.
456. Yen, C.-C., D.-Y. Wang, L.-S. Chang, and H.C. Shih, *Characterization and photocatalytic activity of Fe-and N-co-deposited TiO₂ and first-principles study for electronic structure*. Journal of Solid State Chemistry, 2011. **184**(8): p. 2053-2060.
457. Li, X., J. Lu, Y. Dai, M. Guo, and B. Huang, *The Synthetic Effects of Iron with Sulfur and Fluorine on Photoabsorption and Photocatalytic Performance in Codoped*. International Journal of Photoenergy, 2012. **2012**.
458. Li, W., C. Ni, H. Lin, C. Huang, and S.I. Shah, *Size dependence of thermal stability of TiO₂ nanoparticles*. Journal of Applied Physics, 2004. **96**(11): p. 6663-6668.
459. Hirano, M., T. Joji, M. Inagaki, and H. Iwata, *Direct Formation of Iron (III)-Doped Titanium Oxide (Anatase) by Thermal Hydrolysis and Its Structural Property*. Journal of the American Ceramic Society, 2004. **87**(1): p. 35-41.
460. Zhu, J., W. Zheng, B. He, J. Zhang, and M. Anpo, *Characterization of Fe–TiO₂ photocatalysts synthesized by hydrothermal method and their photocatalytic reactivity for photodegradation of XRG dye diluted in water*. Journal of Molecular Catalysis A: Chemical, 2004. **216**(1): p. 35-43.
461. Yu, J., M. Zhou, H. Yu, Q. Zhang, and Y. Yu, *Enhanced photoinduced super-hydrophilicity of the sol–gel-derived TiO₂ thin films by Fe-doping*. Materials Chemistry and Physics, 2006. **95**(2-3): p. 193-196.
462. Meng, H., B. Wang, S. Liu, R. Jiang, and H. Long, *Hydrothermal preparation, characterization and photocatalytic activity of TiO₂/Fe–TiO₂ composite catalysts*. Ceramics international, 2013. **39**(5): p. 5785-5793.
463. Abazović, N.D., L. Mirengi, I.A. Janković, N. Bibić, D.V. Šojić, B.F. Abramović, and M.I. Čomor, *Synthesis and characterization of rutile TiO₂ nanopowders doped with iron ions*. Nanoscale research letters, 2009. **4**(6): p. 518.
464. Li, L., C.-y. Liu, and Y. Liu, *Study on activities of vanadium (IV/V) doped TiO₂ (R) nanorods induced by UV and visible light*. Materials Chemistry and Physics, 2009. **113**(2-3): p. 551-557.
465. Shi, Z.-L., C. Du, and S.-H. Yao, *Preparation and photocatalytic activity of cerium doped anatase titanium dioxide coated magnetite composite*. Journal of the Taiwan Institute of Chemical Engineers, 2011. **42**(4): p. 652-657.

466. Sernelius, B.E., K.-F. Berggren, Z.-C. Jin, I. Hamberg, and C.G. Granqvist, *Band-gap tailoring of ZnO by means of heavy Al doping*. Physical Review B, 1988. **37**(17): p. 10244.
467. Litter, M. and J.A. Navio, *Photocatalytic properties of iron-doped titania semiconductors*. Journal of Photochemistry and Photobiology A: Chemistry, 1996. **98**(3): p. 171-181.
468. Zhang, H., X. Lv, Y. Li, Y. Wang, and J. Li, *P25-graphene composite as a high performance photocatalyst*. ACS nano, 2010. **4**(1): p. 380-386.
469. Yu, J.C., W. Ho, J. Lin, H. Yip, and P.K. Wong, *Photocatalytic activity, antibacterial effect, and photoinduced hydrophilicity of TiO₂ films coated on a stainless steel substrate*. Environmental science & technology, 2003. **37**(10): p. 2296-2301.
470. Choi, W., A. Termin, and M.R. Hoffmann, *Effects of metal-ion dopants on the photocatalytic reactivity of quantum-sized TiO₂ particles*. Angewandte Chemie International Edition in English, 1994. **33**(10): p. 1091-1092.
471. Khalid, N., Z. Hong, E. Ahmed, Y. Zhang, H. Chan, and M. Ahmad, *Synergistic effects of Fe and graphene on photocatalytic activity enhancement of TiO₂ under visible light*. Applied Surface Science, 2012. **258**(15): p. 5827-5834.
472. Ding, X.-Z., X.-H. Liu, and Y.-Z. He, *Grain size dependence of anatase-to-rutile structural transformation in gel-derived nanocrystalline titania powders*. Journal of materials science letters, 1996. **15**(20): p. 1789-1791.
473. Zhou, W., Q. Liu, Z. Zhu, and J. Zhang, *Preparation and properties of vanadium-doped TiO₂ photocatalysts*. Journal of Physics D: Applied Physics, 2010. **43**(3): p. 035301.
474. Jie, H., H. Park, K.B. Lee, H.J. Chang, J.P. Ahn, and J.K. Park, *A new absorption band and visible absorption properties in V-doped TiO₂ nanopowder*. Surface and interface analysis, 2012. **44**(11-12): p. 1449-1452.
475. Zhang, D.R., H.L. Liu, S.Y. Han, and W.X. Piao, *Synthesis of Sc and V-doped TiO₂ nanoparticles and photodegradation of rhodamine-B*. Journal of Industrial and Engineering Chemistry, 2013. **19**(6): p. 1838-1844.
476. Yu, J.-H., S.-H. Nam, J.W. Lee, D.I. Kim, and J.-H. Boo, *Oxidation state and structural studies of vanadium-doped titania particles for the visible light-driven photocatalytic activity*. Applied Surface Science, 2019. **472**: p. 46-53.
477. Liu, J., R. Han, Y. Zhao, H. Wang, W. Lu, T. Yu, and Y. Zhang, *Enhanced photoactivity of V- N codoped TiO₂ derived from a two-step hydrothermal procedure for the degradation of PCP- Na under visible light irradiation*. The Journal of Physical Chemistry C, 2011. **115**(11): p. 4507-4515.

478. Jaiswal, R., N. Patel, D. Kothari, and A. Miotello, *Improved visible light photocatalytic activity of TiO₂ co-doped with Vanadium and Nitrogen*. Applied Catalysis B: Environmental, 2012. **126**: p. 47-54.
479. Wang, B., G. Zhang, X. Leng, Z. Sun, and S. Zheng, *Characterization and improved solar light activity of vanadium doped TiO₂/diatomite hybrid catalysts*. Journal of hazardous materials, 2015. **285**: p. 212-220.
480. Liu, W., S. Wang, J. Zhang, and J. Fan, *Photocatalytic degradation of vehicle exhausts on asphalt pavement by TiO₂/rubber composite structure*. Construction and Building Materials, 2015. **81**: p. 224-232.
481. Zhao, L., M. Han, and J. Lian, *Photocatalytic activity of TiO₂ films with mixed anatase and rutile structures prepared by pulsed laser deposition*. Thin Solid Films, 2008. **516**(10): p. 3394-3398.
482. Xin, B., L. Jing, Z. Ren, B. Wang, and H. Fu, *Effects of simultaneously doped and deposited Ag on the photocatalytic activity and surface states of TiO₂*. The Journal of Physical Chemistry B, 2005. **109**(7): p. 2805-2809.
483. Devi, L.G., B.N. Murthy, and S.G. Kumar, *Photocatalytic activity of TiO₂ doped with Zn²⁺ and V⁵⁺ transition metal ions: Influence of crystallite size and dopant electronic configuration on photocatalytic activity*. Materials Science and Engineering: B, 2010. **166**(1): p. 1-6.
484. Feng, H., M.-H. Zhang, and E.Y. Liya, *Hydrothermal synthesis and photocatalytic performance of metal-ions doped TiO₂*. Applied Catalysis A: General, 2012. **413**: p. 238-244.
485. Sahoo, C., A. Gupta, and A. Pal, *Photocatalytic degradation of Crystal Violet (CI Basic Violet 3) on silver ion doped TiO₂*. Dyes and Pigments, 2005. **66**(3): p. 189-196.
486. Pollard, D.J. and J.M. Woodley, *Biocatalysis for pharmaceutical intermediates: the future is now*. TRENDS in Biotechnology, 2007. **25**(2): p. 66-73.
487. Sebastian, J., K.M. Jinka, and R.V. Jasra, *Effect of alkali and alkaline earth metal ions on the catalytic epoxidation of styrene with molecular oxygen using cobalt (II)-exchanged zeolite X*. Journal of Catalysis, 2006. **244**(2): p. 208-218.
488. Tong, K.H., *Green approaches to catalytic epoxidation of olefins*. 2004: Hong Kong Polytechnic University (Hong Kong).
489. Cejka, J., H. Van Bekkum, A. Corma, and F. Schueth, *in Studies in Surface Science and Catalysis*. Vol. 168. 2007: Elsevier.
490. Mingjuan, S., Z. Guojun, X. Shan, and W. Xiaolai, *Effect of Structure of CeOHCO₃ Precursor of CeO₂ on Its Catalytic Performance*. Chinese journal of Catalysis, 2012. **33**(7-8): p. 1318-1325.

491. Sahoo*, S., M. Mohapatra, A. Singh, and S. Anand, *Hydrothermal synthesis of single crystalline nano CeO₂ and its structural, optical, and electronic characterization*. Materials and Manufacturing Processes, 2010. **25**(9): p. 982-989.
492. Bäckvall, J.-E., *Modern oxidation methods*. 2011: John Wiley & Sons.
493. Sutradhar, M. and A.J. Pombeiro, *Vanadium complexes in catalytic oxidations*. 2017.
494. SCARSO, A. and G. STRUKUL, *Sustainability trends in homogeneous catalytic oxidations*, in *HANDBOOK OF ADVANCED METHODS AND PROCESSES IN OXIDATION CATALYSIS: From Laboratory to Industry*. 2014, World Scientific. p. 679-766.
495. Rode, C., U. Nehete, and M. Dongare, *Alkali promoted selective epoxidation of styrene to styrene oxide using TS-1 catalyst*. Catalysis Communications, 2003. **4**(8): p. 365-369.
496. Fernandes, C.I., P.D. Vaz, T.G. Nunes, and C.D. Nunes, *Zinc biomimetic catalysts for epoxidation of olefins with H₂O₂*. Applied Clay Science, 2020. **190**: p. 105562.
497. Cejka, J. and H. van Bekkum, *Studies in Surface Science and Catalysis*. Vol. 157. 2005: Elsevier.
498. Li, X. and C. Kotal, *Photocatalytic selective epoxidation of styrene by molecular oxygen over highly dispersed titanium dioxide species on silica*. Journal of materials science letters, 2002. **21**(19): p. 1525-1527.
499. Fox, M.A. and C.-C. Chen, *Mechanistic features of the semiconductor photocatalyzed olefin-to-carbonyl oxidative cleavage*. Journal of the American Chemical Society, 1981. **103**(22): p. 6757-6759.
500. Liao, S. and B. List, *Asymmetric Counteranion-Directed Transition-Metal Catalysis: Enantioselective Epoxidation of Alkenes with Manganese (III) Salen Phosphate Complexes*. Angewandte Chemie International Edition, 2010. **49**(3): p. 628-631.
501. Mayer, S. and B. List, *Asymmetric counteranion-directed catalysis*. Angewandte Chemie International Edition, 2006. **45**(25): p. 4193-4195.
502. Martin, N.J. and B. List, *Highly enantioselective transfer hydrogenation of α , β -unsaturated ketones*. Journal of the American Chemical Society, 2006. **128**(41): p. 13368-13369.
503. Ma, L., F. Su, X. Zhang, D. Song, Y. Guo, and J. Hu, *Epoxidation of alkenes catalyzed by highly ordered mesoporous manganese–salen-based hybrid catalysts*. Microporous and mesoporous materials, 2014. **184**: p. 37-46.
504. Rosati, F. and G. Roelfes, *Artificial metalloenzymes*. ChemCatChem, 2010. **2**(8): p. 916-927.

505. Mor, G.K., K. Shankar, M. Paulose, O.K. Varghese, and C.A. Grimes, *Use of highly-ordered TiO₂ nanotube arrays in dye-sensitized solar cells*. Nano letters, 2006. **6**(2): p. 215-218.
506. Zhu, K., N.R. Neale, A. Miedaner, and A.J. Frank, *Enhanced charge-collection efficiencies and light scattering in dye-sensitized solar cells using oriented TiO₂ nanotubes arrays*. Nano letters, 2007. **7**(1): p. 69-74.
507. Nakata, K. and A. Fujishima, *TiO₂ photocatalysis: Design and applications*. Journal of photochemistry and photobiology C: Photochemistry Reviews, 2012. **13**(3): p. 169-189.
508. Tang, J., N. Qin, Y. Chong, Y. Diao, Z. Wang, T. Xue, M. Jiang, J. Zhang, G. Zheng, *Nanowire arrays restore vision in blind mice*. Nature communications, 2018. **9**(1): p. 1-13.
509. Romero, N.A. and D.A. Nicewicz, *Organic photoredox catalysis*. Chemical reviews, 2016. **116**(17): p. 10075-10166.
510. Kolmakov, A. and M. Moskovits, *Chemical sensing and catalysis by one-dimensional metal-oxide nanostructures*. Annu. Rev. Mater. Res., 2004. **34**: p. 151-180.
511. Ling, D., M.J. Hackett, and T. Hyeon, *Surface ligands in synthesis, modification, assembly and biomedical applications of nanoparticles*. Nano Today, 2014. **9**(4): p. 457-477.
512. Nguyen, L.A., H. He, and C. Pham-Huy, *Chiral drugs: an overview*. International journal of biomedical science: IJBS, 2006. **2**(2): p. 85.
513. Besse, P. and H. Veschambre, *Chemical and biological synthesis of chiral epoxides*. Tetrahedron, 1994. **50**(30): p. 8885-8927.
514. Katsuki, T. and K.B. Sharpless, *The first practical method for asymmetric epoxidation*. Journal of the American Chemical Society, 1980. **102**(18): p. 5974-5976.
515. Zhang, W., J.L. Loebach, S.R. Wilson, and E.N. Jacobsen, *Enantioselective epoxidation of unfunctionalized olefins catalyzed by salen manganese complexes*. Journal of the American Chemical Society, 1990. **112**(7): p. 2801-2803.
516. Finn, M. and K.B. Sharpless, *Mechanism of asymmetric epoxidation. 2. Catalyst structure*. Journal of the American Chemical Society, 1991. **113**(1): p. 113-126.
517. Jacobsen, E.N., W. Zhang, A.R. Muci, J.R. Ecker, and L. Deng, *Highly enantioselective epoxidation catalysts derived from 1, 2-diaminocyclohexane*. Journal of the American Chemical Society, 1991. **113**(18): p. 7063-7064.
518. Cozzi, P.G., *Metal-Salen Schiff base complexes in catalysis: practical aspects*. Chemical Society Reviews, 2004. **33**(7): p. 410-421.
519. Ghosh, B.K., D. Moitra, M. Chandel, H. Lulla, and N.N. Ghosh, *Ag nanoparticle immobilized mesoporous TiO₂-cobalt ferrite nanocatalyst: A highly active, versatile,*

- magnetically separable and reusable catalyst*. Materials Research Bulletin, 2017. **94**: p. 361-370.
520. Fox, M. and M. Dulay, *Chem. Re V.* 1993, 93, 341–357.(c) Fox, MA. Acc. Chem. Res, 1983. **16**: p. 314-321.
 521. Ohno, T., K. Nakabeya, and M. Matsumura, *Epoxidation of olefins on photoirradiated titanium dioxide powder using molecular oxygen as an oxidant*. Journal of Catalysis, 1998. **176**(1): p. 76-81.
 522. Lin, H., J. Qiao, Y. Liu, and Z.-L. Wu, *Styrene monooxygenase from Pseudomonas sp. LQ26 catalyzes the asymmetric epoxidation of both conjugated and unconjugated alkenes*. Journal of Molecular Catalysis B: Enzymatic, 2010. **67**(3-4): p. 236-241.
 523. Katsuki, T., *Mn-salen catalyst, competitor of enzymes, for asymmetric epoxidation*. Journal of Molecular Catalysis A: Chemical, 1996. **113**(1-2): p. 87-107.
 524. Campbell, K.A., M.R. Lashley, J.K. Wyatt, M.H. Nantz, and R.D. Britt, *Dual-mode EPR study of Mn (III) salen and the Mn (III) salen-catalyzed epoxidation of cis- β -methylstyrene*. Journal of the American Chemical Society, 2001. **123**(24): p. 5710-5719.
 525. Tang, H., F. Levy, H. Berger, and P. Schmid, *Urbach tail of anatase TiO₂*. Physical Review B, 1995. **52**(11): p. 7771.
 526. Palucki, M., N.S. Finney, P.J. Pospisil, M.L. Güler, T. Ishida, and E.N. Jacobsen, *The mechanistic basis for electronic effects on enantioselectivity in the (salen) Mn (III)-catalyzed epoxidation reaction*. Journal of the American Chemical Society, 1998. **120**(5): p. 948-954.
 527. Finney, N.S., P.J. Pospisil, S. Chang, M. Palucki, R.G. Konsler, K.B. Hansen, and E.N. Jacobsen, *On the Viability of Oxametallacyclic Intermediates in the (salen) Mn-Catalyzed Asymmetric Epoxidation*. Angewandte Chemie International Edition in English, 1997. **36**(16): p. 1720-1723.
 528. Linde, C., M. Arnold, B. Åkermark, and P.O. Norrby, *Is There a Radical Intermediate in the (salen) Mn-Catalyzed Epoxidation of Alkenes?* Angewandte Chemie International Edition in English, 1997. **36**(16): p. 1723-1725.